



National Library
of Canada

Bibliothèque nationale
du Canada

Canadian Theses Service

Service des thèses canadiennes

Ottawa, Canada
K1A 0N4

NOTICE

The quality of this microform is heavily dependent upon the quality of the original thesis submitted for microfilming. Every effort has been made to ensure the highest quality of reproduction possible.

If pages are missing, contact the university which granted the degree.

Some pages may have indistinct print especially if the original pages were typed with a poor typewriter ribbon or if the university sent us an inferior photocopy.

Reproduction in full or in part of this microform is governed by the Canadian Copyright Act, R.S.C. 1970, c. C-30, and subsequent amendments.

AVIS

La qualité de cette microforme dépend grandement de la qualité de la thèse soumise au microfilmage. Nous avons tout fait pour assurer une qualité supérieure de reproduction.

S'il manque des pages, veuillez communiquer avec l'université qui a conféré le grade.

La qualité d'impression de certaines pages peut laisser à désirer, surtout si les pages originales ont été dactylographiées à l'aide d'un ruban usé ou si l'université nous a fait parvenir une photocopie de qualité inférieure.

La reproduction, même partielle, de cette microforme est soumise à la Loi canadienne sur le droit d'auteur, SRC 1970, c. C-30, et ses amendements subséquents.

UNIVERSITY OF ALBERTA

AN EXPERIMENTAL INVESTIGATION AND
K- ϵ TURBULENCE MODELLING OF SUBMERGED HYDRAULIC JUMPS

BY

DEJIANG LONG

A THESIS

SUBMITTED TO THE FACULTY OF GRADUATE STUDIES AND RESEARCH
IN PARTIAL FULFILLMENT OF THE REQUIREMENTS FOR THE DEGREE
OF DOCTOR OF PHILOSOPHY

DEPARTMENT OF CIVIL ENGINEERING

EDMONTON, ALBERTA

SPRING, 1991



National Library
of Canada

Bibliothèque nationale
du Canada

Canadian Theses Service Service des thèses canadiennes

Ottawa, Canada
K1A 0N4

The author has granted an irrevocable non-exclusive licence allowing the National Library of Canada to reproduce, loan, distribute or sell copies of his/her thesis by any means and in any form or format, making this thesis available to interested persons.

The author retains ownership of the copyright in his/her thesis. Neither the thesis nor substantial extracts from it may be printed or otherwise reproduced without his/her permission.

L'auteur a accordé une licence irrévocable et non exclusive permettant à la Bibliothèque nationale du Canada de reproduire, prêter, distribuer ou vendre des copies de sa thèse de quelque manière et sous quelque forme que ce soit pour mettre des exemplaires de cette thèse à la disposition des personnes intéressées.

L'auteur conserve la propriété du droit d'auteur qui protège sa thèse. Ni la thèse ni des extraits substantiels de celle-ci ne doivent être imprimés ou autrement reproduits sans son autorisation.

ISBN 0-315-66804-0

Canada

October 29, 1990

Faculty of Graduate Studies and Research
University of Alberta
Edmonton, Alberta

To Whom It May Concern:

This is to certify that Mr. Dejiang Long has my permission to use a few figures from my previous publications for his Ph.D. thesis entitled "An Experimental Investigation and K- ϵ Turbulence Modelling of Submerged Hydraulic Jumps".

Sincerely Yours,

A handwritten signature in black ink, appearing to read 'P. M. Steffler', written in a cursive style.

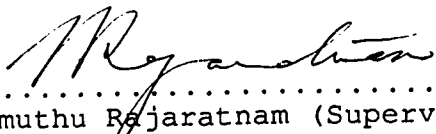
P. M. Steffler


Department of Civil Engineering
University of Alberta
Edmonton, Alberta

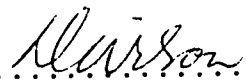
UNIVERSITY OF ALBERTA

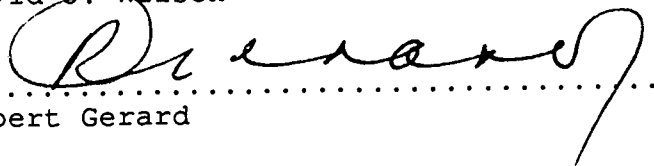
FACULTY OF GRADUATE STUDIES AND RESEARCH


The undersigned certify that they have read, and recommend to the Faculty of Graduate Studies and Research for acceptance, a thesis entitled AN EXPERIMENTAL INVESTIGATION AND K-ε TURBULENCE MODELLING OF SUBMERGED HYDRAULIC JUMPS submitted by DEJIANG LONG in partial fulfillment of the requirements for the degree of DOCTOR OF PHILOSOPHY.


.....
Nallamuthu Rajaratnam (Supervisor)


.....
Peter M. Steffler (Co-supervisor)


.....
David J. Wilson


.....
Robert Gerard


.....
Rangaswami Narayanan (External)
Department of Civil and Structural
Engineering, University of Manchester,
Manchester, England

Date *29 Oct 90*

ABSTRACT

Hydraulic jumps, which constitute the rapid transition from supercritical to subcritical flow, have been investigated extensively by many researchers, because of their importance in energy dissipation. The present knowledge on this subject has been reviewed with the objective of summarizing the major contributions. The following conclusions are formulated: the experimental measurements on detailed internal flow structure of hydraulic jumps are limited; and the existing prediction methods can only predict the macroscopic aspects of hydraulic jumps and some features of the mean velocity field.

Detailed measurements of the internal flow characteristics of submerged hydraulic jumps in a horizontal and rectangular channel have been made by the LDA (Laser Doppler Anemometry) system. The experiments have covered ten conditions with the submergence factor S varying from about 0.2 to about 1.7 and inlet Froude number F_1 approximately equal to 3, 5.5 and 8. The experimental measurements include surface profiles, mean velocity components u and v , turbulence shear stress $-\overline{u'v'}$ and turbulence intensities $\sqrt{u'^2}$ and $\sqrt{v'^2}$. Major flow characteristics of submerged hydraulic jumps are discussed and analyzed. The flow in the fully developed region is found to have some degree of similarity. It is also found that a submerged jump is three dimensional in nature due to the aspect ratio influence. The

roller lengths from the measurements have been compared with those predicted by Stepanov's equation.

The two dimensional κ - ϵ turbulence model is applied to predict the characteristics of submerged hydraulic jumps. An offset control volume method is originally proposed and applied in this study. Further, the numerical prediction is compared with the experimental measurements for three conditions with supercritical Froude numbers F_1 ranging from 3.2 to 8.2 and submergence factors S ranging from 0.24 to 0.85. The prediction from κ - ϵ model has also been compared with that from the integral SIM method. Finally the numerical performance is evaluated and discussed in detail. It is concluded that the model is quite promising in predicting the surface profile, mean velocity field and turbulence structure of submerged hydraulic jumps, even though it has the following shortcomings: overpredicted turbulence production for the initial part of shear layer, no curvature effects on turbulence, inadequacy of gradient diffusion assumption near maximum velocity region and isotropic assumption not representing the normal stresses properly.

ACKNOWLEDGEMENTS

The author is greatly indebted to his supervisor Dr. N. Rajaratnam for his guidance, encouragement, understanding and support throughout this research program. It is his great appreciation for the subject and sincere help to his student that made this research project successful.

The author is also deeply grateful to his co-supervisor Dr. P. M. Steffler for his inspiration, advice and patience in coping with the tough problems in both the numerical and experimental parts of this study.

The tremendous assistance and productive advice of S. Lovell and S. Lodewyk with the experiment is especially appreciated. The warm friendships showed by all his colleagues during his stay at T. Blench Hydraulics Laboratory are also truly appreciated.

This thesis is dedicated to his wife Huilian. Without her love, patience, understanding and support, the completion of this program would be unimaginable.

This study was financially supported by a grant from the Canadian Natural Science and Engineering Research Council to N. Rajaratnam. The scholarship from the Chinese Education Ministry and the Edmonton Campus Scholarship from the University of Alberta awarded to the author during this study are also acknowledged.

TABLE OF CONTENTS

INTRODUCTION.....	1
PART ONE - LITERATURE REVIEW.....	3
1.1 Introduction.....	3
1.2 Theoretical Framework.....	4
1.2.1 Introduction.....	4
1.2.2 Governing Equations.....	5
1.2.3 Belanger Equation.....	6
1.2.4 Integral Momentum Equation.....	7
1.2.5 Integral Energy Equation.....	9
1.3 Experimental Studies.....	11
1.3.1 Introduction.....	11
1.3.2 Main Length characteristics.....	12
1.3.3 Mean Velocity Field.....	13
1.3.4 Main Flow characteristics.....	14
1.3.5 Wall Shear Stress.....	15
1.3.6 Air Model of Free Jumps.....	16
1.3.7 Water Model of Free Jumps.....	18
1.3.8 Summary.....	19
1.4 Prediction Methods.....	20
1.4.1 Introduction.....	20
1.4.2 Narayanan's Method.....	21
1.4.3 The Method of McCorquodale and Khalifa.....	22
1.4.4 The Method of Madsen and Svendsen.....	24
1.4.5 Turbulence Modelling.....	27

1.4.5.1 Strategies.....	27
1.4.5.2 Basic Concepts.....	28
1.4.5.3 Zero Equation Model.....	29
1.4.5.4 One Equation Model.....	30
1.4.5.5 Two Equation Model.....	32
1.4.5.6 Reynolds Stress Model.....	34
1.4.6 Summary.....	34
1.5 Objectives.....	35
PART TWO - LDA EXPERIMENTAL STUDIES.....	37
2.1 Introduction.....	37
2.2 Facilities.....	39
2.2.1 Experimental Arrangement.....	39
2.2.2 Measuring Equipment.....	40
2.3 Experimental Results.....	42
2.4 Discussion and Analysis.....	45
2.4.1 Experimental errors.....	45
2.4.2 Inlet Condition.....	51
2.4.3 Major Flow Characteristics.....	52
2.4.4 An Equation for the Length Scale L.....	55
2.4.5 Fully Developed Region.....	59
2.4.6 Three Dimensional Features.....	62
2.5 Conclusions.....	67
PART THREE - NUMERICAL STUDIES USING K- ϵ	
TURBULENCE MODEL.....	70
3.1 Introduction.....	70

3.2 Problem Formulation.....	72
3.2.1 Governing Equations.....	72
3.2.2 Boundary Conditions.....	74
3.2.2.1 Inlet Conditions.....	74
3.2.2.2 Outlet Conditions.....	74
3.2.2.3 Surface Conditions.....	75
3.2.2.4 Wall Conditions.....	75
3.3 Offset Control Volume Method.....	77
3.4 Hybrid Numerical Scheme.....	83
3.5 Solution Algorithm.....	85
3.6 Results and Discussion.....	87
3.7 Comparison of κ - ϵ model and SIM.....	96
3.8 Conclusions.....	102
CONCLUSION.....	106
REFERENCES.....	255
APPENDIX A - FINITE DIFFERENCE EQUATIONS.....	262
APPENDIX B - COMPUTER PROGRAM OF κ - ϵ MODEL	270
APPENDIX C - ORDINARY DIFFERENTIAL EQUATIONS OF SIM.....	311
APPENDIX D - COMPUTER PROGRAM OF SIM.....	314

LIST OF TABLES

Table	page
1. Maximum turbulence quantities of hydraulic jumps from Leutheusser et al	112
2. Constants in K- ϵ turbulence model	113
3. Experimental conditions	114
4. Surface profile measurements	115
5. Lengths of the rollers	116

LIST OF FIGURES

Figure	Page
1. Schematic diagram of a classical free hydraulic jump	117
2. Schematic diagram of a classical submerged hydraulic jump	118
3. Main length characteristics (Courtesy of N. Rajaratnam)	119
4. Similarity of velocity profiles for free jumps (Courtesy of N. Rajaratnam)	120
5. Similarity of velocity profiles for submerged jumps (Courtesy of N. Rajaratnam)	121
6. A typical longitudinal velocity distribution	122
7. Main flow characteristics for free jumps (Courtesy of N. Rajaratnam)	123
8. Main flow characteristics for submerged jumps (Courtesy of N. Rajaratnam)	124
9. Wall shear stress for free jumps (Courtesy of N. Rajaratnam)	125
10. Wall shear stress for submerged jumps (Courtesy of N. Rajaratnam)	126
11. Layer model of longitudinal velocity distribution	127
12. Model definition of a free jump	128
13. Schematic diagram of experimental layout	129
14. Schematic diagram of LDA setup (Courtesy of P. M. Steffler)	130
15. Surface profiles for all conditions	131
16. u/U_1 distribution over the depth at the plane of $z/W=0.36$ for $F_1=3.11$ and $S=0.26$	132
17. u/U_1 distribution over the depth at the plane of $z/W=0.36$ for $F_1=3.20$ and $S=0.53$	133
18. u/U_1 distribution over the depth at the plane of $z/W=0.36$ for $F_1=3.19$ and $S=0.85$	134

19.	u/U_1 distribution over the depth at the plane of $z/W=0.36$ for $F_1=3.01$ and $S=1.69$	135
20.	u/U_1 distribution over the depth at the plane of $z/W=0.36$ for $F_1=5.61$ and $S=0.22$	136
21.	u/U_1 distribution over the depth at the plane of $z/W=0.36$ for $F_1=5.49$ and $S=0.63$	137
22.	u/U_1 distribution over the depth at the plane of $z/W=0.36$ for $F_1=5.43$ and $S=1.01$	138
23.	u/U_1 distribution over the depth at the plane of $z/W=0.36$ for $F_1=8.19$ and $S=0.22$	139
24.	u/U_1 distribution over the depth at the plane of $z/W=0.36$ for $F_1=8.00$ and $S=0.62$	140
25.	u/U_1 distribution over the depth at the plane of $z/W=0.36$ for $F_1=8.11$ and $S=1.00$	141
26.	v/U_1 distribution over the depth at the plane of $z/W=0.36$ for $F_1=3.11$ and $S=0.26$	142
27.	v/U_1 distribution over the depth at the plane of $z/W=0.36$ for $F_1=3.20$ and $S=0.53$	143
28.	v/U_1 distribution over the depth at the plane of $z/W=0.36$ for $F_1=3.19$ and $S=0.85$	144
29.	v/U_1 distribution over the depth at the plane of $z/W=0.36$ for $F_1=3.01$ and $S=1.69$	145
30.	v/U_1 distribution over the depth at the plane of $z/W=0.36$ for $F_1=5.61$ and $S=0.22$	146
31.	v/U_1 distribution over the depth at the plane of $z/W=0.36$ for $F_1=5.49$ and $S=0.63$	147
32.	v/U_1 distribution over the depth at the plane of $z/W=0.36$ for $F_1=5.43$ and $S=1.01$	148
33.	v/U_1 distribution over the depth at the plane of $z/W=0.36$ for $F_1=8.19$ and $S=0.22$	149
34.	v/U_1 distribution over the depth at the plane of $z/W=0.36$ for $F_1=8.00$ and $S=0.62$	150

35.	v/U_1 distribution over the depth at the plane of $z/W=0.36$ for $F_1=8.11$ and $S=1.00$	151
36.	$\sqrt{u'^2}/U_1$ distribution over the depth at the plane of $z/W=0.36$ for $F_1=3.11$ and $S=0.26$	152
37.	$\sqrt{u'^2}/U_1$ distribution over the depth at the plane of $z/W=0.36$ for $F_1=3.20$ and $S=0.53$	153
38.	$\sqrt{u'^2}/U_1$ distribution over the depth at the plane of $z/W=0.36$ for $F_1=3.19$ and $S=0.85$	154
39.	$\sqrt{u'^2}/U_1$ distribution over the depth at the plane of $z/W=0.36$ for $F_1=3.01$ and $S=1.69$	155
40.	$\sqrt{u'^2}/U_1$ distribution over the depth at the plane of $z/W=0.36$ for $F_1=5.61$ and $S=0.22$	156
41.	$\sqrt{u'^2}/U_1$ distribution over the depth at the plane of $z/W=0.36$ for $F_1=5.49$ and $S=0.63$	157
42.	$\sqrt{u'^2}/U_1$ distribution over the depth at the plane of $z/W=0.36$ for $F_1=5.43$ and $S=1.01$	158
43.	$\sqrt{u'^2}/U_1$ distribution over the depth at the plane of $z/W=0.36$ for $F_1=8.19$ and $S=0.22$	159
44.	$\sqrt{u'^2}/U_1$ distribution over the depth at the plane of $z/W=0.36$ for $F_1=8.00$ and $S=0.62$	160
45.	$\sqrt{u'^2}/U_1$ distribution over the depth at the plane of $z/W=0.36$ for $F_1=8.11$ and $S=1.00$	161
46.	$\sqrt{v'^2}/U_1$ distribution over the depth at the plane of $z/W=0.36$ for $F_1=3.11$ and $S=0.26$	162
47.	$\sqrt{v'^2}/U_1$ distribution over the depth at the plane of $z/W=0.36$ for $F_1=3.20$ and $S=0.53$	163
48.	$\sqrt{v'^2}/U_1$ distribution over the depth at the plane of $z/W=0.36$ for $F_1=3.19$ and $S=0.85$	164
49.	$\sqrt{v'^2}/U_1$ distribution over the depth at the plane of $z/W=0.36$ for $F_1=3.01$ and $S=1.69$	165

50.	$\sqrt{v'^2}/U_1$ distribution over the depth at the plane of $z/W=0.36$ for $F_1=5.61$ and $S=0.22$	166
51.	$\sqrt{v'^2}/U_1$ distribution over the depth at the plane of $z/W=0.36$ for $F_1=5.49$ and $S=0.63$	167
52.	$\sqrt{v'^2}/U_1$ distribution over the depth at the plane of $z/W=0.36$ for $F_1=5.43$ and $S=1.01$	168
53.	$\sqrt{v'^2}/U_1$ distribution over the depth at the plane of $z/W=0.36$ for $F_1=8.19$ and $S=0.22$	169
54.	$\sqrt{v'^2}/U_1$ distribution over the depth at the plane of $z/W=0.36$ for $F_1=8.00$ and $S=0.62$	170
55.	$\sqrt{v'^2}/U_1$ distribution over the depth at the plane of $z/W=0.36$ for $F_1=8.11$ and $S=1.00$	171
56.	$-\overline{u'v'}/U_1^2$ distribution over the depth at the plane of $z/W=0.36$ for $F_1=3.11$ and $S=0.26$	172
57.	$-\overline{u'v'}/U_1^2$ distribution over the depth at the plane of $z/W=0.36$ for $F_1=3.20$ and $S=0.53$	173
58.	$-\overline{u'v'}/U_1^2$ distribution over the depth at the plane of $z/W=0.36$ for $F_1=3.19$ and $S=0.85$	174
59.	$-\overline{u'v'}/U_1^2$ distribution over the depth at the plane of $z/W=0.36$ for $F_1=3.01$ and $S=1.69$	175
60.	$-\overline{u'v'}/U_1^2$ distribution over the depth at the plane of $z/W=0.36$ for $F_1=5.61$ and $S=0.22$	176
61.	$-\overline{u'v'}/U_1^2$ distribution over the depth at the plane of $z/W=0.36$ for $F_1=5.49$ and $S=0.63$	177
62.	$-\overline{u'v'}/U_1^2$ distribution over the depth at the plane of $z/W=0.36$ for $F_1=5.43$ and $S=1.01$	178
63.	$-\overline{u'v'}/U_1^2$ distribution over the depth at the plane of $z/W=0.36$ for $F_1=8.19$ and $S=0.22$	179
64.	$-\overline{u'v'}/U_1^2$ distribution over the depth at the plane of $z/W=0.36$ for $F_1=8.00$ and $S=0.62$	180
65.	$-\overline{u'v'}/U_1^2$ distribution over the depth at the	

	plane of $z/W=0.36$ for $F_1=8.11$ and $S=1.00$	181
66.	u/U_1 distribution across the channel at the plane of $y/Y_1=0.36$ for $F_1=3.11$ and $S=0.26$	182
67.	u/U_1 distribution across the channel at the plane of $y/Y_1=0.36$ for $F_1=3.20$ and $S=0.53$	183
68.	u/U_1 distribution across the channel at the plane of $y/Y_1=0.36$ for $F_1=3.19$ and $S=0.85$	184
69.	u/U_1 distribution across the channel at the plane of $y/Y_1=0.36$ for $F_1=3.01$ and $S=1.69$	185
70.	u/U_1 distribution across the channel at the plane of $y/Y_1=0.36$ for $F_1=5.61$ and $S=0.22$	186
71.	u/U_1 distribution across the channel at the plane of $y/Y_1=0.36$ for $F_1=5.49$ and $S=0.63$	187
72.	u/U_1 distribution across the channel at the plane of $y/Y_1=0.36$ for $F_1=5.43$ and $S=1.01$	188
73.	u/U_1 distribution across the channel at the plane of $y/Y_1=0.36$ for $F_1=8.19$ and $S=0.22$	189
74.	u/U_1 distribution across the channel at the plane of $y/Y_1=0.36$ for $F_1=8.00$ and $S=0.62$	190
75.	u/U_1 distribution across the channel at the plane of $y/Y_1=0.36$ for $F_1=8.11$ and $S=1.00$	191
76.	Three dimensional structure of the u velocity for $F_1=5.49$ and $S=0.63$	192
77.	Three dimensional structure of $\overline{-u'v'}$ for $F_1=5.49$ and $S=0.63$	193
78.	Typical vertical distributions of velocity component u and turbulence shear stress $\overline{-u'v'}$	194
79.	u_m/U_1 vs x/L plots. (a) Data from present study; (b) Data from Rajaratnam (1972)	195
80.	Variation of normalized maximum turbulence shear stress and intensities of a vertical section against x/L	196
81.	Variation of nondimensionalized maximum turbulence	

shear stress and turbulence intensities against inlet F_1	197
82. Variation of nondimensionalized maximum turbulence shear stress against submergence factor S	198
83. The growth of length scales b/Y_1 , d/Y_1 and $\bar{\delta}/Y_1$ with x/Y_1	199
84. (a) Relationship between $(dH/dx)_L$ and S ; (b) Relationship between L/Y_1 and F_1 and S	200
85. Similarity of velocity profiles in fully developed region for (a) $F_1=3.11$ and $S=0.26$; (b) $F_1=3.20$ and $S=0.53$	201
86. Similarity of velocity profiles in fully developed region for (a) $F_1=3.19$ and $S=0.85$; (b) $F_1=3.01$ and $S=1.69$	202
87. Similarity of velocity profiles in fully developed region for (a) $F_1=5.61$ and $S=0.22$; (b) $F_1=5.49$ and $S=0.63$; (c) $F_1=5.43$ and $S=1.01$	203
88. Similarity of velocity profiles in fully developed region for (a) $F_1=8.19$ and $S=0.22$; (b) $F_1=8.00$ and $S=0.62$; (c) $F_1=8.11$ and $S=1.00$	204
89. Similarity of turbulence shear stress profiles in fully developed region for (a) $F_1=3.11$ and $S=0.26$; (b) $F_1=3.20$ and $S=0.53$	205
90. Similarity of turbulence shear stress profiles in fully developed region for (a) $F_1=3.19$ and $S=0.85$; (b) $F_1=3.01$ and $S=1.69$	206
91. Similarity of turbulence shear stress profiles in fully developed region for (a) $F_1=5.61$ and $S=0.22$; (b) $F_1=5.49$ and $S=0.63$; (c) $F_1=5.43$ and $S=1.01$	207
92. Similarity of turbulence shear stress profiles in fully developed region for (a) $F_1=8.19$ and $S=0.22$; (b) $F_1=8.00$ and $S=0.62$; (c) $F_1=8.11$ and $S=1.00$	208
93. Similarity of longitudinal turbulence intensity profiles in fully developed region for (a) $F_1=3.11$ and $S=0.26$; (b) $F_1=3.20$ and $S=0.53$	209
94. Similarity of longitudinal turbulence intensity	

profiles in fully developed region for (a) $F_1=3.19$ and $S=0.85$; (b) $F_1=3.01$ and $S=1.69$	210
95. Similarity of longitudinal turbulence intensity profiles in fully developed region for (a) $F_1=5.61$ and $S=0.22$; (b) $F_1=5.49$ and $S=0.63$; (c) $F_1=5.43$ and $S=1.01$	211
96. Similarity of longitudinal turbulence intensity profiles in fully developed region for (a) $F_1=8.19$ and $S=0.22$; (b) $F_1=8.00$ and $S=0.62$; (c) $F_1=8.11$ and $S=1.00$	212
97. Similarity of vertical turbulence intensity profiles in fully developed region for (a) $F_1=3.11$ and $S=0.26$; (b) $F_1=3.20$ and $S=0.53$	213
98. Similarity of vertical turbulence intensity profiles in fully developed region for (a) $F_1=3.19$ and $S=0.85$; (b) $F_1=3.01$ and $S=1.69$	214
99. Similarity of vertical turbulence intensity profiles in fully developed region for (a) $F_1=5.61$ and $S=0.22$; (b) $F_1=5.49$ and $S=0.63$; (c) $F_1=5.43$ and $S=1.01$	215
100. Similarity of vertical turbulence intensity profiles in fully developed region for (a) $F_1=8.19$ and $S=0.22$; (b) $F_1=8.00$ and $S=0.62$; (c) $F_1=8.11$ and $S=1.00$	216
101. Unit discharge q distributions along the jump at the vertical plane of $z/W=0.36$ for all conditions	217
102. Unit kinematic momentum flux M distributions along the jump at the vertical plane of $z/W=0.36$ for all conditions	218
103. Unit discharge q and unit kinematic momentum flux M distributions across the flume for three cross section for $F_1=5.69$ and $S=0.63$	219
104. The ratio of predicted roller length over measured roller length vs F_1 and S	220
105. A typical discretization of offset control volumes	221
106. A typical control volume for the conservation of mass	222
107. Water surface condition for the	

conservation of mass	223
108. Different control volumes	224
109. Calculation flow chart	225
110. Calculation mesh for $F_1=3.19$ and $S=0.85$	226
111. Calculation mesh for $F_1=5.49$ and $S=0.63$	227
112. Calculation mesh for $F_1=8.19$ and $S=0.24$	228
113. Velocity vector field from numerical calculation for $F_1=3.19$ and $S=0.85$	229
114. Velocity vector field from numerical calculation for $F_1=5.49$ and $S=0.63$	230
115. Velocity vector field from numerical calculation for $F_1=8.19$ and $S=0.24$	231
116. Comparison of water surface profiles from the prediction and experiment	232
117. Comparison of longitudinal velocity distribution between the experiment and prediction for $F_1=3.19$ and $S=0.85$	233
118. Comparison of longitudinal velocity distribution between the experiment and prediction for $F_1=5.49$ and $S=0.63$	234
119. Comparison of longitudinal velocity distribution between the experiment and prediction for $F_1=8.19$ and $S=0.24$	235
120. Comparison of vertical velocity distribution between the experiment and prediction for $F_1=3.19$ and $S=0.85$	236
121. Comparison of vertical velocity distribution between the experiment and prediction for $F_1=5.49$ and $S=0.63$	237
122. Comparison of vertical velocity distribution between the experiment and prediction for $F_1=8.19$ and $S=0.24$	238
123. Comparison of turbulence intensity $\sqrt{u'^2}$ distribution between the experiment and prediction for $F_1=3.19$ and $S=0.85$	239

124.	Comparison of turbulence intensity $\sqrt{u'^2}$ distribution between the experiment and prediction for $F_1=5.49$ and $S=0.63$	240
125.	Comparison of turbulence intensity $\sqrt{u'^2}$ distribution between the experiment and prediction for $F_1=8.19$ and $S=0.24$	241
126.	Comparison of turbulence intensity $\sqrt{v'^2}$ distribution between the experiment and prediction for $F_1=3.19$ and $S=0.85$	242
127.	Comparison of turbulence intensity $\sqrt{v'^2}$ distribution between the experiment and prediction for $F_1=5.49$ and $S=0.63$	243
128.	Comparison of turbulence intensity $\sqrt{v'^2}$ distribution between the experiment and prediction for $F_1=8.19$ and $S=0.24$	244
129.	Comparison of turbulence shear stress $-\overline{u'v'}$ distribution between the experiment and prediction for $F_1=3.19$ and $S=0.85$	245
130.	Comparison of turbulence shear stress $-\overline{u'v'}$ distribution between the experiment and prediction for $F_1=5.49$ and $S=0.63$	246
131.	Comparison of turbulence shear stress $-\overline{u'v'}$ distribution between the experiment and prediction for $F_1=8.19$ and $S=0.24$	247
132.	Departure of pressure from hydrostatic distribution along the jump from numerical prediction for $F_1=3.19$ and $S=0.85$	248
133.	Departure of pressure from hydrostatic distribution along the jump from numerical prediction for $F_1=5.49$ and $S=0.63$	249
134.	Departure of pressure from hydrostatic distribution along the jump from numerical prediction for $F_1=8.19$ and $S=0.24$	250
135.	Comparison of major flow characteristics between the experiment and the prediction for $F_1=3.19$ and $S=0.85$ (a) u_m/U_1 vs x/Y_1 ; (b) $(\overline{u'v'})_m/U_1^2$ vs x/Y_1 ; (c) $(\sqrt{u'^2})_m/U_1$ vs x/Y_1 ; (d) $(\sqrt{v'^2})_m/U_1$ vs x/Y_1	251

136.	Comparison of major flow characteristics between the experiment and the prediction for $F_1=5.49$ and $S=0.63$ (a) u_m/U_1 vs x/Y_1 ; (b) $(\overline{u'v'})_m/U_1^2$ vs x/Y_1 ; (c) $(\sqrt{\overline{u'^2}})_m/U_1$ vs x/Y_1 ; (d) $(\sqrt{\overline{v'^2}})_m/U_1$ vs x/Y_1	252
137.	Comparison of major flow characteristics between the experiment and the prediction for $F_1=8.19$ and $S=0.24$ (a) u_m/U_1 vs x/Y_1 ; (b) $(\overline{u'v'})_m/U_1^2$ vs x/Y_1 ; (c) $(\sqrt{\overline{u'^2}})_m/U_1$ vs x/Y_1 ; (d) $(\sqrt{\overline{v'^2}})_m/U_1$ vs x/Y_1	253
138.	Comparison of shear stress coefficients C_t between the prediction and experiment for the three runs	254
B.1	Computer program listing	255
D.1	SIM program listing	314

LIST OF SYMBOLS

The following symbols may appear with different subscripts. The subscript "1" refers to quantities at the inlet. The subscripts of "m" and "mm" refer to a maximum of a vertical distribution and a maximum for each condition respectively. The subscripts "n1" and "n2" refer to the variables at node 1 and 2 of a calculation mesh.

A_i	coefficient
$a(x)$	edge of shear layer
B_i	coefficient
b	length scale for u , $u=u_m/2$ and $\partial u/\partial y < 0$ when $y=b$
$b(x)$	height of turbulent region
C	constant
C_i	coefficient
C_B	modelling constant
C_L	a constant related to L
C_{L1}	a constant related to L
C_{L2}	a constant related to L
C_{L3}	a constant related to L
C_1	modelling constant
C_2	modelling constant
C_f	bed friction coefficient
C_μ	modelling constant
c	constant
d	length scale for shear stress, $\overline{u'v'} = \overline{(u'v')}_m/2$ and

$$\partial(\overline{u'v'})/\partial y < 0 \text{ when } y=d$$

D_i	coefficient
E	modelling constant
f_D	Doppler frequency
f_d	shifted Doppler frequency
f_0	shifted frequency
f_i	a function ($i=1, 2, 3$ and 4)
f_i'	derivative of the function f_i
F_i	inlet Froude number
g	gravitational acceleration
G	turbulence production term
H	water depth
K	diffusivity
k	Von Karman constant
l	representative length of a control volume
l_m	mixing length
L	a length scale, $u_m/U_1=0.5$ when $x=L$
L_c	length scale of a computational grid
L_j	length of free hydraulic jumps
L_{rj}	roller length of free hydraulic jumps
L_{sj}	length of submerged hydraulic jumps
L_{rsj}	roller length of submerged hydraulic jumps
L_t	length scale for turbulence
m	exponent
M	unit momentum in longitudinal direction
M_0	inlet unit momentum in longitudinal direction
n	outward direction normal to a surface

n_w	refractive index of water
N_c	number of offset control volumes
p	pressure
P_e	Peclet number
P_d	non-dimensional pressure departure
p_s	piezometric pressure
q	unit discharge
q_1	inlet unit discharge
q_x	net inflow of mass into a control volume in longitudinal direction
q_y	net inflow of mass into a control volume in vertical direction
R	ratio of predicted roller length over measured roller length
Re_i	inlet Reynolds number
Re_c	computational Reynolds number
s	surface of a region
S	submergence factor
S_s	surface slope
u	longitudinal velocity component
u_c	velocity on the bed
u_{in}	instantaneous velocity
$\overline{u_B}$	mean velocity in blue direction
$\overline{u'_B{}^2}$	mean square turbulence intensity in blue direction
$\overline{u_G}$	mean velocity in green direction
$\overline{u'_G{}^2}$	mean square turbulence intensity in blue direction
$\overline{u'_G u'_B}$	covariance of velocity fluctuation

u_m	maximum longitudinal velocity at one section
u_s	longitudinal velocity on the water surface
u_*	shear velocity
u^+	u/u_*
u_∞	$u=u_\infty$ when $y \rightarrow \infty$
U_1	inlet longitudinal velocity
U_c	velocity scale of a numerical calculation
U_t	velocity scale for turbulence
v	vertical velocity component
V	enclosed volume of a region
V_1	inlet vertical velocity
v_s	vertical velocity on the water surface
$\sqrt{\overline{u'^2}}$	longitudinal turbulence intensity
$\sqrt{\overline{v'^2}}$	vertical turbulence intensity
$\overline{u'v'}$	turbulence fluctuation covariance
W	channel width
x	longitudinal distance from the inlet
X	body force per unit mass
y	vertical distance from the bed
y_c	critical depth
y^+	yu_*/ν
Y_1	inlet opening
Y_2	conjugate depth of ordinary hydraulic jump
Y_3	back-up depth of submerged hydraulic jump
Y_c	vertical distance separating offset and non-offset control volumes
Y_t	tailwater depth of submerged hydraulic jump

y_*	$y=y_*$ when maximum shear stress occurs
z	spanwise coordinate
z'	traverse reading
z_0'	traverse reading when $z=0$
γ	specific weight
Δx	control volume thickness in longitudinal direction
Δy	control volume thickness in vertical direction
ϵ	turbulence dissipation rate
ϵ_1	inlet turbulence dissipation rate
k	turbulence kinetic energy
k_1	inlet turbulence kinetic energy
ν	kinematic viscosity
ν_{ct}	turbulence eddy viscosity scale for numerical calculation
ν_t	turbulence eddy viscosity
ρ	density
λ	wavelength
θ	beam intersection angle
α	rotation angle of optics
σ_k	modelling constant
σ_ϵ	modelling constant
τ_t	turbulent shear stress
τ_w	wall shear stress
τ_0	shear stress on bed
δ	$y=\delta$ when $u=u_m$
$\bar{\delta}$	$y=\bar{\delta}$ when shear stress goes to zero

and $\partial \overline{(u'v')}/\partial y > 0$

δ_{ij}	Kronecker delta
ψ	beam intersection angle
μ	dynamic viscosity
Φ	transportive quantity
Ω_r	empirical constant

INTRODUCTION

Because of its importance in energy dissipation in hydraulic structure, hydraulic jumps have been investigated extensively by many researchers. Most of the physical model studies on hydraulic jumps have been directed to obtain the large scale features of the flow and its energy transformation capability. There are a few detailed measurements of free hydraulic jumps but only for a limited range of flows. Very few studies have been performed on the internal flow structure of submerged hydraulic jumps. Furthermore, the existing prediction methods for hydraulic jumps are of the integral type. They can predict the macroscopic aspects of hydraulic jumps and also some aspects of mean velocity field. The internal structure of the flow is part of the assumptions rather than a part of the predictions.

The current research project is directed toward obtaining detailed experimental measurements of submerged hydraulic jumps in a horizontal and rectangular channel and applying the widely tested $k-\epsilon$ turbulence model to predict the macroscopic and internal structure of the flow. This thesis reports the results and major findings of this study. Globally the thesis is divided into three main parts. The first part reviews our present knowledge on this subject with the objective of summarizing the major contributions. The second part of the thesis presents the LDA (Laser Doppler

Anemometry) experimental measurements and the analysis of data. The third part summarizes the numerical results from the prediction. The prediction method is also discussed and evaluated in detail in the final part of the thesis.

1. PART ONE - LITERATURE REVIEW

1.1 Introduction

Hydraulic jumps, which constitute the rapid transition from supercritical to subcritical flow, have been studied extensively because of their importance in energy dissipation in hydraulic structures. Experimental investigations of physical models have been carried out to study both the macroscopic and internal structure of the jumps, but most of the studies have been directed to the macroscopic features of the phenomenon. Macroscopic features of hydraulic jumps include the relationship of sequent depths and different length characteristics. Internal structure of hydraulic jumps refer to their mean velocity distribution and turbulence characteristics. Major contributions to this subject were reviewed by Rajaratnam (1967) and more recently by McCorquodale (1986).

Theoretical analysis of hydraulic jumps is based on the conservation laws of mass and momentum. Simplification of these governing equations leads to the well-known Belanger equation which relates the ratio of the sequent depths to the inlet supercritical Froude number. Rouse et al (1958) applied these principles to analyze their experimental results and obtained detailed information on momentum conservation and energy transformation in the jumps. Numerical simulations of hydraulic jumps using the integral approach have been made by

Narayanan (1975), McCorquodale and Khalifa (1983) and Madsen and Svendsen (1983).

A very extensive literature exists on hydraulic jumps. Contributions to hydraulic jumps have been made by Rouse et al (1958), Bowers and Tsai (1963), Rajaratnam (1965), Betchov and Criminale (1967), Vasiliev and Bukreyev (1967), Wisner (1967), Keir et al (1969), Narayanan and Reynolds (1972), Resch and Leutheusser (1972), Abdul Khader and Elango (1974), Narayanan (1975), Narasimhan and Bhargava (1976), Mehrotra (1976), Nece and Mahmood (1976), Song (1977), Smith (1976), Khalifa and McCorquodale (1979) and many others. As pointed out by McCorquodale (1986) one paper published by the ASCE Task Force (1964) on energy Dissipation and Outlet Works listed about 500 references. No attempt has been made to review all the papers published to date on this subject. However, major contributions related to the current thesis topics are reviewed in this part of the thesis. At the end of the review, the current research objectives will be presented.

1.2 Theoretical Framework

1.2.1 Introduction

Hydraulic jumps can be classified by either their physical configuration or their inlet and outlet conditions. In actual hydraulic applications, hydraulic jumps can take a variety of forms, subject to bed slope, plan shape of

boundary, shape of cross-section, appurtenance and submergence to name a few.

The classical free hydraulic jump formed in a smooth, wide and horizontal rectangular channel without submergence as shown in Figure 1 is the simplest type. It has been the focus of continuous researches for understanding the jump phenomenon and establishing the theoretical framework. As a simple but important example, the classical free jump is used to define the jump problem discussed in this section.

1.2.2 Governing Equations

The equation of continuity and Reynolds-averaged momentum equation for steady state and incompressible turbulent flow in a generalized coordinate system can be given as follows:

$$\frac{\partial u_j}{\partial x_j} = 0 \quad (1)$$

$$u_j \frac{\partial u_i}{\partial x_j} = -\frac{1}{\rho} \frac{\partial p}{\partial x_i} + \frac{\partial \overline{(-u_i' u_j')}}{\partial x_j} + \nu \frac{\partial^2 u_i}{\partial x_j \partial x_j} + X_i \quad (2)$$

$$(i, j = 1, 2, 3)$$

where x_i or x_j denotes the coordinate; u_i is a time-averaged velocity component; p is the pressure; $\overline{-u_i' u_j'}$ is a Reynolds stress component; ρ is the density of water; ν is kinematic viscosity; and X_i is a body force component per unit mass.

If the classical free jump is regarded as a two dimensional problem, equations (1) and (2) can be further simplified as follows,

$$\frac{\partial u}{\partial x} + \frac{\partial v}{\partial y} = 0 \quad (3)$$

$$u \frac{\partial u}{\partial x} + v \frac{\partial u}{\partial y} = -\frac{1}{\rho} \frac{\partial p.}{\partial x} + \frac{\partial}{\partial x} (\overline{-u'^2 + v \frac{\partial u}{\partial x}}) + \frac{\partial}{\partial y} (\overline{-u'v' + v \frac{\partial u}{\partial y}}) \quad (4)$$

$$u \frac{\partial v}{\partial x} + v \frac{\partial v}{\partial y} = -\frac{1}{\rho} \frac{\partial p.}{\partial y} + \frac{\partial}{\partial x} (\overline{-u'v' + v \frac{\partial v}{\partial x}}) + \frac{\partial}{\partial y} (\overline{-v'^2 + v \frac{\partial v}{\partial y}}) \quad (5)$$

Here the coordinate system as shown in Figure 1 is adopted. u and v are the velocity components in the longitudinal (x) and vertical (y) directions respectively. $p.$ is the piezometric pressure defined as

$$p. = p + \gamma y \quad (6)$$

where y is the vertical distance from the boundary (bed) referred to as the wall and γ is the specific weight of water.

The system of equations from (3) to (5) is not closed, because Reynolds stress terms like $\overline{u'^2}$, $\overline{v'^2}$ and $\overline{u'v'}$ are not known. In order to obtain a solution, modelling relationships to determine the Reynolds stresses are required.

1.2.3 Belanger Equation

Using the definition in Figure 1 the inlet Froude number F_1 is defined as follows

$$F_1 = \frac{U_1}{\sqrt{gY_1}} \quad (7)$$

where U_1 is the supercritical velocity, Y_1 is the supercritical depth and g is the acceleration due to gravity.

If it is assumed that the velocity distribution is uniform and the pressure distribution is hydrostatic both at the beginning and the end of the jump and if the boundary shear stress on the bed and the turbulent velocity fluctuations at the beginning and end are neglected, integration of equations (3) to (5) results in the well-known Belanger momentum equation

$$\frac{Y_2}{Y_1} = \frac{1}{2} (\sqrt{1 + 8 F_1^2} - 1) \quad (8)$$

where Y_2 is the subcritical depth at the end. Y_2/Y_1 is called the ratio of the sequent depths. This simple equation reveals that the behavior of the classical free jump is mostly determined by its inlet Froude number F_1 .

1.2.4 Integral Momentum Equation

The following analysis is adapted from Rouse et al (1958). Integrating equation (2) over the jump region by using Green's theorem

$$\int_V \frac{\partial \Phi}{\partial x_j} dV = \int_S \Phi \frac{\partial x_i}{\partial n} ds \quad (9)$$

one obtains the following equation

$$\begin{aligned} & \int_S \rho u_i u_j \frac{\partial x_i}{\partial n} ds + \int_S \rho \overline{u_i' u_j'} \frac{\partial x_i}{\partial n} ds \\ & = - \int_S p_i \frac{\partial x_i}{\partial n} ds + \int_V \rho x_i dV + \int_S \mu \frac{\partial u_i}{\partial x_j} \frac{\partial x_i}{\partial n} ds \end{aligned} \quad (10)$$

here Φ is any physical quantity; s denotes the surface of the region over which the integration is performed; n the outward normal to the surface; V the enclosed volume; and μ is the dynamic viscosity. Equation (10) reflects the macroscopic dynamics of hydraulic jumps. The terms at the left hand side are the net flux of the mean flow and the turbulence out of the region. The first term at the right hand side denotes the mean normal force exerted externally on the surface of the region. The second term represents the weight of the fluid contained within the region; and the third accounts for the mean tangential force exerted on the water surface. Equation (10) provides a powerful tool to analyze different forces acting upon a jump. If it is assumed that the turbulence is negligible at the toe of the jump and that the pressure distribution is hydrostatic throughout the jump, then applying equation (10) to a control volume delineated by

the initial section and any other section at a distance x with a mean depth y gives

$$\begin{aligned} & \int_0^y \rho u^2 dy - \int_0^{y_1} \rho u^2 dy + \int_0^y \overline{\rho u'^2} dy \\ &= \frac{\gamma y_1^2}{2} - \frac{\gamma y^2}{2} - \int_0^x \mu \left(\frac{\partial u}{\partial y} \right)_{y=0} dx \end{aligned} \quad (11)$$

The first two terms at the left hand side represent the mean momentum at the respective sections, and the third term represents the momentum flux of the turbulence. The first two terms on the right represent the mean pressure forces, and the last term represents the integrated bed shear stress.

1.2.5 Integral Energy Equations

Rouse et al (1958) also analyzed the integrated energy equation within a jump. Using the same method as above the energy equation for the mean flow can be obtained as

$$\begin{aligned} & \int_0^y \frac{u^2}{2g} u dy - \int_0^{y_1} \frac{u^3}{2g} dy + \int_0^y \frac{u \overline{u'^2} + v \overline{u'v'}}{g} dy \\ & - \iint_{00}^{yx} \left[\frac{\overline{u'v'}}{g} \left(\frac{\partial u}{\partial y} + \frac{\partial v}{\partial x} \right) + \frac{\overline{u'^2} - \overline{v'^2}}{g} \frac{\partial u}{\partial x} \right] dy dx = qy_1 - qy \\ & \int_0^y \frac{\mu}{\gamma} \left[2u \frac{\partial u}{\partial x} + v \left(\frac{\partial u}{\partial y} + \frac{\partial v}{\partial x} \right) \right] dy - \iint_{00}^{yx} \frac{\mu}{\gamma} \left[4 \left(\frac{\partial u}{\partial x} \right)^2 + \left(\frac{\partial u}{\partial y} + \frac{\partial v}{\partial x} \right)^2 \right] dy dx \end{aligned} \quad (12)$$

The first two terms on each side of the equation correspond to those of the usual one dimensional open channel relationship, with due account taken of the variation in velocity over the cross section. The third terms represent work done on the end section by the turbulent and viscous stresses. The last terms combine to indicate the rate at which turbulence is produced by the mean motion and the rate at which energy is dissipated by the mean viscous stresses.

The energy equation for the turbulent motion reads

$$\begin{aligned}
 & \int_0^y \frac{\overline{v'^2}}{2g} u \, dy + \int_0^y \frac{\overline{v'^2 u'}}{2g} \, dy + \iint_{00}^{yx} \left[\frac{\overline{u'v'}}{g} \left(\frac{\partial u}{\partial y} + \frac{\partial v}{\partial x} \right) + \frac{\overline{u'^2 - v'^2}}{g} \frac{\partial u}{\partial x} \right] dy dx \\
 & = - \int_0^y \frac{\overline{p'u'}}{\gamma} \, dy + \int_0^y \frac{\mu}{\gamma} \left[\frac{\partial u}{\partial x} \left(\frac{\overline{v'^2}}{2} + \overline{u'^2} \right) + \frac{\partial \overline{u'v'}}{\partial y} \right] dy \\
 & - \iint_{00}^{yx} K \frac{\mu}{\gamma} \overline{\left(\frac{\partial u'}{\partial x} \right)^2} \, dy dx \tag{13}
 \end{aligned}$$

The first two terms at the left hand side are the flux of turbulent kinetic energy. The last term at the left hand side is the production rate of turbulent kinetic energy. The first two terms on the right hand side are the rates of work by fluctuating pressure and viscous stresses of turbulence respectively. The last term at the right hand side is the rate of dissipation of turbulent kinetic energy.

Both the integral momentum and energy equations had been used by Rouse et al (1958) to interpret their experimental

results (to be discussed later) and explain the major momentum and energy transport processes within a free jump.

1.3 Experimental studies

1.3.1 Introduction

For the following review of experimental studies, attention is focused on two major types of jumps: the classical free hydraulic jump and the classical submerged hydraulic jump. The classical submerged jump (shown as in Figure 2) is formed in a smooth, wide and horizontal rectangular channel. Its tailwater depth Y_t is greater than the subcritical depth Y_2 of the corresponding free jump and the tailwater advances over the jump resulting in a submerged jump.

As discussed by Rajaratnam (1967) submerged jumps occur mostly below barrages, weirs and canal head sluices, and in some cases, when the tailwater depths are very large, below spillways and river outlets. The classical submerged hydraulic jump, together with the classical free jump, not only represent most of practical jumps, but also constitute two simplest cases which researchers can tackle by experimenting in a physical model and obtaining scientific data from measurements and for which theoretician can establish the mathematical formulation and solve them by different techniques. Providing accurate and detailed flow measurements of these two types of jumps have been the continuous pursuits of many researchers.

1.3.2 Main Length Characteristics

For the classical free jump the sequent depth Y_2 predicted from Belanger equation is generally good for most of engineering problems. Rajaratnam (1967) showed that the effect of bed friction on Y_2/Y_1 increased with increasing F_1 , reaching a reduction of 4% at $F_1=10$. The length of the jump L_j is defined as the horizontal distance from the toe to the section where the water surface becomes essentially level and the mean surface elevation is maximum (Rajaratnam 1967). The length of the surface roller L_{rj} is the horizontal distance from the toe to where the roller ends on the water surface. The experimental results from Rajaratnam (1965), Rouse et al (1958) and Safranez (1934) are reproduced as in Figure 3. The Bradly-Peterka Curve (1957) in Figure 3 was developed from practical considerations according to Rajaratnam (1967). It is clear from Figure 3 that L_{rj} is generally less than L_j and approaches L_j as the supercritical Froude number F_1 increases.

For the classical submerged jump the submergence factor S is defined as

$$S = \frac{Y_t - Y_2}{Y_2} \quad (14)$$

S becomes zero for a free jump but is large for deeply submerged jumps. If the length of a submerged jump and its surface roller are defined the same way as in a free jump,

according to Rajaratnam (1967) the following empirical equation holds

$$\frac{L_{srj}}{Y_2} = 4.9S + 6.1 \quad (15)$$

This equation shows that the length of the submerged jump exceeds that of corresponding free jump by the term 4.9S and that as submergence increases the length of the submerged jump increases. According to Stepanov (1959) the length of the roller L_{srj} is given by the equation

$$\frac{L_{rsj}}{y_c} = \frac{3.31}{[(Y_t - Y_3)/Y_3/F_1]^{0.885}} \quad (16)$$

where y_c is the critical depth and it is found that the equation (16) is satisfactory for $S < 2$ and Froude numbers F_1 up to about 8.

1.3.3 Mean Velocity Field

Rajaratnam's studies (1965a and 1965b) showed that in the forward-flow portion of both free jumps and submerged jumps, the distribution of the mean longitudinal velocity u in y direction was similar to that in the wall jet. Recognition of this aspect is not only of great assistance in synthesizing the large number of the mean velocity measurements but also in building an integral analysis. The measurements for free jumps and submerged jumps from

Rajaratnam (1965) are reproduced as in Figure 4 and Figure 5, in which the term classical wall jet refers to a wall jet with potential inflow in stagnant surroundings within a wide flume with a flat bed. Actually this concept has been used by several researchers as a basic assumption for numerical prediction and more will be said about this in the next section of Prediction Methods.

1.3.4 Main Flow Characteristics

A typical vertical distribution of velocity u for free and submerged jumps is shown in Figure 6, which also serves to define the symbols used in the following discussion. The subscript m refer to a maximum in a vertical distribution. The length scale b is for the mean velocity and $u=u_m/2$ when $y=b$ and $\frac{\partial u}{\partial y} < 0$.

If hydraulic jumps are analyzed as two-dimensional flows as a first approximation, from dimensional analysis as by Rajaratnam (1976), it is easy to show that

$$\frac{u_m}{U_1} = f \left(\frac{x}{Y_1}, F_1, S \right) \quad (17)$$

$$\frac{b}{Y_1} = f \left(\frac{x}{Y_1}, F_1, S \right) \quad (18)$$

These two equations are applicable for large Reynolds numbers, under which the jumps are turbulent flows. The data from Rajaratnam (1976) for both free jumps and submerged

jumps are reproduced as in Figure 7 and 8. It is clear from the figures that the decay of u_m for hydraulic jumps is faster than that of a wall jet and the length scale l grows faster in hydraulic jumps. This will become obvious if hydraulic jumps are considered wall jets under adverse pressure gradient as proposed by Rajaratnam (1965). The adverse pressure gradient slows down the velocity and also produces a recirculating roller on top of the jet. This reversing flow generates more mixing in a jump than in a wall jet so that u_m/U_1 decays faster in jumps than in wall jets.

1.3.5 Wall Shear Stress

Rajaratnam (1967) defined the skin friction coefficient C_f by the equation

$$\tau_w = C_f \frac{\rho U_1^2}{2} \quad (19)$$

where τ_w is the wall (or boundary) shear stress along the bed. The experimental results for free jump are reproduced as in Figure 9, in which the curve indicates the mean of different experimental conditions with different inlet Froude numbers. It was found that C_f decreased from about 0.0037 at the beginning of the jump to about 0.0001 near the end of the jump. The effect of increasing submergence on the bed shear stress was also reported by Rajaratnam (1965). It was found that for any given Froude number at any section the reduction

of the bed shear stress was slowed down by increasing submergence. The experimental results by Rajaratnam (1965) are reproduced in Figure 10, where the effects of submergence are obvious.

1.3.6 Air Model Of Free Jumps

The paper on the air model of free hydraulic jumps by Rouse et al (1958) was the first attempt to make detailed turbulence measurements of hydraulic jumps. The paper was a milestone in hydraulic jump research and provided insight into the structure of the flow and energy transformation related to hydraulic jumps. Even though air models were used instead of the real jumps, the results were enlightening. As McCorquodale (1986) put it, their work was a breakthrough in the understanding of the internal mechanics of the hydraulic jumps and had provided a framework for future research.

The air model they used conformed to the mean depth configurations of natural free hydraulic jumps. The air duct was shaped according to the profile of the free jump. This model was justified analytically and experimentally by its similarity in mean flow pattern and pressure distribution on the boundaries to the natural free jumps. It was assumed that, if the mean flow patterns were similar and the energy changes and Reynolds number comparable, the patterns of turbulence would also be similar. The turbulence field was measured by hot-wire technique for inlet Froude numbers of 2, 4 and 6. The measurements included the mean flow, the

turbulence intensities and the Reynolds stresses. The maximum turbulence intensities for $F_1=2, 4$ and 6 are $0.20, 0.24$ and $0.28 U_1$, respectively and the maximum turbulence covariances are $0.024, 0.023$ and $0.028 U_1^2$ respectively.

Rouse et al (1958) calculated the integrals of the distribution curves of the turbulence production, dissipation and convection. The results showed that the maximum turbulence production occurred at about $x/Y_2=1$ and the maximum turbulence occurred at a later section. It was clear that the process of turbulence production to dissipation occurred in a short distance ($0 < x/Y_2 < 5$).

The results from the calculation of energy transformation by Rouse et al (1958) show that the velocity head, pressure head and dissipation loss are the dominant terms in the conservation of energy along the jump. The kinetic energy of turbulence and work done by the Reynolds stresses are significantly small. This further shows that turbulence in hydraulic jumps mainly acts to transfer mean energy to dissipation but had minor effects on the conservation laws of the mean flow.

Air model studies by Rouse et al (1958) were a big leap forward in the understanding of hydraulic jumps, but the air model did not simulate all aspects of a real hydraulic jump. The shortcomings resulted from its incapacibilities to include the effects of the surface gravity waves, the entrainment of air and certain aspects of the actual pressure field. In addition, the solid boundary of the air model at the surface

introduced a shear stress which would be higher than the corresponding stress for the air-water interface of an actual jump.

1.3.7 Water Model Of Free Jump

The studies of Leutheusser et al (from 1972 to 1979) on the real water model of hydraulic jumps threw some new light on the internal flow structure of free jumps. They used the hot-film anemometer to measure the turbulence field in actual hydraulic jumps. Even though the measurements were limited to two Froude numbers of 2.85 and 6.00, they made some additional observations on the turbulence structure of the flow with developed inflow.

Their results for the (almost) uniform flow were in general agreement with the air model data by Rouse et al (1958), but their results for the developed initial boundary layer were quite different. The maximum turbulence intensities and shear stress from their experiments are listed in Table 1. It clearly shows that the turbulence field of developed inflow was significantly stronger than that of potential inflow.

They also found that the development of the initial boundary layer affected the entrainment of air. For jumps with developed inflow more air was entrained in the upstream portion of jumps than was with potential inflow. The jumps with developed inflow affected the flow separation as well. They found, for example, that with developed inflow the range

of potential separation was $5 < x/Y_2 < 7$ for $F_1=4$ while for undeveloped inflow, it was about $3 < x/Y_2 < 7$.

1.3.8 Summary

Major experimental studies in hydraulic jumps have been reviewed. Because there are a great number of papers on this subject, no attempt has been made to include all of them. However, attention has been focused on the understanding of the phenomenon and our current knowledge on the subject. Most of the experimental studies on hydraulic jumps have been on the macroscopic aspects of the phenomenon. Unfortunately, the internal flow characteristics have received much less attention. The turbulence measurements on free jumps by Rouse et al (1958) in an air conduct and Leutheusser and Kartha (1972) in a water model are the only detailed data in the literature and these data are limited. The experiments by Rouse et al (1958) covered inlet Froude numbers of only 2, 4 and 6 (8 was not successful). The experiment by Leutheusser and Kartha (1972) covered two inlet Froude numbers of 2.85 and 6.00. No detailed measurements are available beyond $F_1=6$. On submerged hydraulic jumps Rajaratnam (1965, 1972) and many others collected a lot of data on the mean velocity fields, but to my knowledge no detailed turbulence measurements are available in the literature. It is of interest to make accurate measurements both for free jumps and submerged jumps.

1.4. Prediction Methods

1.4.1 Introduction

Belanger equation is the most widely used equation to calculate the sequent depth ratio of the classical free jump. Some empirical relationships exist for calculating other length characteristics, such as equation (15) on L_{sj} . The theoretical framework had been established some time ago, like that by Rouse et al (1958), but the equations involved are too difficult to solve. Some simple models of treating hydraulic jumps as wall jets under adverse pressure gradient have been tried by Rajaratnam (1965) and others. In the past two decades, as computer power increased tremendously, numerical simulations of hydraulic jumps using integral approach based on similarity assumptions have been made by Narayanan (1975), McCorquodale and Khalifa (1983) and Madsen and Svendsen (1983).

On the other hand turbulence modelling techniques have become more and more sophisticated. The reviews by Rodi (1980), Lakshminarayana (1986), Nallasamy (1987), ASCE Task Committee (1988) and many others summarized the progress made in the past two decades on turbulence modelling. Therefore, equations (4) to (5) become relatively easier to solve with less restrictive assumptions.

This section will review not only the major numerical work done so far to simulate hydraulic jumps but also state-of-the-art turbulence modelling to provide better prediction methods for turbulent flows.

1.4.2 Narayanan's Method

Narayanan's prediction method (1975), referred to as the SIM (Strip Integral Method) for free hydraulic jumps is a representative of the prediction techniques used during the 70s. His paper (1975) is selected for the review because it reflects all the major contributions from the experiments and theories up to that time.

The major assumption involved in Narayanan's method was the significant experimental realization by Rajaratnam (1965) that the mean motion in the jump behaved in a manner that was typical of a plane turbulent wall jet. He divided the mean u velocity profile into two distinct layers as shown in Figure 11 and further assumed

$$\frac{u}{u_m} = \left(\frac{y}{\delta}\right)^m \quad (\text{for inner layer}) \quad (20)$$

and

$$u = -u_s + \frac{u_m + u_s}{2} \left(1 + \cos\pi \frac{y-\delta}{H-\delta}\right) \quad (\text{for outer layer}) \quad (21)$$

where u_m was the maximum u at a section of x ; m was the exponent varying with x ; δ denoted a vertical distance from the bed where $u=u_m$; H was the depth and u_s was equal to the reverse flow velocity u at $y=H$.

Equation (20) and (21) were substituted into the equations of continuity and momentum and integration over the

flow depth H was performed. In order to solve the resulting equations further assumptions regarding the shear stresses at different levels of flows were needed. Again he used the experimental measurements on wall jets by Gartshore and Newman (1969) and hydraulic jumps by Rouse et al (1958) and Leutheusser and Kartha (1972) to extrapolate the information on shear stresses.

The final equations were first order differential equations which could be easily solved. The decay of the maximum velocity u_m , the surface profile, the variation of surface velocity and the growth of the boundary layer could be predicted from this technique. The major characteristics of jumps, such as the length of the roller and the extent of the jump, could also be predicted. However, he found that the prediction for the length characteristics was sensitive to the turbulent stress. There was another obvious weak point for this method, which relied too heavily on the experimental results directly related to hydraulic jumps. Too many assumptions were made and they were too specific and not universal. Also this method can only be used to calculate the mean flow. The turbulence field was a part of the assumptions rather than a part of the prediction.

1.4.3 The Method of McCorquodale and Khalifa

McCorquodale and Khalifa (1983) refined the SIM method of Narayanan (1975) as described below.

- (1) The Gaussian velocity distribution suggested by Rajaratnam (1976) was used for the outer layer. So the u velocity profile was assumed to have the form of

$$\frac{u}{u_m} = \left(\frac{y}{\delta}\right)^{1/7} \quad (\text{for inner layer}) \quad (22)$$

and

$$u = u_\infty + u_m \exp\left[-4c \frac{y-\delta}{(H-\delta)^2}\right] \quad (\text{for outer layer}) \quad (23)$$

where u_∞ was the velocity u as y went to infinity and c was a constant;

- (2) The effect of entrained air on the hydrostatic force and on the turbulence shear was incorporated;
- (3) The kinematic boundary condition was used at the water surface;
- (4) The turbulence pressure was included;
- (5) The centrifugal force was included.

The resulting set of first order differential equations was thus solved for. This method, like SIM by Narayanan, could predict the mean characteristics of hydraulic jumps. The study by McCorquodale and Kartha (1983) found that air played a minor role in determining the shape of the jump; The effect of turbulence pressure was to lower the water surface near the beginning of the jump, although the length of the

jump was not significantly changed; and the relative importance of the centrifugal force increased as F_1^2 .

Abdel-Gawad and McCorquodale (1984) also applied this method to a radial hydraulic jump with and without submergence. They also found that the roller length was sensitive to the turbulent shear stress. Even though this method improved the SIM of Narayanan to some extent, it still had the same shortcomings as the SIM.

1.4.4 The Method of Madsen and Svendsen

Madsen and Svendsen (1983) developed an integral model for the mean velocity field and the surface profile of hydraulic jumps and turbulent bores based on a simplified κ - ϵ model, in which they only allowed for non-equilibrium for turbulent kinetic energy κ . The assumptions involved in the model were as follows:

- (1) Pressure field was hydrostatic and F_1^2 was greater than 2 to exclude the possibility of undular jumps;
- (2) The horizontal length scale for the flow was much larger than the vertical scale, so equations (4) and (5) were simplified as one equation

$$u \frac{\partial u}{\partial x} + v \frac{\partial u}{\partial y} = - \frac{1}{\rho} \frac{\partial p}{\partial x} + \frac{\partial}{\partial y} (\overline{-u'v'}) \quad (24)$$

- (3) Boundary effects on the wall were neglected, so the flow considered was like that shown in Figure 12;

(4) The velocity profile for u was given by

$$u = u_0(x) \quad (0 < y < a(x)) \quad (25)$$

and

$$u = u_0(x) (1 + \Gamma(x) f(\delta)) \quad (a(x) < y < H(x)) \quad (26)$$

where $u_0(x)$ was the velocity u on the bed. δ was defined as

$$\delta = \frac{y - a(x)}{b(x)} \quad (27)$$

where $b(x)$ was the height of the turbulent region, $H(x)$ was the flow depth and $a(x) = H(x) - b(x)$. The function $f(\delta)$ was given by

$$f(\delta) = -A \delta^3 + (1+A) \delta^2 \quad (0 < \delta < 1) \quad (28)$$

where A was a constant. $\Gamma(x)$ was given by

$$\Gamma(x) = \frac{u_s}{u_0} - 1 \quad (29)$$

where u_s was the surface velocity u ;

(5) Using κ - ϵ model proposed by Launder and Spalding (1972), they further simplified it and obtained the following:

$$\overline{-u'v'} = \nu_t \frac{\partial u}{\partial y} \quad (30)$$

$$\nu_t = \sqrt{\kappa} (H-a) \quad (31)$$

$$\sqrt{\kappa} = X(x) g(\delta) \quad (32)$$

where κ is the turbulence kinetic energy and finally they obtained

$$\overline{-u'v'} = \Omega_\tau u_0 (u_0 - u_s) f'(\delta) \quad (33)$$

where Ω_τ was the only empirical constant required.

Thus integral equations of continuity and momentum over the flow depth could be solved for. This method could predict the surface profile, velocity and shear stress variations along the jump, but it neglected the bottom boundary layer and shear stresses.

This method by Madsen and Svendsen (1983) used an advanced κ - ϵ turbulence model. However, they limited their efforts by presuming the profile for velocity u and turbulence kinetic energy κ . At the same time only the mean flow characteristics of jumps could be predicted. Like the

solutions provided through SIM by Narayanan and McCorquodale et al, this method relied on the detailed measurements of hydraulic jumps to determine the closure relationship and shapes of u and K profiles.

1.4.5 Turbulence Modelling

From the review so far it becomes clear that a more robust method with less restrictive assumptions and empirical relationships is needed to provide a prediction not only for the mean flow characteristics of jumps but also the detailed internal flow structure. In order to achieve this objective a more sophisticated turbulence model has to be used. Therefore, the next section will review the major achievements made in turbulence modelling so as to choose a more universal and successful closure. Again a comprehensive review on turbulence modelling is beyond the scope of this thesis. Instead major problems related to and state-of-the-art of turbulence modelling are reviewed.

1.4.5.1 Strategies

At the present time a complete time-dependent solution of turbulent flows by Navier-Stokes equations is almost impossible even using the fastest computer in the world. This is because turbulence is always three-dimensional and with a wide spectrum of eddy sizes so that even the biggest and fastest computer nowadays does not have the storage and speed required. Therefore, alternative strategies like LES (Large

Eddy Simulation, see reviews by Ferziger in 1981 and 1987) and closure schemes through Reynolds equations have been developed. LES is still at a research stage and has not been applied extensively. Turbulence modelling through Reynolds equations can be traced back to Prandtl (1925). This strategy enjoyed the popularity for the past 50 years and has developed into a very mature stage. Up to date, a number of models have been extensively tested and applied in a variety of engineering problems.

1.4.5.2 Basic Concepts

The first important concept in turbulence modelling through Reynolds equations is the Boussineq's eddy viscosity. It is assumed that, in analogy to the viscous stresses by the molecular motion in laminar flows, that the turbulent stresses are proportional to the mean velocity gradients. This is also called gradient diffusion assumption. The eddy viscosity concept can be generalized as

$$\overline{-u_i' u_j'} = \nu_t \left(\frac{\partial u_i}{\partial x_j} + \frac{\partial u_j}{\partial x_i} \right) - \frac{2}{3} \kappa \delta_{ij} \quad (34)$$

where ν_t is eddy viscosity; κ is turbulence Kinetic energy; and δ_{ij} is Kronecker delta. The turbulence stresses are thus related to the mean flow.

Another important concept is the characterization of the local state of turbulence by two parameters. From dimensional

reasoning the eddy viscosity ν_t is proportional to a velocity scale U_t and a length scale L_t characterizing the turbulent motion

$$\nu_t \propto U_t L_t \quad (35)$$

Thus the success of the turbulence models based on eddy viscosity assumption relies on how well the distribution of U_t and L_t can be determined.

There are two shortcomings for this assumption. The eddy viscosity concept breaks down when shear stresses (such as $-u'v'$) and velocity gradients (such as $\frac{\partial u}{\partial y}$) have opposite sign. The implied isotropic eddy viscosity may be too crude for certain types of turbulent flows.

1.4.5.3 Zero Equation Model

This is also called mixing length model, which was proposed by Prandtl (1925) for describing the distribution of ν_t . It was designed for thin shear layer flows where the only significant velocity gradient is $\frac{\partial u}{\partial y}$. In this model the eddy viscosity is related to the velocity gradient through

$$\nu_t = l_m^2 \left| \frac{\partial u}{\partial y} \right| \quad (36)$$

where l_m is called mixing length. Distribution of l_m over the flow field has to be prescribed with the aid of empirical

information. The main drawback with this model is the evaluation of l_m for different turbulent flows. Further problems arise because the eddy viscosity and diffusivity vanish whenever the mean velocity gradient is zero. This close link with the velocity gradient implies that the model is based on the assumption of local equilibrium of turbulence, which means that the turbulence is locally dissipated at the same rate as it is produced. This assumption neglects the transport and history effects. Hence the mixing length model is not very suitable when these effects are important as is the case in rapidly developing flows and recirculating flows. Further, the model is of little use in complex flows because of great difficulties in specifying the distribution of the mixing length. Incorporating the effects of curvature, buoyancy or rotation in the model is totally empirical.

1.4.5.4 One Equation Model

This is also called the energy equation model. It requires the solution of turbulent kinetic energy κ from the following equation

$$u \frac{\partial \kappa}{\partial x} + v \frac{\partial \kappa}{\partial y} = \frac{\partial}{\partial x} \left(\frac{v_t}{\sigma_\kappa} \frac{\partial \kappa}{\partial x} \right) + \frac{\partial}{\partial y} \left(\frac{v_t}{\sigma_\kappa} \frac{\partial \kappa}{\partial y} \right) + G - \epsilon \quad (37)$$

where G and ϵ are turbulence production and dissipation rates respectively. This equation involves a gradient diffusion assumption for diffusive transport of K and the following

$$\epsilon = C_D \frac{K^{3/2}}{L_t} \quad (38)$$

$$v_t = C_\mu \sqrt{K} L_t \quad (39)$$

where C_D and C_μ are assumed to be constants. The length scale L_t is specified algebraically and hence is flow dependent.

One equation model is an important step forward from the mixing length model, since it gives up the direct link between the fluctuating velocity scale and the mean velocity gradients. It determines this scale from a transport equation. The main limitation in equation (38) is that it relates the small-scale turbulence associated with the dissipation process to the length scale L_t , which characterizes the large-scale and energy-containing eddies. Because the amount of energy dissipated is controlled by the energy fed from the large-scale motion through the spectrum to the small motion, ϵ may be considered a parameter characterizing the large scale motion. However, strictly speaking, it is the rate of energy passed on by this motion for dissipation at smaller scale, not energy itself. The one equation model is not very popular since it performs only marginally better than the zero equation model (Rodi, 1980).

1.4.5.5 Two Equation Model

The need to calculate the length scale L characterizing the size of energy containing eddies stimulated the efforts to find a L equation. As discussed by Launder & Spalding (1974) κ - ϵ equation became the most popular model because of the practical advantage that ϵ equation requires no extra terms near walls and also that ϵ itself appears in the κ equation and the ϵ equation requires no secondary source term.

It is obvious from equation (35) that L_t can be calculated if ϵ is known, so looking for either ϵ or L_t is identical for this purpose. An exact transport equation can be derived from the Navier-Stokes equations for the fluctuating vorticity and thus for ϵ . The ϵ equation contains a number of complex correlations for which fairly drastic model assumptions have to be introduced in order to make the equation tractable. As a result, the resulting model equation has a highly empirical nature. The ϵ equation reads

$$u \frac{\partial \epsilon}{\partial x} + v \frac{\partial \epsilon}{\partial y} = \frac{\partial}{\partial x} \left(\frac{v_x}{\sigma_\epsilon} \frac{\partial \epsilon}{\partial x} \right) + \frac{\partial}{\partial y} \left(\frac{v_y}{\sigma_\epsilon} \frac{\partial \epsilon}{\partial y} \right) + C_1 \frac{\epsilon}{\kappa} G - C_2 \frac{\epsilon^2}{\kappa} \quad (40)$$

The terms on the left hand side are the convective transports of ϵ . The first two terms on the right hand side are the diffusive transports of ϵ . The last two terms on the right hand side are the generation and destruction of ϵ . The main limitation of ϵ equation is the idea that ϵ can be diffused,

produced and destroyed through a simple balance equation based on local gradients of ϵ .

The empirical constants C_1 and C_2 in ϵ equation were determined as described below. C_2 is the only constant appearing in the simple case of grid turbulence and was found from the measured decay rate of κ behind grids to lie in the range of 1.8 to 2.0. For non-buoyant shear layers under local equilibrium, production of turbulence is balanced by dissipation at each point, so that equations (37) and (39) can be combined to $C_\mu = \overline{u'v'}/\kappa^2$. Measurements in these flows yielded $\overline{u'v'}/\kappa = 0.3$ so that $C_\mu = 0.09$. In near-wall regions, a logarithmic velocity profile prevails; G is approximately equal to ϵ and the convection of ϵ is negligible. Therefore, the ϵ equation reduces to $C_1 = C_2 - \kappa^2 / (\sigma_\epsilon \sqrt{C_\mu})$. This relation fixes the value of the constant C_1 when the values of the other constants have been chosen. The diffusion constants σ_κ and σ_ϵ are assumed to be close to unity and they as well as C_2 were tuned by computer optimization. The ϵ equation is very sensitive to the choices of C_1 and C_2 (Rodi, 1980).

The standard κ - ϵ model has been tested widely and has been shown to predict, with the same empirical input, many different turbulent flows, including separating and three dimensional flows, with an accuracy sufficient for practical purposes. However, the constants used in standard κ - ϵ model need to be changed in order to accommodate the effects such as curvature, low Reynolds number, presence of wall, etc. (Rodi, 1980)

1.4.5.6 Reynolds Stress Models

One of the limitations for κ - ϵ model is the assumption of isotropic eddy viscosity. In order to account for the different development of the individual stress, transport equations for $\overline{u_i u_j}$ have to be introduced. A particular advantage of the Reynolds stress model is that terms accounting for buoyancy, rotation and other effects are in principle introduced automatically. However, turbulent stress transport equations contain higher order correlations to be modelled. One such model was proposed by Launder et al (1975). Models of this type are rather complex and computationally expensive so that they are not much in use for practical applications. To reduce the computational effort, Rodi (1976) proposed an algebraic relation for calculating the Reynolds stresses. Together with the κ - ϵ equations, the algebraic stress model accounts for most of the effects described by full turbulent stress equations, and thus appears to be sufficiently refined for most engineering problems. However, algebraic stress relations are basically like eddy viscosity formulations and therefore are not applicable to cases where counter gradient transports occur.

1.4.6 Summary

For hydraulic jumps the existing prediction methods, such as those by Narayanan (1972), McCorquodale and Khalifa (1983) and Madsen and Svendsen (1983) are of the integral type. The main characteristics of hydraulic jumps can be well

predicted by these methods. However, all these methods rely too heavily on detailed experimental measurements of hydraulic jumps. The turbulence field is a part of the assumptions instead of being a part of the prediction. Therefore, in order to provide a better prediction method, which is able to predict both the mean flow and turbulence characteristics, a better turbulence model of differential type is needed.

The current review of turbulence modelling shows that $k-\epsilon$ model is the most widely tested and the most successful turbulence model. The constants used are relatively universal compared to most of the models tested so far. $k-\epsilon$ turbulence model is capable of dealing with a variety of turbulent flows encountered in engineering applications.

1.5 Objectives

In this part of the thesis major contributions towards our understanding of the hydraulic jumps have been reviewed. It is the objective of this research program to provide more thorough turbulence measurements of submerged hydraulic jumps and test a prediction method, which can calculate not only the mean flow characteristics but also the turbulence structure of hydraulic jumps. Due to some major difficulties encountered in both the experimental and numerical techniques, which will be discussed in detail in the next two parts, submerged hydraulic jumps in horizontal and

rectangular channel were selected as the problem instead of free hydraulic jumps, in this study.

The detailed measurements of mean flow and turbulence in submerged hydraulic jumps will be obtained using the LDA (Laser Doppler Anemometry) system available at the T. Blench Hydraulics Laboratory at the University of Alberta. These measurements will, at the first time, provide detailed and accurate experimental data under different conditions. These data can then be used as a basis to test and improve the prediction methods. If submerged hydraulic jumps are viewed as transitional phenomena between free jumps and wall jets, this study will then also serve the purpose of comparing these three classes of flows.

The popular $k-\epsilon$ turbulence model will be applied in this study to simulate submerged hydraulic jumps. The numerical results will be compared with the measurements from the experiment. Finally the performance of the model, which includes its success and limitations, will be evaluated.

PART TWO - LDA EXPERIMENTAL STUDIES

2.1 Introduction

The experiments described in this part of the thesis deal with submerged hydraulic jumps in a horizontal rectangular channel of constant width. At the beginning of the experimental program, it was attempted to study the free jumps using the LDA (Laser Doppler Anemometry) system available at the T. Blech Hydraulics Laboratory at the University of Alberta but it was not successful. Because free jumps entrained significant amount of air bubbles, the laser beams were reflected and refracted by the air bubbles. As a result the data acquisition rate was so low that it was almost impossible to obtain data at a reasonable rate. The measurement of free jumps was thus discarded altogether and the effort was focused on the measurement of submerged jumps.

The experiment was conducted by utilizing the existing facilities of Hydraulics Laboratory, which included the flume, pump, sump and laser equipment. The experimental set-ups were designed by both the technicians in the Laboratory and the author with the guidance of his supervisors. The author was mainly responsible to obtain data and exercise quality control in the measurement. The objective of this experimental work was to use the LDA system to obtain accurate and detailed measurements of mean velocities and turbulent stresses. The measurements included surface

profiles, mean velocity components u and v , turbulent shear stress $\overline{u'v'}$ and turbulence intensities $\sqrt{\overline{u'^2}}$ and $\sqrt{\overline{v'^2}}$. The experimental results then can be used to study the following:

- (1) The major flow characteristics of submerged hydraulic jumps, including the decay of the maximum mean velocity, turbulence quantities and their related length scales;
- (2) Similarities of mean velocity and turbulence fields in fully developed region of submerged jumps, which include the similarity analysis of u velocity profile, $\sqrt{\overline{u'^2}}$, $\sqrt{\overline{v'^2}}$ and $\overline{-u'v'}$ profiles;
- (3) Three dimensional features of submerged jumps subject to aspect ratio influence;
- (4) Comparison among wall jets, free jumps and submerged jumps, considering submerged jumps as transitional phenomena between free jumps and wall jets;
- (5) Testing and improving the prediction methods.

The current investigation covers ten experimental conditions with the submergence factor S varying from about 0.20 to about 1.70 and inlet Froude number F_1 approximately equal to 3.0, 5.5 and 8.0. The actual experimental conditions are listed in Table 3.

2.2 Facilities

2.2.1 Experimental Arrangement

The schematic diagram of the experimental layout is shown in Figure 13, which also serves to define the symbols used. The submerged jumps were formed just below a vertical gate in a horizontal rectangular channel. The channel is 0.467 m wide, 0.515 m deep and 7.5 m long with glass walls on both sides of the flume and an aluminum bed. The thickness of the glass wall is 12 mm. Water was supplied by a 19 kW capacity and 0.22 m³/s rated discharge pump. The discharge was measured with an in-line magnetic flow meter, which was digitized and was used to monitor the flow. There were two valves along the pipe line so as to adjust the discharge. In any experiment, the discharge and the water level in the head-tank were maintained constant. Therefore, the inlet velocity could be kept constant and thus the inlet Froude number F_1 at the entrance. In order to achieve a relatively uniform stream at the gate, a special entrance device with curved lower section was fitted to the gate. This device was actually a quarter of a pipe with 0.152 m radius and 0.467 m length. With this device the flow contraction after the entrance was nearly eliminated. Downstream water level was controlled by a vertical plate that rose from the bed of the flume. By changing the discharge and the inlet opening different inlet condition could be achieved. By regulating the downstream level,

different submergence condition could be obtained for any given supercritical Froude number.

2.2.2 Measuring Equipment

The experimental results were collected using a two color back-scatter LDA system. A detailed description of this system has been written by Steffler (1984). The schematic diagram of the LDA setup is reproduced from Steffler (1984) in Figure 14.

The LDA technique is a non-intrusive, instantaneous fluid velocity measurement method. Durst et al (1976) had made an extensive review on the history, theory and application of the LDA technique. Buchave et al (1979) discussed the expected accuracies of this technique.

The laser of this system was a 4 W Argon-Ion laser with actual power of about 500 mW. The three laser beams, one blue (488 nm), one green (514.5 nm) and one mixed, were focused at a measuring point from one side of the flume. In order to obtain the best signal quality and excellent spatial resolution, the optical lens with focal length of 160 mm was selected for all the measurements. The nominal measuring probe volume of the intersecting beams was an ellipsoid with diameter 0.04 mm and length 0.64 mm. The position of the mirror and lens in the traversing system was controlled by a computer. The nominal position accuracy was ± 0.01 mm.

Counter processors were used to evaluate the Doppler frequencies. Subsequent computer analysis consisted of velocity bias averaging (to be discussed later) and outlier rejection. The number of samples taken at every point was 20,000. This corresponded to a sample averaging time of about 300 seconds. For submerged hydraulic jumps with higher inlet Froude number and lower submergence, more air was entrained into the flow. When air bubbles were present, the data acquisition rate was low, provided other conditions were not changed. So for a region with relatively high concentration of air bubbles the sampling time was up to 900 seconds.

The sump used was a big reservoir and was shared by a number of users. In order to enhance the signals for the LDA system because of the short focal length and small measuring volume, the water was seeded with latex paint. Since the sump was large, the latex paint had to be added two or three times a day so as to maintain a good data acquisition rate. The particle size of latex paint was approximately 0.1μ . The concentration of about 1 ppm (part per million) gave the best data acquisition rate.

Considering the thickness of the glass side wall of the channel and the effect of refraction, the actual maximum distance of the measuring plane from the side wall was about 195 mm using the following formula:

$$z = (z' - z'_1) \frac{n}{\cos(\psi/2)} \sqrt{1 - \frac{\sin^2(\psi/2)}{n^2}} \quad (41)$$

where z is the distance from the inside of the wall to the measuring point; z' the traverse reading; z'_1 traverse reading when measuring point was focused on the inside of the wall; n refractive index of water (1.33) and ψ is the beam intersection angle.

The flume was constructed with a thick and heavy steel plate at the base. This plate projected out of the side wall and restricted the downward movement of the focusing lens mounted on the threaded tracks, if the lens was too close to the side wall. This portion of the steel base could have been cut, but doing so would have damaged the stability of the existing equipment. Therefore, this option was abandoned. Because of this restriction, most of the measurements were conducted at the plane of $z=167$ mm, i.e. $z/W=0.36$, where z is the transverse distance from the side wall as shown in Figure 13.

2.3 Experimental Results

Table 3 lists the ten experimental conditions with serial numbers from S1 to S10. For series S1 to S7 the same inlet opening of $Y_1 = 25$ mm was used. For series S8 to S10 a smaller inlet opening of $Y_1 = 15$ mm was used to obtain a higher inlet Froude number. U_1 listed in Table 3 is the averaged longitudinal velocity at the inlet opening; Y_1 the

tailwater depth, F_1 the inlet Froude number and Re_1 is the inlet Reynolds number defined as

$$Re_1 = \frac{U_1 Y_1}{\nu} \quad (42)$$

The surface profile $H(x)$ and the downstream tailwater depth Y_t were measured with a point gauge. Because the water surface along the jump was fluctuating, especially for higher inlet Froude numbers and smaller submergences, $H(x)$ was obtained as an averaged depth profile from the point gauge readings. The results from the surface profile measurements for all the experimental conditions are shown in Table 4. The observations were nondimensionlized by Y_1 and plotted in Figure 15, which can indicate the hydrostatic pressure field along the jump.

For each experimental condition, detailed measurements at the plane of $z = 167$ mm, i.e. $z/W = 0.36$, were carried out to obtain vertical profiles of the internal flow characteristics. These characteristics include the time-averaged longitudinal component of velocity u and vertical component v , kinematic turbulence shear stress $-\overline{u'v'}$ and turbulence intensities $\sqrt{\overline{u'^2}}$ and $\sqrt{\overline{v'^2}}$. The number of measured sections for each run ranged from 10 to 17 depending on different experimental conditions. More sections were covered near the gate than downstream of the recirculating zone. For each section about 20 data points

were measured, with the variation of more data points used for sections near inlet and for regions near the bed and in the shear layer, and less data for the sections downstream and the regions away from the wall jet. The raw experimental data were too numerous to be included in this thesis. Instead, they have been stored in a data bank and can be archived from the T. Blench Hydraulics Laboratory at the University of Alberta. The results of mean velocities u and v , turbulence quantities $\sqrt{u'^2}$, $\sqrt{v'^2}$ and $-\overline{u'v'}$ from the measurements at $z/W = 0.36$ for all the conditions are plotted from Figure 16 to 65. It should be noticed that all the plots are nondimensionalized by a length scale Y_1 and a velocity scale U_1 .

For each section, extra measurements were made in vertical planes with $z/W=0.30$ and 0.04 . Usually only five carefully selected data points at both these planes were measured to check the spanwise variation of the flow. Besides these measurements, another set of data points to indicate spanwise variation were taken for each section at the plane of $y = \text{constant}$. A constant y plane was selected close to the surface and kept constant for each run. The results of this spanwise variation for all the conditions are plotted from Figure 66 to 75, where only the measurements for longitudinal velocity u profiles are plotted. The original intention for these extra measurements was to validate the two dimensionality of submerged jumps as they were previously treated. Much to

our surprise, the results revealed that the flow was very three dimensional in nature due to influence of the side walls of the flume. In light of this fact, three representative sections at $x/Y_1 = 4, 32$ and 64 in the condition of $F_1 = 5.49$ and $S = 0.63$ were selected to undergo more detailed measurements with 7 vertical profiles taken from $z/W = 0.02$ to 0.36 . The particular series S6 was chosen, because its inlet Froude number and submergence factor are in the middle range of the ten series. The longitudinal velocity u and turbulence shear stress $-\overline{u'v'}$ profiles from these measurements are plotted in Figure 76 and 77 respectively. These results will be further analyzed in the next section.

2.4 Discussion and Analysis

2.4.1 Experimental Errors

The experimental errors could be introduced by using point gauge in measuring surface profiles and by using LDA in measuring velocities. Possible sources of errors in obtaining the experimental data were identified and discussed in this section.

For the surface profile measurements along the center plane, three readings from the point gauge were recorded for each measuring point. The averaged value was presented in Table 4. Since the accuracy of the reading relied on the visual judgement, the error introduced to the surface profile data could only be estimated. For some experimental

conditions, where the inlet Froude number was high and submergence was low, the water surface could fluctuate up to 10 mm at locations closer to the gate. For example, the lowest depth measured for S8 was 112 mm and this could lead to about 9% fluctuation and approximately $\pm 5\%$ accuracy in obtaining the average value. This is the worst estimate though. For distances further downstream, the water surface fluctuated less and the accuracy would improve. For a still water surface, the accuracy of point gauge was ± 0.5 mm.

The accuracy of position in longitudinal and vertical directions was determined by the nominal position accuracy of LDA traverse system i.e., ± 0.01 mm. In spanwise direction, the position accuracy was governed by both the traverse system and the ruler, which was used to measure the distance between the side wall and the lens. The accuracy for the position in z direction would be about ± 0.5 mm.

The instantaneous Doppler frequency measured by the LDA system was given by

$$f_D = f_d - f_0 \quad (43)$$

where Doppler frequency is denoted by f_D ; f_d is the shifted Doppler frequency; and f_0 is the shifted frequency. The shifted frequency f_0 was introduced to enhance signal quality and insure flow direction information. The shifted Doppler frequency f_d measured at the counter introduced about $\pm 1\%$ error, and the shifted frequency f_0 would

introduce another $\pm 0.5\%$ error. For example, a 1 MHz frequency measured in the counter minus a 500 Hz frequency shift would result in ± 12.5 KHz or about $\pm 2.5\%$ error in calculating the Doppler frequency f_D .

The instantaneous Doppler frequency was related to the instantaneous velocity by the following relationship,

$$u_{in} = \frac{f_D \lambda}{2 \sin(\theta/2)} \quad (44)$$

where u_{in} is the instantaneous velocity; λ is the wavelength; and θ is the intersection angle by one set of beams. The error in measuring θ was estimated at about $\pm 0.1^\circ$. For example, if θ was about 8° , f_D about 500 KHz and λ equal to 488 nm, the error in calculation u_{in} would be about ± 0.06 m/s with a mean of 1.749 m/s, or u_{in} was in error by about $\pm 3\%$. The accuracy of u_{in} is mainly controlled by the error in θ . Extreme care was taken in the actual measurement to ensure the accuracy of 0.1° in θ was approximately achieved. It was also noticed that the error introduced in f_D was random, whereas the error in θ could be systematic.

The flow statistics obtained were the following,

- $\overline{u_G}$ - mean velocity in green direction;
- $\overline{u_B}$ - mean velocity in blue direction;
- $\overline{u'_G{}^2}$ - mean square turbulence intensity in green direction;

$\overline{u'^2_B}$ - mean square turbulence intensity in blue
 direction;
 $\overline{u'_G u'_B}$ - covariance of velocity fluctuation.

In calculating these average values, a velocity bias correction method proposed by Bachave et al (1979) was applied. Theoretically speaking, no bias would exist if the particle residence time was measured and time average was formed by integrating only during the time measurement. For example, in an unbiased manner the mean velocity can be approximated by

$$\overline{u} = \frac{\sum_{i=1}^N u_i \Delta t_i}{\sum_{i=1}^N \Delta t_i} \quad (45)$$

Since the residence time Δt_i was not available for u_i , an alternative was to weigh each sample by a factor inversely proportional to the measured velocity such as the formulas used as in the following,

$$\overline{u_G} = \frac{\sum_{i=1}^N \frac{u_{Gi}}{|u_i|}}{\sum_{i=1}^N \frac{1}{|u_i|}} \quad (46)$$

$$\overline{u_B} = \frac{\sum_{i=1}^N \frac{u_{Bi}}{|u_i|}}{\sum_{i=1}^N \frac{1}{|u_i|}} \quad (47)$$

$$\overline{u'_G{}^2} = \frac{\sum_{i=1}^N \frac{u_{Gi}^2}{|u_i|}}{\sum_{i=1}^N \frac{1}{|u_i|}} - \overline{(u_G)}^2 \quad (48)$$

$$\overline{u'_B{}^2} = \frac{\sum_{i=1}^N \frac{u_{Bi}^2}{|u_i|}}{\sum_{i=1}^N \frac{1}{|u_i|}} - \overline{(u_B)}^2 \quad (49)$$

$$\overline{u'_G u'_B} = \frac{\sum_{i=1}^N \frac{u_{Bi} u_{Gi}}{|u_i|}}{\sum_{i=1}^N \frac{1}{|u_i|}} - \overline{u_B} \overline{u_G} \quad (50)$$

where:

$$u_i = \sqrt{u_{Bi}^2 + u_{Gi}^2} \quad (51)$$

N = number of accepted samples

The expected errors by using these formulas were discussed in details by McLaughlin and Tiederman (1973).

The velocities obtained in the blue and green beam directions were transferred to the horizontal and vertical values by the following formulas:

$$\overline{u} = \overline{u_B} \cos\alpha - \overline{u_G} \sin\alpha \quad (52)$$

$$\overline{v} = \overline{u_B} \sin\alpha + \overline{u_G} \cos\alpha \quad (53)$$

$$\overline{u'^2} = \overline{u_B'^2} \cos^2\alpha - 2 \overline{u'_G u'_B} \sin\alpha \cos\alpha + \overline{u'_G'^2} \sin^2\alpha \quad (54)$$

$$\overline{v'^2} = \overline{u_B'^2} \sin^2\alpha + 2 \overline{u'_G u'_B} \sin\alpha \cos\alpha + \overline{u'_G'^2} \cos^2\alpha \quad (55)$$

$$\begin{aligned} \overline{u'v'} &= \overline{u_B'^2} \sin\alpha \cos\alpha + \overline{u'_G u'_B} (\cos^2\alpha - \sin^2\alpha) \\ &\quad + \overline{u'_G'^2} \sin\alpha \cos\alpha \end{aligned} \quad (56)$$

The angle of rotation of the optics α was set to 45° by eyes. Estimated error of $\Delta\alpha$ would be about $\pm 0.5^\circ$. By neglecting the errors of $\overline{\Delta u_G}$ and $\overline{\Delta u_B}$, the errors for the calculated quantities from equations (52) to (56) were approximated by the following,

$$\overline{\Delta u} \approx -\overline{v} \Delta\alpha \quad (57)$$

$$\overline{\Delta v} \approx \overline{u} \Delta\alpha \quad (58)$$

$$\overline{\Delta u'^2} \approx -2 \overline{u'v'} \Delta\alpha \quad (59)$$

$$\overline{\Delta v'^2} \approx 2 \overline{u'v'} \Delta\alpha \quad (60)$$

$$\overline{\Delta u'v'} \approx (\overline{u'^2} - \overline{v'^2}) \Delta\alpha \quad (61)$$

In a region close to the bed, where velocity was dominantly horizontal and \bar{v} was in the order of 1% of \bar{u} , the relative error in \bar{v} could be 100%. For this reason, \bar{v} could only be considered at best to be of qualitative merit in these regions. On the other hand, in a recirculating region where \bar{u} was about 1% of \bar{v} , the relative error in \bar{u} could also be 100%. In the strong shear layers, where maximum $\overline{u'^2}$, $\overline{v'^2}$ and $\overline{u'v'}$ occurred and $\overline{u'^2}$ was in the order of $3\overline{u'v'}$ and $\overline{v'^2}$ was in the order of $1.7\overline{u'v'}$, the relative error due to Δu for $\overline{u'^2}$ was about 0.6%, $\overline{v'^2}$ about 1% and $\overline{u'v'}$ about 0.7%. However, in region away from the shear layer where $\overline{u'v'}$ was small but $\overline{u'^2}$ and $\overline{v'^2}$ were large, the relative error in $\overline{u'v'}$ would be large and data in $\overline{u'v'}$ would be more scatter.

2.4.2 Inlet Condition

Despite the efforts to achieve an uniform inflow, the measurements at the inlet still indicate a slightly skewed longitudinal velocity distribution and downward vertical velocities. The longitudinal velocity u at the inlet (above the very thin boundary layer) can be well approximated by a straight line with an averaged slope as

$$\frac{u}{U_1} = 0.99 + 0.02 \frac{y}{Y_1} \quad (62)$$

This gives about 2% difference in velocity with a maximum at the top and a minimum at the bottom. The maximum downward

velocity is about 2 to 6% of U_1 depending on different conditions. The averaged turbulence intensities $\sqrt{\overline{u'^2}}$ and $\sqrt{\overline{v'^2}}$ at the inlet are about 3% of U_1 . The inlet turbulence shear stress is almost zero. The flow at the inlet could approximately be regarded as potential flow.

2.4.3 Major Flow Characteristics

Major flow characteristics referred to in this study include the decay of mean velocity and turbulence quantities and their length scales. For following discussion, the typical vertical distributions of u and $\overline{u'v'}$ are shown in Figure 78, which also serves to define the symbols used in the following analysis. The subscript m always refers to a maximum in a vertical distribution. The length scale b is for the mean velocity and $y = b$ where $u = u_m/2$ and $\frac{\partial u}{\partial y} < 0$. The length scale d is for the shear stress and $y = d$ where $\overline{u'v'} = \frac{(u'v')_m}{2}$ and $\frac{\partial (u'v')}{\partial y} < 0$. The symbol $\bar{\delta}$ defines the point at y where shear stress is zero and $\frac{\partial (u'v')}{\partial y} > 0$.

If submerged jumps are analyzed as two dimensional flows as a first approximation, equations (17) and (18) can be obtained from dimensional analysis. These two equations show that the decay of u_m/U_1 and growth of b/Y_1 are determined by x/Y_1 , F_1 and S . If the measurements from the plane $z/W=0.36$ are selected as representative data for a submerged jump, then the decay of u_m/U_1 is shown as in Figure 79(a). In this figure a length scale L is used

instead of Y_1 , where L is defined as the distance from the inlet where $u_m/U_1=0.5$. This length scale turns out to be capable of grouping all the major flow characteristics together. In order to show this point, the data from Rajaratnam (1972) were re-plotted in Figure 79(b). The data in Figure 79(b) are slightly different from that of Figure 79(a), because U_1 and Y_1 are defined differently by Rajaratnam (1972) where a sharp-edge sluice gate was used. Nevertheless, Figure 79 reveals an important observation that if a length scale L is applied, the decay of u_m/U_1 behaves more or less the same in free jumps, submerged jumps and wall jets for x/L up to about 1.5. The decay behaviors of u_m in longitudinal direction deviate after x reaches L from free jumps to wall jets. For example, at $x/L=2$, u_m differs by 100 to 150% comparing free jumps and wall jets.

It is interesting to find out that this length scale L is also capable of grouping the maximum $(\overline{u'v'})_m$, $(\sqrt{\overline{u'^2}})_m$ and $(\sqrt{\overline{v'^2}})_m$ together for different submerged jumps. These results are plotted in Figure 80, where the subscript mm refers to the maximum value in the variation of the sectional maximum value with x . Even though the decay of shear stress $(\overline{u'v'})_m$ demonstrates some degree of scatter, the turbulence intensities $(\sqrt{\overline{u'^2}})_m$ and $(\sqrt{\overline{v'^2}})_m$ are better correlated. It can also be noticed that the mean approximate curves in Figure 80(b) and (c) are the same.

Figure 81 plots $(\overline{u'v'})_{mm}$, $(\sqrt{\overline{u'^2}})_{mm}$ and $(\sqrt{\overline{v'^2}})_{mm}$ against inlet Froude number F_1 for all conditions. This

figure shows a noticeable trend of decrease in these maximum quantities with the increase of inlet Froude number. It is also clear that submergence plays a role in differentiating them but not as significantly as the inlet Froude number. For example, Figure 81 shows that for $F_1=3.1$ $\overline{(u'v')}_{\text{mm}}$ decreases from 0.023 to 0.018 U_1^2 with the increase of S from 0.26 to 1.69. The change is about 30%. However, with about the same submergence factor $S=0.24$, $\overline{(u'v')}_{\text{mm}}$ decreases from 0.023 to 0.012 U_1^2 with increase of inlet Froude number from 3.1 to 8.1. The change is about 90%. Even though there was an uncertainty in determining the maximum shear stress and intensities based on about 13 vertical profiles in this experiment, Figure 80 has been used in extrapolating the maxima from the limited data points. This procedure warranted that the errors in determining the maximums would be confined to about 10%. In Figure 82, $\overline{(u'v')}_{\text{mm}}$ decrease with increase of submergence with the exception for $F_1=5.5$. This exception was considered due to the experimental error and uncertainty. The increase of maximum turbulent quantities with decrease of submergence could be explained by the fact that smaller submergence generated higher curvature streamline in the mean flow so that there was a stronger centrifugal force and thus the turbulence production.

The variations of length scales b/Y_1 , d/Y_1 and $\overline{\delta}/Y_1$ with x/Y_1 are plotted in Figure 83. This figure shows that both the mean velocity and turbulence shear stress diffuse

faster than those in the classical wall jet. This is reasonable if a submerged jump is treated as a wall jet under adverse pressure gradient. This can also explain why the length scale of a submerged jump with lower submergence grows faster than those with higher submergence. Figure 83 also shows that for a submerged jump the shear stress diffuses faster than the mean velocity.

2.4.4 An Equation for the Length Scale L

The analysis above will become very valuable if the length scale L can be determined for each condition. A relationship between L and F_1 and S is developed based on the data from the present study and Rajaratnam (1972). The derivation is given as follows.

To develop an equation for the length scale L, which is equal to x where $u_m/U_1=0.5$, the flow of a submerged jump is assumed to be two dimensional. Further the flow in the fully developed region is assumed similar.

From the continuity equation

$$\frac{\partial u}{\partial x} + \frac{\partial v}{\partial y} = 0 \quad (3)$$

the vertical velocity v can be expressed as

$$v = - \int_0^y \frac{\partial u}{\partial x} dy \quad (63)$$

Assuming hydrostatic pressure distribution along the jump the momentum equation becomes

$$u \frac{\partial u}{\partial x} + v \frac{\partial u}{\partial y} = -g \frac{dH}{dx} + \frac{\partial(-\overline{u'v'})}{\partial y} \quad (64)$$

Assume

$$\begin{aligned} u &= u_m f_1\left(\frac{y}{b}\right) \\ &= U_1 f_2\left(\frac{x}{L}\right) f_1\left(\frac{y}{b}\right) \end{aligned} \quad (65)$$

and

$$\begin{aligned} -\overline{u'v'} &= -(\overline{u'v'})_m f'_3\left(\frac{y - \bar{\delta}}{d - \bar{\delta}}\right) \\ &= -(\overline{u'v'})_{mm} f_4\left(\frac{x}{L}\right) f'_3\left(\frac{y - \bar{\delta}}{d - \bar{\delta}}\right) \end{aligned} \quad (66)$$

If $(\overline{u'v'})_{mm}/U_1^2$ is assumed to be a constant, which is independent of the inlet condition, then $(\overline{u'v'})_{mm} = C_{mm}U_1^2$, where C_{mm} is a constant. The present data and those from wall jets show $\bar{\delta}/d=0.07$ to 0.15 . If $\bar{\delta}/d$ is further assumed to be a constant, equation (66) can be replaced by

$$-\overline{u'v'} = -U_1^2 f_4\left(\frac{x}{L}\right) f_3\left(\frac{y}{d}\right) \quad (67)$$

Replacing y/b , x/L and y/d by

$$X_1 = \frac{y}{b} ; X_2 = \frac{z}{L} ; X_3 = \frac{y}{d} \quad (68)$$

and substituting equations (63), (65) to (68) in the equation (64) and performing the necessary derivation yield

$$\begin{aligned} & U_1^2 f_1 f_2 \left(\frac{f_1}{L} \frac{df_2}{dX_2} - \frac{f_2}{b^2} \frac{df_1}{dX_1} \frac{db}{dx} \right) - \frac{U_1^2 f_2}{b} \frac{df_1}{dX_1} \left(\frac{f_1}{L} \frac{df_2}{dX_2} y - \frac{y^2 f_2}{2b^2} \frac{df_1}{dX_1} \right. \\ & \left. \frac{db}{dx} \right) \\ & = -g \frac{dH}{dx} - \frac{U_1^2 f_4}{d} \frac{df_3}{dX_3} \end{aligned} \quad (69)$$

Let $x=L$ and $y=b$ then $X_1=1$, $X_2=1$, $X_3=b/d$ and f_1 , f_2 , f_3 , f_4 , f_1' , f_2' , f_3' , f_4' and $(dH/dx)_{x=L}$ become constants. Substituting these conditions into the equation (69) yields

$$\frac{L}{Y_1} = \frac{1}{C_1 + C_2 \left(\frac{dH}{dx} \right)_L F_1^{-2}} \quad (70)$$

C_1 and C_2 are constants.

For a classical wall jet

$$\left(\frac{dH}{dx} \right)_L = 0 \text{ and } \frac{L}{Y_1} = 49$$

substituting these conditions into equation (70) yields

$$\frac{L}{Y_1} = \frac{49}{1 + C_3 \left(\frac{dH}{dx} \right)_L F_1^{-2}} \quad (71)$$

C_3 is a constant to be determined.

From the present measurements and the data from Rajaratnam (1972), it seems that $(dH/dx)_{x=L}$ is mainly influenced by the submergence factors S as shown in Figure 84(a). An approximate equation is obtained from curve fitting as

$$\left(\frac{dH}{dx}\right)_L = 0.18 \times 10^{-0.5S} \quad (72)$$

Substituting equation (72) in equation (71) yields

$$\frac{L}{Y_1} = \frac{49}{1 + C 10^{-0.5S} F_1^{-2}} \quad (73)$$

The constant C in equation (73) is the only constant that needs to be determined. Using the data of L/Y_1 from the present measurements and the data from Rajaratnam (1972) a best fit curve with $C = 27$ is obtained as shown in Figure 84(b). Then equation (73) is as follows,

$$\frac{L}{Y_1} = \frac{49}{1 + 27 \times 10^{-0.5S} F_1^{-2}} \quad (74)$$

This equation is valid for free jumps, submerged jumps and wall jets. Therefore, L/Y_1 can be estimated when S and F_1 are known.

$$\frac{L}{Y_1} = \frac{49}{1 + 27 \times 10^{-0.5S} F_1^{-2}} \quad (75)$$

L/Y_1 can be calculated from this equation if F_1 and S are known. As shown in Figure 84(b), the dimensionless length scale L/Y_1 from the experiments is in large degree of scatter. The equation (75) over predicts the length scale L by up to 44% in one instance, and under predicts by up to 11% in another. Therefore, the empirical equation (75) can only be used as a very rough estimate of the length scale L . The large degree of scatter is considered to be caused both the semi-empirical derivation of the equation and the error introduced in determining L from the experimental data.

2.4.5 Fully Developed Region

From the flow development point of view a submerged jump can be divided into three distinguishable regions. These are the developing, the fully developed and the recovering regions as shown in Figure 13. The end of the potential core denotes the end of the developing region and the beginning of the fully developed region. If the length of the roller L_{rsj} is defined as the length of a submerged jump as by Rajaratnam (1967), L_{rsj} denotes the end of the fully developed region and the beginning of the recovering region.

The developing region in a submerged jump is similar to that of a wall jet. One difference is that the flow near the gate in a submerged jump undergoes acceleration due to negative pressure gradient caused by falling water surface. This trend is noticeable in Figure 79(a). Because this region is limited to about 15% of L_{rsj} , the following discussion will concentrate on the fully developed region which occupies almost 85% of L_{rsj} .

The data for classical wall jets in a stagnant surrounding with a plane bed are taken from Wilson and Goldstein (1976). For further information about the experimental measurements on wall jets one can refer to a recent critical review by Launder and Rodi (1981). The reason that the data from Wilson and Goldstein (1976) are chosen is because the data are consistent and close to most of those from other reliable experiments.

The flow in the fully developed region demonstrates some degree of similarity. Because the maximum vertical velocity v in the recirculating zone for all submerged jumps is only about 8% of U_1 , the attention will be placed on the analysis of u . If u_m and b at a section are selected as the velocity and length scales respectively, u/u_m can be plotted against y/b as shown from Figure 85 to 88. From this figure it is obvious that u/u_m profiles are similar to those of a classical wall jet for y/b up to about 1.5. Beyond this the profile of u/u_m is mostly influenced by the reversing flow. This observation validates the model

proposed by Rajaratnam (1965), in which a submerged jump is considered as a wall jet under adverse pressure gradient. Similar analysis can be made regarding the turbulence shear stress $\overline{u'v'}$ and intensities $\sqrt{\overline{u'^2}}$ and $\sqrt{\overline{v'^2}}$. As shown in Figure 80 the decay curves of $(\overline{u'v'})_m$ and $(\sqrt{\overline{u'^2}})_m$ are quite different from that of u_m , but the decays of $(\sqrt{\overline{u'^2}})_m$ and $(\sqrt{\overline{v'^2}})_m$ are similar. This observation is quite different from a wall jet in which the decay of those quantities are all similar. Because of this reason $(\overline{u'v'})_m$ and $(\sqrt{\overline{u'^2}})_m$ are selected instead of u_m as the scales for the turbulence shear stress and turbulence intensities respectively. At the same time d is used instead of b as a length scale for the turbulence quantities, since the observation shows that b is not capable of correlating turbulence quantities as in a wall jet. The results are plotted from Figure 89 to 100. The shape of $\overline{u'v'}/(\overline{u'v'})_m$ profiles in submerged jumps is almost identical to that of a wall jet. The shapes of $\sqrt{\overline{u'^2}}/(\sqrt{\overline{u'^2}})_m$ and $\sqrt{\overline{v'^2}}/(\sqrt{\overline{u'^2}})_m$ distributions are slightly different from those of a wall jet. Figure 93 to 100 also show that the shapes of $\sqrt{\overline{u'^2}}/(\sqrt{\overline{u'^2}})_m$ and $\sqrt{\overline{v'^2}}/(\sqrt{\overline{u'^2}})_m$ distributions are dependent on submergence factors and that the background turbulence intensities in the recirculating zone are about 30 to 40% of $(\sqrt{\overline{u'^2}})_m$. Furthermore, Figure 93 to 100 indicates that $(\sqrt{\overline{v'^2}})_m$ is about 75% of $(\sqrt{\overline{u'^2}})_m$ throughout the developed region.

2.4.6 Three Dimensional Features

Liu (1949) reported that there were two distinguishable vortices on the water surface of a submerged jump at the corners of the gate, but how they influenced the flow was not clear. He speculated the effects as follows:

- (1) Distorting the two dimensional characteristics of the flow pattern, in that spiral motion will be introduced; in the central region of the flow, velocities are increased, and so near the boundary velocities are reduced;
- (2) Additional energy is withdrawn from the mean flow.

The present study shows not only the existence of such vortex motion but also its significance. As shown in Figure 76(a) the vortex motion near the gate extends from the water surface to the center of the shear layer. Therefore, it is reasonable to expect that its influence will be significant under relatively high submergence. This vortex motion also alters the downstream flow development quite significantly. As shown in Figure 76(b) at $x/Y_1=32$, u_m near the center plane of the channel is about 30% smaller than that near the side wall. Further downstream at $x/Y_1 = 64$, which is near the end of the fully developed region, the difference between the maximum u_m near the side wall and the minimum u_m near the center plane is up to 50% as shown in Figure 76(c). Another effect is that the length scale b for u near the side wall is higher than that near the center plane. This phenomena is called the "climb" of a wall jet near the side

wall by George (1959) and Rajaratnam (1968). This climbing effect is believed due to the influence of this vortex motion. As shown in Figure 76(a) the flow close to the bed is two dimensional shortly after the inlet, but on top of this there is vortex motion. This motion causes reversing flow near the center plane and forward flow near the side wall. As shown in Figure 77(a) the shear stress near the center plane is about 50% higher than that near the side wall. Therefore, this vortex motion causes faster diffusion near the center plane than near the side wall at locations further downstream. The results are of course that u_m near the center plane is smaller than that near the side wall.

Let unit discharge q be defined as

$$q = \int_0^H u \, dy \quad (76)$$

and the unit kinematic pressure plus momentum flux be defined as

$$M = \int_0^H u^2 \, dy + \frac{gH^2}{2} \quad (77)$$

The unit discharge and unit momentum distributions along the plane of $z/W=0.36$ are calculated based on the u velocity profiles and the results are shown in Figure 101 to 102. The unit discharge distribution near the center plane strongly indicates that the flow is so three dimensional

that the unit discharge close to the inlet is up to 100% less than the inlet unit discharge q_1 , the value it should have if the flow is two dimensional. Figure 101 shows that the flow after the jump recovers to a constant unit discharge q_1 , where the flow can be regarded as two dimensional. The unit momentum distribution in Figure 102 shows that the maximum loss of initial momentum near the center plane due to the loss of discharge is up to 30% even when the loss of momentum due to friction is excluded.

When there are unit discharge and unit momentum losses near the center plane, there should be unit discharge and momentum gains near the side wall to satisfy the conservation laws. That is exactly what Figure 103 shows. In Figure 103 the spanwise unit discharge and momentum distributions for three cross sections in the series S6 are plotted. Figure 103(a) shows an interesting observation that at the plane of $z/W = 1/4$, or at the "quarter" plane, the unit discharge appears to be constant, i.e. $q/q_1 = 1$.

The influence of the vortex motion is believed to be mainly confined to the reversing part of the flow. The forward part of the flow has a strong momentum in the developing and early part of developed regions so that this portion of the flow is less influenced by the vortex motion. For example, Figure 76(a) shows a $0.4U_1$ difference in u for reversing part whereas for the forward part there is no difference. Even though the unit discharge varies a lot along the plane closer to the center, the unit momentum

varies much less than the unit discharge. This also indicates that the forward part of the flow, which carries most of the momentum, is less influenced by this vortex motion. Moreover, its influence on the turbulent field is less important. Figure 77 shows only about 25% variation at $x/Y_1=4$ and about 20% at $x/Y_1=32$.

This analysis raises a very important question of whether or not a submerged jump should be considered a two dimensional flow. If a two dimensional prediction is obtained, its limitation should be emphasized and its results should be interpreted properly.

2.4.7 Length of the roller

The distance from the efflux section to the end of the roller in submerged hydraulic jumps is defined as the length of the roller. It is denoted by L_{rsj} as shown in Figure 13. In his review, McCarquodale (1986) pointed out that lengths of the rollers in submerged hydraulic jumps were found to be in a large degree of scatter. The roller lengths observed visually and determined by velocity measurements are known to differ considerably.

In this experiment, the roller length could not be accurately determined, because only a few vertical profiles were measured for each experimental condition. However, the roller lengths could be estimated from extrapolating the lines of zero longitudinal velocities of vertical profiles.

The roller lengths determined this way only indicate those on the plane of $z/W=0.36$, since the detailed measurements were taken on this plane. The estimated roller lengths for the ten experimental conditions are listed in Table 5.

For comparison, the roller lengths predicted from empirical equation (16) by Stepanov (1959) are also listed in Table 5, in which the ratio of predicted to measured roller lengths are also included. Figure 104 shows the variations of this ratio with both inlet Froude numbers and submergence factors. For small submergence factors, say $S=0.25$, Stepanov's equation underpredicts the roller lengths by about 30%. For high submergence factor, say $S=1$, the empirical relationship overpredicts by almost 190%. The trend of discrepancies appears to be more closely related to submergence factors than inlet Froude numbers.

The discrepancies could be partially due to the errors in estimating roller lengths, but these errors are considered to be less than 10%. Another reason is the position of measuring plane where roller lengths are determined. The spanwise measurements of u , as shown from Figure 66 to 75, indicate that the distance of zero u velocity from the inlet differs by 10 to 20%. Other factors, such as inlet turbulence levels and aspect ratio influences to the flow, could also contribute to the discrepancies among different experimental results.

2.5 Conclusions

The experimental measurements of submerged hydraulic jumps under the ten conditions have been presented in this part of the thesis. The extensive coverage of experimental conditions provides, at the first time, detailed and accurate data on internal structure of submerged hydraulic jumps. Further these data can be used as a reference for comparison with the theoretical predictions.

From the discussion and analysis of these data, the following conclusions can be drawn from the present study of submerged hydraulic jumps in a horizontal and rectangular channel of constant width.

- (1) If a length scale L is defined so that $u_m/U_1=0.5$ when $x=L$, this length scale L is capable of grouping all major flow characteristics u_m/U_1 , $(\overline{u'v'})_m/(\overline{u'v'})_{mm}$, $(\sqrt{\overline{u'^2}})_m/(\sqrt{\overline{u'^2}})_{mm}$ and $(\sqrt{\overline{v'^2}})_m/(\sqrt{\overline{v'^2}})_{mm}$ together for different submerged jumps. The correlation is good for x/L up to about 1.5. An empirical equation for L was proposed and it can be used to roughly estimate L , but the equation can be in error up to about 45%. The maximum turbulence quantities can also be estimated from F_1 and S . Therefore, the major flow characteristics can be approximately determined for submerged jumps under different conditions.
- (2) It appears that there is a noticeable trend of decrease in maximum turbulent stress and intensities

with increasing inlet Froude number. For the same submergence factor the maximum turbulent shear stresses can be different by 90% from $F_1=3$ to 8. The maximum turbulent stress decreases with increase of submergence.

- (3) In the fully developed region of a submerged jump, which occupies about 85% of roller length L_{rsj} , the flow demonstrates some degree of similarity. The distribution of u/u_m against y/b is similar to that of a wall jet for y/b up to about 1.5. The shape of $\overline{u'v'}/(\overline{u'v'})_m$ against $(y-\bar{\delta})/(d-\bar{\delta})$ is almost identical to that of a wall jet. The shapes $\sqrt{\overline{u'^2}}/(\sqrt{\overline{u'^2}})_m$ and $\sqrt{\overline{v'^2}}/(\sqrt{\overline{u'^2}})_m$ against y/d are self-similar among different submerged jumps.
- (4) Submerged hydraulic jumps are three dimensional in nature. The climbing effect of mean velocity component u near side walls is due to the vortex motion near the gate. The losses of unit discharge q and unit kinematic pressure plus momentum flux M at the center plane occur along with their gains near the side walls. After the jump the flow will recover into a two dimensional flow. The influence of this vortex motion has stronger effect on the reversing portion of the flow than that of the forward portion. Its influence on the turbulent field is less significant.
- (5) The lengths of the roller from this experiment have been compared with those predicted by Stepanov's

equation. It is found that the equation can be in error by a factor of two.

If LDA technique is used to obtain data on free hydraulic jumps, the low data acquisition rate problem discussed has to be resolved. Shooting the laser beams from the bottom of the bed is one choice, but a three color type LDA would have to be used otherwise the main shear stress can not be obtained by using two color type. Using stronger laser equipment is another choice. Certainly it is of considerable interest to obtain detailed measurements of free hydraulic jumps, especially for $F_1 > 6$.

**PART THREE - NUMERICAL STUDIES
USING K- ϵ TURBULENCE MODEL**

3.1 Introduction

The internal flow structure of submerged hydraulic jumps is very complicated in nature. Numerical simulation of all aspects of the flow is, therefore, difficult and challenging. The integral approaches, such as the methods of Narayanan (1975), McCorquodale and Khalifa (1983) and Madsen and Svendsen (1983), involved assumptions and restrictive mathematical derivation. The resulting first order partial differential equations through the integral approach are relatively easy to solve numerically, but this method can only predict the macroscopic features and certain aspects of the mean flow. The turbulence field is a part of the assumptions rather than a part of the predictions.

In order to test and provide a new prediction method for submerged hydraulic jump, a two equation K- ϵ model proposed by Launder and Spalding (1974) is applied and tested in this study. This approach eliminates the need for the macroscopic similarity assumption and is based on a more refined turbulence model. This model has been widely and successfully tested. It can predict not only the detailed structure of mean flow but also the major turbulent stresses.

Submerged hydraulic jumps are selected instead of free jumps as the problem to study for numerical simulation,

because it is believed that submerged jumps are somewhat easier to deal with both physically and numerically. Free jumps entrain tremendous amounts of air, an extra transport equation for the air-water mixture would be required and the mechanism of air entrainment would need to be modelled. Furthermore, free jumps have abrupt free surfaces, which imposes difficulty in generating a solution grid. Unless there is an economical way to deal with this problem, the numerical calculation will become very inefficient.

In the current numerical simulation a simple offset control volume method is developed to handle the free surface in submerged jumps. In addition, the hybrid numerical scheme by Spalding (1972) and the SIMPLE (Semi-Implicit Method for Pressure-Linked Equations) solution algorithm by Garreto et al (1972) are implemented in the present computing codes.

The numerical results are then compared with the experimental measurements so as to test and evaluate the performance of the method. Even though the experimental results reveal that the flow of submerged hydraulic jumps is three dimensional in nature due to actual aspect ratio influence, a two dimensional model is used for testing how well it will predict the flow and also for the sake of simplicity. Three experimental conditions with serial number S3, S5 and S8 as shown in Table 3 are selected as numerical test cases. S8 has the highest inlet Froude number ($F_1 = 8.19$) and smallest submergence ($S = 0.24$), whereas S3

has the smallest inlet Froude number ($F_1 = 3.19$) and deepest submergence ($S = 0.85$) and S5 has moderate inlet Froude number ($F_1 = 5.49$) and submergence ($S = 0.63$), among the ten experimental conditions.

3.2 Problem Formulation

The flow configuration and dimensions of the problem which is studied in this investigation are shown in Figure 2. The governing equations and boundary conditions of the problem are presented in the following sections.

3.2.1 Governing Equations

The equation of continuity, Reynolds' momentum equations and κ - ϵ modelling equations for two dimensional, steady, incompressible turbulent flow are given as follows (some of the equations have been presented in the early part of the thesis but listed here for convenience):

$$\frac{\partial u}{\partial x} + \frac{\partial v}{\partial y} = 0 \quad (3)$$

$$u \frac{\partial u}{\partial x} + v \frac{\partial u}{\partial y} = - \frac{1}{\rho} \frac{\partial p^*}{\partial x} + \frac{\partial (-\overline{u'^2})}{\partial x} + \frac{\partial (-\overline{u'v'})}{\partial y} \quad (4)$$

$$u \frac{\partial v}{\partial x} + v \frac{\partial v}{\partial y} = - \frac{1}{\rho} \frac{\partial p^*}{\partial y} + \frac{\partial (-\overline{u'v'})}{\partial x} + \frac{\partial (-\overline{v'^2})}{\partial y} \quad (5)$$

$$u \frac{\partial \kappa}{\partial x} + v \frac{\partial \kappa}{\partial y} = \frac{\partial}{\partial x} \left(\frac{v_t}{\sigma_\kappa} \frac{\partial \kappa}{\partial x} \right) + \frac{\partial}{\partial y} \left(\frac{v_t}{\sigma_\kappa} \frac{\partial \kappa}{\partial y} \right) + G - \epsilon \quad (37)$$

$$u \frac{\partial \epsilon}{\partial x} + v \frac{\partial \epsilon}{\partial y} = \frac{\partial}{\partial x} \left(\frac{v_t}{\sigma_\epsilon} \frac{\partial \epsilon}{\partial x} \right) + \frac{\partial}{\partial y} \left(\frac{v_t}{\sigma_\epsilon} \frac{\partial \epsilon}{\partial y} \right) + C_1 \frac{\epsilon}{\kappa} G - C_2 \frac{\epsilon^2}{\kappa} \quad (40)$$

$$p^* = p + \gamma y \quad (6)$$

$$\overline{u'^2} = \frac{2}{3} \kappa - 2v_t \frac{\partial u}{\partial x} \quad (78)$$

$$\overline{v'^2} = \frac{2}{3} \kappa - 2v_t \frac{\partial v}{\partial y} \quad (79)$$

$$\overline{u'v'} = -v_t \left(\frac{\partial u}{\partial y} + \frac{\partial v}{\partial x} \right) \quad (80)$$

$$v_t = C_\mu \frac{\kappa^2}{\epsilon} \quad (81)$$

$$G = v_t \left[\left(\frac{\partial u}{\partial y} + \frac{\partial v}{\partial x} \right)^2 + 2 \left(\frac{\partial u}{\partial x} \right)^2 + 2 \left(\frac{\partial v}{\partial y} \right)^2 \right] \quad (82)$$

Here u , v and p^* are the local Reynolds-averaged values of the velocity components in the longitudinal (x) and vertical (y) directions and the piezometric pressure respectively. p is the local Reynolds-averaged value of pressure and y is the vertical distance from the boundary (bed) referred to as the wall. κ and ϵ are the Reynolds-averaged values of turbulent kinetic energy and its dissipation rate respectively. v_t is turbulent eddy viscosity and G in κ - ϵ equations is the

turbulence production term. The constants used in the model are listed in Table 2.

3.2.2 Boundary Conditions

3.2.2.1 Inlet Condition

The inlet velocity and turbulence quantities are specified as the inlet condition and taken to be the same as those from the measurement. The longitudinal velocity u at the inlet is approximated by a straight line as

$$\frac{u}{U_1} = 0.99 + 0.02 \frac{y}{Y_1} \quad (62)$$

The maximum downward velocity v is 2 to 6% of U_1 depending on different conditions. Assuming that the turbulence is locally isotropic and in equilibrium at the inlet, from the experimental results the turbulence kinetic energy κ_1 and dissipation rate ϵ_1 are worked out to be $1.4 \times 10^{-3} U_1^2$ and $2.2 \times 10^{-5} U_1^3 / Y_1$ respectively.

3.2.2.2 Outlet Condition

The downstream depth Y_t is specified and hydrostatic pressure distribution is assumed. Other variables are assumed to be unchanging in the downstream direction and can be expressed as:

$$\frac{\partial u}{\partial x} = \frac{\partial v}{\partial x} = \frac{\partial \kappa}{\partial x} = \frac{\partial \epsilon}{\partial x} = 0 \quad (83)$$

3.2.2.3 Surface Condition

The surface pressure p is assumed to be zero. No mass or momentum fluxes are allowed across the free surface. It is further assumed that the first derivatives of u , κ and ϵ with respect to y are approximately zero. So the surface conditions are:

$$P = 0 \quad (84)$$

$$v_s = \frac{dH}{dx} u_s \quad (85)$$

$$\frac{\partial u}{\partial y} = \frac{\partial \kappa}{\partial y} = \frac{\partial \epsilon}{\partial y} = 0 \quad (86)$$

where u_s and v_s are the surface velocities in the longitudinal and vertical directions respectively.

3.2.2.4 Wall Condition

The wall function method proposed by Launder and Spalding (1974) are used in this investigation due to the following reasons:

- (1) The turbulence model need not be modified to account for the laminar effects near the wall;
- (2) It saves a considerable amount of computer time and storage, since the flow near walls is not solved for;
- (3) The surface roughness can be introduced through some model constants.

To a good approximation the velocity profile of turbulent boundary layer near a smooth wall is as follows:

$$u^* = y^* ; \text{ when } y^* \leq 11.6 \quad (87)$$

$$u^* = \frac{1}{k} \ln(Ey^*) ; \text{ when } y^* > 11.6 \quad (88)$$

where $u^* = u/u_*$ and $y^* = yu_*/\nu$, and u_* is the shear velocity defined as $u_* = \tau_w/\rho$. k and E are given the values of 0.4 and 9 respectively. Imposing local equilibrium conditions near the wall yields:

$$\kappa = \frac{u_*^2}{C_\mu^{1/2}} \quad (89)$$

$$\varepsilon = \frac{u_*^3}{ky} \quad (90)$$

The wall model iteration technique proposed by Benim and Zinser (1985) is employed. It is assumed that the first two grid points in the solution domain are away from the viscous layer, but within the logarithmic layer. At the beginning, u_* is assumed and u_{n1} , v_{n1} , κ_{n1} and ε_{n1} at node 1 can be determined. These will be used as wall conditions. After each iteration the information at node 2 is fed back to node 1 through the following relationship for the wall shear stress:

$$\tau_w = \frac{\rho k u_{n2} C_\mu^{1/4} K_{n1}^{1/2}}{\ln(E y_{n2} C_\mu^{1/4} K_{n1}^{1/2} / \nu)} \quad (91)$$

Therefore, the u_* can be corrected.

3.3 Offset Control Volume Method

Numerical calculation of free surface problems in hydraulics (and other fields) is difficult owing to non-rectangular and changing geometry. Even for steady state situations the free surface must be adjusted iteratively until the surface conditions are satisfied. Many methods for generating "body fitted" coordinates are available and have been used (e.g. in the review by Thompson et al (1982)). Disadvantages of this method include the necessity of transforming the governing equations (no mean task for the Reynolds' and $K-\epsilon$ equations) and the need to solve, in effect, a potential problem for nodal locations whenever the free surface changes. In addition, the transformed equations, due to their complexity, may lose their simple physical interpretations, in particular making it difficult to judge the relative importance of various terms.

Control volume formulations in general coordinate systems likewise become very complex. Unless the transformed coordinate system is orthogonal and the velocities are also appropriately transformed, a profusion of extra boundary flux terms arises. Significant coding effort (especially testing and debugging) is therefore required.

The approximate offset control volume method originally proposed and used in this thesis circumvents most of the above difficulties while capturing the essence of free surface, variable geometry hydraulics problems. It is, above all, a simple approach and is very easily included in existing software. The success of the method relies on assumptions that the water surface slope is relatively small (say $< 1:3$), the channel bed is flat, the flow is dominantly horizontal ($u \gg v$) and that steep velocity gradients are confined to a layer near the channel bed.

A typical discretization of offset control volumes is shown in Figure 105. Up to an elevation of Y_c the control volumes are normal rectangles. Above Y_c and up to H the control volumes are also rectangular but of a thickness Δy dependent on the local depth H , i.e.

$$\Delta y = \frac{H - Y_c}{N_0} \quad (92)$$

where N_0 is the number of offset control volumes. Note that since the control volumes are rectangular, some extra space above the water surface is included while other parts below the water surface are excluded. This will be accounted for with a form of kinematic surface boundary condition below.

Using a staggered grid approach (as in the SIMPLE procedure) a typical offset control volume for the conservation of mass is shown in Figure 106. Vertical

velocities are evaluated at points n and s and horizontal velocities at points w and e. While the calculation of vertical transport of mass (or any other quantity) is straightforward, the calculation of horizontal transports are subject to some approximation. A simple approach is to use the nodal velocities as representative of the velocity over the entire side of the control volume, so that the net horizontal inflow of mass into the control volume is approximated by

$$q_x = (U_p - U_e) \Delta y \quad (93)$$

Clearly, this approximation is of a lower order of accuracy compared to a centered approximation but may be expected to converge correctly as $\Delta y \rightarrow 0$. In practice, the requirement that the points w and e lie on the control volume boundary leads to a restriction on control volume aspect ratio. Strictly

$$\frac{\Delta y}{\Delta x} > |S_s| \quad (94)$$

where S_s is the water surface slope ($S_s = dH/dx$). Restricting the point to the middle third of the volume face, or selecting

$$\frac{\Delta y}{\Delta x} > 3 |S_s| \quad (95)$$

results in a much improved accuracy. This approach, while simple and easy to apply, is obviously not conservative, in particular when the value of u varies significantly in the vertical direction or in other words the velocity gradient is large.

For solution of the momentum and turbulence transport equations such a method may be adequate. The modelling relations are necessarily approximate to begin with and are usually subject to uneven order numerical treatment (e.g. upwinding). Under these circumstances there is little benefit to be gained by enforcing strict conservation of momentum compared to the effort that would be required to implement it. The exception, of course, is in the presence of steep velocity gradients. The remedy adopted herein is simply to use non-offset control volumes in the near-bed and shear layer regions where these large gradients are expected. Corrections similar to those outlined below for the mass conservation equation could also be used if desired, but would be somewhat cumbersome to incorporate.

Conservation of mass is easily restored by changing only the computation of mass imbalance in the SIMPLE procedure. The mass flow across the west face, for example, is calculated from (for $S_s > 0$)

$$q_{xw} = u_{wn} l_{nww} + u_{ws} l_{sww} \quad (96)$$

where l_{nw} and l_{sw} are the distances between points nw and w and between points w and sw respectively. u_{wn} , which is located midway between points nw and w, is linearly interpolated between u_n and u_p . In the same way u_{ws} , which is located midway between points w and sw, is linearly interpolated between u_p and u_s . Now on any vertical section between control volumes the total flow leaving the left control volumes is equal to the flow entering the right control volumes and the formulation is therefore conservative of mass.

At the water surface the situation is as shown in Figure 107. The condition for mass conservation here is

$$q_{x1} = q_{y1} \quad (\text{external flow does not enter}) \quad (97)$$

and

$$q_{x2} = q_{y2} \quad (\text{internal flow does not leave}) \quad (98)$$

or

$$q_{x1} + q_{x2} = q_{y1} + q_{y2} \quad (99)$$

Approximating the flows by representative velocities yields

$$v_s = \frac{U_1 l_1 + U_2 l_2}{\Delta x} \quad (100)$$

which is readily observed to be a form of the kinematic free surface condition, i.e. equation (85).

The offset control volume method thus offers a very simple handling of the variable geometry free surface. All that is required is an adjustment of nodal elevations according to equation (92) for which only a value of H at that vertical section is needed. Conservation of mass is retained by modification of the imbalance calculation and a careful statement of the free surface condition. Conservation of momentum is only approximately satisfied but it is expected that the resulting errors will be of the order of or smaller than the errors resulting from other approximations and uncertainties in these equations.

A complete conservation of mass and momentum can be achieved by a more complex formulation. A similar problem concerning the conservative scheme was encountered in the zonal handling of a complex solution domain and has been discussed by Rai (1984, 1986). Rai (1984) emphasized the importance of maintaining conservation at nodal boundaries and the necessity of exercising extreme care to treat grid points on the zonal boundaries. Rai (1986) also demonstrated that this goal could be achieved to first order and second order accuracy.

3.4 Hybrid Numerical Scheme

For convection dominated problems, such as submerged hydraulic jumps, careless numerical discretization of transport equations will result in serious numerical diffusion. The hybrid scheme of Spalding (1972) offers a simple and economical approach. Careful selection of mesh or grid spacings can help to avoid the serious numerical diffusion involved. Other discretization schemes, such as streamline upwind scheme by Hughes and Brooks (1979) and skew upwind scheme by Raithby (1976), relax the restriction imposed by hybrid scheme and limit the artificial diffusion to the flow direction only. The QUICK (Quadratic Upwind Interpolation for Convective Kinematics) scheme by Leonard (1979) uses a higher degree upwind weighted interpolation to achieve better accuracy and avoid artificial diffusion.

Due to the empirical nature of turbulence modelling, not much could be gained by using high order numerical schemes, so the hybrid scheme is applied in this study. Because the hybrid scheme was originally used to develop the $k-\epsilon$ turbulence model, there is an advantage to make full use of the experience related to the scheme. Grid spacings will be refined in the regions where serious numerical diffusion can be identified.

For different transport equations different control volumes have to be used. All variables, with the exception of velocities, are located at the grid nodes. The latter are

located midway between the pressures which drive them. Three different control volumes are demonstrated in Figure 108.

The hybrid scheme combines both upwind and central differences in approximating the transport terms considering both the accuracy and stability of the finite difference counterpart. What the hybrid scheme does is basically to shift from upwind to central differences or vice versa in evaluating the convection terms according to local Peclet Number. For example, the flux across BC is evaluated by

$$\left(U_E \frac{\phi_P + \phi_E}{2} - K_{BC} \frac{\phi_P - \phi_E}{\Delta x_{PE}} \right) l_{BC} ; \text{ when } | P_e | < 2 \quad (101)$$

$$U_E \phi_P l_{BC} ; \text{ when } | P_e | > 2 \quad (102)$$

$$U_E \phi_E l_{BC} ; \text{ when } | P_e | < -2 \quad (103)$$

where ϕ is the transporting quantity; K is diffusivity, which represents ν_t in the momentum equations, ν_t/σ_k in the k equation and ν_t/σ_ϵ in the ϵ equation; and P_e is the local Peclet number and it is defined as:

$$P_e = \frac{U_E \Delta x_{PE}}{K_{BC}} \quad (104)$$

The detailed derivaton of the finite difference counterparts of governing equations are attached in Appendix

A, where the formulation procedure recommended by Runchal (1972) was followed. The finite difference equations read

$$C_{uP}U_P = C_{uE}U_E + C_{uW}U_W + C_{uN}U_N + C_{uS}U_S + C_{u\phi} \quad (105)$$

$$C_{vP}V_P = C_{vE}V_E + C_{vW}V_W + C_{vN}V_N + C_{vS}V_S + C_{v\phi} \quad (106)$$

$$C_{kP}K_P = C_{kE}K_E + C_{kW}K_W + C_{kN}K_N + C_{kS}K_S + C_{k\phi} \quad (107)$$

$$C_{\epsilon P}\epsilon_P = C_{\epsilon E}\epsilon_E + C_{\epsilon W}\epsilon_W + C_{\epsilon N}\epsilon_N + C_{\epsilon S}\epsilon_S + C_{\epsilon\phi} \quad (108)$$

$$C_{pP}P'_P = C_{pE}P'_E + C_{pW}P'_W + C_{pN}P'_N + C_{pS}P'_S + C_{p\phi} \quad (109)$$

3.5 Solution Algorithm

To solve the resulting set of finite difference equations, the particular procedure or solution algorithm which is chosen is not very important, unless numerical efficiency is a great concern. Otherwise, any solution algorithm which has reasonable speed can be used to solve the problem. Because SIMPLE by Garetto et al (1972) was developed together with $k-\epsilon$ model, this procedure is applied in the present study.

The followings will outline the basic steps in SIMPLE and demonstrate how iteration is employed to achieve convergence.

Firstly a field of intermediate velocities u and v are obtained by solving the associated momentum equations using

the assumed pressure p , turbulence κ and ϵ fields. Then continuity is enforced by solving the equations for a pressure correction P' and therefore determining the required adjustments to the velocities and the pressures. The equations for the remaining variables κ and ϵ are then solved in turn, and the whole process is repeated until a satisfactory solution is obtained.

For the present calculation a line-iteration method has been employed, wherein the unknown variables along each grid line are calculated by application of the tridiagonal matrix algorithm, on the assumption that values on neighboring lines are known. This operation is performed in turn on the sets of lines lying in the x , y directions: it usually suffices to perform one such "double sweep" on the velocities (u and v) and turbulence quantities, and three sweeps on P' , per cycle of calculation. This method is substantially faster than point iteration. The above process is summarized in the calculation flow chart as shown in Figure 109.

The computer programs are attached in this thesis as Appendix B. Several important observations from numerical computation are summarized as follows:

- (1) Define a computational Reynolds' number as

$$R_{ec} = \frac{U_c L_c}{\nu_{tc}} \quad (110)$$

where U_c , L_c and v_{tc} are typical velocity and length scales of the flow field and eddy viscosity respectively. Small Re_c should be assumed at the start of the calculation. Otherwise, numerical instability is observed.

- (2) κ and ϵ are always positive scalars. Caution and prevention measures should be taken to avoid negative values occurring during actual computation.
- (3) The simultaneous and nonlinear character of the equations necessitates that special measures be employed to procure numerical stability. These include under-relaxation of the solution of the momentum and turbulence equations with factors typically in the range of 0.3 to 0.5 when the calculation starts and 0.1 to 0.3 when the iteration reaches the final stage and linearization of the nonlinear source/sink terms in the equations for κ and ϵ .
- (4) Numerical calculation indicates that the final results are not sensitive to the inlet κ and ϵ at all and so the inlet conditions for κ and ϵ should not be treated as critical values rather than a way to help to start the solution.

3.6 Results and Discussions

The numerical simulation was conducted on the Amdahl 5890 computer in the University of Alberta. Three different

calculation grid meshes were used for the three different conditions.

For illustration purposes, the actual grid mesh for calculation and the final velocity vector fields for three cases are plotted from Figure 110 to 115. Notice that the lower grid lines are parallel to the bed and the upper grid lines are slightly skewed and that the grid mesh is denser near the shear region and inlet in order to avoid serious numerical diffusion.

The prediction for water surface profiles, velocities u and v , turbulence quantities $\overline{u'^2}$, $\overline{v'^2}$ and $\overline{u'v'}$ are compared with the experimental measurements as shown from Figure 116 to 131. The pressure field predictions are also included from Figure 132 to 134.

Before the performance of the numerical prediction is evaluated, three basic sources of errors which might cause the discrepancies between the measurements and predictions are discussed as below:

- (1) Due to the aspect ratio influence in the actual experimental conditions, the roller of a submerged hydraulic jump is three dimensional in nature. This phenomenon is discussed in detail in the second part of the thesis, according to which there is a strong vortex-like motion near the gate on the water surface. The effect is narrowing the passing area for the reversing flow in the roller, so negative velocities in the center plane will increase. The influence of this

vortex motion is important to the mean flow especially for the reversing portion. However, it is less significant to the forward portion of the mean flow and the turbulent fields. To test how well a two dimensional model can predict the flow, the two dimensional numerical prediction is used to compare with the detailed measurement at a plane closer to the center line. The average longitudinal velocities at a y -constant plane and a few vertical profiles, which are available from the detailed spanwise measurement, are also used to compare with the two dimensional prediction.

- (2) Numerical errors could be introduced due to the use of offset control volumes in the region of reversing flow. As an example an error analysis has been done for the case of $F_1=3.19$ and $S=0.85$. The unit discharge predictions are in error by up to 2% and the unit momentum predictions are in error by up to 3% in this case. The error for unit discharge is believed due to incomplete convergence instead of the numerical method, and the error for unit momentum is due to both the discharge error and the numerical method itself. At the same time the hybrid numerical scheme used can cause numerical diffusion as well.
- (3) The k - ϵ turbulence model has its own limitations when it is applied to strong recirculating flows. As pointed out by McGuirk et al (1979), the eddy viscosity

hypothesis is inadequate in some parts of the flow: in the initial region of the shear layer the turbulence production far exceeds its dissipation; the strong streamline curvature limits the applicability of the hypothesis; the isotropic assumption does not represent the normal stresses properly; towards the end of the jump turbulence dissipation is much higher than its production so that C_μ is no longer a constant; finally the gradient diffusion assumption breaks down near the regions of maximum velocities, as found out for the wall jet by Tailland and Mathieu (1967).

Based on the above reasoning, the performance of the numerical prediction can be summarized as follows:

- (1) As shown in Figure 116 the water surface profiles are well predicted except for the central part of the jump. In the numerical calculation the conservation of the mass flux is imposed. Also the downstream depth is fixed as a boundary condition. As a result the predicted water surface is higher than the measured profile, wherever the influence of three dimensional characteristics of the flow is significant. This discrepancy will eventually change the predicted pressure field so that the velocity predictions are influenced by this factor as well. It seems that the predicted surface profile is in better agreement with the measurement for higher submergence and lower inlet Froude number. For example, for $F_1=8.19$ and $S=0.24$, the

surface profile is over predicted by up to 6% while only up to 2% error is encountered for $F_1=3.09$ and $S=0.85$.

- (2) The prediction of the mean velocity component u for the three tested cases are generally in good agreement with the measurement as shown in Figure 117 to 119. However, a few discrepancies are observed when the predicted u is compared with the measurement at a plane of $z/W=0.36$. For the reversing portion of the flow near inlet, the velocity u is over predicted by up to $0.1U_1$. This is due to the three dimensional effect causing stronger negative flow near the center plane. The comparison of predicted u with the average u of spanwise measurement indicates a much better agreement. For example, for $F_1=5.49$ and $S=0.63$ as shown in Figure 118, where detailed spanwise measurement is available at $x/Y_1=4$, the predicted u in reversing part of the flow is only in error by up to $0.02U_1$ when compared with the average value. For the three tested cases, the predicted u is generally in better agreement with the average value than that at the $z/W=0.36$ plane, especially for the reversing portion of the mean flow where the effect of three dimensionality is more important. In the forward portion of the mean flow, where the three dimensional effect is less significant, the predicted u is in good agreement with both the value at the plane $z/W=0.36$ and the average u . For the

same example at $x/Y_1=4$ under $F_1=5.49$ and $S=0.63$ as shown in Figure 116, the predicted u_m is almost the same as both the u_m at the plane $z/W=0.36$ and the average u_m . As shown in Figure 135 to 137, however, the predicted u_m further downstream is higher than the measurement at $z/W=0.36$ plane. This can be explained by the fact that u_m at the center plane is smaller than that near the side walls as previously discussed. Again, the comparison of the predicted u_m with the average value for these regions indicates a better agreement. For example, at $x/Y_1=64$ under $F_1=5.49$ and $S=0.63$ as shown in Figure 118, where the detailed spanwise measurement is available, the predicted u_m agrees with the average u_m while it over predicts the u_m at $z/W=0.36$ plane by $0.09U_1$.

- (3) Since the measurement for the velocity component v is not accurate as previously discussed, the comparison of v between the prediction and measurement only has a qualitative merit. As shown from Figure 120 to 122, the trend of v distribution is in agreement between the experimental data and prediction while the prediction gives a better indication of v near the bed than the measurement. For the three tested cases, the predicted v can be in error by up to $0.04U_1$ to the experimental data, which give the maximum v of $0.06U_1$ for all the tested submerged jumps.

(4) Turbulence quantities $\sqrt{u'^2}$, $\sqrt{v'^2}$ and $\overline{u'v'}$ are reasonably well predicted for three cases. The gradient diffusion assumption breaks down near the maximum velocity region, but the negative turbulence production region is so small in comparison with the whole flow depth that the κ - ϵ model still works very well in this particular application. The effect due to imposing gradient diffusion assumption in this region is to shift the u_m closer to the bed, which will eventually influence the shear stress prediction along the bed to some extent. As shown in Figure 136, where bed shear stress coefficient C_f is defined as $C_f = 2\tau_w / \rho U_1^2$, bed shear stress is in error of up to 100%. As well known for hydraulic jumps the bed shear stress, which can be neglected in traditional analysis, is trivial in the conservation of momentum. So this discrepancy does not bear any practical significance. As shown from Figure 135 to 137, the maximum $\overline{u'v'}_m$ and $(\sqrt{u'^2})_m$ and $(\sqrt{v'^2})_m$ are under predicted up to 50% for the initial part of the shear layer, but are well predicted further downstream. Also some fluctuating behaviors of $\overline{u'v'}_m$ and $(\sqrt{u'^2})_m$ and $(\sqrt{v'^2})_m$ in the initial part of the solution domain are also observed. This is believed to be caused by the unrealistic turbulence production for the initial part of the shear layer resulting from the numerical calculation. The dominant term in calculating the

turbulent production from equation (82) for the initial shear layer is given by $\nu_t (\partial u / \partial y)^2$. Depending on how refined the Δy is near the shear layer, this production term would result in a large value. Figure 80 shows that the maximum turbulent shear stresses develop from zero at the inlet to a maximum at $5 < x/Y_1 < 10$. The large and unrealistic turbulent production would, therefore, cause large turbulent stresses and lead to undulated shape of $\overline{(u'v')}_{\text{m}}$ distribution with regular Δx . There are two ways to correct this error. One is to modify the turbulent production term calculation for the initial part of the shear layer, but this would lead to modifying the standard κ - ϵ model, which is beyond the scope of this thesis. Another way is to use a much smaller Δx for the initial part of the shear layer. This remedy would smooth the transition from a large shear stress to a more realistic one further downstream so as to smear out the undulated shape. However, this approach would introduce a large number of grid lines near the inlet causing much longer computation times. This correction method would have generated smoother curves, but it would still cause unrealistic turbulent stresses near the inlet. In light of these facts, the standard κ - ϵ modelling relationships were used and no correction was made in smoothing the undular shapes of maximum turbulent stresses.

- (5) Because the pressure fields have not been measured, no comparisons have been made for the pressure fields. Instead, only the pressure fields from the prediction are discussed below. A non-dimensional pressure departure from hydrostatic can be defined by the following,

$$P_d = \frac{\gamma(H-y) - P}{\rho U_1^2 / 2} \quad (111)$$

where the depth of flow is denoted by H ; the vertical distance from the bed is expressed by y ; P is the pressure; U_1 is the inlet velocity; and P_d denotes the non-dimensional pressure departure from hydrostatic. The distribution of P_d for the three runs are presented from Figure 132 to 134. It appears that the pressure distributions are quite hydrostatic for $x/Y_1 \geq 50$. Near the inlet, the pressure can deviate from hydrostatic distribution by up to 10% of $\rho U_1^2 / 2$. At about $x/Y_1 = 25$, the maximum P_d is about 5%. This departure from hydrostatic distribution is believed to be caused by flow curvature, which induces centrifugal forces in the recirculating region. It is also in accordance with what was reported by Rajaratnam (1967) for free hydraulic jumps.

3.7 Comparison of k-ε Model and SIM

In order to demonstrate the advantages and disadvantages of the differential and integral approaches in predicting submerged hydraulic jumps, the results from the k-ε model prediction will be compared with those from one of the integral methods as discussed in the Literature Review in the first part of this thesis. As previously discussed, the integral method of McCorquodale and Khalifa (1983) refined the SIM (Strip Integral Method) of Narayanan (1975), so the SIM by McCorquodale and Khalifa (1983) is chosen for comparison. Because the integral method by Madsen and Svendsen (1983) was based on the k-ε model, the results from this method are expected to be similar to this study. Therefore, only the integral method by McCorquodale and Khalifa (1983) is considered in this comparison.

The SIM of McCorquodale and Khalifa (1983) was applied to predict submerged radial hydraulic jumps by Abdel-Gawad and McCorquodale in 1984. The methodology described by Abdel-Gawad and McCorquodale (1984) was adopted in this study to predict submerged hydraulic jumps in rectangular channels. The governing equations, basic assumptions and numerical methods of SIM applied to submerged hydraulic jumps were summarized in the following.

(1) The governing equations read

$$\frac{\partial u}{\partial x} + \frac{\partial v}{\partial y} = 0 \quad (3)$$

$$u \frac{\partial u}{\partial x} + v \frac{\partial u}{\partial y} = -\frac{1}{g} \frac{dH}{dx} + \frac{1}{\rho} \frac{\partial \tau_t}{\partial y} \quad (112)$$

where hydrostatic pressure distribution is assumed. In equation (112) τ_t denotes the turbulent shear stress and it is given by

$$\tau_t = -\rho \overline{u'v'} \quad (113)$$

(2) As defined in Figure 11, the following velocity profiles are assumed for submerged hydraulic jumps,

$$u = u_m \left(\frac{y}{\delta}\right)^{1/7} \quad (0 \leq y \leq \delta) \quad (22)$$

$$u = -u_s + (u_m + u_s) \exp\left[-c \left(\frac{y-\delta}{H-\delta}\right)^2\right] \quad (\delta \leq y \leq H) \quad (23)$$

where the coefficient c was optimized by Abdel-Adwad and McCorquodale (1984) for submerged hydraulic jumps and determined to be $c=1.38*Y_s/Y_1$.

(3) Integration is performed for the following equations between different limits as given below,

$$\int_0^H u \frac{\partial u}{\partial x} dy = - \int_0^H v \frac{\partial v}{\partial x} dy = -u_s \frac{dH}{dx} \quad (114)$$

$$\int_0^\delta u \frac{\partial u}{\partial x} dy + \int_0^\delta v \frac{\partial u}{\partial y} dy = -g \int_0^\delta \frac{dH}{dx} dy + \frac{1}{\rho} \int_0^\delta \frac{\partial \tau_t}{\partial y} dy \quad (115)$$

$$\int_{\delta}^{y^*} u \frac{\partial u}{\partial x} dy + \int_{\delta}^{y^*} v \frac{\partial u}{\partial y} dy = -g \int_{\delta}^{y^*} \frac{dH}{dx} dy + \frac{1}{\rho} \int_{\delta}^{y^*} \frac{\partial \tau_t}{\partial y} dy \quad (116)$$

$$\int_{\delta}^H u \frac{\partial u}{\partial x} dy + \int_{\delta}^H v \frac{\partial u}{\partial y} dy = -g \int_{\delta}^H \frac{dH}{dx} dy + \frac{1}{\rho} \int_{\delta}^H \frac{\partial \tau_t}{\partial y} dy \quad (117)$$

in which y^* is the ordinate of the maximum turbulent shear and it is defined by

$$y^* = \frac{H-\delta}{\sqrt{8c}} + \delta \quad (118)$$

Equations (114) to (117) contain four unknown parameters u_m , u_∞ , δ and H , which are the variables to be predicted.

- (4) Equations (114) to (117) introduce the shear stresses at $y=0$, δ , y^* and H , which are assumed to be given by the following,

$$\tau_t (y=0) = \frac{0.0424}{\left(\frac{u_m \delta}{v}\right)^{0.25}} \rho \frac{u_m^2}{2} \quad (119)$$

$$\tau_t (y=\delta) = 0 \quad (120)$$

$$\tau_t (y=y^*) = -\rho (0.019x)^2 \left\{ \frac{2c(u_s+u_m)}{(H-d)^2} \exp\left[-c\left(\frac{y-\delta}{H-\delta}\right)^2\right] \right\}^2 \quad (121)$$

$$\tau_t (y=H) = 0 \quad (122)$$

- (5) A set of four ordinary differential equations are obtained by substituting the velocities from equations (22) to (23) and the shear functions from equation (119) to (122) into the integral equations (114) to (118). These equations are expressed in the form of

$$A_i \frac{dH}{dx} + B_i \frac{d\delta}{dx} + C_i \frac{du_\infty}{dx} + D_i \frac{du_m}{dx} = E_i \quad (i=1,2,3,4) \quad (123)$$

The coefficients A_i , B_i , C_i , D_i and E_i are functions of the unknowns H , δ , u_∞ and u_m . These functions are given in Appendix C.

- (6) In order to start the computation, the initial condition at the end of the potential core has to be determined. The method used herein is to assume a uniform velocity distribution at the inlet and length of the potential core about $6Y_1$. The continuity and momentum equations are applied to the inlet section and the end of potential core as below,

$$U_1 Y_1 = \int_0^H u \, dy \quad (124)$$

$$\frac{1}{2} \gamma (Y_s^2 - H^2) - 6Y_1 \tau_0 = \rho \left(\int_0^H u^2 \, dy - \int_0^{Y_1} U_1^2 \, dy \right) \quad (125)$$

Equations (124) and (125) can be solved for u_∞ and H by assuming δ and u_m at the end of the potential core as the following,

$$u_m = U_1 \quad (126)$$

$$\delta = 5 \sqrt{\frac{6Y_1V}{U_1}} \quad (127)$$

The resulting sets of equations to be solved are listed in Appendix C.

- (7) A program was written to solve the set of ordinary differential equations. The source code is attached in Appendix D. The solution procedure is explained as the following: the submerged depth Y_s is initially estimated; this value is then used and calculation proceeds downstream; at the end of the jump the predicted depth is compared with Y_t and the necessary correction is made for the new starting value of Y_s ; and the routine is repeated several times until the predicted Y_t falls within a specified tolerance (1 mm in this study).

The two important parameters H and u_m predicted for the conditions of serial S3, S6 and S8 are compared with the data from the experiment and the prediction from K- ϵ model. As shown in Figure 116 the predictions of surface profiles from both methods are fairly good for low inlet Froude number and

high submergence but not as good for high inlet Froude number and low submergence. However, the differential approach generally gives better prediction. For example, for the condition of $F_1=8.19$ and $S=0.24$ the prediction from $k-\epsilon$ model is in error up to 6% but the prediction from SIM method is in error up to 20%. The comparison of u_m from Figure 135(a) to 137(a) indicates that the differential method generally gives better prediction than the integral approach. For example, as shown in Figure 135(a) for the condition of $F_1=3.19$ and $S=0.85$, the SIM method can not predict the accelerated trend of u_m near the inlet. Near the end of the jump, the prediction of u_m from $k-\epsilon$ model is in error up to 10% while the prediction from SIM method is in error up to 20%.

Even though this study indicates a slightly better performance by $k-\epsilon$ model than SIM method, both methods are believed to be in about same degree of success in predicting the major flow parameters of submerged hydraulic jumps, such as H and u_m . The integral method is usually easy to apply and it requires less computation efforts than the differential approach. However, as pointed out in the Literature Review, the assumptions for the integral method are problem specific and less universal than $k-\epsilon$ model. Further, for the integral method the turbulent stresses and velocity profiles are parts of the assumptions rather than the solution. Finally, the differential approach is capable of dealing with different boundary and inlet conditions while the integral method is less capable or even impossible.

3.8 Conclusions

The two dimensional standard $k-\epsilon$ turbulence model has been applied to predict the characteristics of submerged hydraulic jumps. The predicted surface profiles, mean velocities and the turbulence stresses for the three tested runs have been compared with those from the measurement. The selected integral method SIM of McCorquodale and Khalifa (1983) has also been applied for the three test cases to predict the main flow parameters, in which the two important variables H and u_m have been compared with both the measurement and the prediction from $k-\epsilon$ model. Based on this numerical study, the following conclusions can be drawn.

- (1) The offset control volume method was originally developed in this study, and it has been successfully applied in the numerical prediction of submerged hydraulic jumps. The proper use of offset control volumes, coupled with hybrid numerical scheme and SIMPLE solution algorithm, can offer an economical solution which is reasonably accurate. The errors introduced in calculating the unit momentum using this method are up to about 3% for the tested runs. Above all, this method is simple and straightforward. Its application may be a useful alternative in the solution of other similar free surface problems in hydraulics.
- (2) It appears that the $k-\epsilon$ model has a slightly better performance than SIM method in predicting the surface profiles. For both methods, the predicted surface

profile is in better agreement with the measurement for high submergence and low inlet Froude number than for low submergence and high inlet Froude number. In the run of $F_1=8.19$ and $S=0.24$, which has the highest inlet Froude number and lowest submergence, the surface profile is over predicted by up to 6% using $K-\epsilon$ model and under predicted by up to 20% using SIM method.

- (3) The prediction of u velocity distributions using $K-\epsilon$ model is generally in fair agreement with the measurement. Comparison of u profiles at $z/W=0.36$ from the experiment with those from $K-\epsilon$ model indicates a good agreement for the forward portion of the flow near inlet but bad agreement with the reversing portion of the flow and flow near the end of the jumps. However, the predicted u is in good agreement with the average value for both the reversing flow and the flow near the end of jumps, since the average u smears out the three dimensional effects. In the run of $F_1=5.49$ and $S=0.63$, the predicted u can be in error up to $10\%U_1$ when compared with the reversing portion of the flow near inlet at $z/W=0.36$ plane, but only up to $2\%U_1$ discrepancy is observed when it is compared with the average velocity. Near the end of the jump, u_m is over predicted by up to $9\%U_1$ when compared with that at $z/W=0.36$ plane, but it agrees well with the average u_m .
- (4) The predictions of u_m along the jumps by both methods are good, even though the differential approach gives

better prediction. The accelerated trend of u_m near inlet can not be predicted by SIM method. Near the end of the jump, the prediction of u_m from κ - ϵ model is in error up to 10% while the prediction from SIM method is in error up to 20%.

- (5) The comparison of v profiles between the prediction and the measurement has only a qualitative merit. The difference of v between the experimental data and the numerical results can be in error up to $4\%U_1$ or about 70% of maximum measured velocity v .
- (6) Turbulent quantities are reasonably predicted. The maximum $\overline{(u'v')}$, $(\sqrt{u'^2})_m$ and $(\sqrt{v'^2})_m$ are under predicted by κ - ϵ model by up to 50% for the initial part of the shear layer, but are well predicted further downstream. The standard κ - ϵ model has several major shortcomings when applied to the submerged hydraulic jump. These include overpredicted turbulence production for the initial part of shear layer, no curvature effects on turbulence, inadequacy of the gradient diffusion assumption near the maximum velocity region and the isotropic assumption not representing the normal stresses properly.
- (7) The pressure departure from hydrostatic distribution P_d predicted by κ - ϵ model shows about 5% near inlet. The predicted pressure distributions are very close to hydrostatic for $x/Y_1 \geq 50$ in the three tested runs.

The major processes of turbulence production and diffusion in submerged hydraulic jumps are successfully captured by the κ - ϵ turbulence model, so the present prediction is quite promising in spite of the fact that the model has a few shortcomings in strong recirculating flows. The two dimensional numerical prediction for the mean velocity fields compare fairly well with the average flows of submerged hydraulic jumps.

It will be a challenging task to apply κ - ϵ turbulence model to free hydraulic jumps. More modelling relationships have to be introduced to describe the transport of air-water mixture and the mechanism of air entrainment. Numerically, difficulties have to be overcome to create a solution mesh in an easy way. Regarding the numerical schemes, better discretization procedure such as QUICK can be implemented to avoid the numerical or artificial diffusion. Regarding the solution algorithm, a fully implicit method can be applied to improve the overall numerical efficiency to reach a converged solution. Nevertheless, more research has to be done to resolve all these questions so as to apply κ - ϵ model to free jumps successfully.

CONCLUSION

Major contributions towards our understanding of hydraulic jumps have been reviewed. Among all the experimental studies conducted so far, most of them concerned with the macroscopic features of hydraulic jumps. Many empirical relationships have been developed for practical purposes. On the other hand, the internal flow characteristics of hydraulic jumps have received much less attention. The air model study of Rouse et al (1958) and water model study of Resch and Leutheusser (1972) were the only turbulence measurements available for free hydraulic jumps. To my knowledge, there are no detailed turbulence measurements on submerged hydraulic jumps in the literature.

The theoretical framework on hydraulic jumps has been well established. The existing prediction methods are of the integral type. The main length characteristics and some aspects of mean velocity can be predicted by these methods. However, all these methods rely too heavily on the experimental data specifically related to hydraulic jumps. The turbulence field in hydraulic jumps is a part of the assumptions rather than being a part of predictions.

In the experimental part of this study, detailed and accurate measurements have been made on submerged hydraulic jumps. The data were collected by the LDA system available at T. Blench Hydraulics Laboratory at the University of Alberta. The experiments covered ten conditions with the

submergence factor S varying from about 0.2 to about 1.7 and inlet Froude number F_1 approximately equal to 3.0, 5.5 and 8.0. From the analysis of the experimental data, the following conclusions have been drawn.

- (1) If a length scale L is defined so that $u_m/U_1=0.5$ when $x=L$, this length scale L is capable of grouping all major flow characteristics u_m/U_1 , $\overline{(u'v')}_{m}/\overline{(u'v')}_{mm}$, $(\sqrt{u'^2})_m/(\sqrt{u'^2})_{mm}$ and $(\sqrt{v'^2})_m/(\sqrt{v'^2})_{mm}$ together for different submerged jumps. The correlation is good for x/L up to about 1.5. An empirical equation for L was proposed and it can be used to roughly estimate L , but the equation can be in error up to about 45%. The maximum turbulence quantities can also be estimated from F_1 and S . Therefore, the major flow characteristics can be approximately determined for submerged jumps under different conditions.
- (2) It appears that there is a noticeable trend of decrease in maximum turbulent stress and intensities with increasing inlet Froude number. For the same submergence factor the maximum turbulent shear stresses can be different by 90% from $F_1=3$ to 8. The maximum turbulent stress decreases with increase of submergence.
- (3) In the fully developed region of a submerged jump, which occupies about 85% of roller length L_{rsj} , the flow demonstrates some degree of similarity. The

distribution of u/u_m against y/b is similar to that of a wall jet for y/b up to about 1.5. The shape of $\overline{u'v'}/(\overline{u'v'})_m$ against $(y-\bar{\delta})/(d-\bar{\delta})$ is almost identical to that of a wall jet. The shapes $\sqrt{\overline{u'^2}}/(\sqrt{\overline{u'^2}})_m$ and $\sqrt{\overline{v'^2}}/(\sqrt{\overline{u'^2}})_m$ against y/d are self-similar among different submerged jumps.

(3) Submerged hydraulic jumps are three dimensional in nature. The climbing effect of mean velocity component u near side walls is due to the vortex motion near the gate. The losses of unit discharge q and unit kinematic pressure plus momentum flux M at the center plane occur along with their gains near the side walls. After the jump the flow will recover into a two dimensional flow. The influence of this vortex motion has stronger effect to the reversing portion of the flow than that of the forward portion. Its influence to the turbulent field is less significant.

(4) The lengths of the roller from this experiment have been compared with those predicted by Stepanov's equation. It is found that the equation can be in error by 190%.

In the numerical part of this study, a widely tested two dimensional $k-\epsilon$ turbulence model is applied to simulate submerged hydraulic jumps. An offset control volume method is originally proposed and applied in this study. Further, the results predicted from $k-\epsilon$ model have been compared with the measurements and those predicted from SIM method. Based

on this numerical study, the following conclusions have been drawn.

- (1) The offset control volume method was originally developed in this study, and it has been successfully applied in the numerical prediction of submerged hydraulic jumps. The proper use of offset control volumes, coupled with hybrid numerical scheme and SIMPLE solution algorithm, can offer an economical solution which is reasonably accurate. The errors introduced in calculating the unit momentum using this method are up to about 3% for the tested runs. Above all, this method is simple and straightforward. Its application may be a useful alternative in the solution of other similar free surface problems in hydraulics.
- (2) It appears that the $k-\epsilon$ model has a slightly better performance than SIM method in predicting the surface profiles. For both methods, the predicted surface profile is in better agreement with the measurement for high submergence and low inlet Froude number than for low submergence and high inlet Froude number. In the run of $F_1=8.19$ and $S=0.24$, which has the highest inlet Froude number and lowest submergence, the surface profile is over predicted by up to 6% using $k-\epsilon$ model and under predicted by up to 20% using SIM method.
- (3) The prediction of velocity u distributions using $k-\epsilon$ model is generally in fair agreement with the measurement. Comparison of u profiles at $z/W=0.36$ from

the experiment with those from $k-\epsilon$ model indicates a good agreement for the forward portion of the flow near inlet but bad agreement with the reversing portion of the flow and flow near the end of the jumps. However, the predicted u is in good agreement with the average value for both the reversing flow and the flow near the end of jumps, since the average u smears out the three dimensional effects. In the run of $F_1=5.49$ and $S=0.63$, the predicted u can be in error up to $10\%U_1$ when compared with the reversing portion of the flow near inlet at $z/W=0.36$ plane, but only up to $2\%U_1$ discrepancy is observed when it is compared with the average velocity. Near the end of the jump, u_m is over predicted by up to 9% of U_1 when compared with that at $z/W=0.36$ plane, but it agrees well with the average u_m .

- (4) The predictions of u_m along the jumps by both methods are good, even though the differential approach gives better prediction. The accelerated trend of u_m near inlet can not be predicted by SIM method. Near the end of the jump, the prediction of u_m from $k-\epsilon$ model is in error up to 10% while the prediction from SIM method is in error up to 20% .
- (5) The comparison of v profiles between the prediction and the measurement only has a qualitative merit. The difference of v between the experimental data and the numerical results can be in error up to $4\%U_1$ or about 70% of maximum measured velocity v .

- (6) Turbulent quantities are predicted reasonably well. The maximum $\overline{(u'v')}$, $(\sqrt{u'^2})_m$ and $(\sqrt{v'^2})_m$ are under predicted by κ - ϵ model by up to 50% for the initial part of the shear layer, but are well predicted further downstream. The standard κ - ϵ model has several major shortcomings when applied to submerged hydraulic jump. These include overpredicted turbulence production for the initial part of shear layer, no curvature effects on turbulence, inadequacy of gradient diffusion assumption near maximum velocity region and isotropic assumption not representing the normal stresses properly.
- (7) The pressure departure from hydrostatic distribution P_d predicted by κ - ϵ model shows about 5% near inlet. The predicted pressure distributions are quite hydrostatic for $x/Y_1 \geq 50$ in the three tested runs.
- (8) The major process of turbulence production and diffusion in submerged hydraulic jumps is successfully captured by the κ - ϵ turbulence model, so present prediction is quite promising in spite of the fact that the model has a few shortcomings in strong recirculating flows. The two dimensional numerical prediction for the mean velocity fields compare fairly well with the average flows of submerged hydraulic jumps.

Table 1. Maximum turbulence quantities of free hydraulic jumps from Resch and Leutheusser

Condition	F_1	$\frac{(\sqrt{u'^2})_{\max}}{U_1}$	$\frac{(\overline{u'v'})_{\max}}{U_1^2}$
Undeveloped inflow	2.85	0.23	0.016
	6	0.32	0.026
Developed inflow	2.85	0.38	0.1
	6	0.29	0.035

Table 2. Constants in κ - ϵ turbulence model

C_μ	C_1	C_2	σ_κ	σ_ϵ
0.09	1.43	1.92	1.0	1.3

Table 3. Experimental conditions

Series	Y_1 (mm)	U_1 (m/s)	Y_t (mm)	F_1	S	$Re_1 (x10^{-3})$
S1	25	1.54	124	3.11	0.26	3.85
S2	25	1.59	156	3.20	0.53	3.98
S3	25	1.58	187	3.19	0.85	3.95
S4	25	1.49	255	3.01	1.69	3.73
S5	25	2.78	227	5.61	0.22	6.95
S6	25	2.72	299	5.49	0.63	6.80
S7	25	2.69	361	5.43	1.01	6.73
S8	15	3.14	206	8.19	0.24	4.71
S9	15	3.07	263	8.00	0.62	4.61
S10	15	3.11	329	8.11	1.00	4.67

Table 4. Surface profile measurements.

S1	S2	S3	S4	S5	S6	S7	S8	S9	S10
x (mm)	H (mm)	x (mm)	H (mm)	x (mm)	H (mm)	x (mm)	H (mm)	x (mm)	H (mm)
10	78	10	162	10	132	12	318	20	222
50	76	50	161	50	126	100	309	100	214
100	72	100	156	100	122	200	304	200	205
150	74	150	157	200	112	300	303	300	203
200	82	200	156	300	121	400	306	400	200
250	90	250	155	400	141	500	303	500	196
300	95	300	154	500	153	600	300	600	201
350	101	350	154	600	167	700	300	700	212
400	108	400	155	700	183	800	298	800	219
450	112	450	153	800	190	900	305	900	228
500	114	500	159	900	201	1000	306	1000	239
550	117	550	161	1000	209	1100	312	1100	251
600	119	600	167	1100	218	1200	317	1200	256
650	122	650	170	1200	220	1300	327	1300	260
700	122	700	173	1300	223	1400	337	1400	261
750	124	750	177	1400	225	1500	341	1500	263
800	123	800	180	1500	225	1600	346	1600	262
900	124	900	185	1600	225	1700	355	1700	262
1000	125	1000	186	1700	225	1800	355	1800	262
1100	125	1100	188	1800	224	1900	357	1900	263
1200	125	1200	188	1900	225	2000	358	2000	263
1300	125	1300	188	2000	225	2100	360	2100	263
1400	125	1400	188	2100	225	2200	360	2200	263
1500	124	1500	187	2200	226	2300	360	2300	263
1600	124	1600	187	2300	226	2400	360	2400	263
1700	124	1700	186	2400	227	2500	361	2500	263
1800	124	1800	187	2500	227	2600	362	2600	263
1900	124	1900	187	2600	227				
2000	124	2000	188						

Table 5. Lengths of the rollers

S	F ₁	L _{rsj} (measured)	L _{rsj} (predicted)	R
0.26	3.11	0.60	0.39	0.65
0.53	3.20	0.90	0.87	0.97
0.85	3.19	0.95	1.39	1.46
1.69	3.01	1.32	2.65	2.01
0.22	5.61	1.20	0.97	0.66
0.63	5.49	1.60	1.85	1.16
1.01	5.43	1.95	3.21	1.65
0.24	8.19	1.11	1.16	1.05
0.62	8.00	1.25	2.82	2.26
1.00	8.11	1.50	4.29	2.86

Note: $R = \frac{L_{rsj} \text{ (predicted)}}{L_{rsj} \text{ (measured)}}$

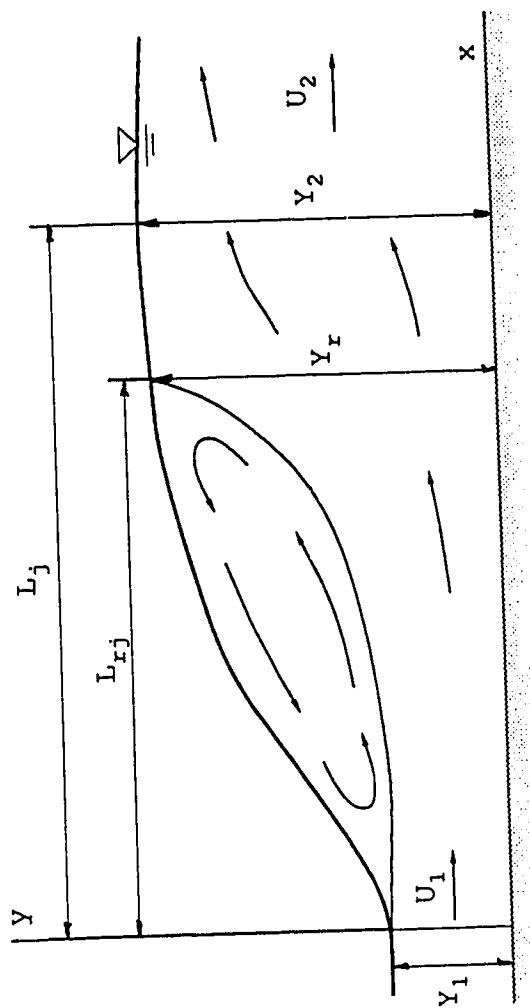


Figure 1. Schematic diagram of a classical free hydraulic jump

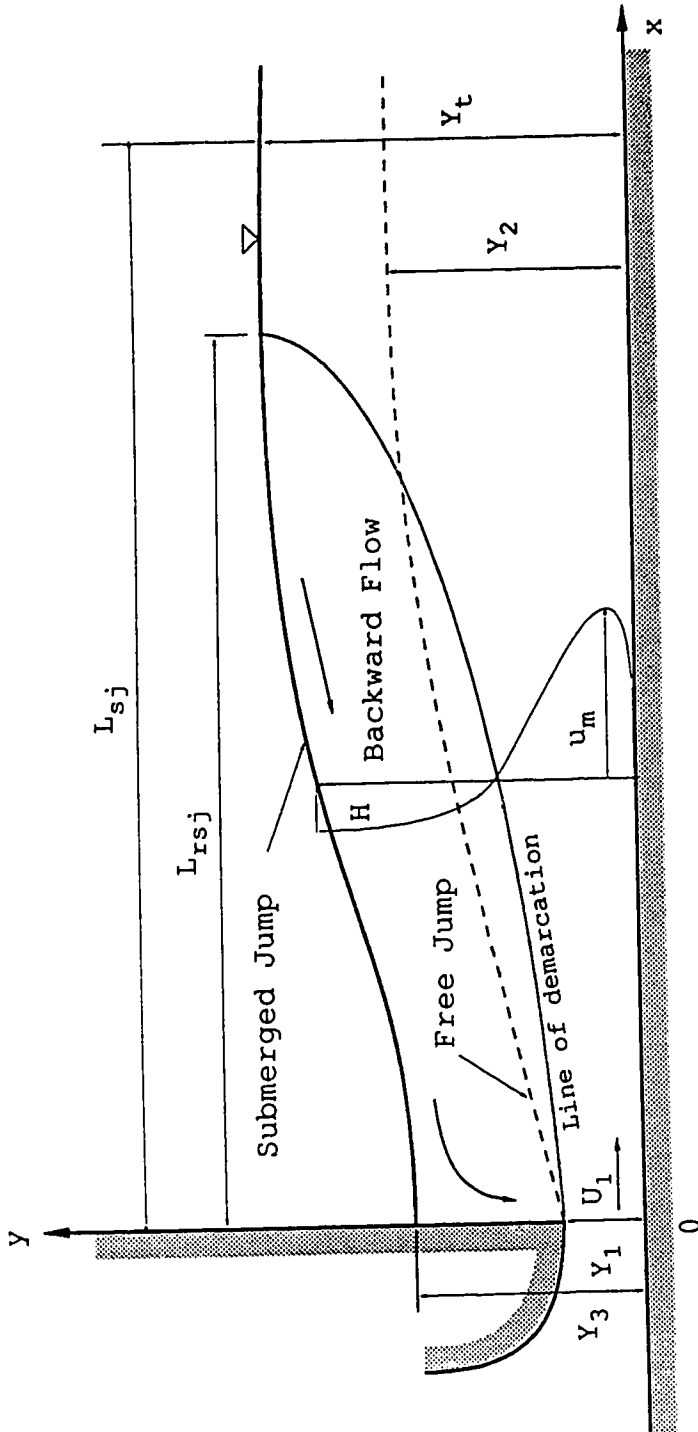


Figure 2. Schematic diagram of a classical submerged hydraulic jump

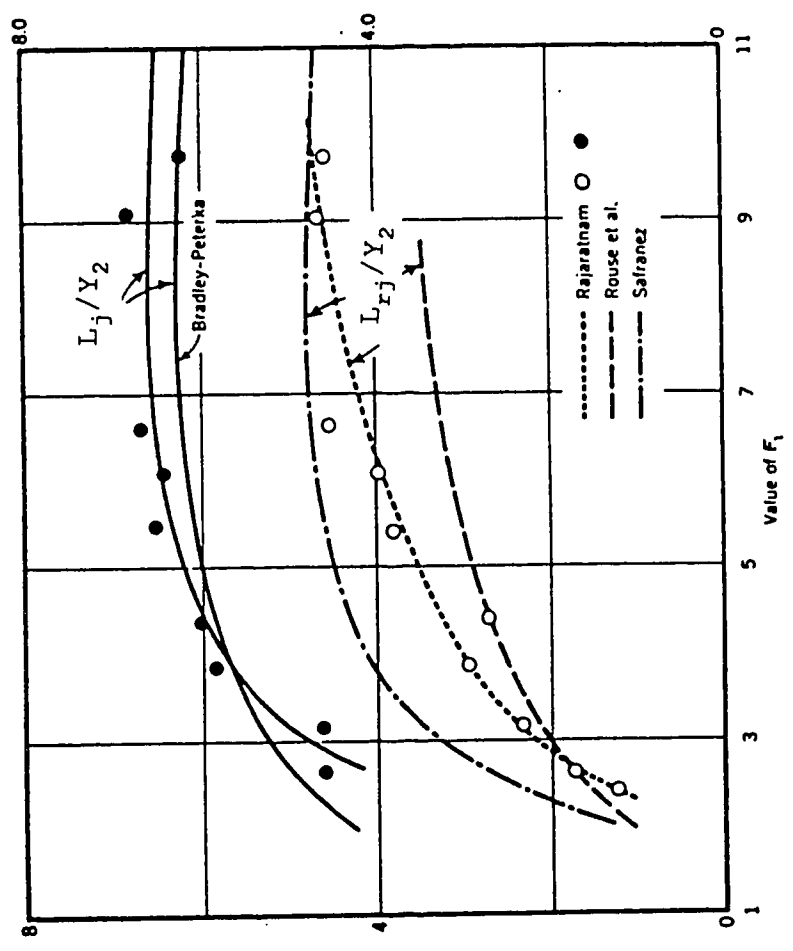


Figure 3. Main length characteristics (Courtesy of N. Rajaratnam)

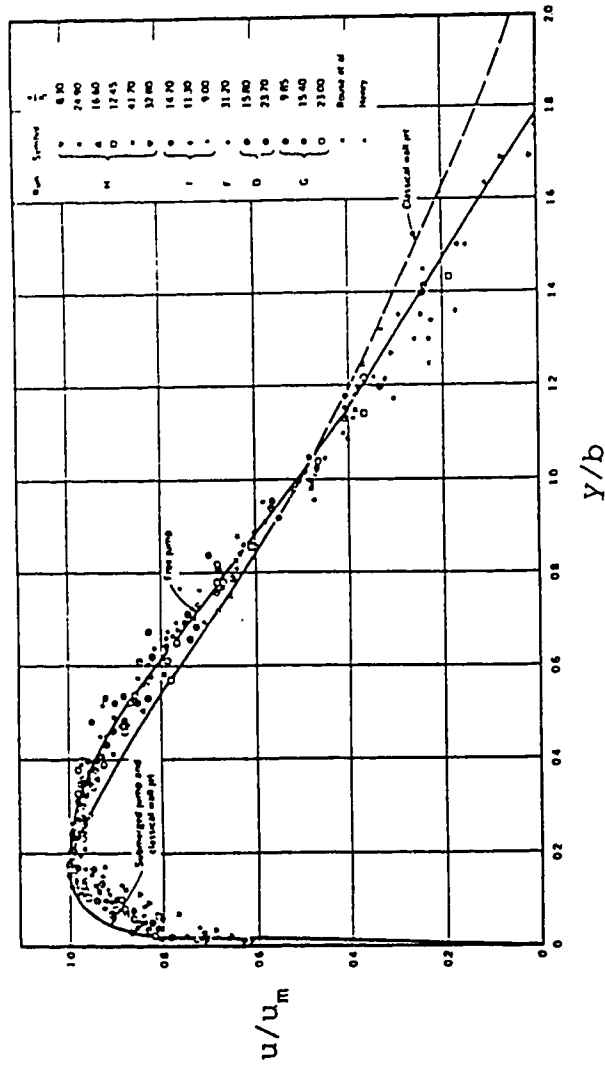


Figure 4. Similarity of velocity profiles for free jumps (Courtesy of N. Rajaratnam)

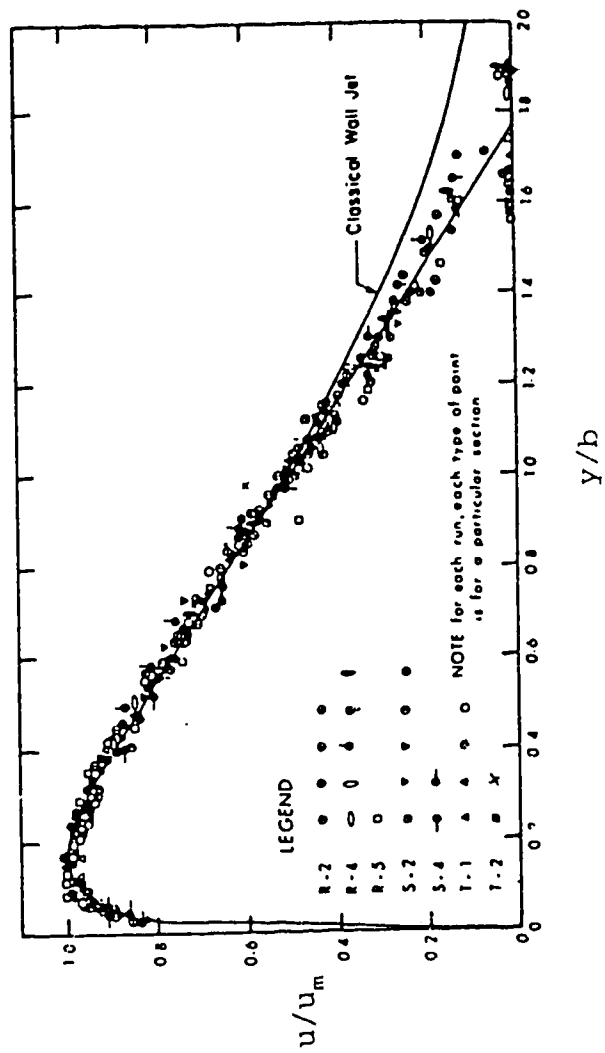


Figure 5. Similarity of velocity profiles for submerged jumps (Courtesy of N. Rajaratnam)

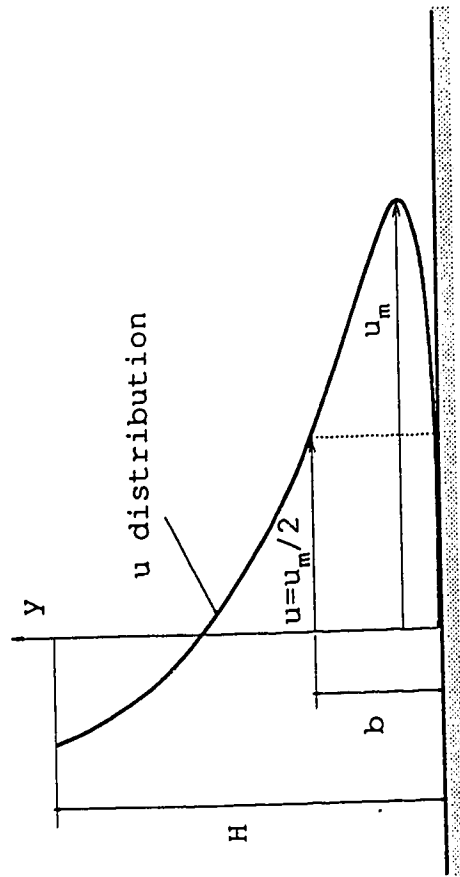


Figure 6. A typical u distribution.

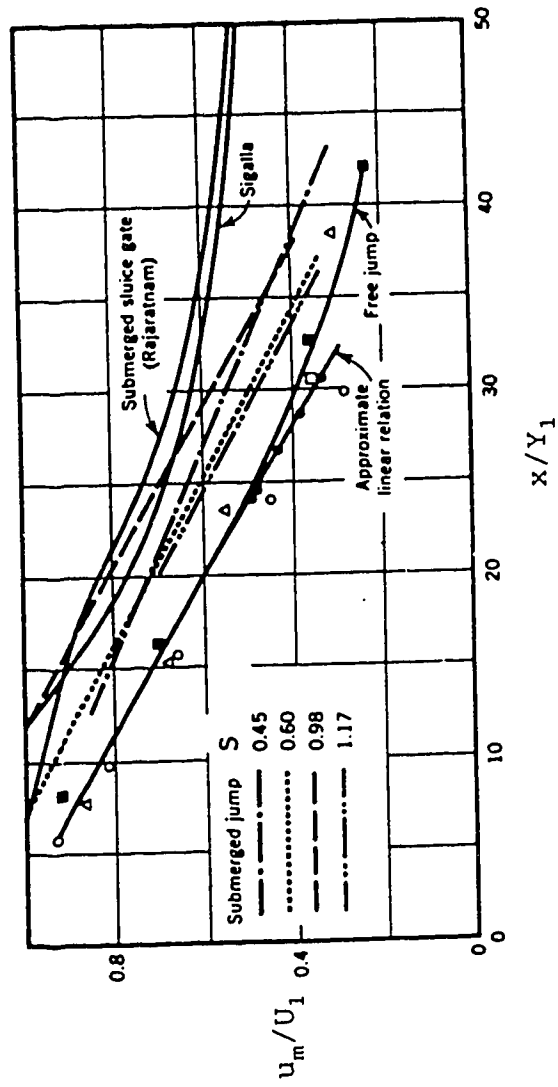


Figure 7. Main flow characteristics for free jumps (Courtesy of N. Rajaratnam)

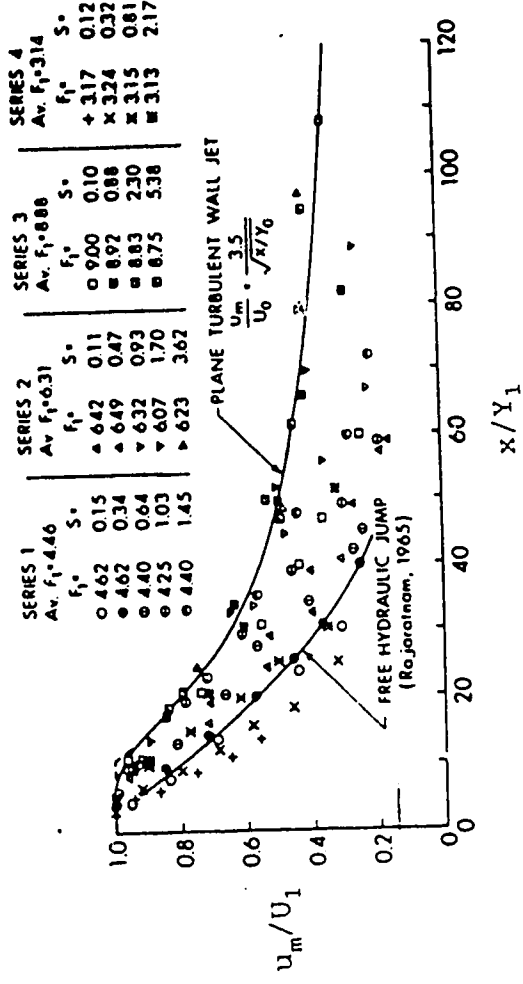


Figure 8. Main flow characteristics for submerged jumps (Courtesy of N. Rajaratnam)

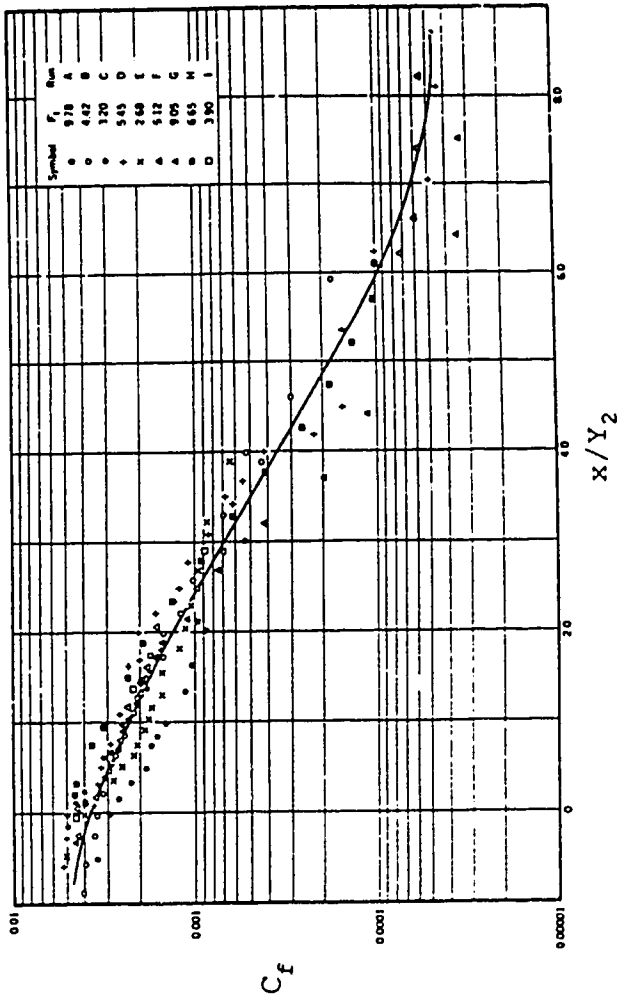


Figure 9. Wall shear stress for free jumps
(Courtesy of N. Rajaratnam)

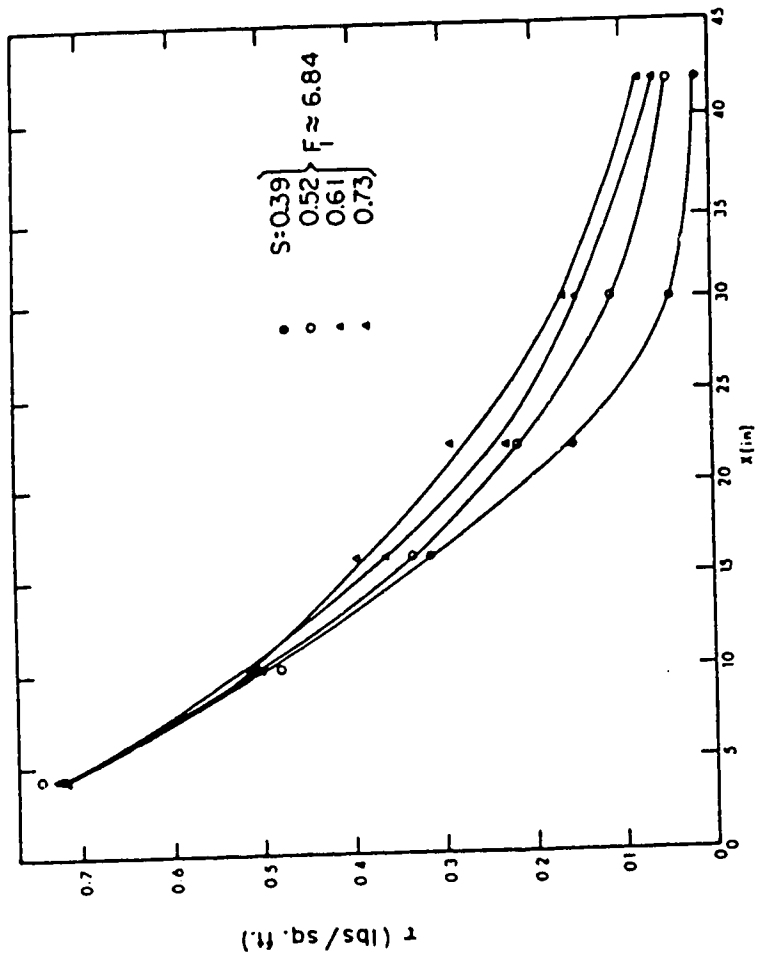


Figure 10. Wall shear stress for submerged jumps
(Courtesy of N. Rajaratnam)

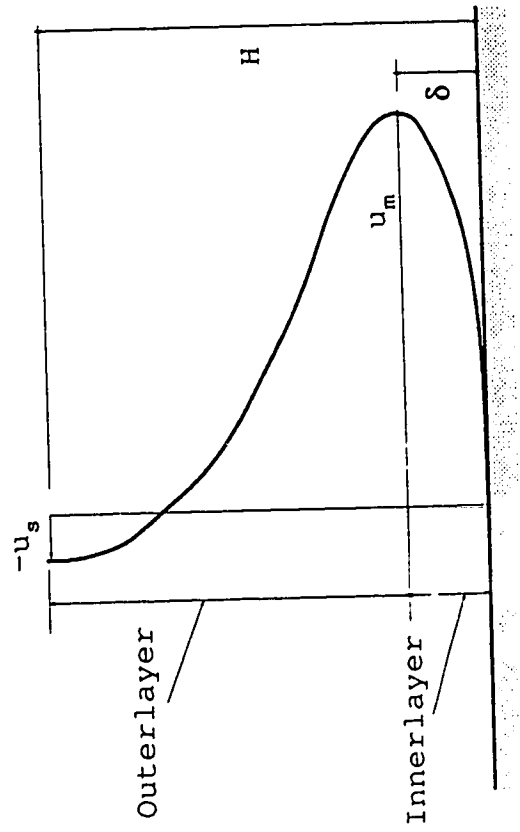


Figure 11. Layer model of longitudinal velocity distribution

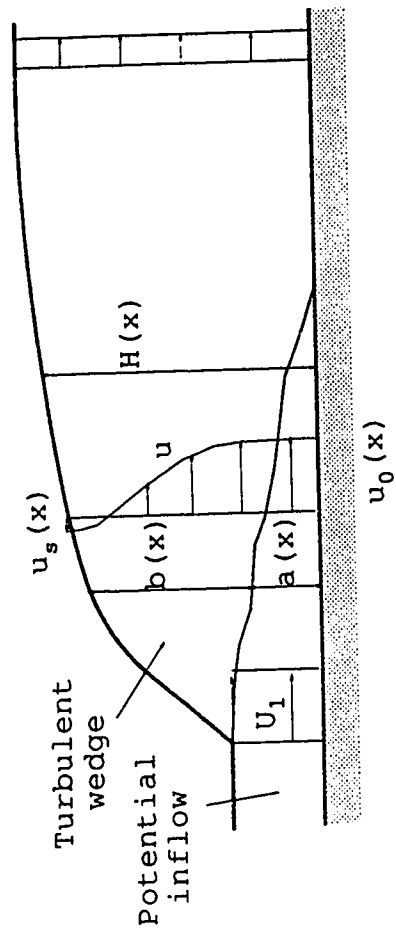


Figure 12. Model definition of a free jump by Madsen and Svendsen (1983).

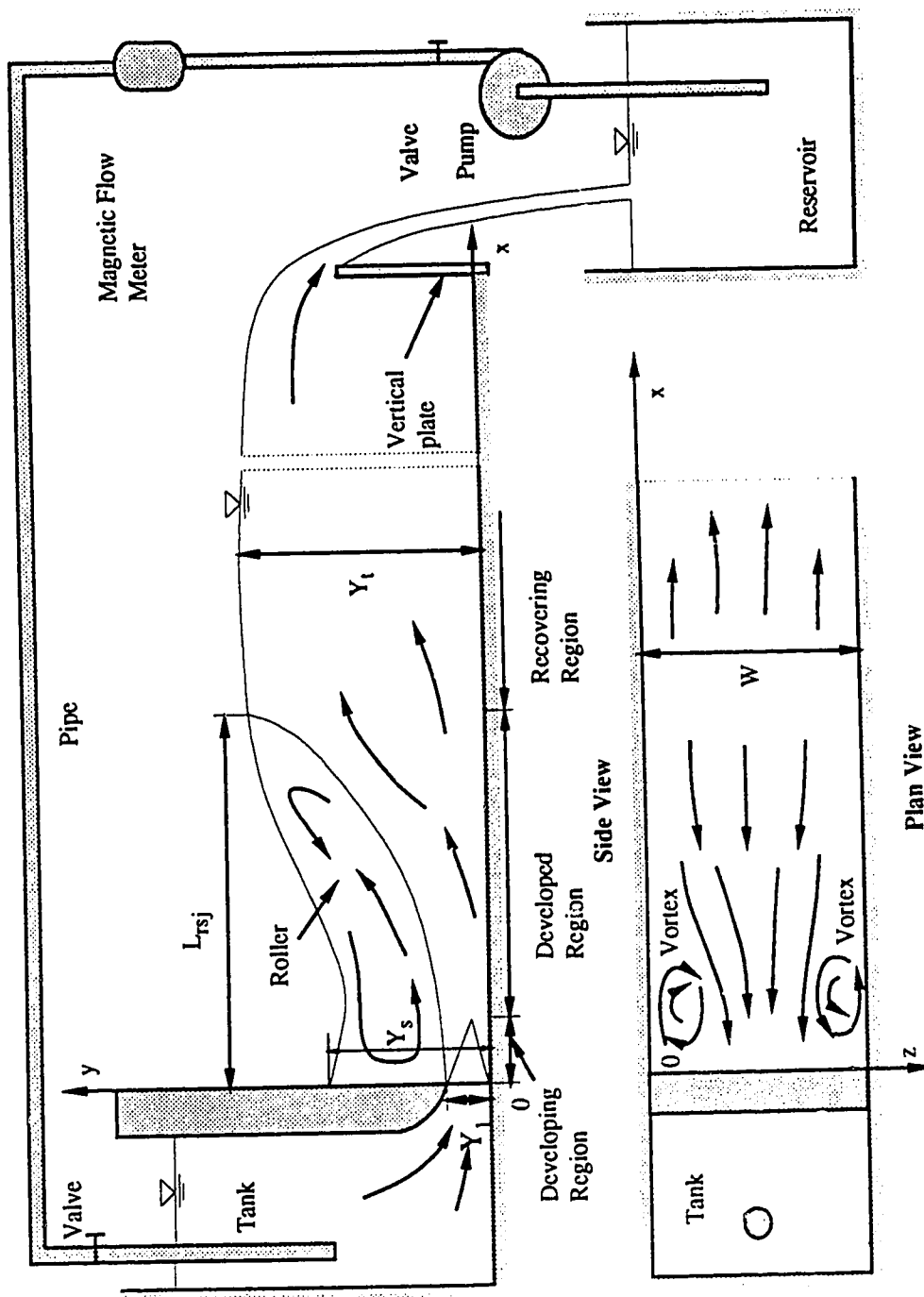


Figure 13. Schematic diagram of experimental layout.

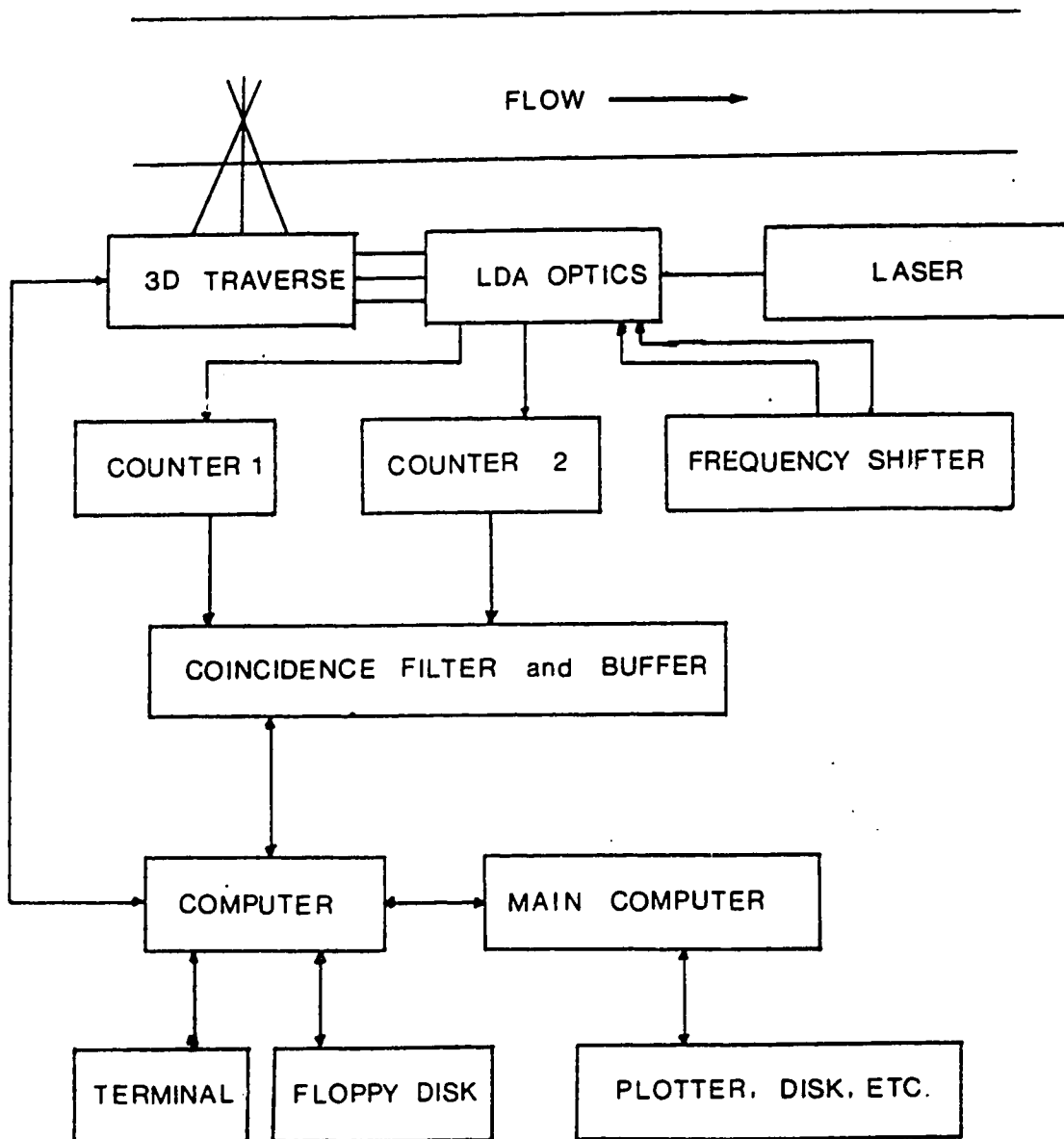


Figure 14. Schematic diagram of LDA setup
(Courtesy of P. M. Steffler)

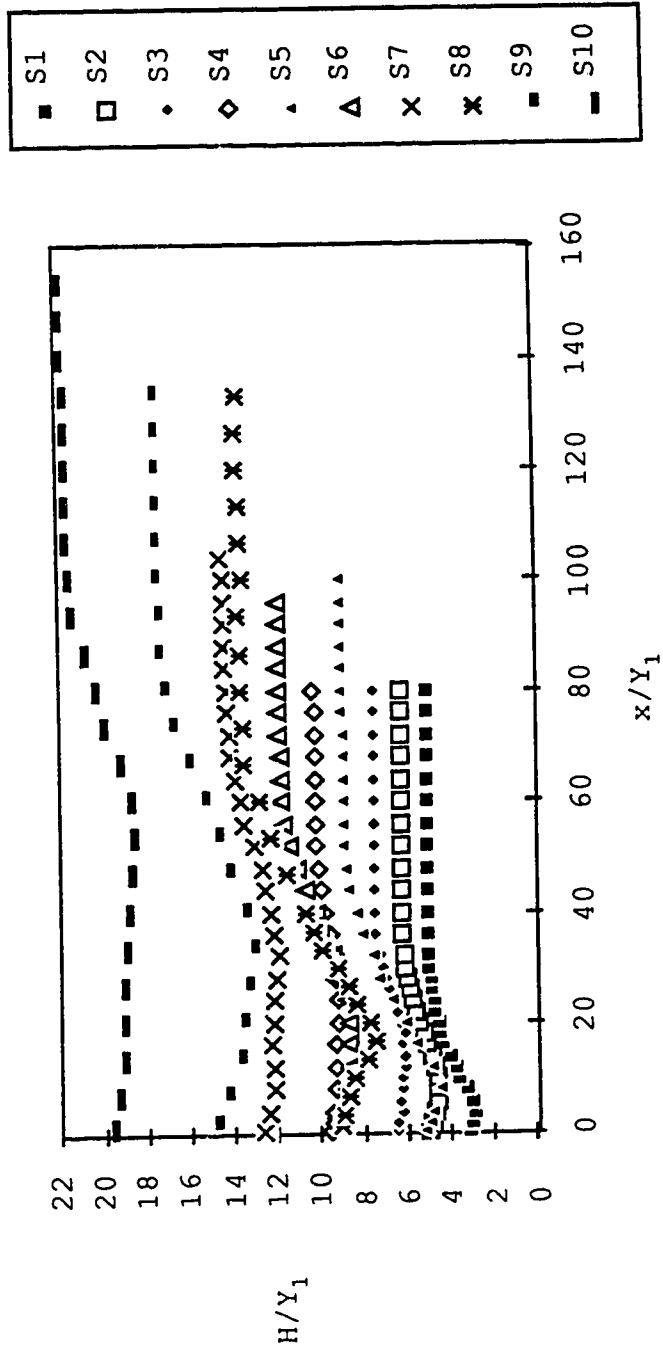


Figure 15. Surface profiles for all conditions

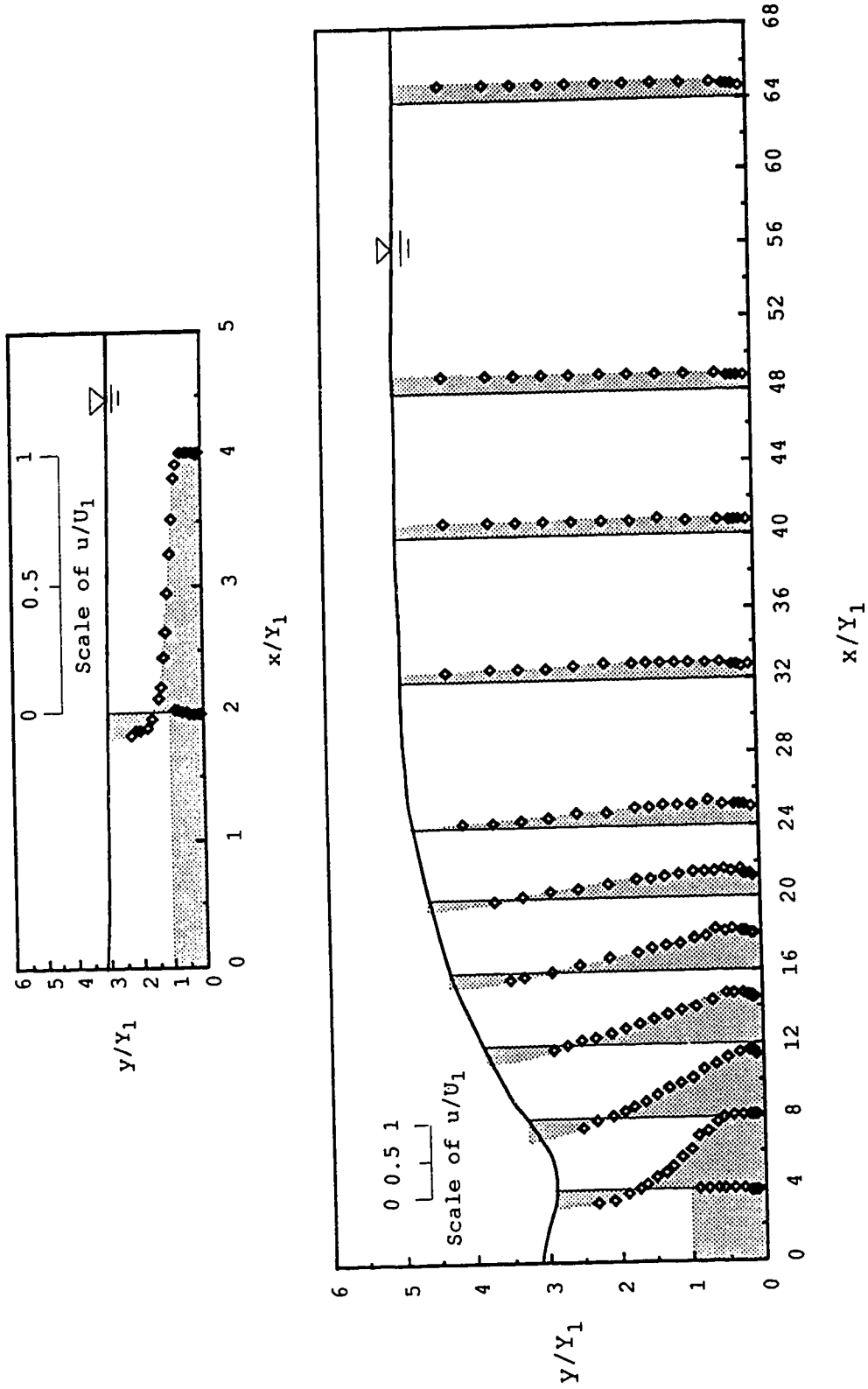


Figure 16. u/U_1 distribution over the depth at the plane of $z/W=0.36$ for $F_1=3.11$ and $S=0.26$

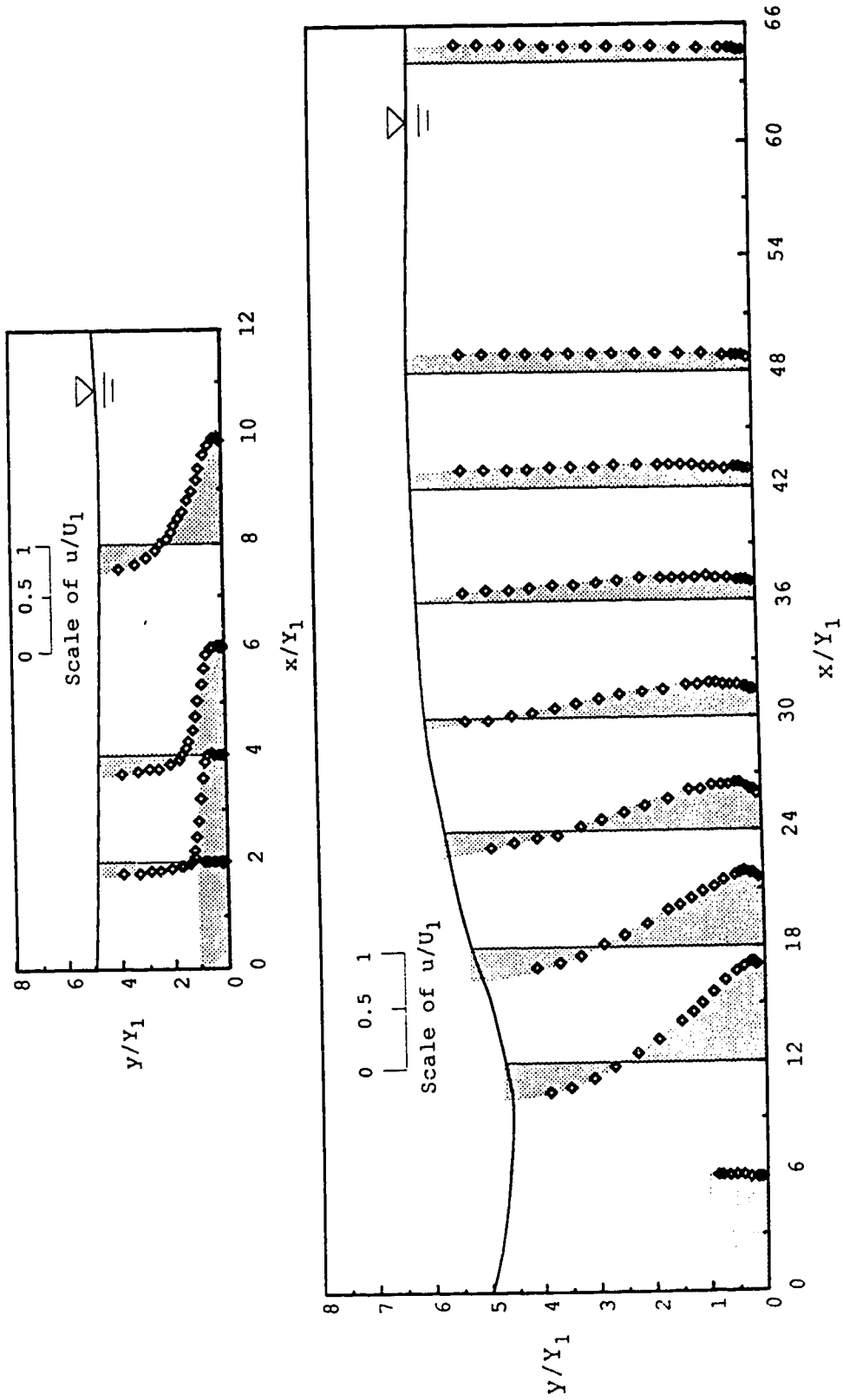


Figure 17. u/U_1 distribution over the depth at the plane of $z/W=0.36$ for the condition of $F_1=3.20$ and $S=0.53$.

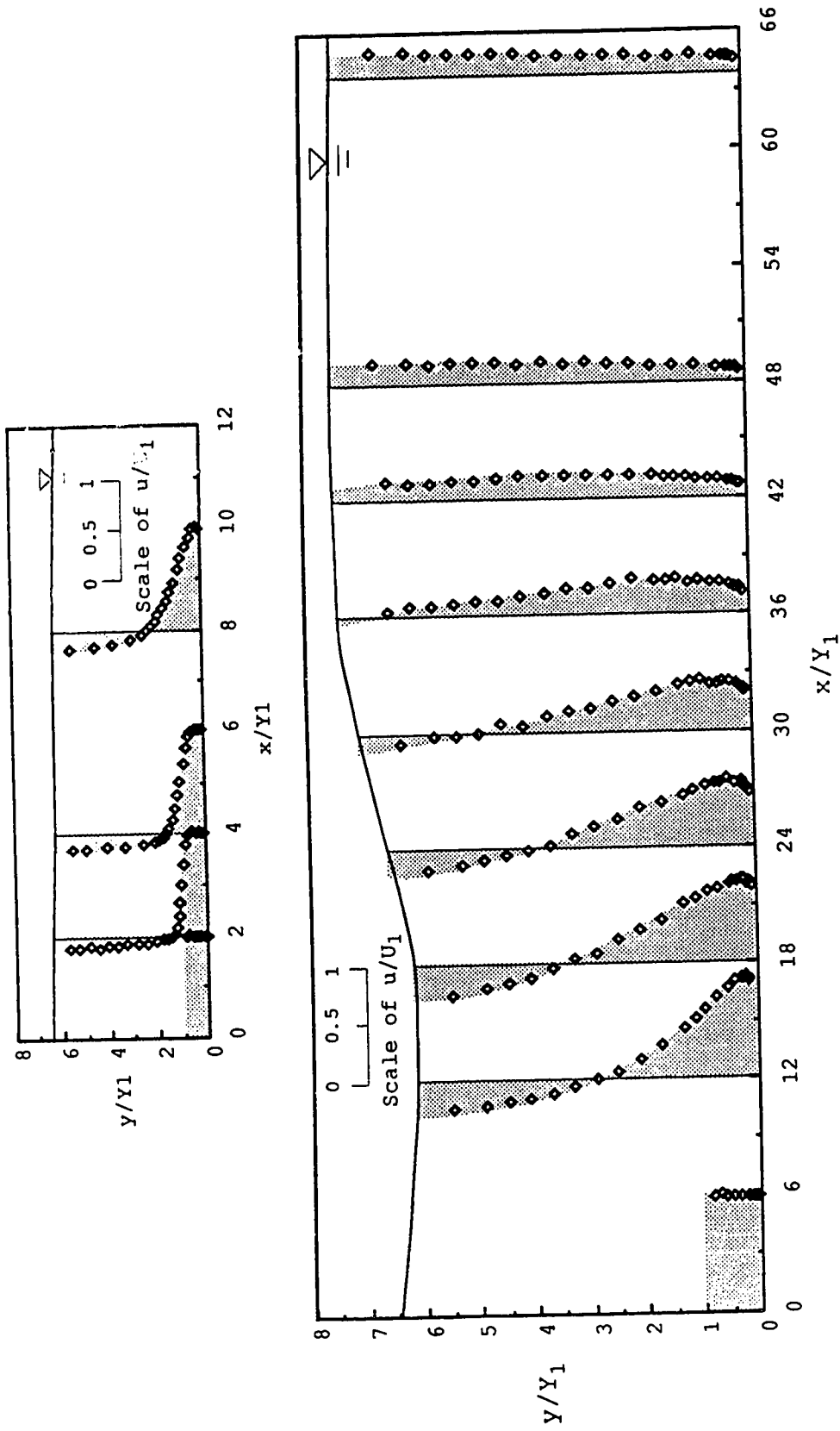


Figure 18. u/U_1 distribution over the depth at the plane of $z/W=0.36$ for the condition of $F_1=3.19$ and $S=0.85$.

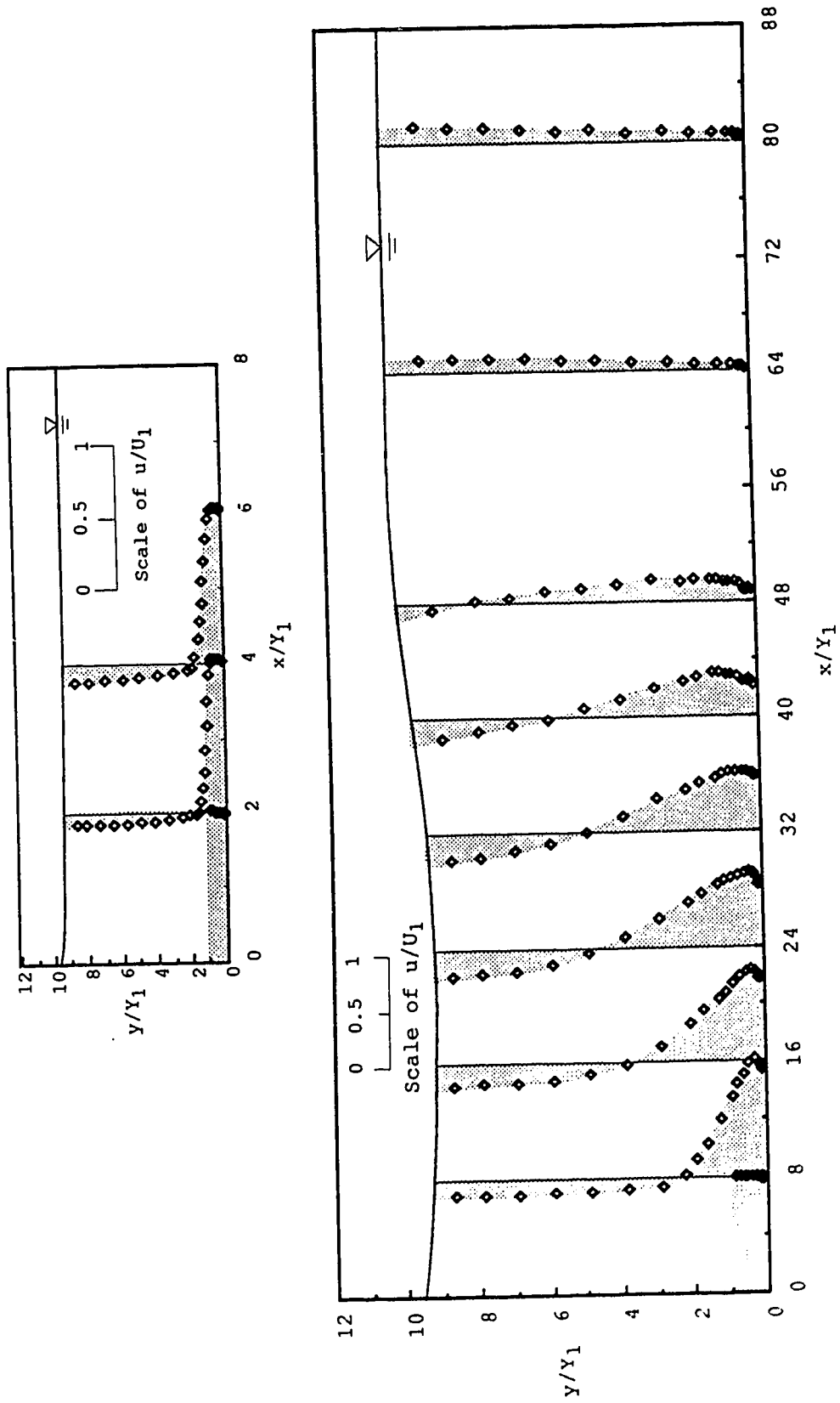


Figure 19. u/U_1 distribution over the depth at the plane of $z/W=0.36$ for the condition of $F_1=3.01$ and $S=1.69$.

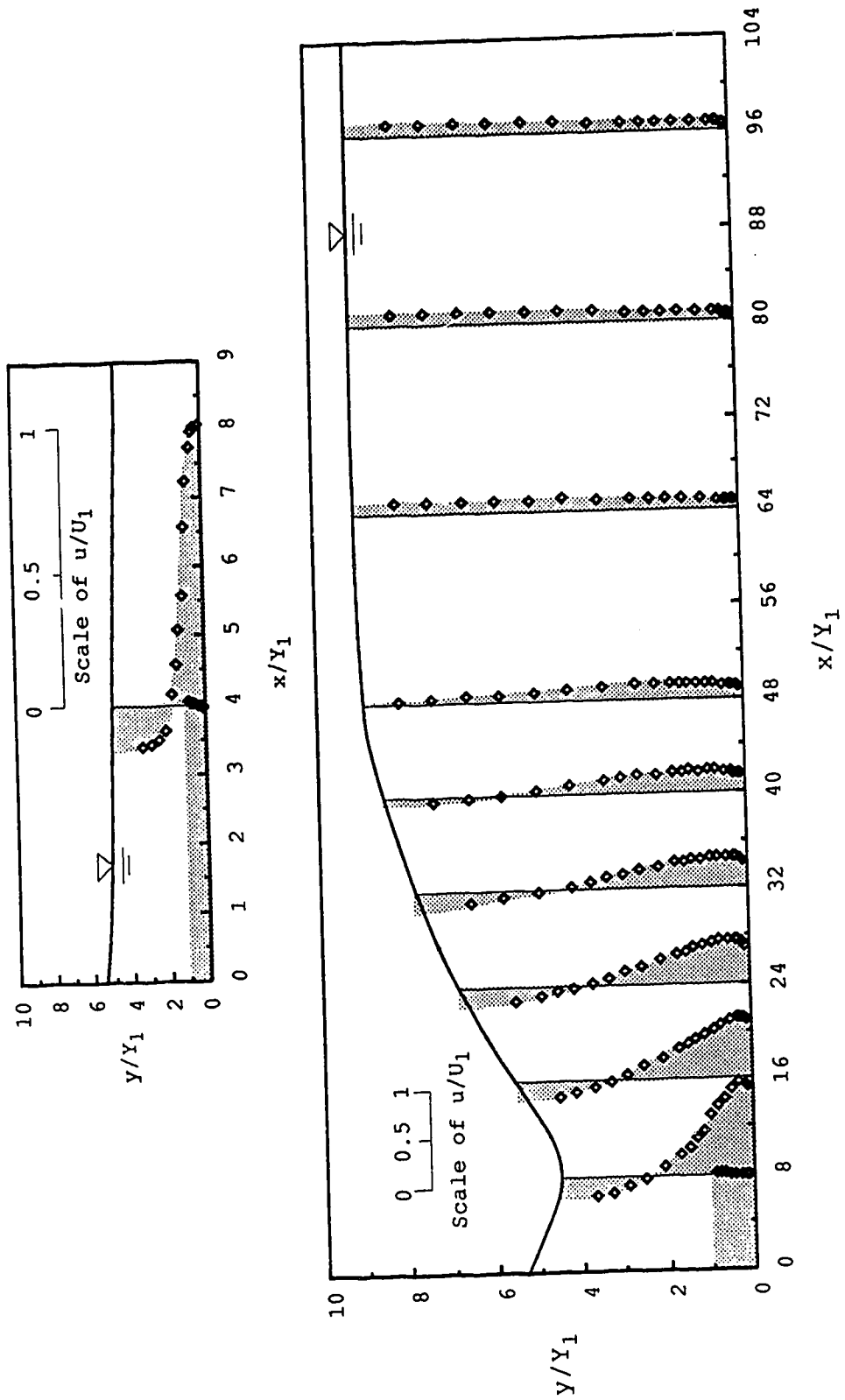


Figure 20. u/U_1 distribution over the depth at the plane of $z/W=0.36$ for the condition of $F_1=5.61$ and $S=0.22$

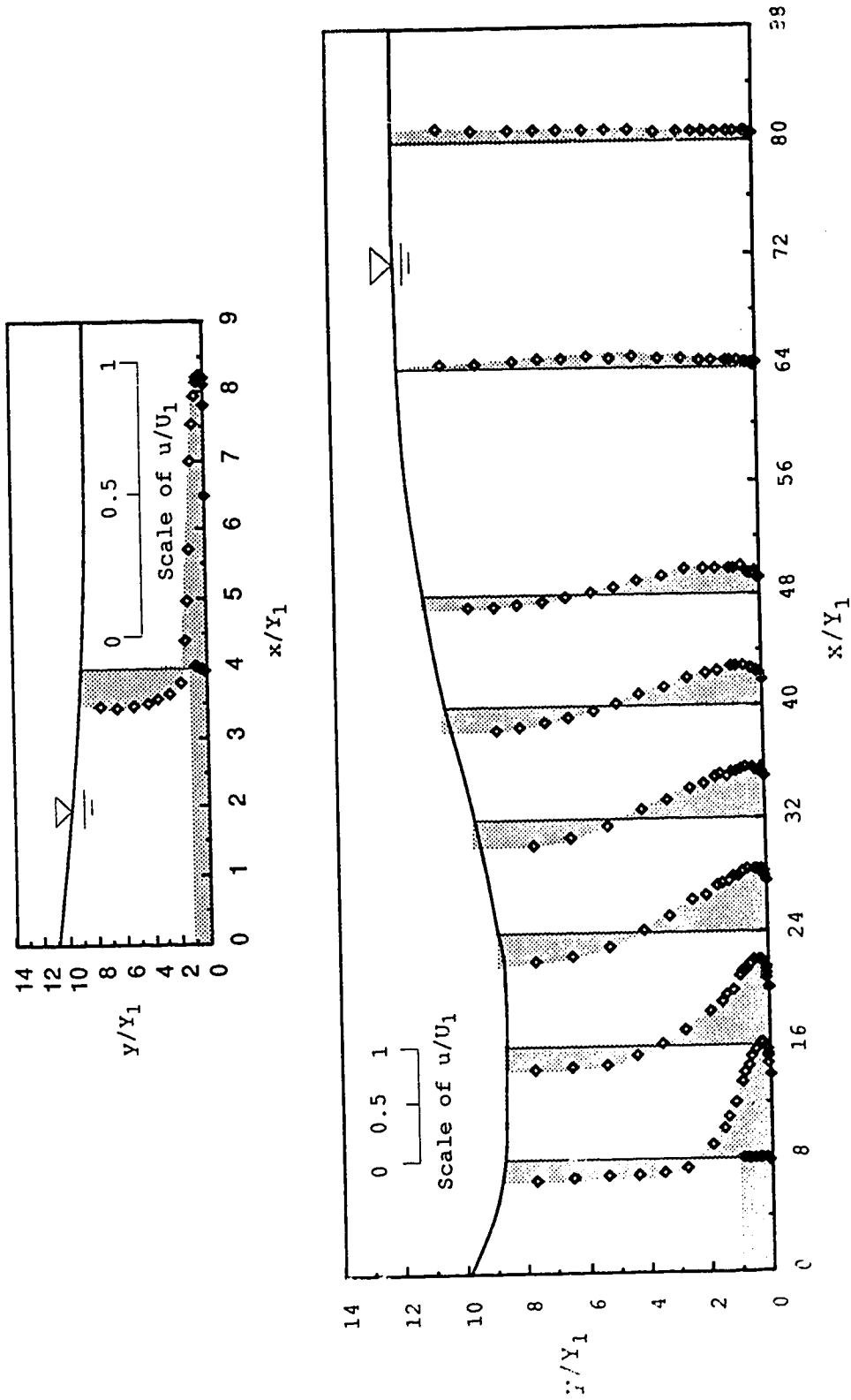


Figure 21. u/U_1 distribution over the depth at the plane of $z/W=0.36$ for the condition of $F_1=5.49$ and $S=0.63$.

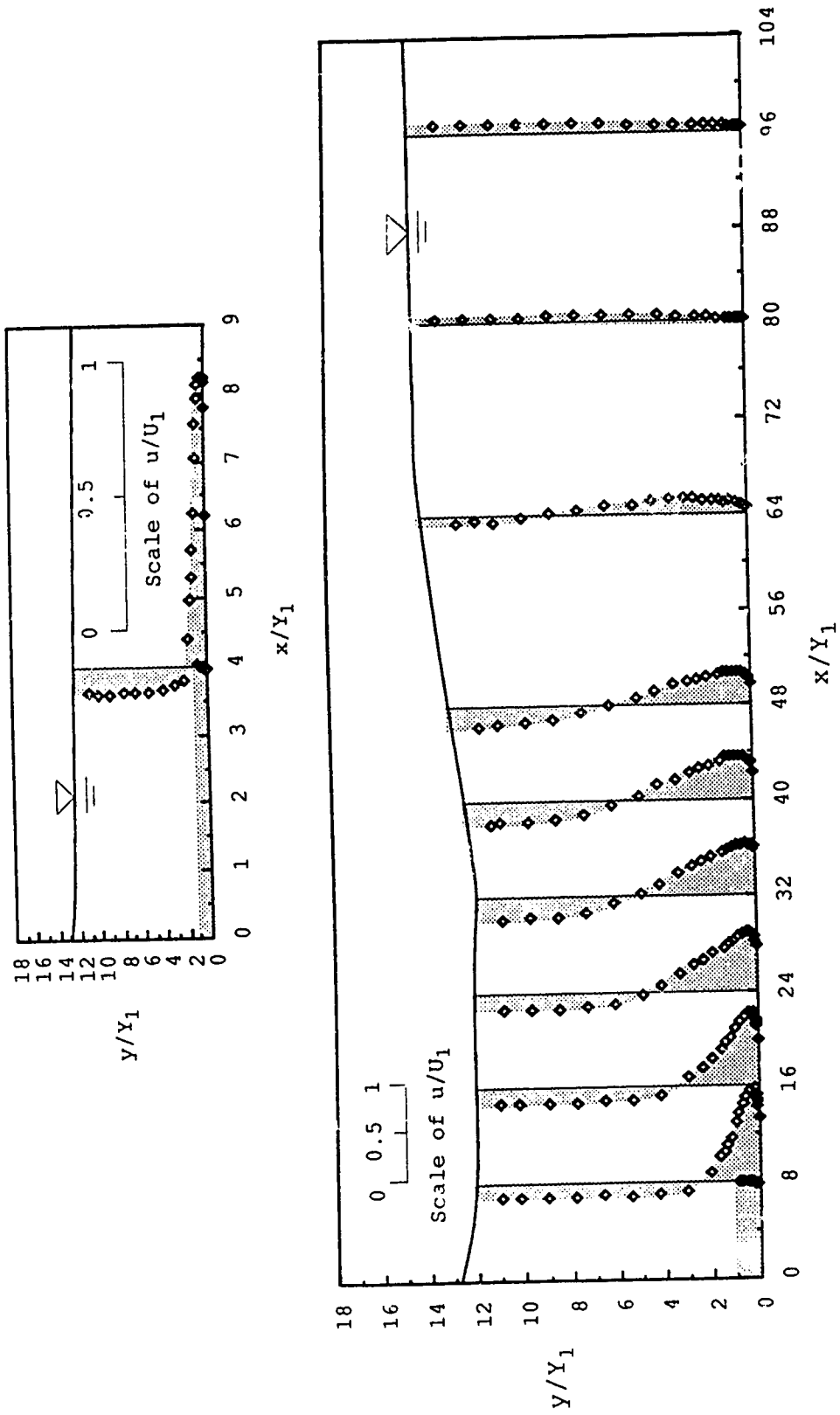


Figure 22. u/U_1 distribution over the depth at the plane of $z/W=0.36$ for the condition of $F_1=5.43$ and $S=1.01$.

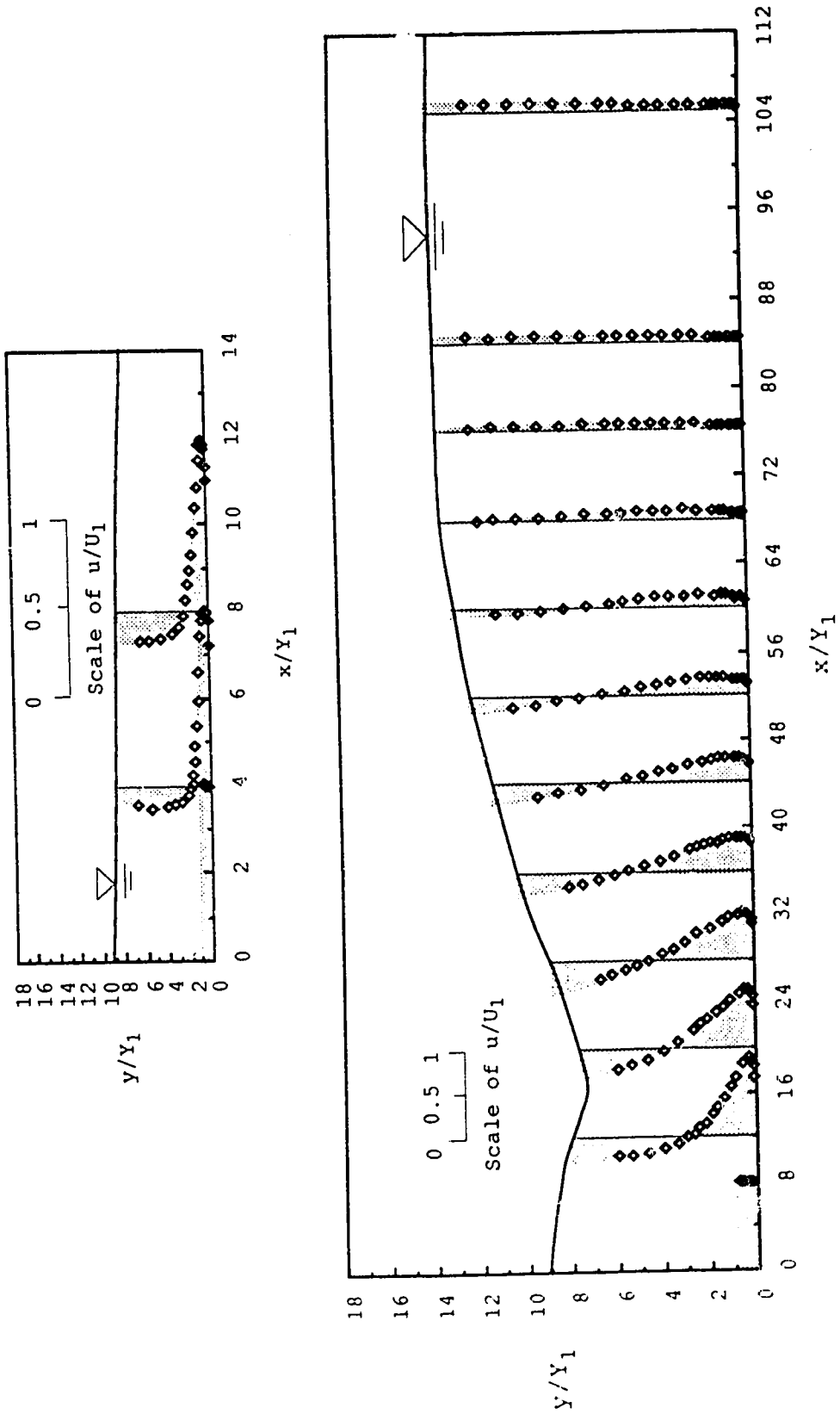


Figure 23. u/U_1 distribution over the depth at the plane of $z/w=0.36$ for $F_1=8.19$ and $S=0.24$.

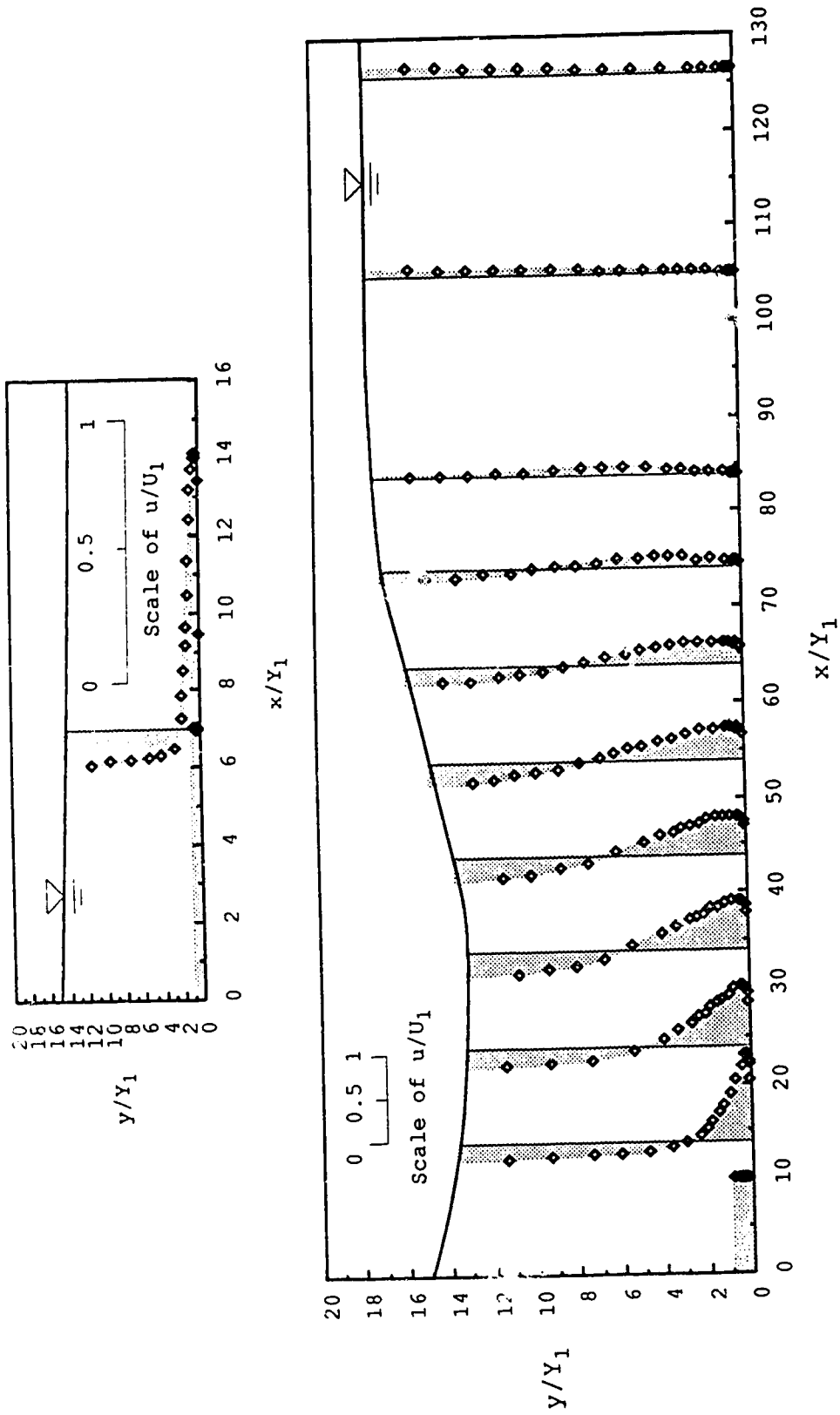


Figure 24. u/U_1 distribution over the depth at the plane of $z/w=0.36$ for the condition of $F_1=8$ and $S=0.62$.

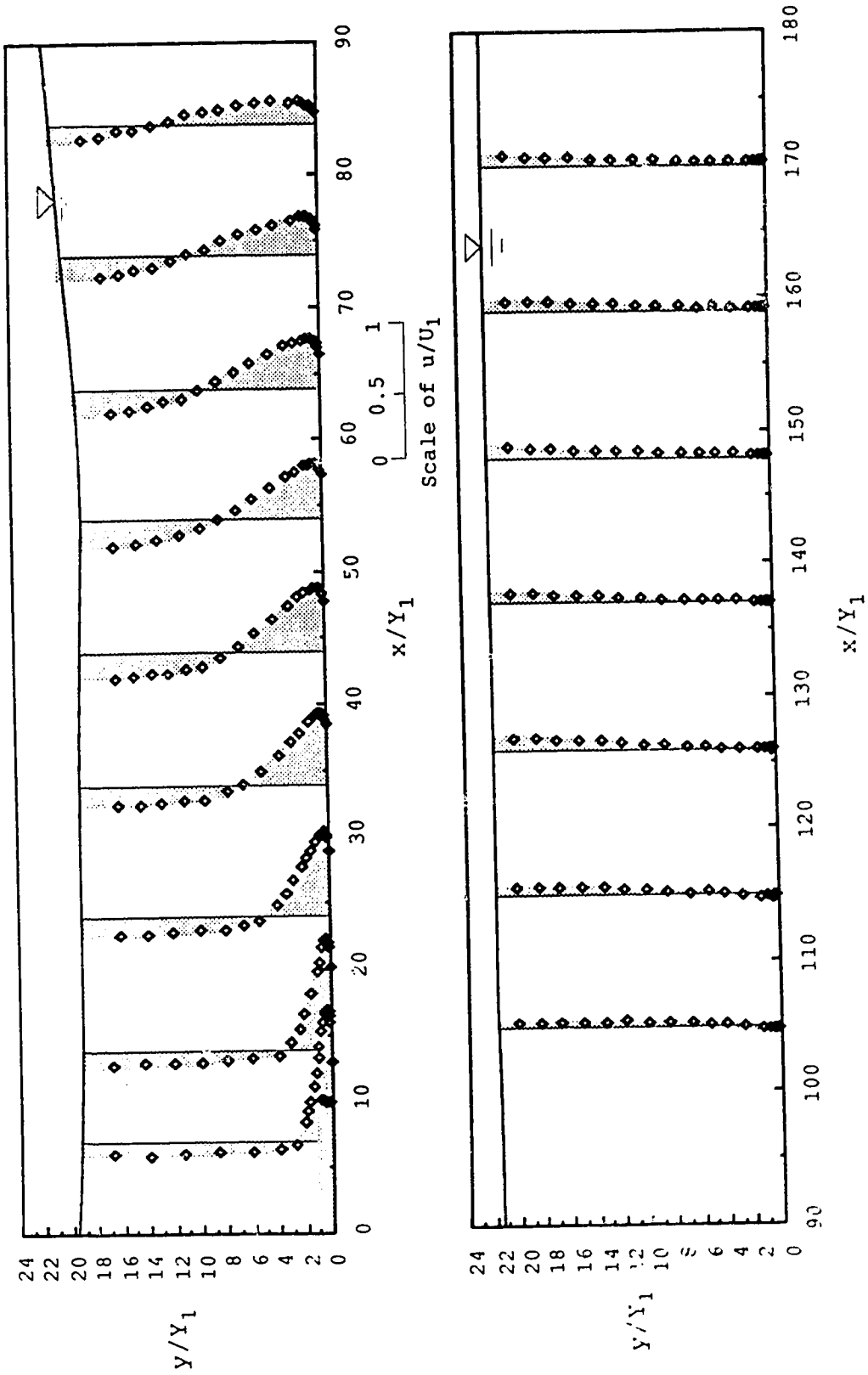


Figure 25. u/U_1 distribution over the depth at the plane of $z/W=0.36$ for the condition of $F_1=8.11$ and $S=1.00$.

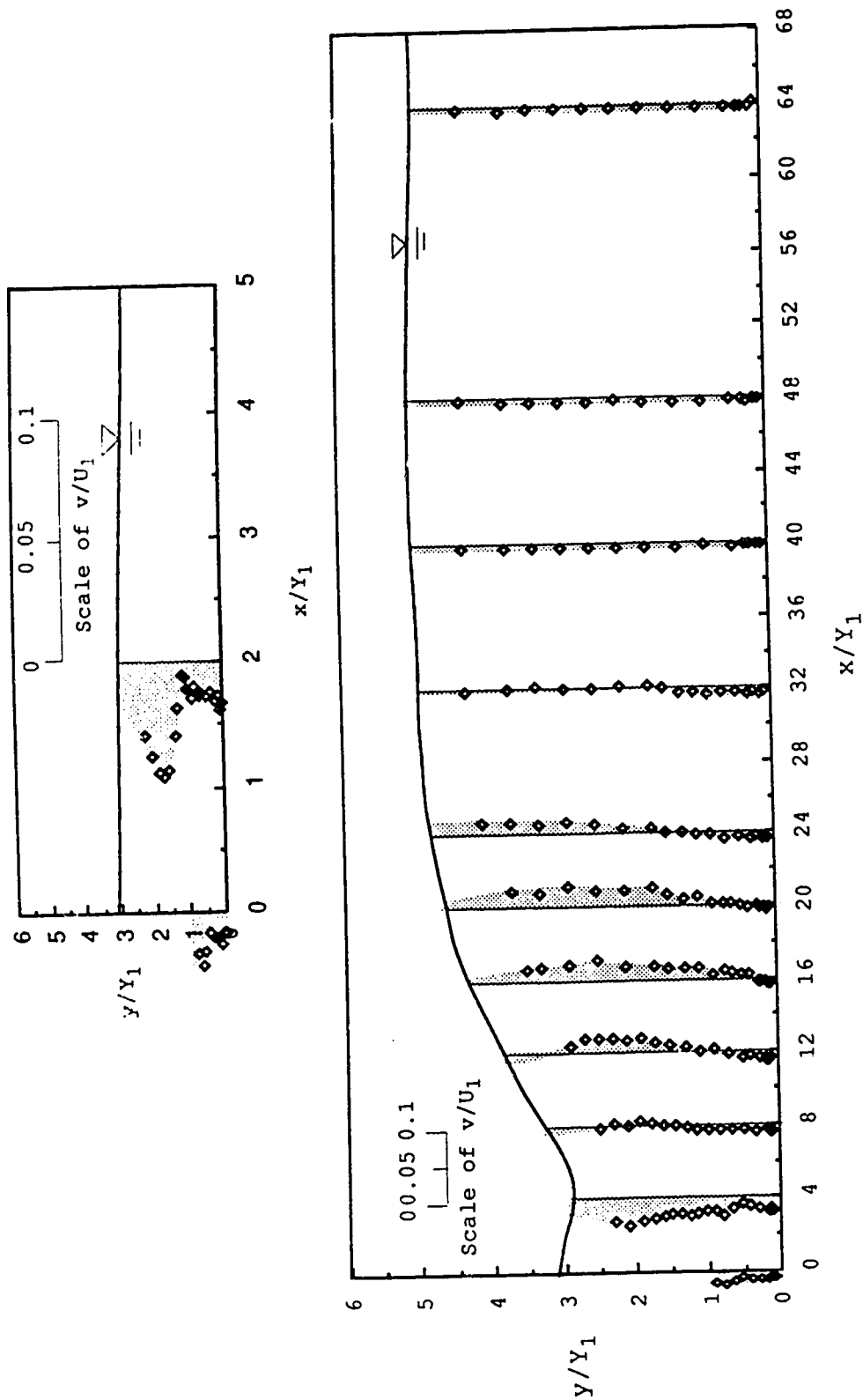


Figure 26. v/U_1 distribution over the depth at the plane of $z/W=0.36$ for the condition of $F_1=3.11$ and $S=0.26$.

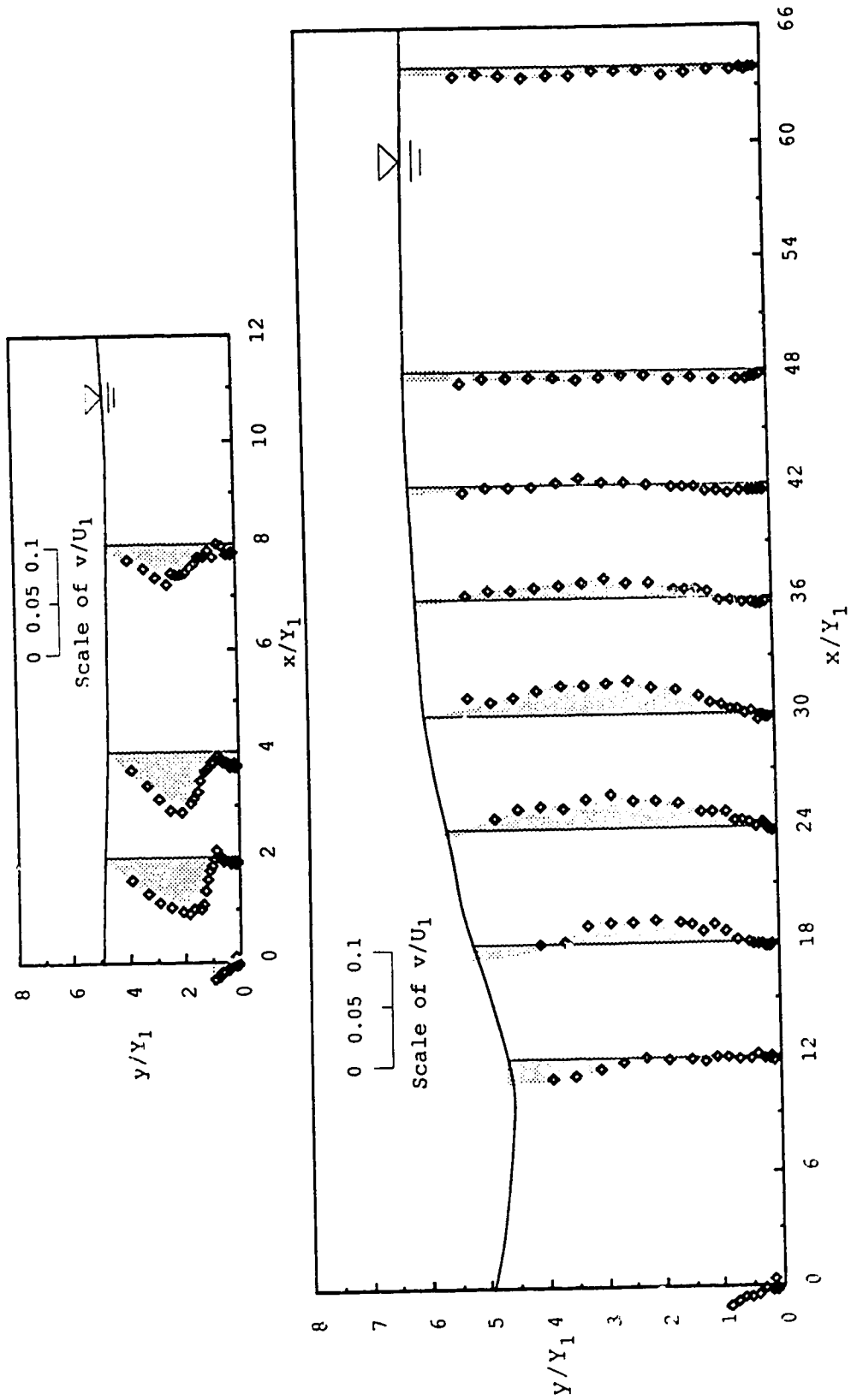


Figure 27. v/U_1 distribution over the depth at the plane of $z/W=0.36$ for the condition of $F_1=3.20$ and $S=0.53$.

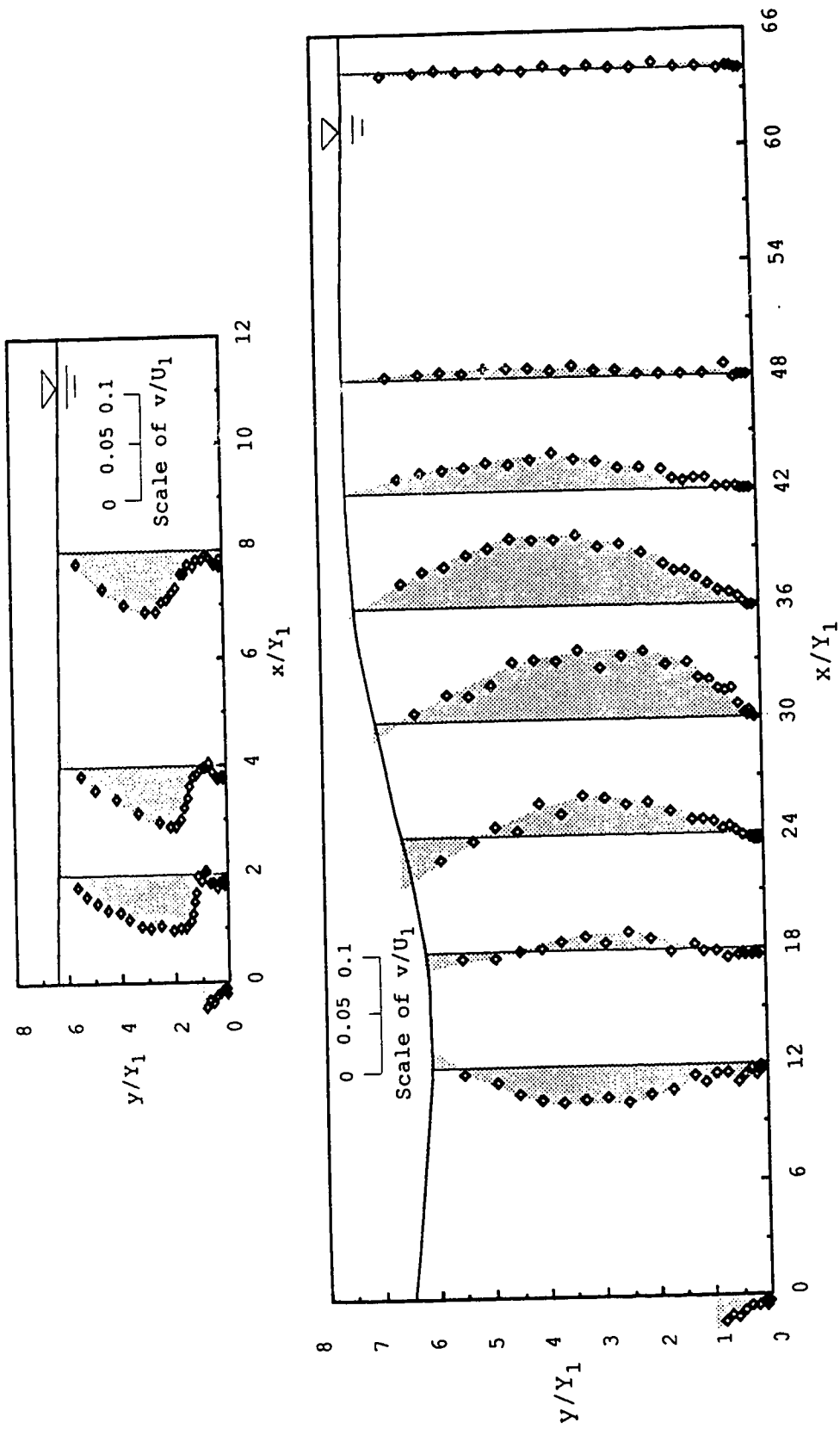


Figure 28. v/U_1 distribution over the depth at the plane of $z/W=0.36$ for the condition of $F_1=3.19$ and $S=0.85$.

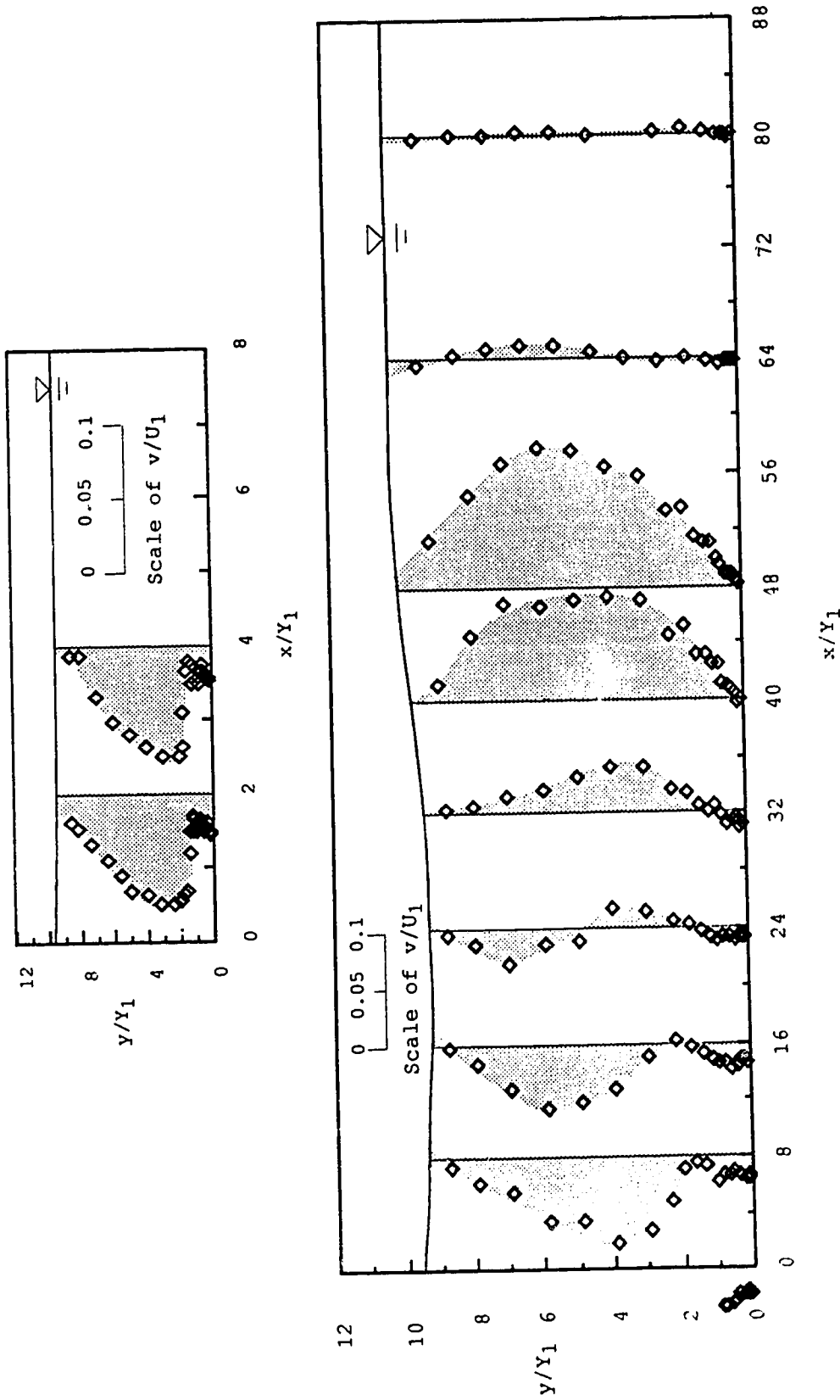


Figure 29. v/U_1 distribution over the depth at the plane of $z/W=0.36$ for the condition of $F_1=3.01$ and $S=1.69$.

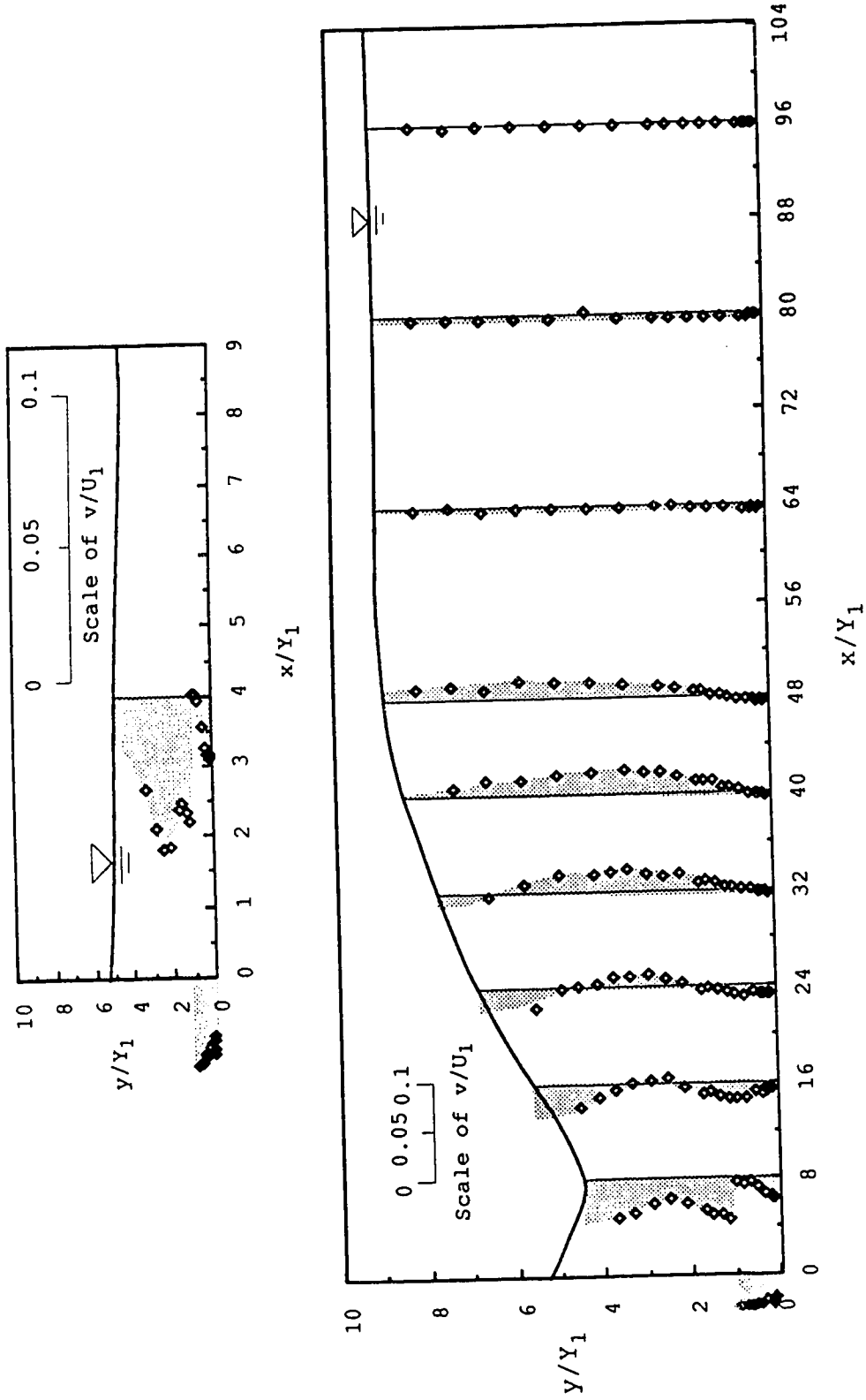


Figure 30. v/U_1 distribution over the depth at the plane of $z/W=0.36$ for the condition of $F_1=5.61$ and $S=0.22$.

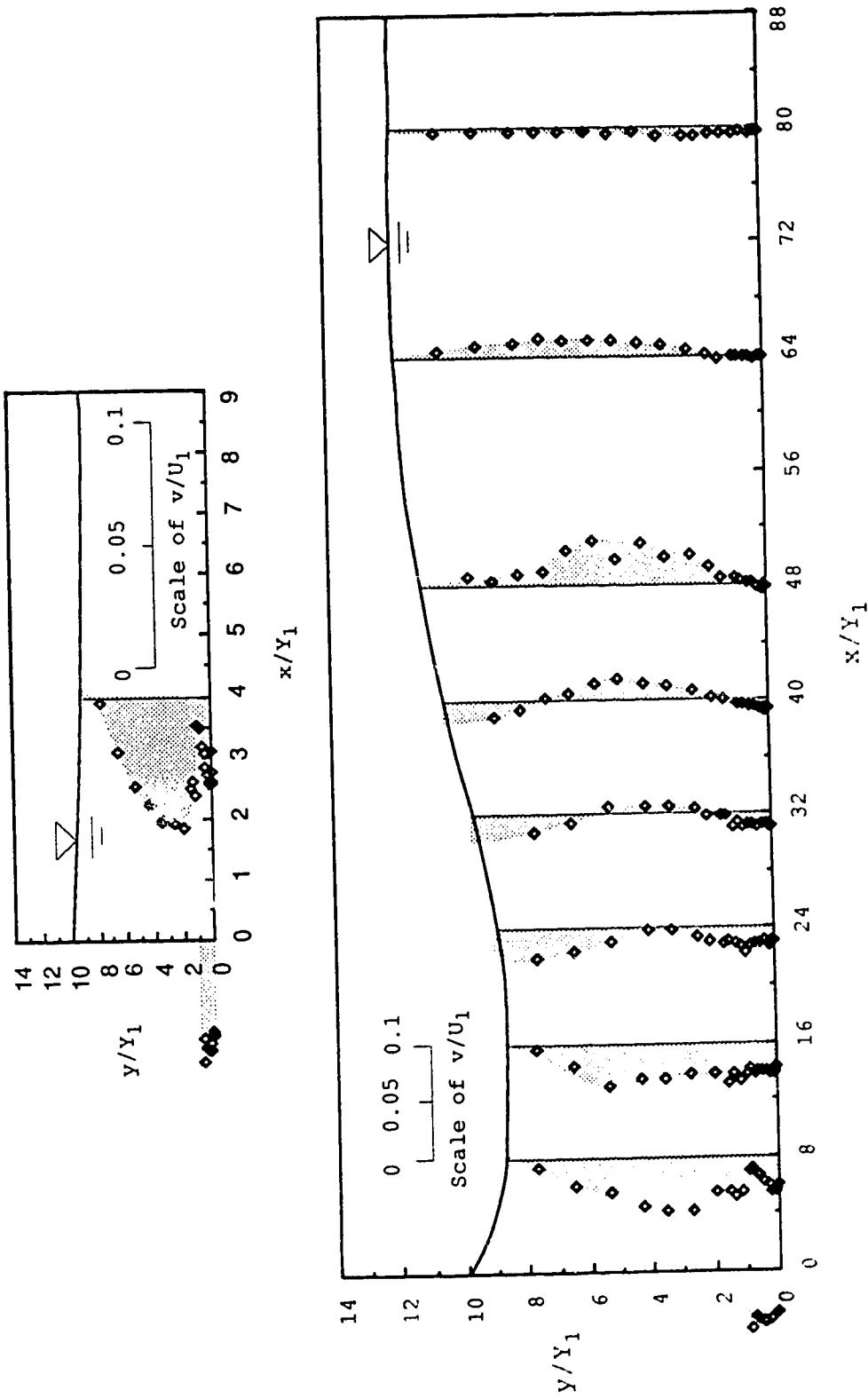


Figure 31. v/U_1 distribution over the depth at the plane of $z/W=0.36$ for the condition of $F_1=5.49$ and $S=0.63$.

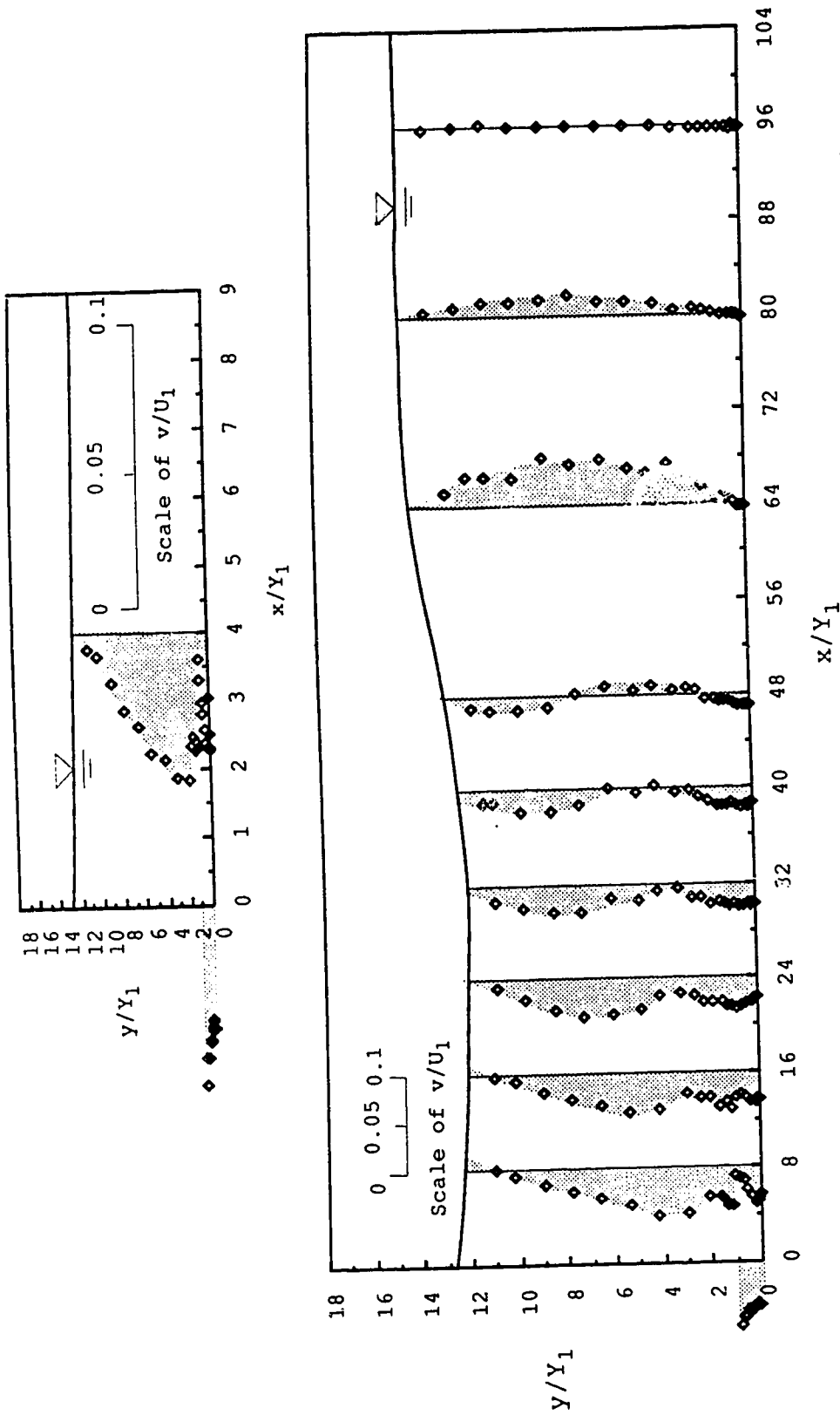


Figure 32. v/U_1 distribution over the depth at the plane of $z/W=0.36$ for the condition of $F_1=5.43$ and $S=1.01$.

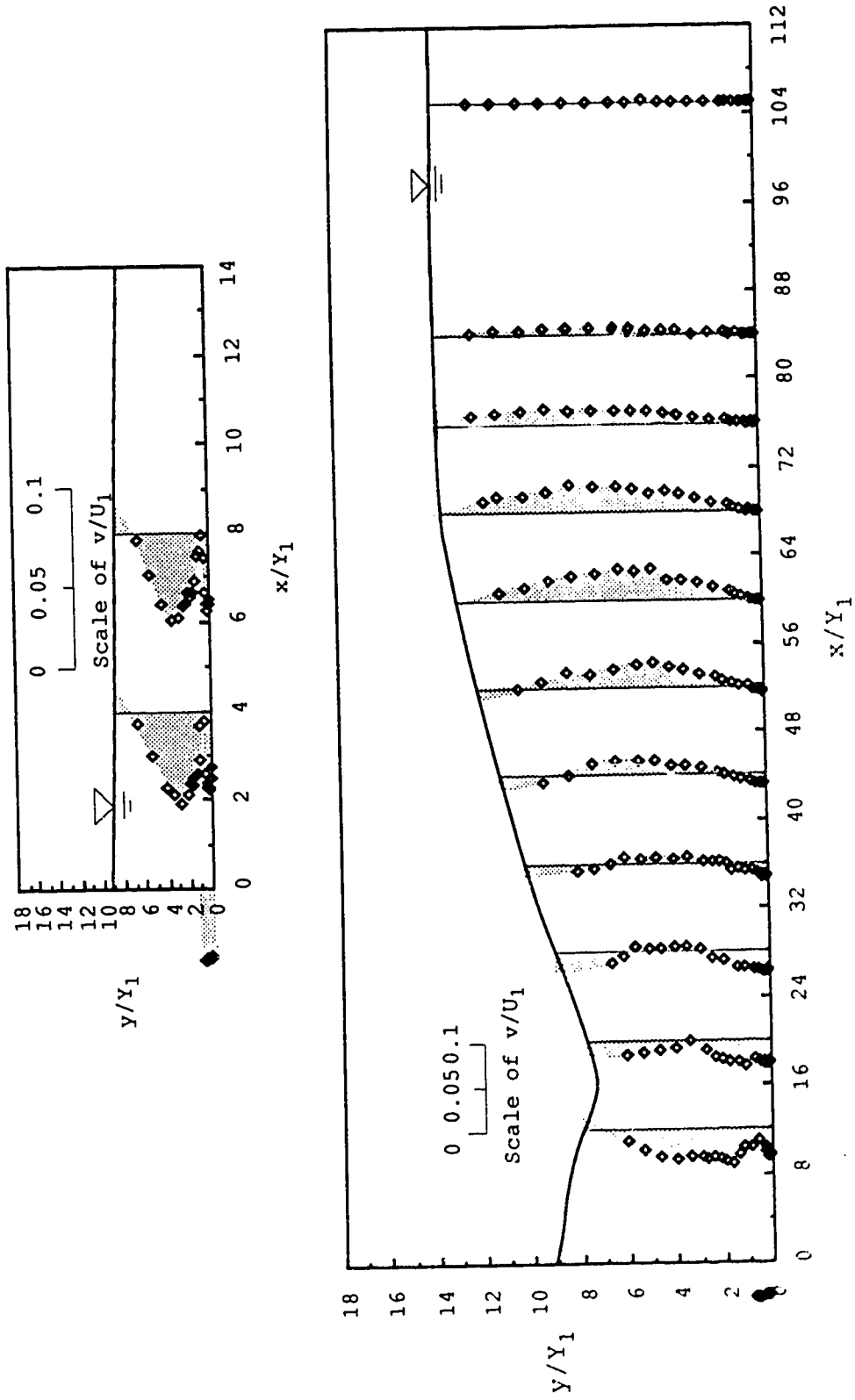


Figure 10. v/U_1 distribution over the depth at the plane of $z/W=0.36$ for $F_1=8.19$ and $S=0.24$.

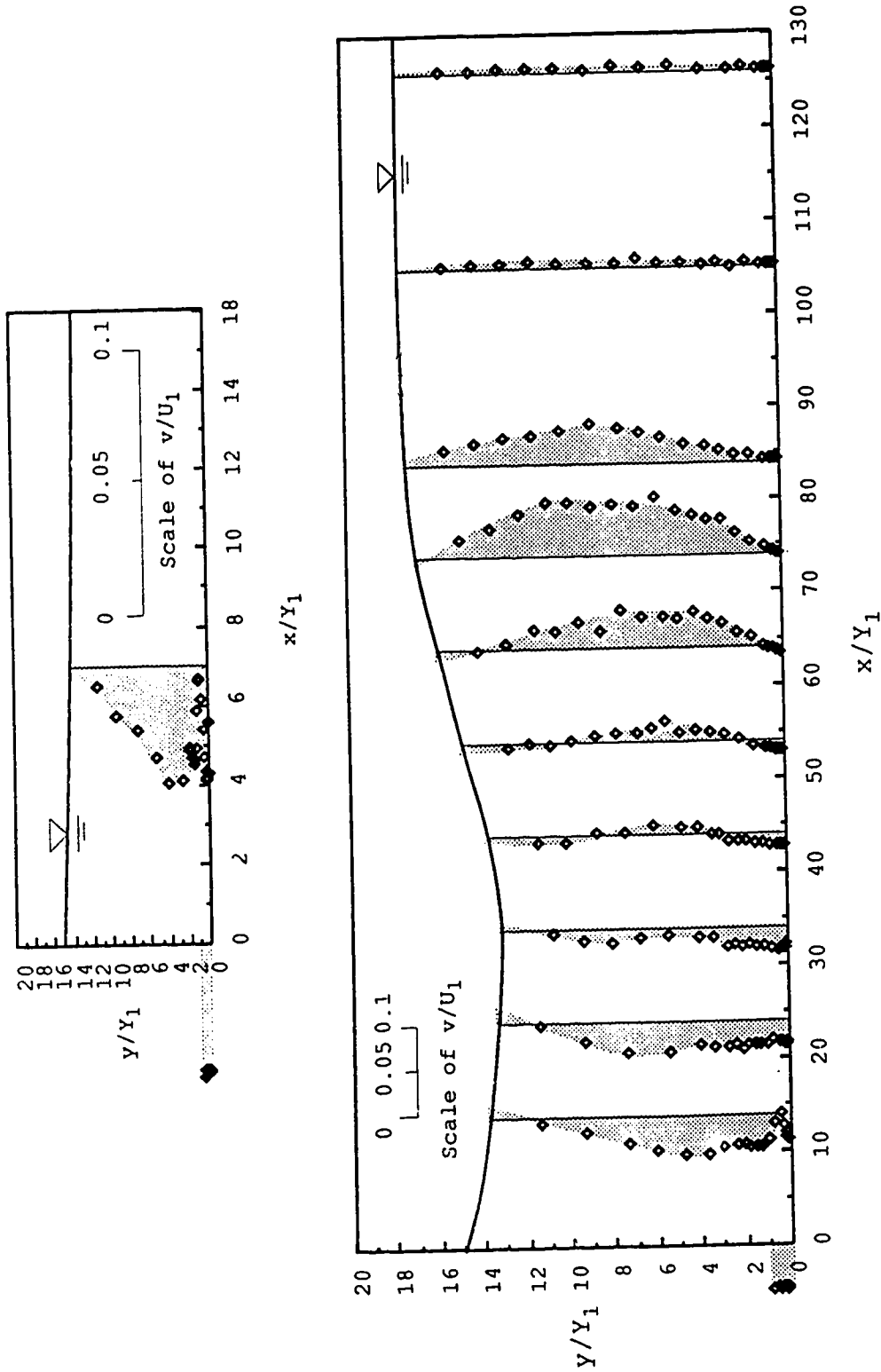


Figure 34. v/U_1 distribution over the depth at the plane of $z/W=0.36$ for the condition of $F_1=8$ and $S=0.62$.

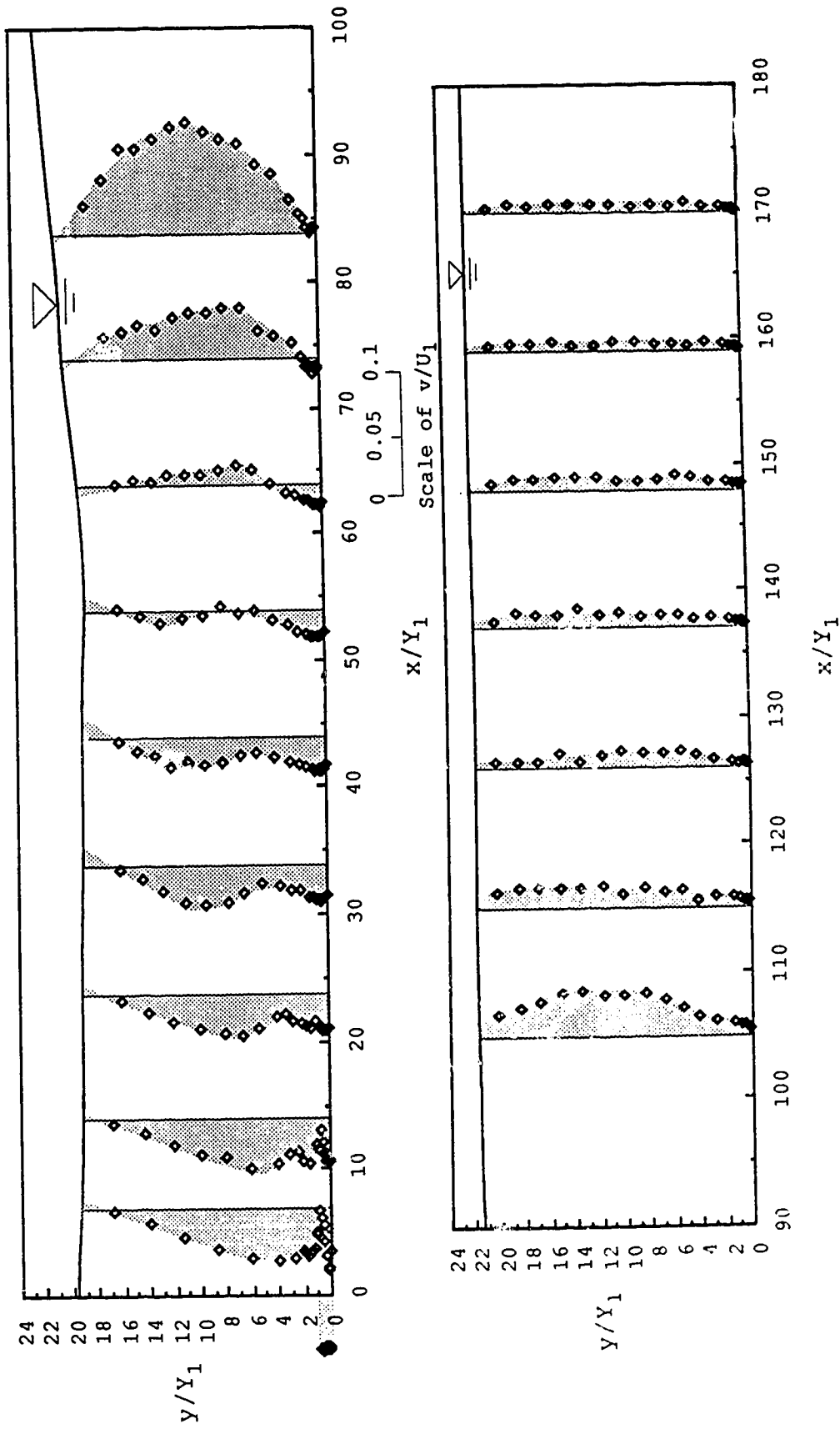


Figure 35. v/U_1 distribution over the depth at the plane of $z/W=0.36$ for the condition of $F_1=8.11$ and $S=1.00$.

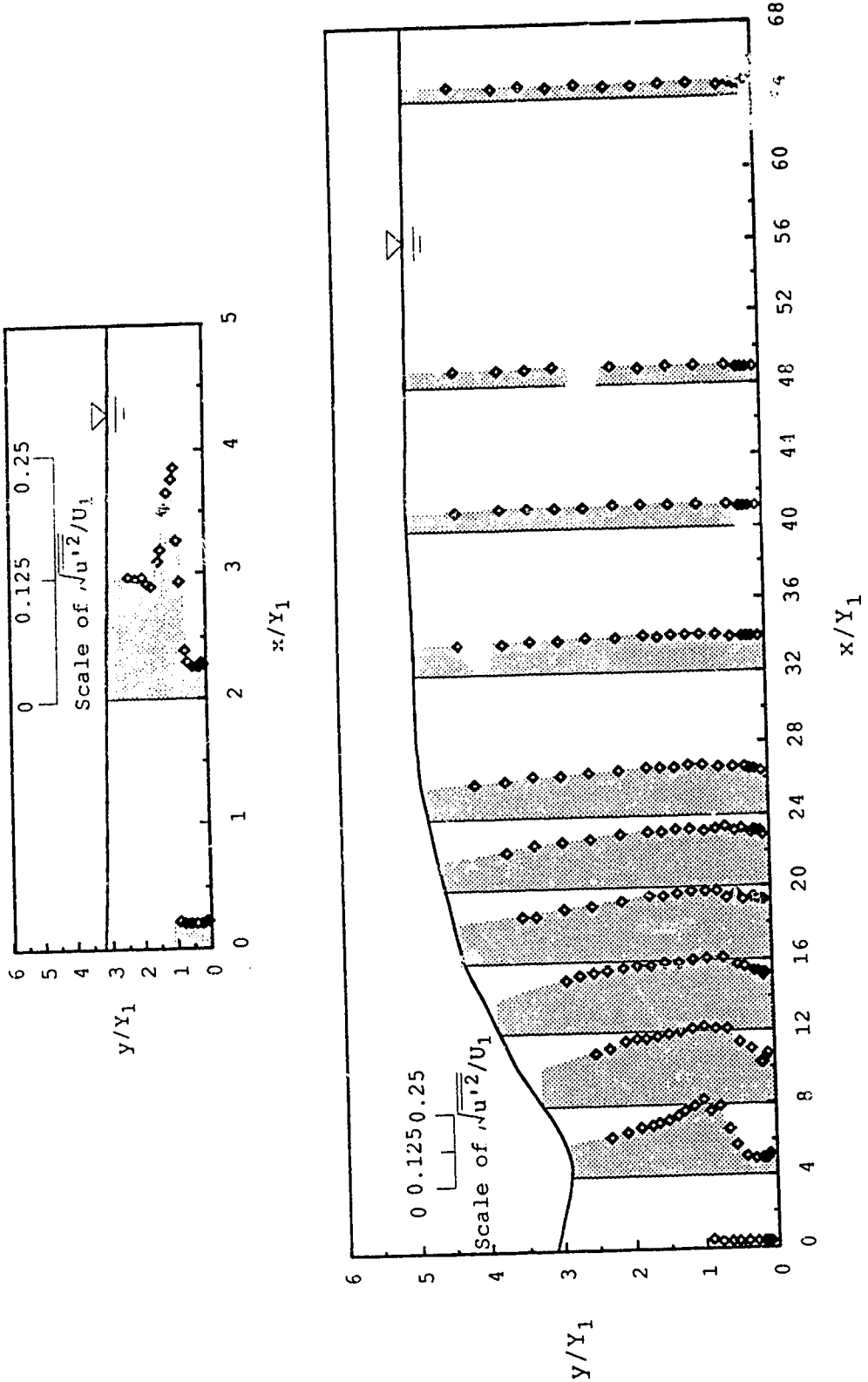


Figure 36. $\sqrt{u'^2}/U_1$ distribution over the depth at the plan $z/W=0.36$ for the condition of $F_1=3.11$ and $\alpha=0.25$.

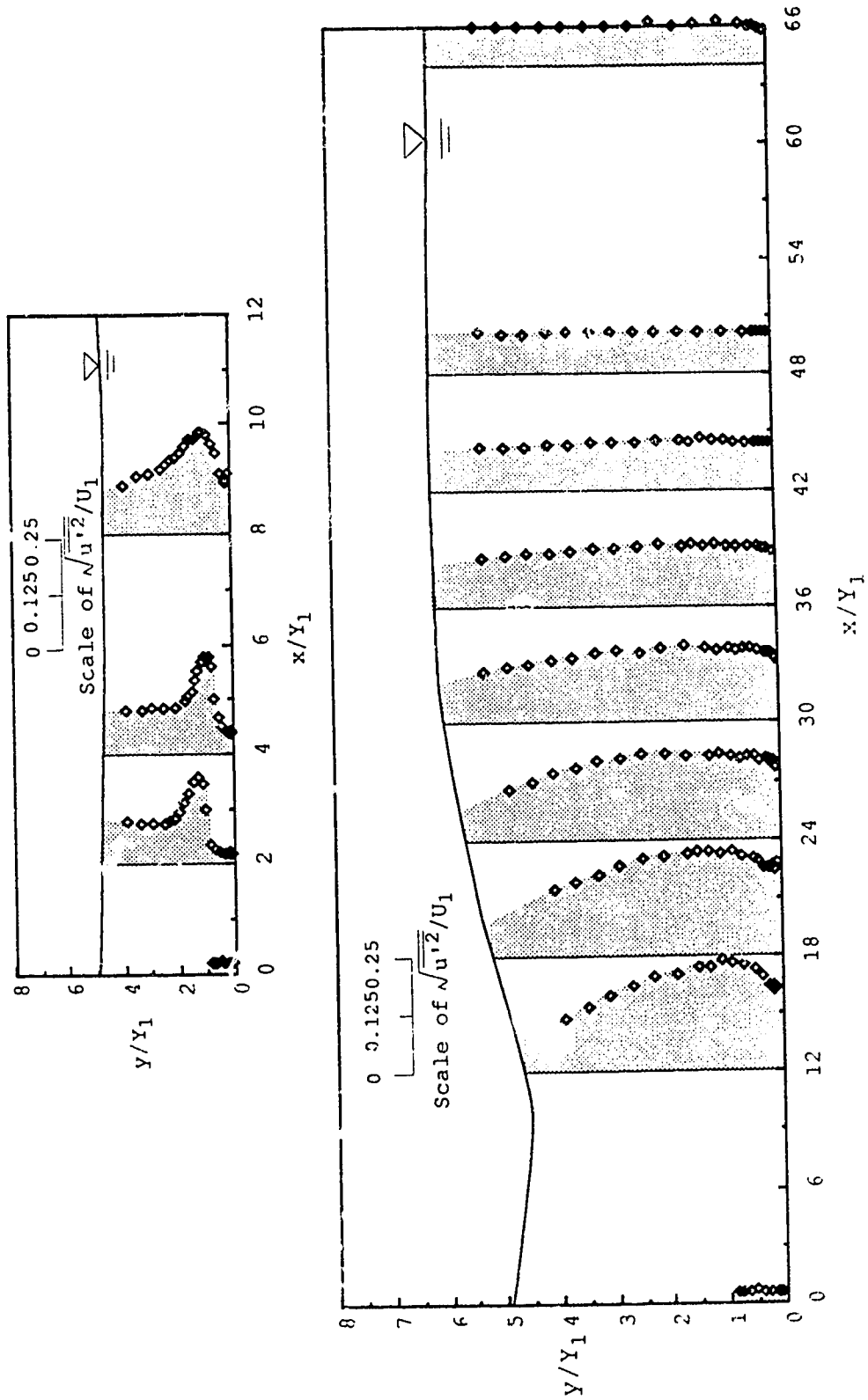


Figure 37. $\sqrt{u'^2}/U_1$ distribution over the depth at the plane of $z/W=0.36$ for the condition of $F_1=3.20$ and $S=0.53$.

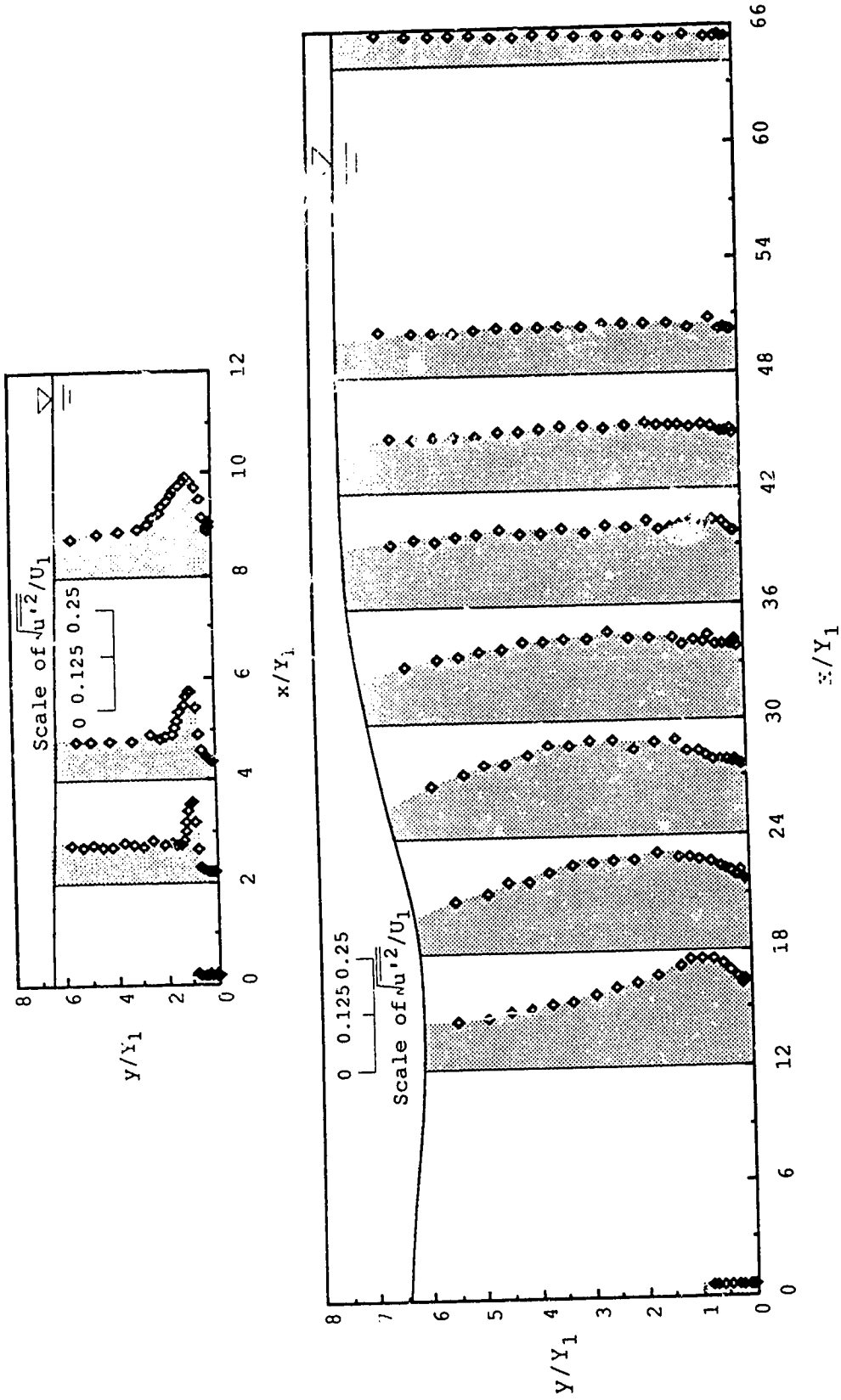


Figure 38. $\sqrt{u'^2}/U_1$ distribution over the depth at the plane of $z/W=0.36$ for the condition of $F_1=3.19$ and $S=0.85$.

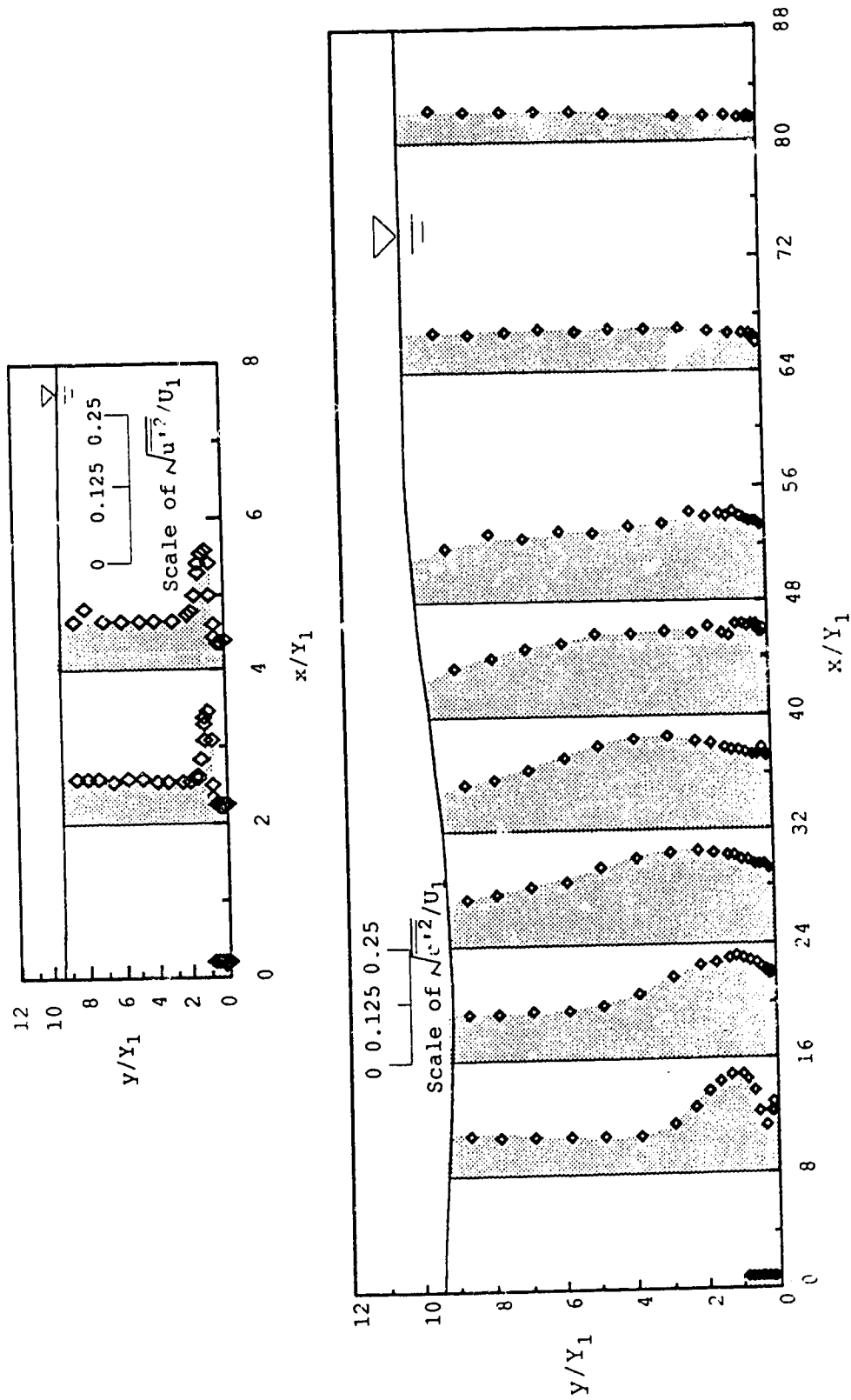


Figure 39. $\sqrt{u'^2}/U_1$ distribution over the depth at the plane of $z/W=0.36$ for the condition of $F_1=...01$ and $S=1.69$.

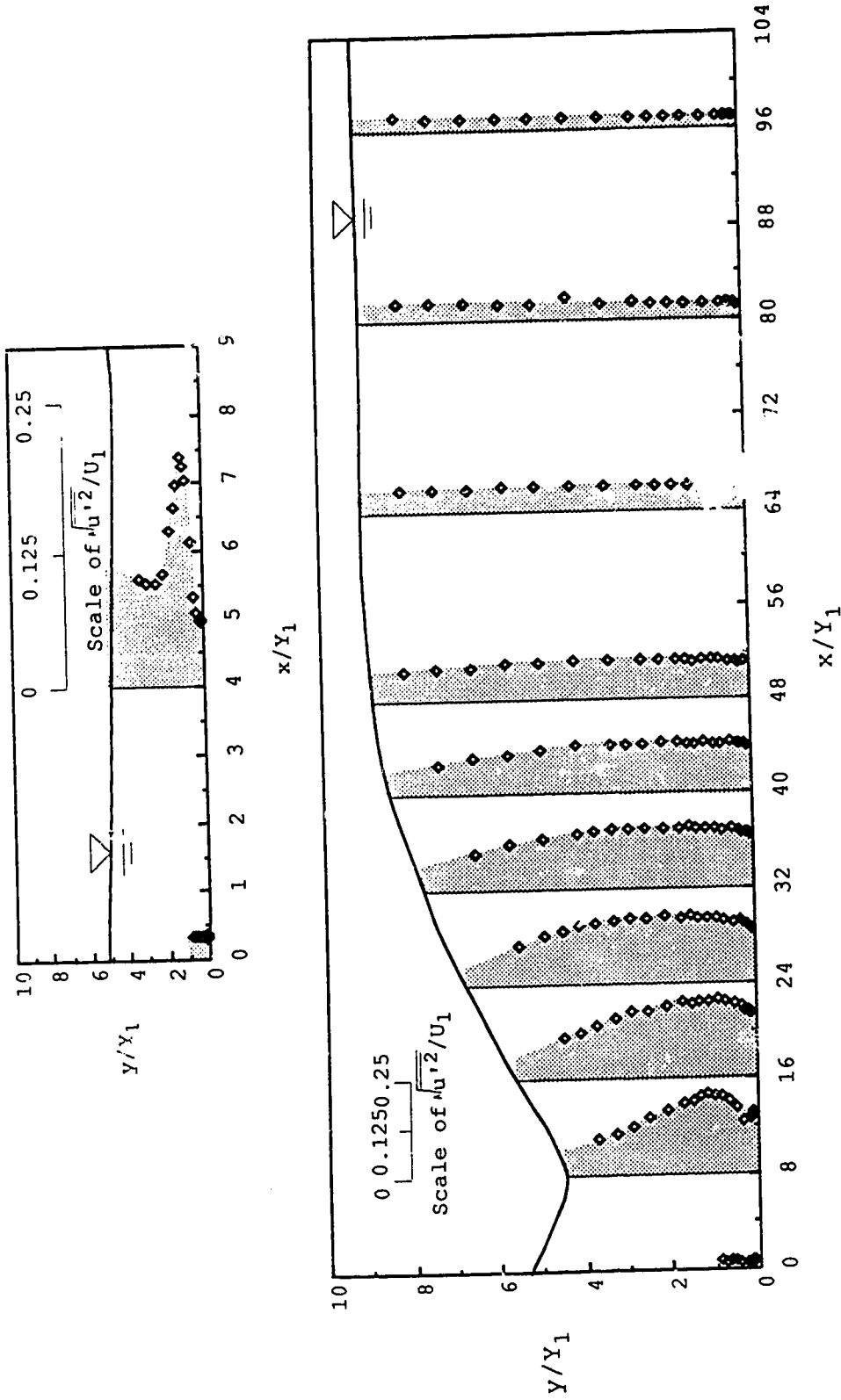


Figure 40. $\sqrt{u'^2}/U_1$ distribution over the depth at the plane of $z/W=0.36$ for the condition of $F_1=5.61$ and $S=0.22$.

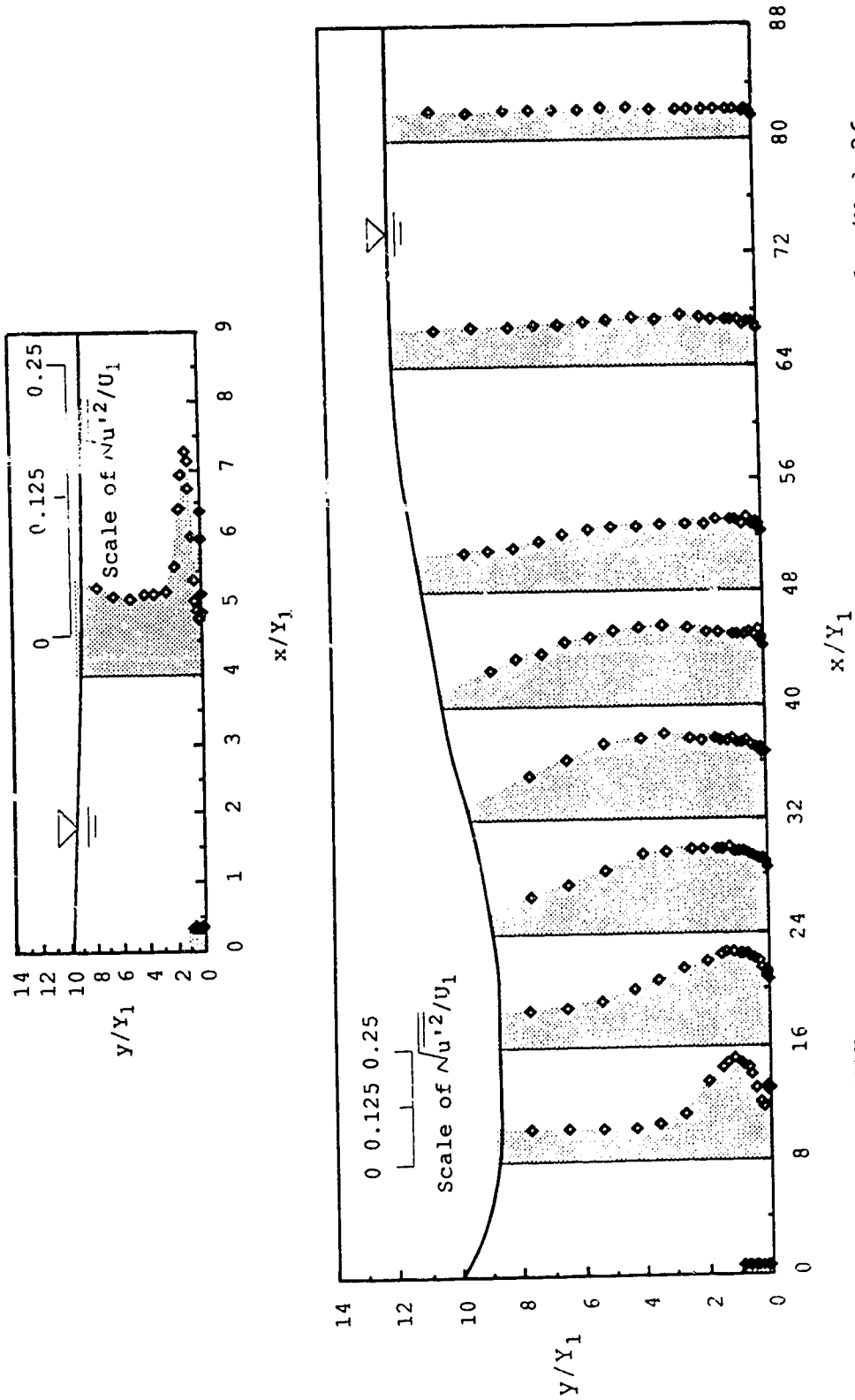


Figure 41. $\sqrt{u'^2}/U_1$ distribution over the depth at the plane of $z/W=0.36$ for the condition of $F_1=5.49$ and $S=0.63$.

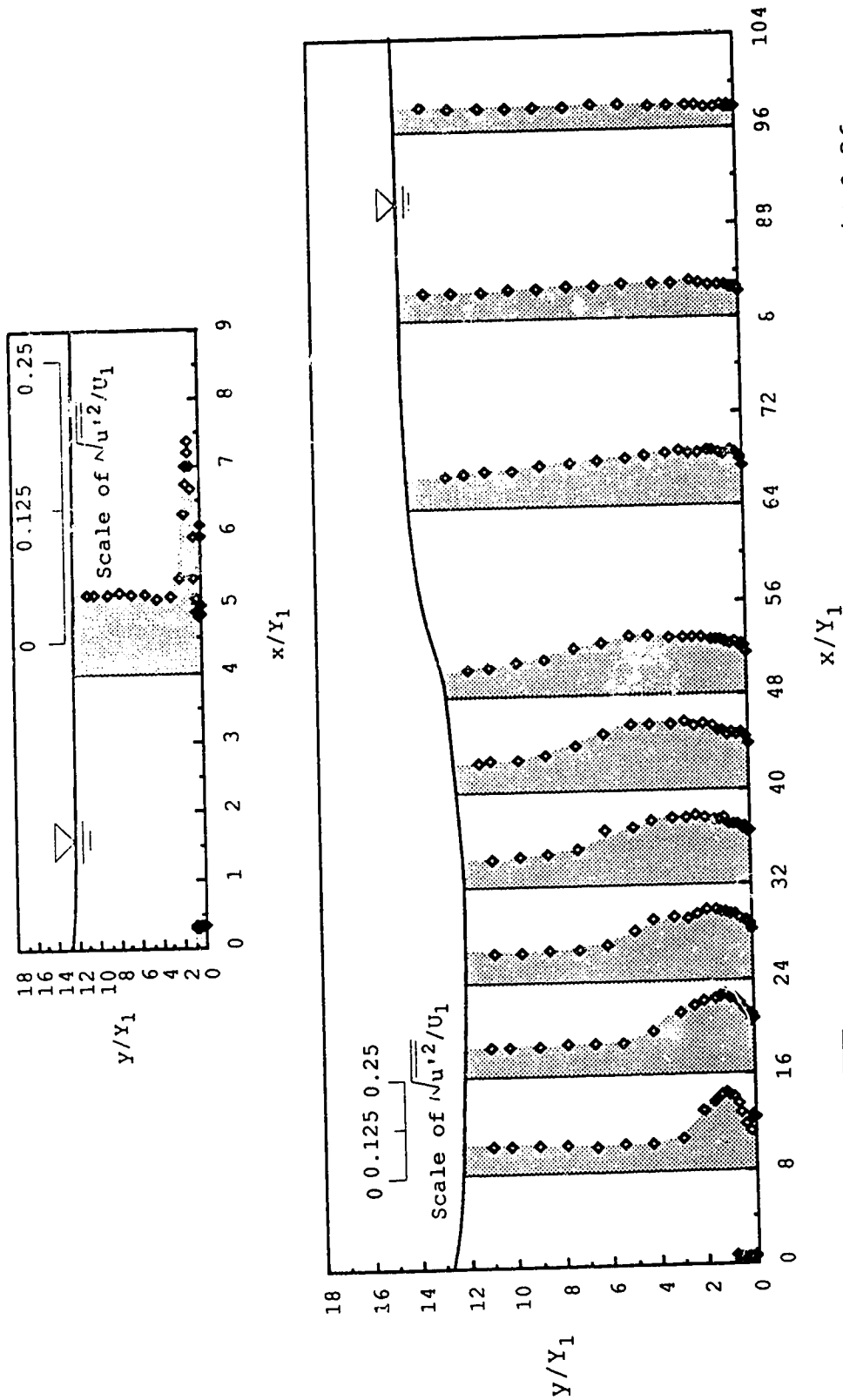


Figure 42. $\sqrt{u'^2}/U_1$ distribution over the depth at the plane of $z/W=0.36$ for the condition of $F_1=5.43$ and $S=1.01$.

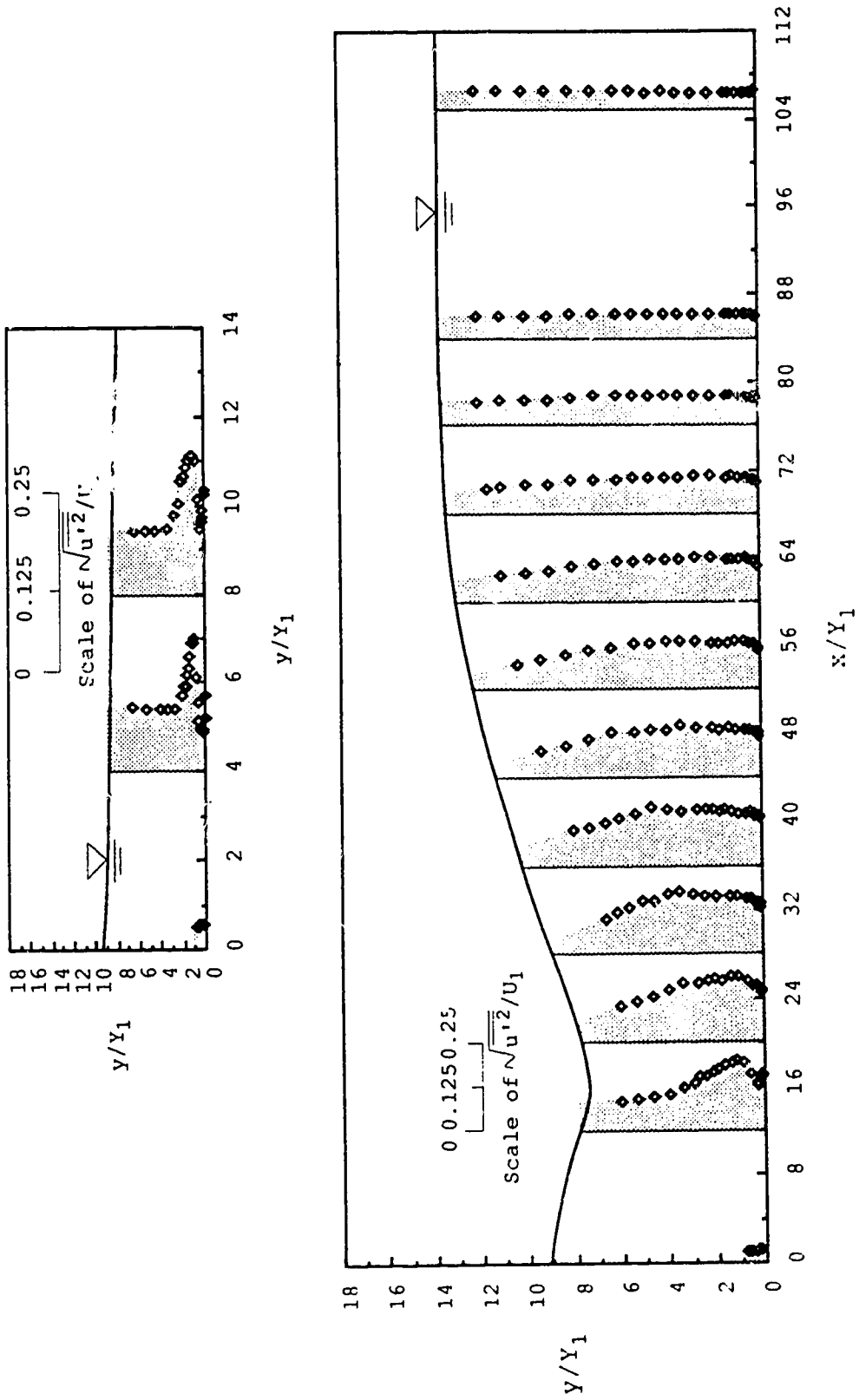


Figure 43. $\sqrt{u'^2}/U_1$ distribution over the depth at the plane of $z/W=0.36$ for $F_1=8.19$ and $S=0.24$.

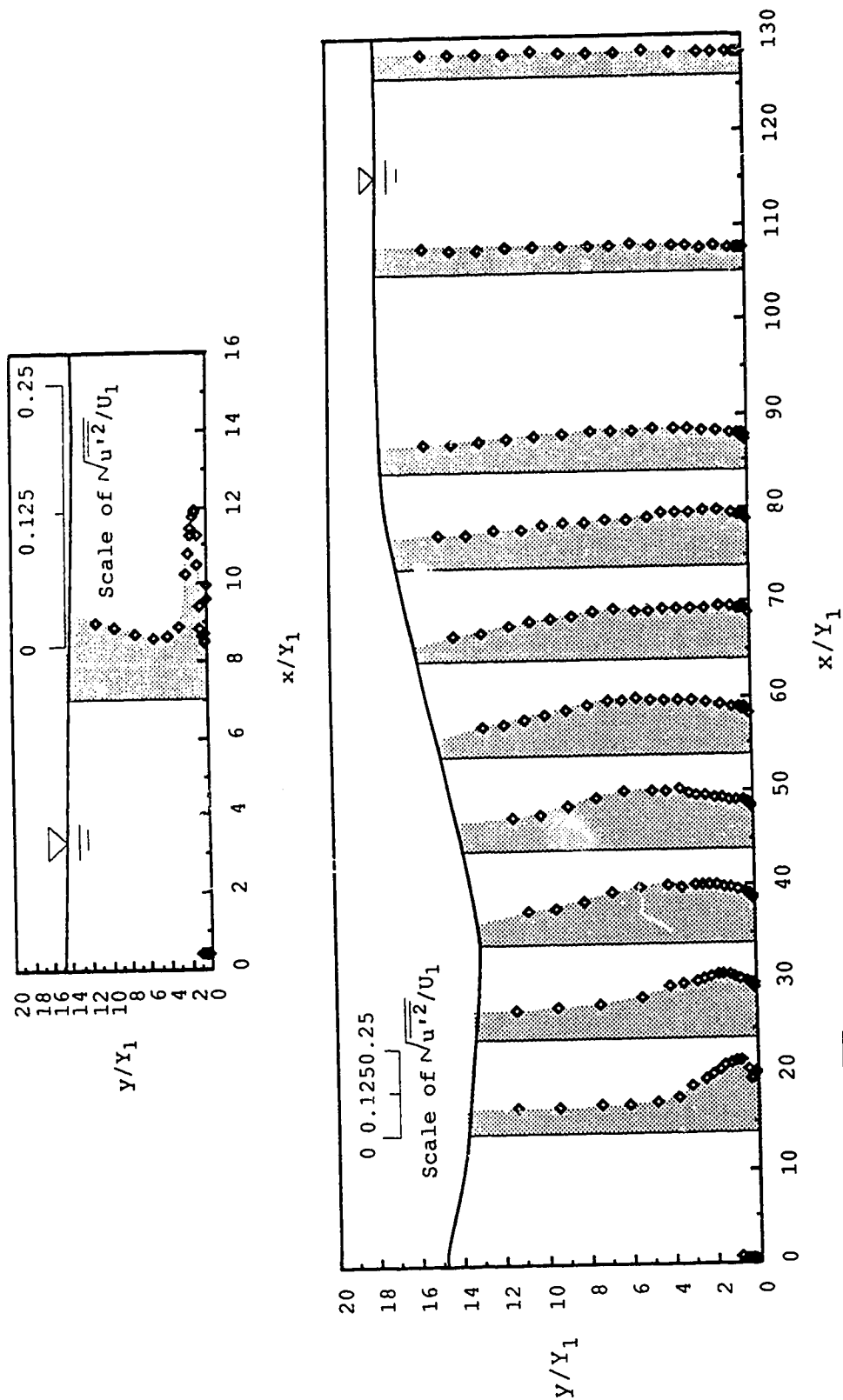


Figure 44. $\sqrt{u'^2}/U_1$ distribution over the depth at the plane of $z/W=0.36$ for the condition of $F_1=8$ and $S=0.52$.

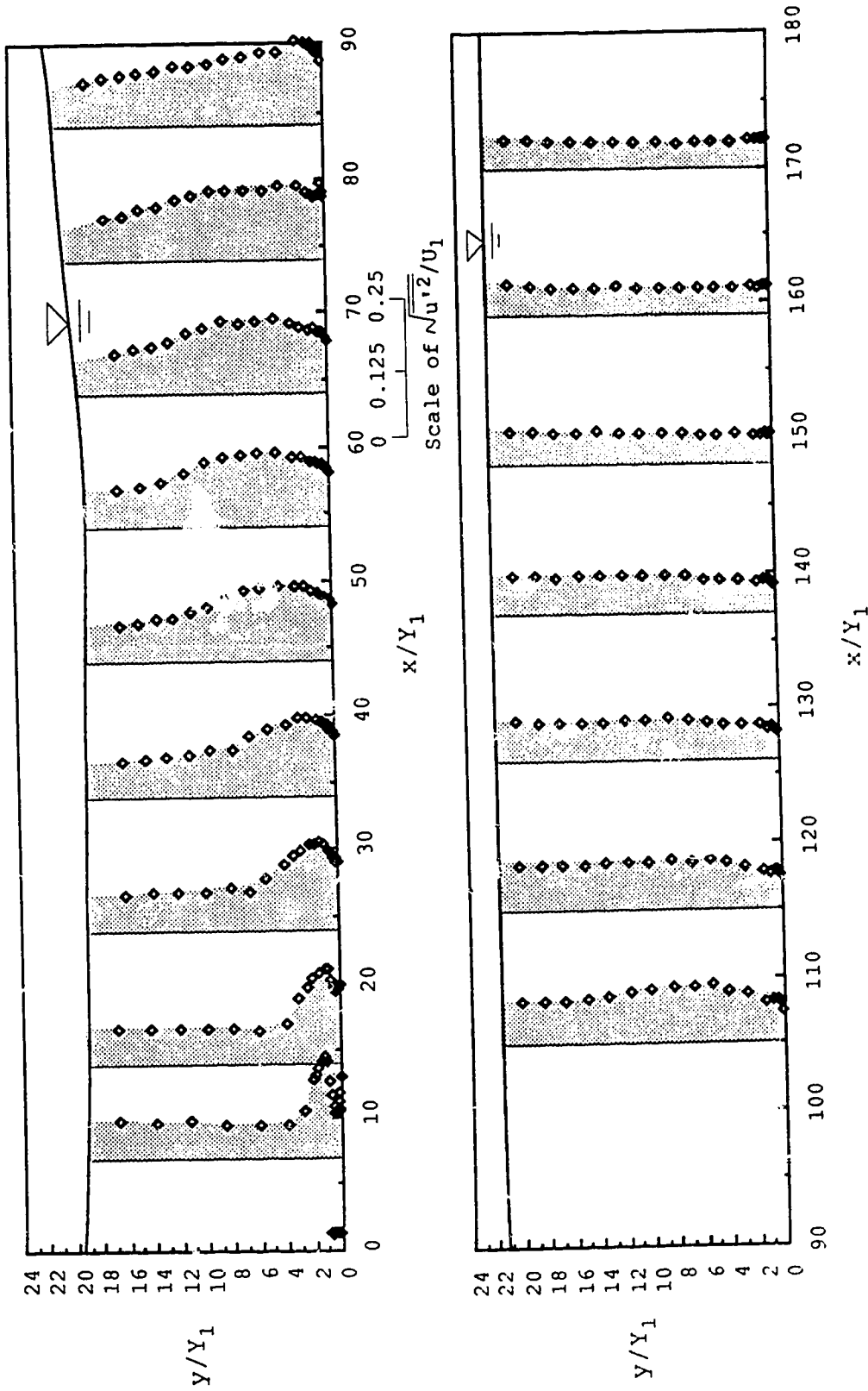


Figure 45. $\sqrt{u'^2}/U_1$ distribution over the depth at the plane of $z/W=0.36$ for the condition of $F_1=8.11$ and $S=1.00$.

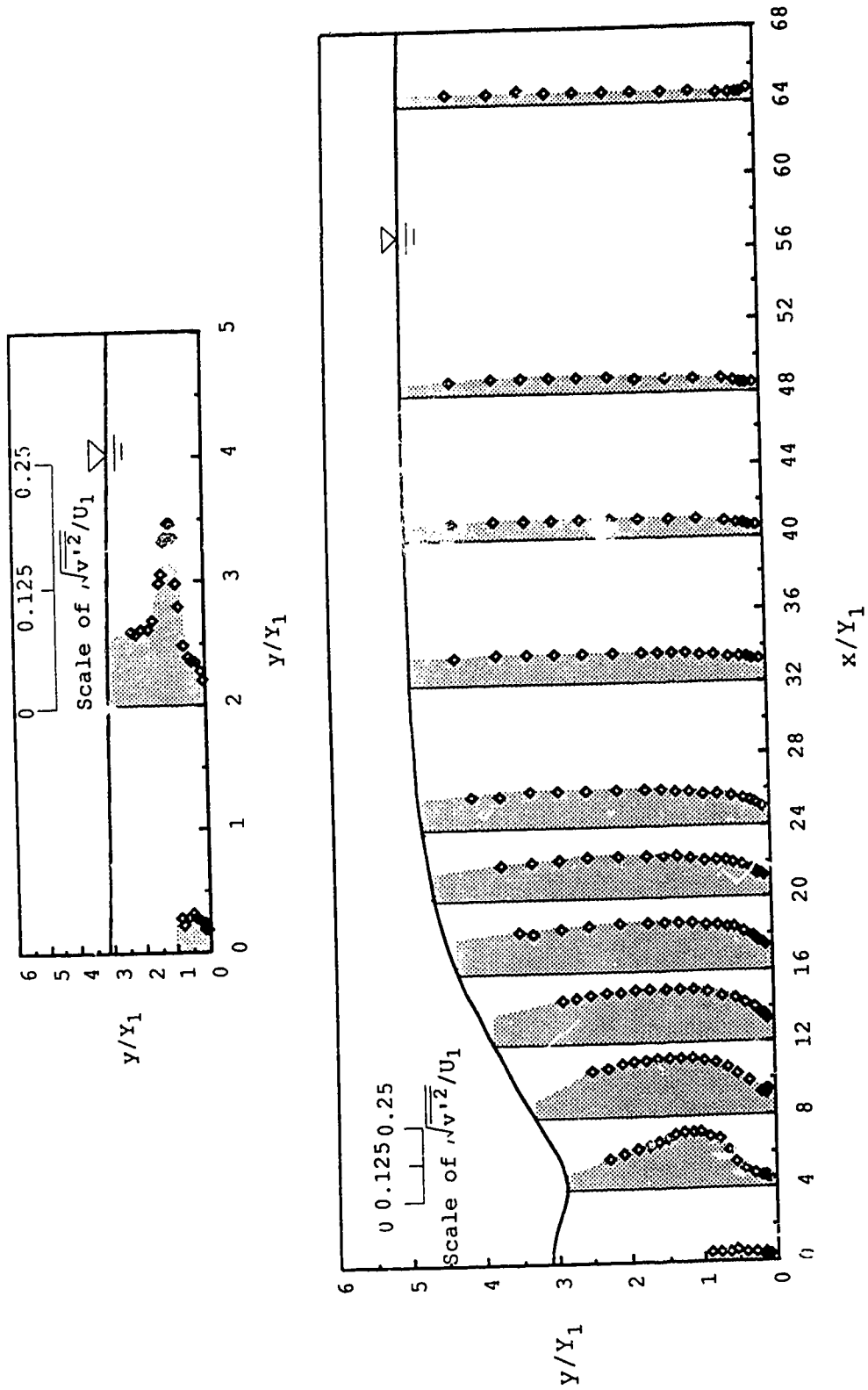


Figure 46. $\sqrt{v'^2}/U_1$ distribution over the depth at the plane of $z/W=0.36$ for the condition of $F_1=3.11$ and $S=0.26$.

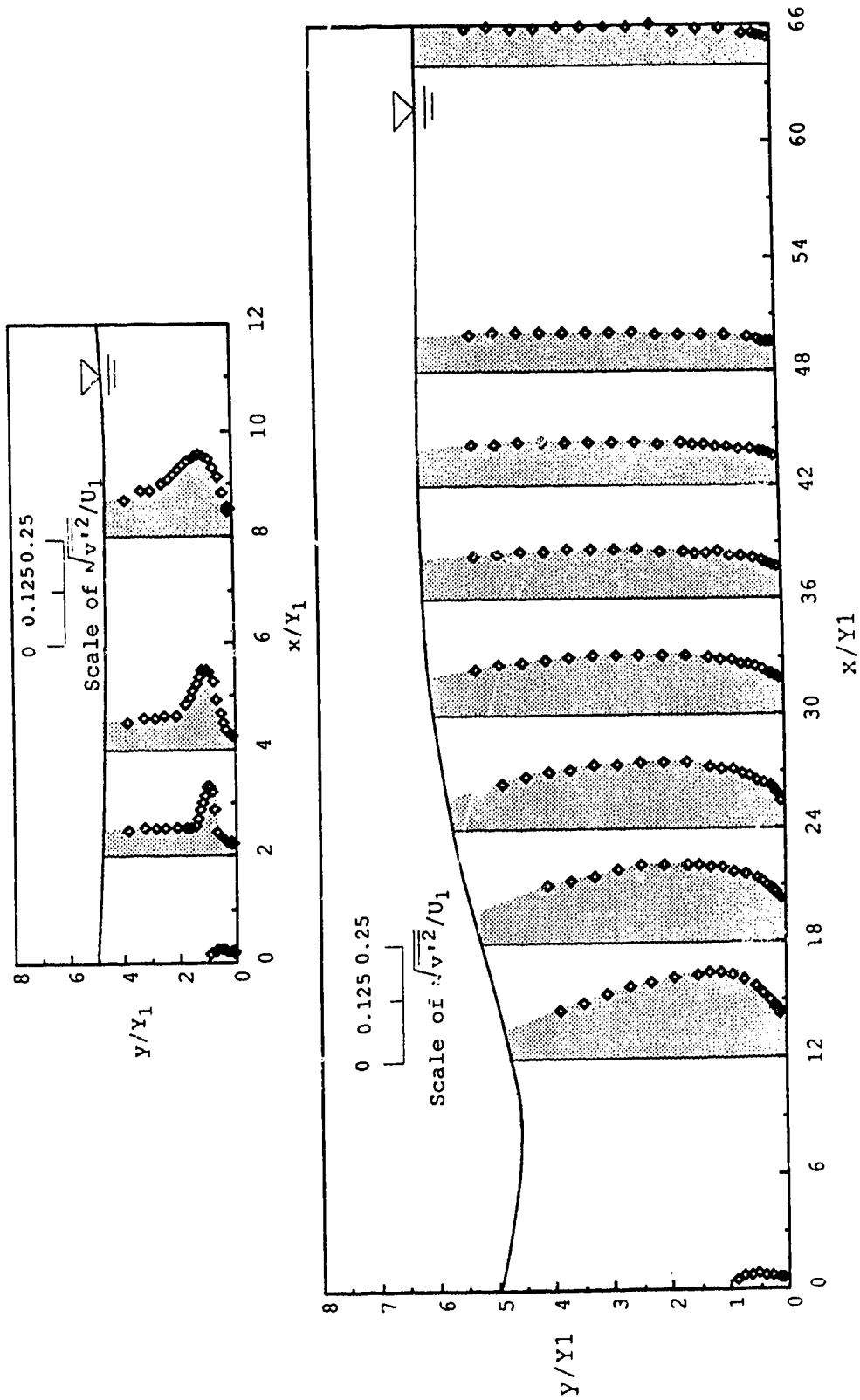


Figure 47. $\sqrt{v'^2}/U_1$ distribution over the depth at the plane of $z/W = 0.5$ for the condition of $F_1 = 3.20$ and $S = 0.53$.

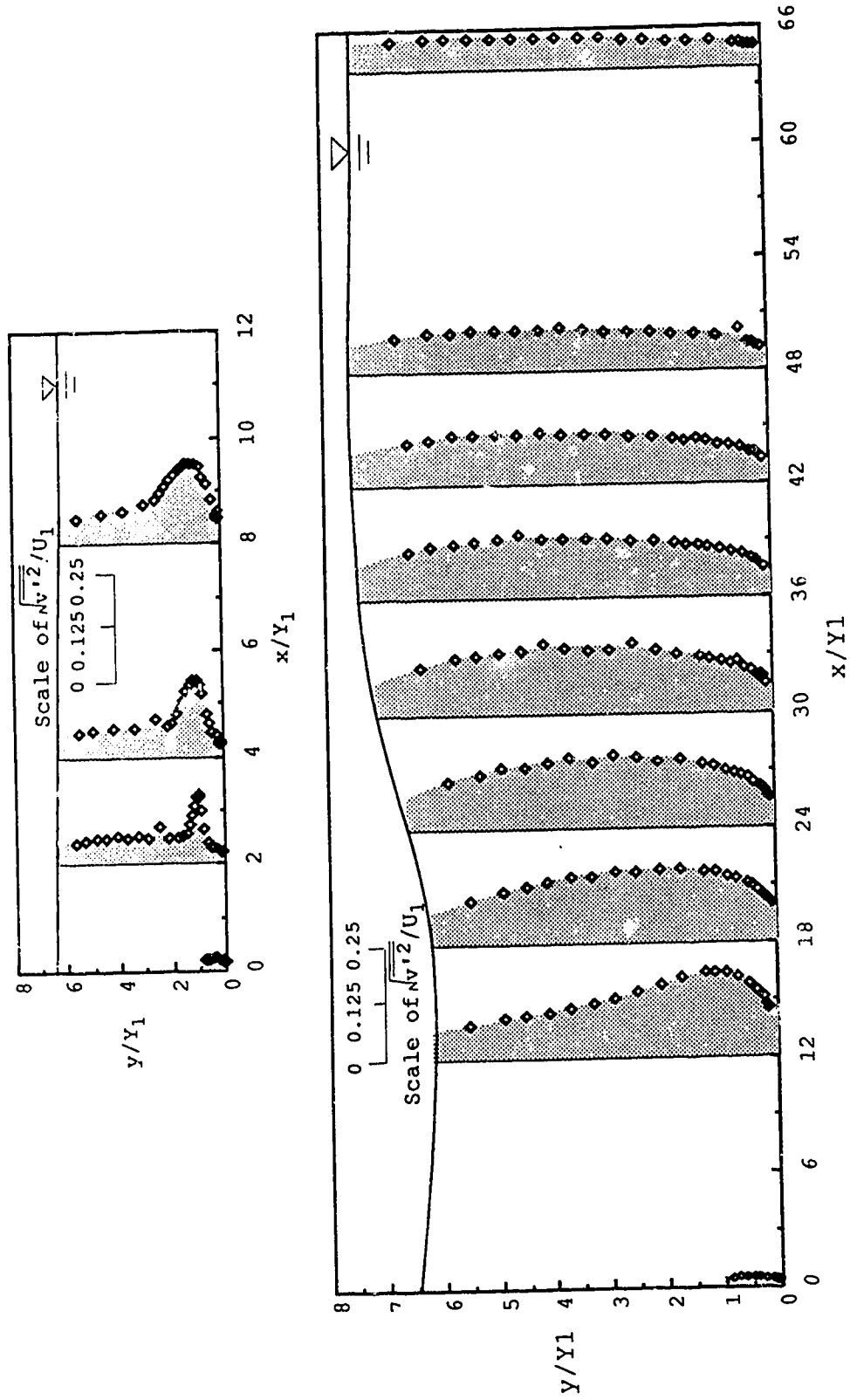


Figure 48. $\sqrt{v'^2}/U_1$ distribution over the depth at the plane of $z/W=0.36$ for the condition of $F_1=3.19$ and $S=0.85$.

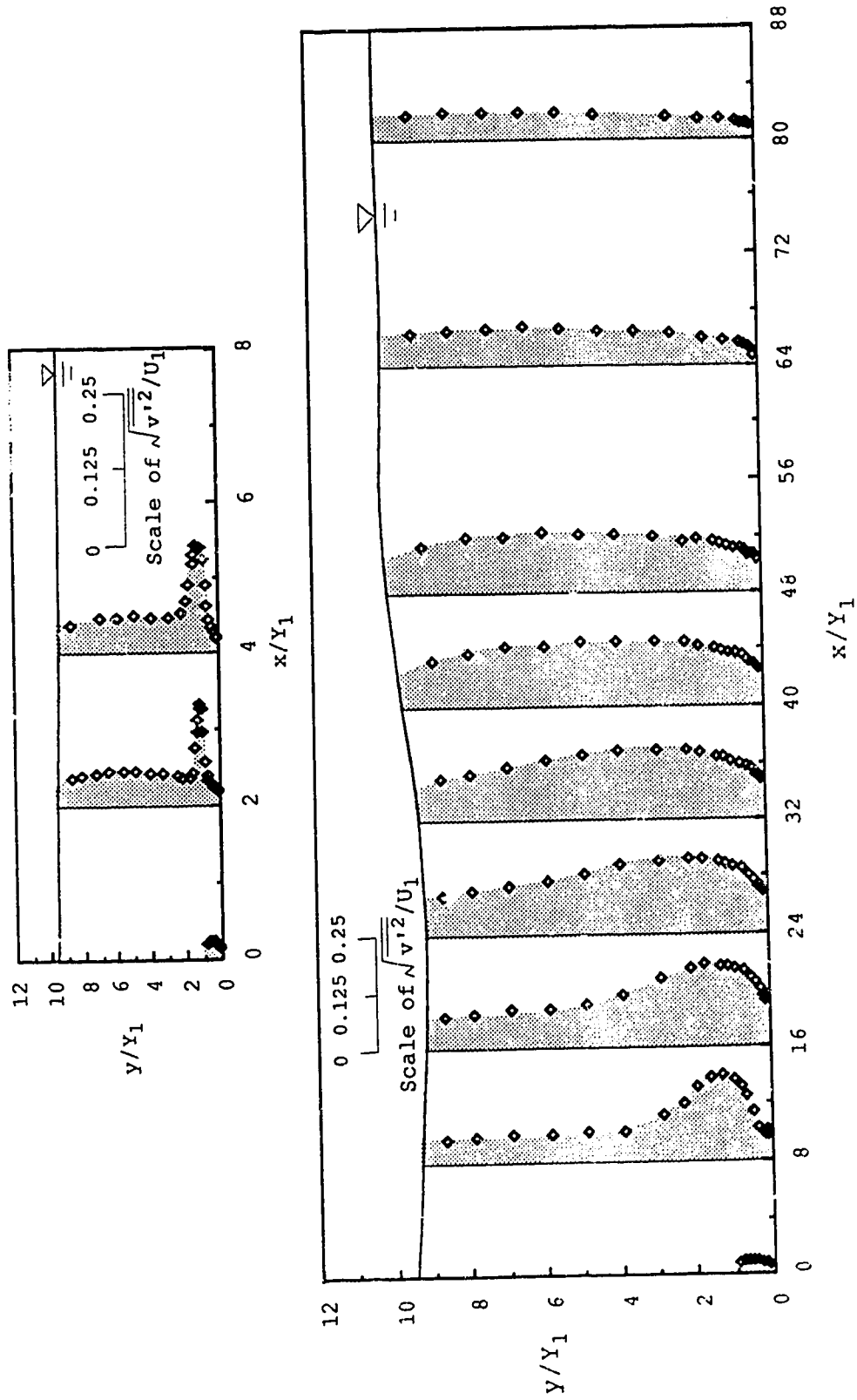


Figure 49. $\sqrt{v'^2}/U_1$ distribution over the depth at the plane of $z/W=0.36$ for the condition of $F_1=3.01$ and $S=1.69$.

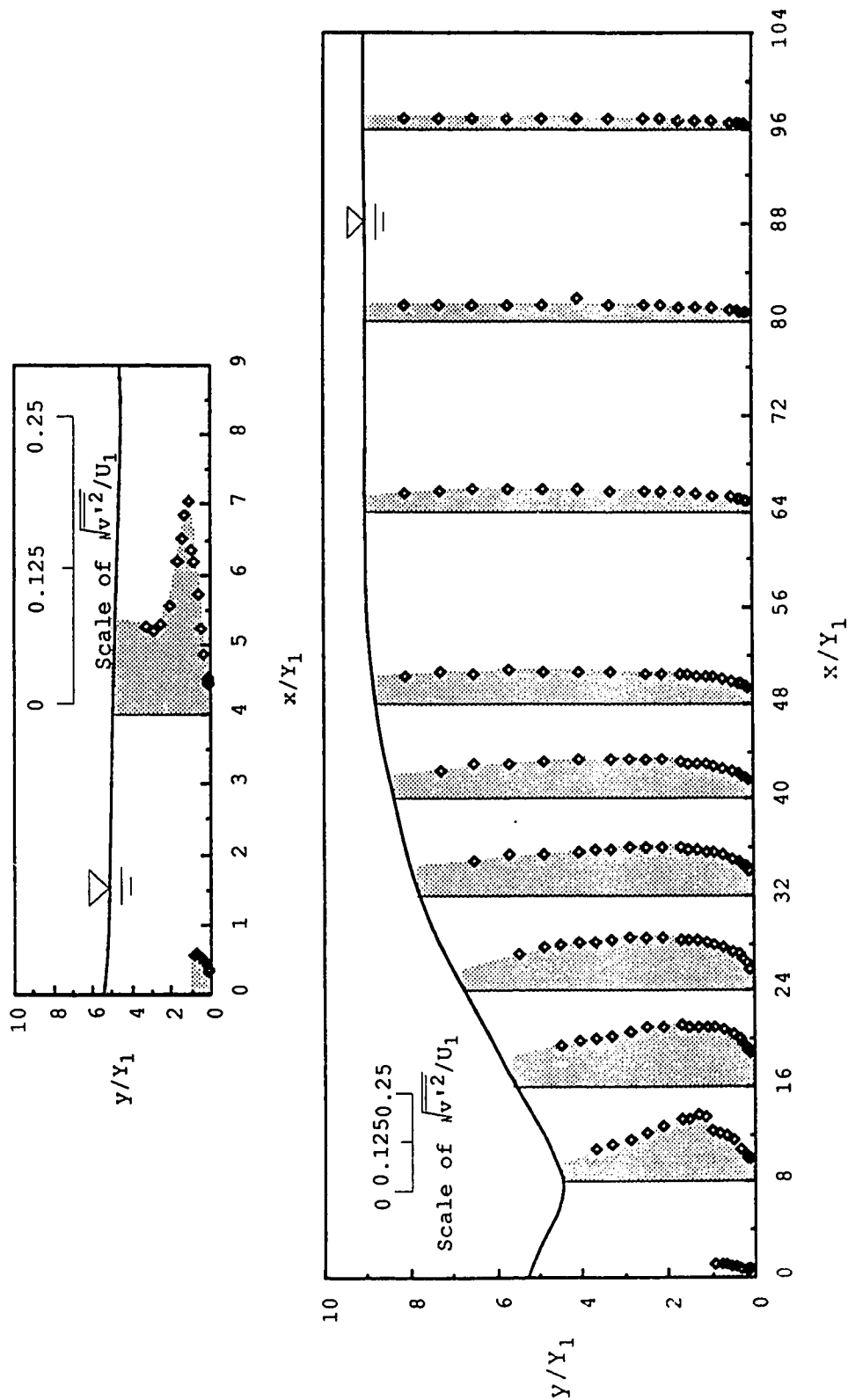


Figure 50. $\sqrt{v'^2}/U_1$ distribution over the depth at the plane of $z/W=0.36$ for the condition of $F_1=5.61$ and $S=0.22$.

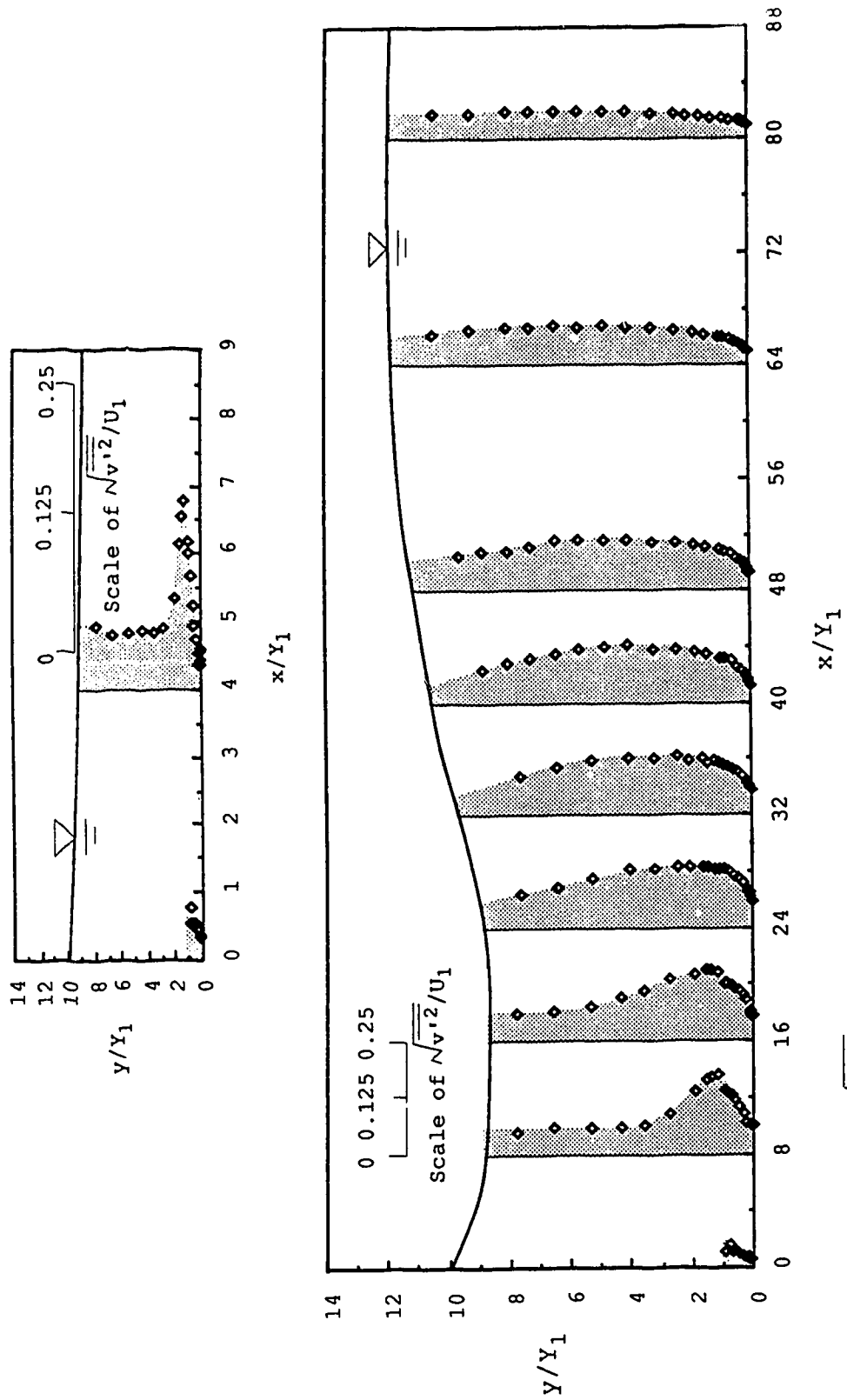


Figure 51. $\sqrt{v'^2}/U_1$ distribution over the depth at the plane of $z/W=0.36$ for the condition of $F_1=5.49$ and $S=0.63$.

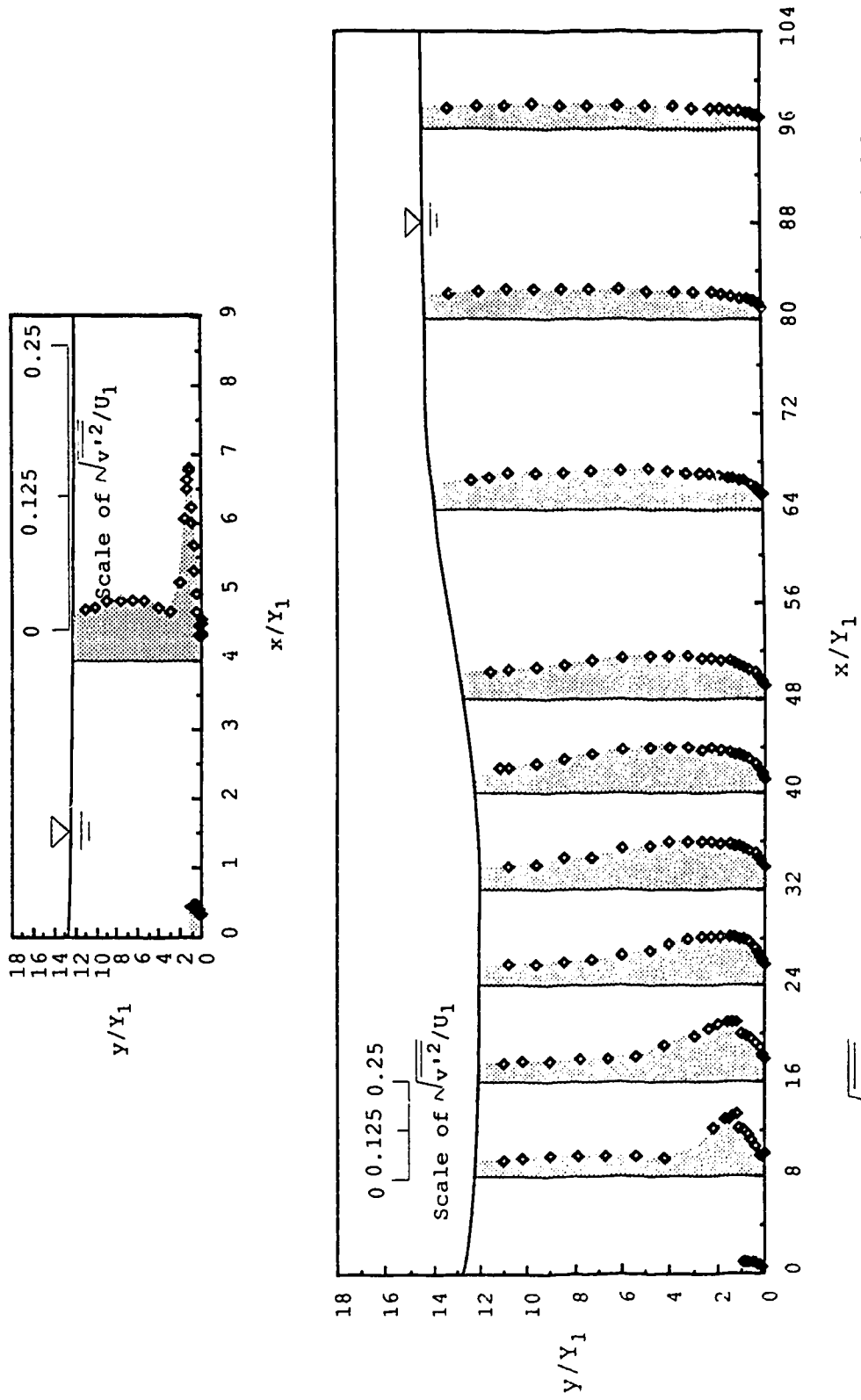


Figure 52. $\sqrt{v'^2}/U_1$ distribution over the depth at the plane of $z/W=0.36$ for the condition of $F_1=5.43$ and $S=1.01$.

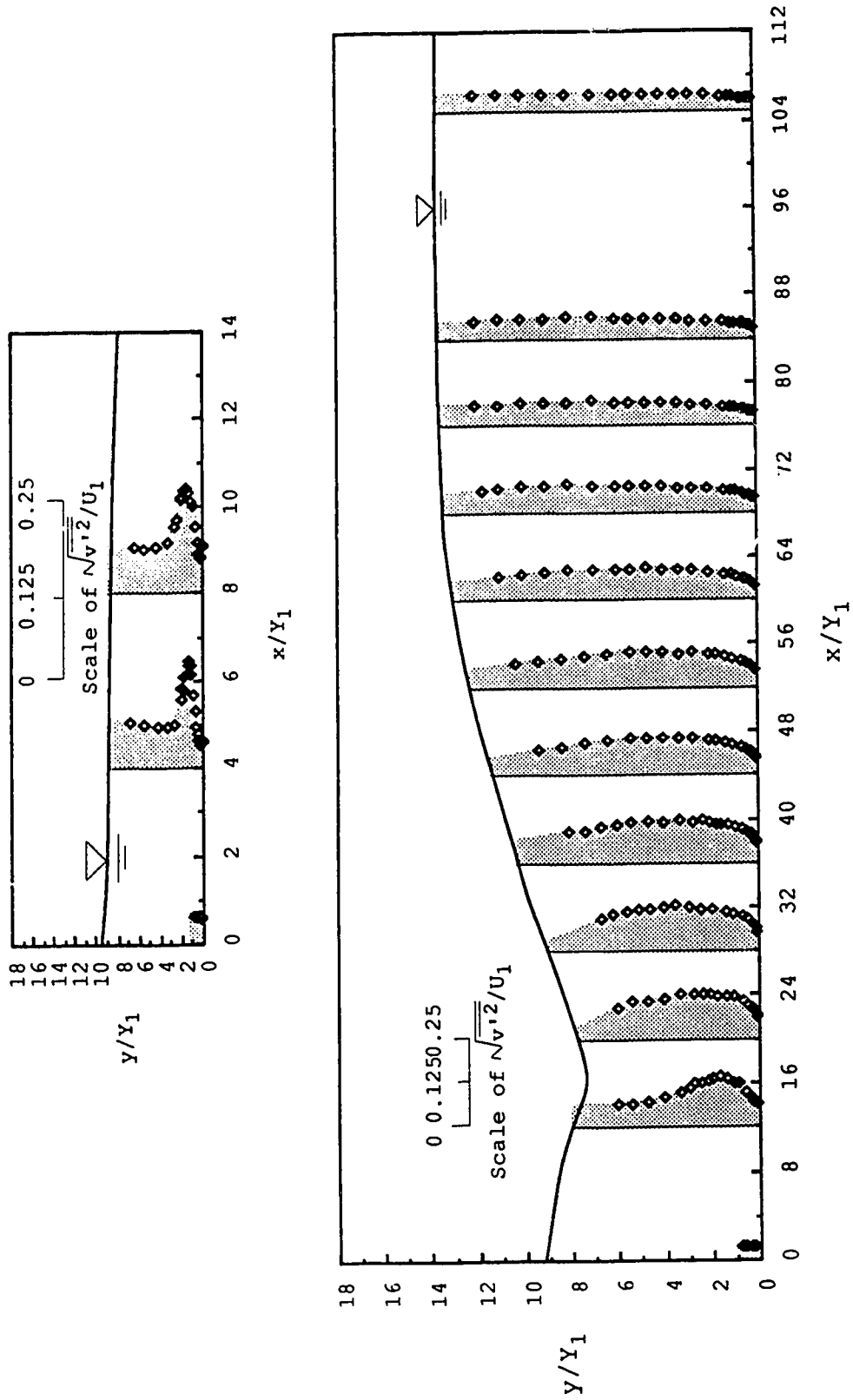


Figure 53. $\sqrt{v'^2}/U_1$ distribution over the depth at the plane of $z/W=0.36$ for $F_1=8.19$ and $S=0.24$.

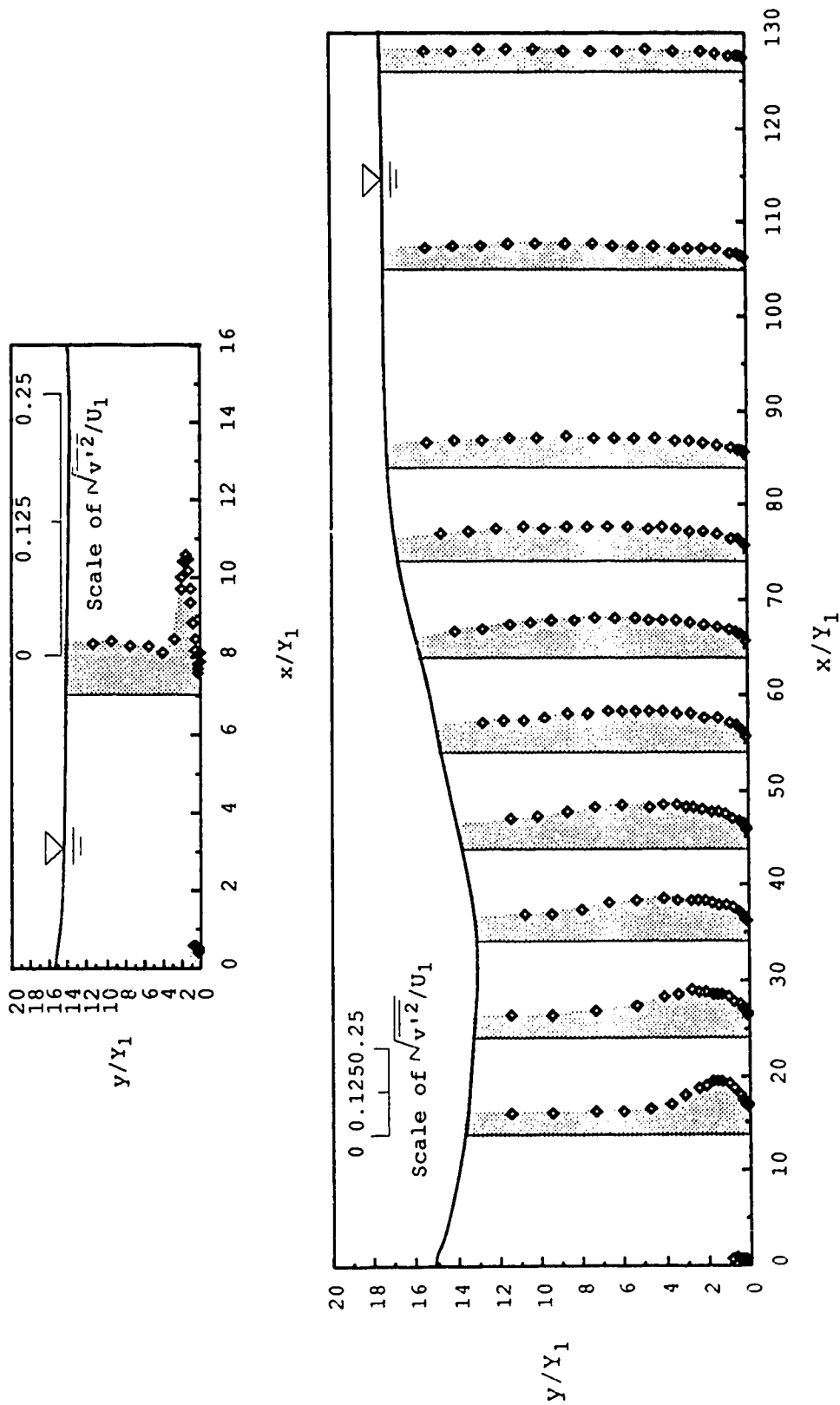


Figure 54. $\sqrt{v'^2}/U_1$ distribution over the depth at the plane of $z/W=0.36$ for the condition of $F_1=8$ and $S=0.62$.

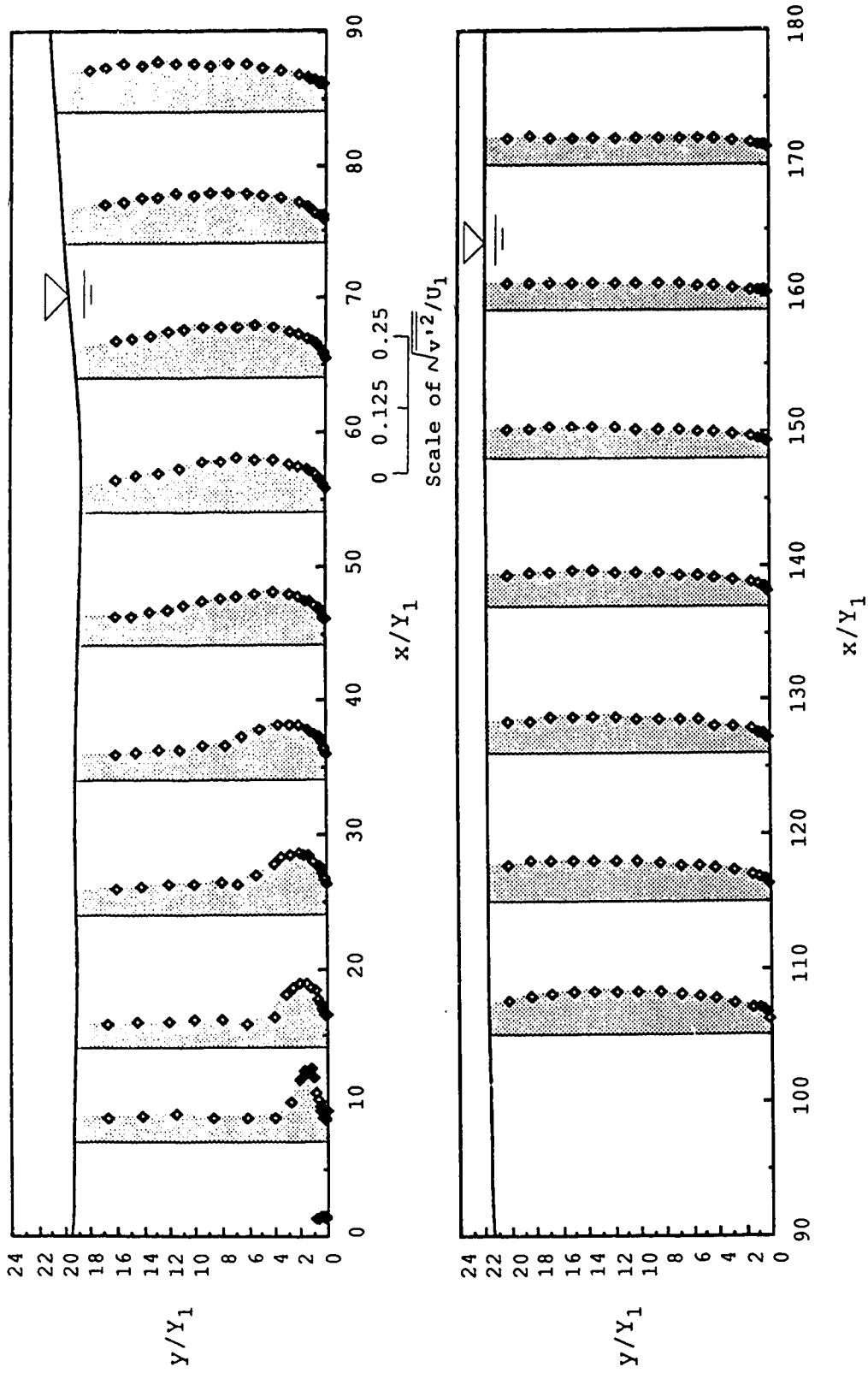


Figure 55. $\sqrt{v'^2}/U_1$ distribution over the depth at the plane of $z/W=0.36$ for the condition of $F_1=8.11$ and $S=1.00$.

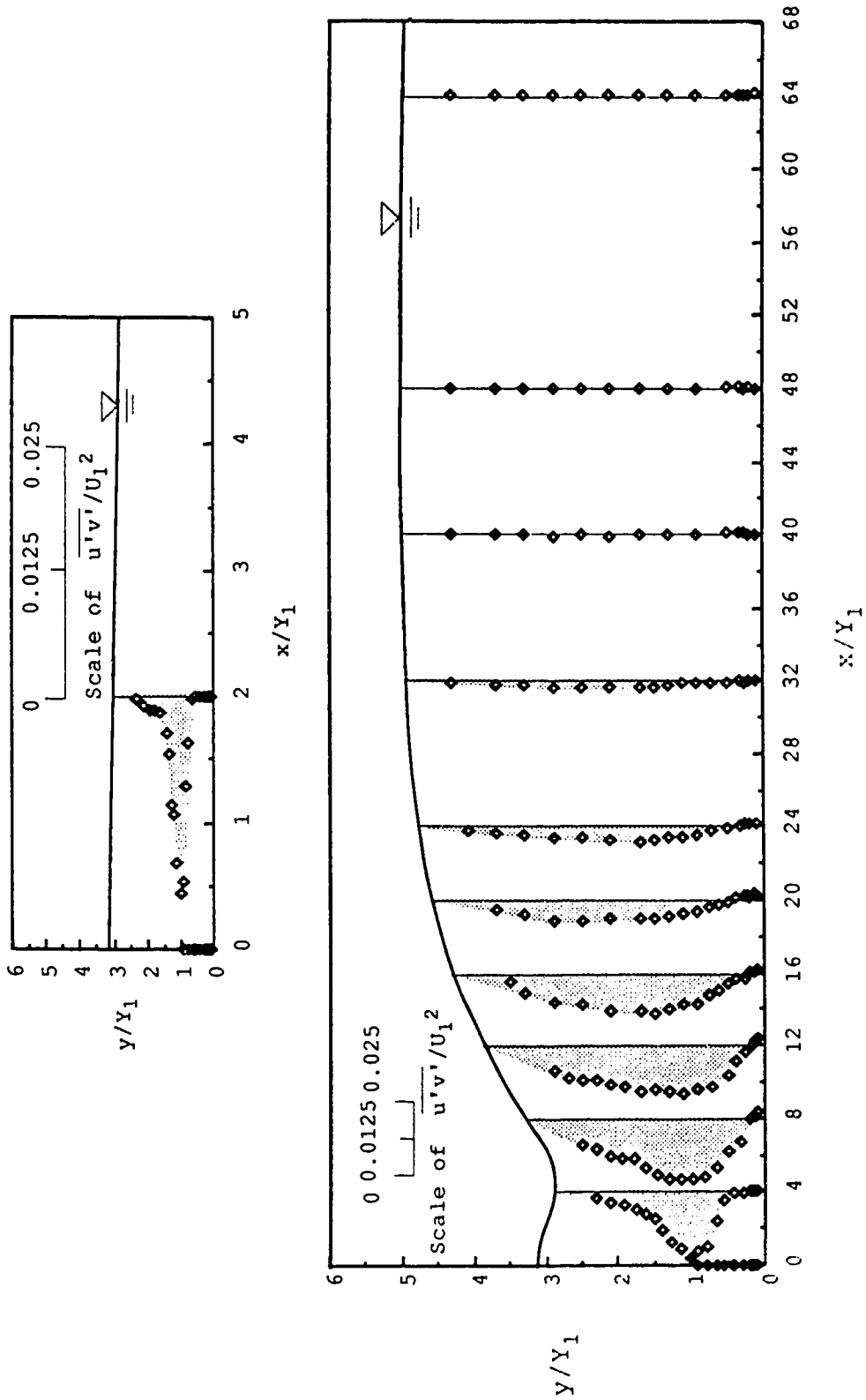


Figure 56. $\overline{u'v'}/U_1^2$ distribution over the depth at the plane of $z/W=0.36$ for the condition of $F_1=3.11$ and $S=0.26$.

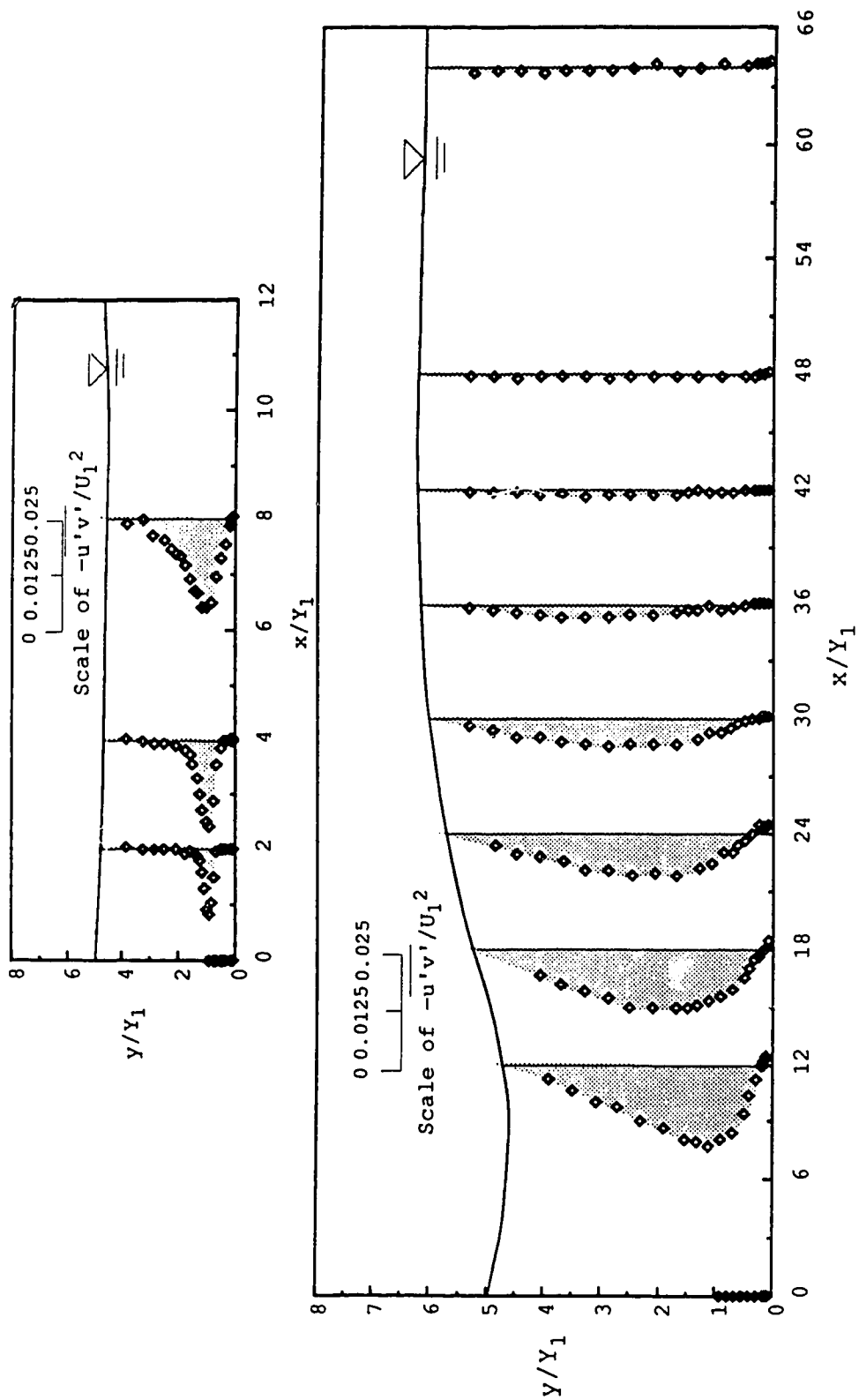


Figure 57. $-\overline{u'v'}/U_1^2$ distribution over the depth at the plane of $z/W=0.36$ for the condition of $F_1=3.20$ and $S=0.53$.

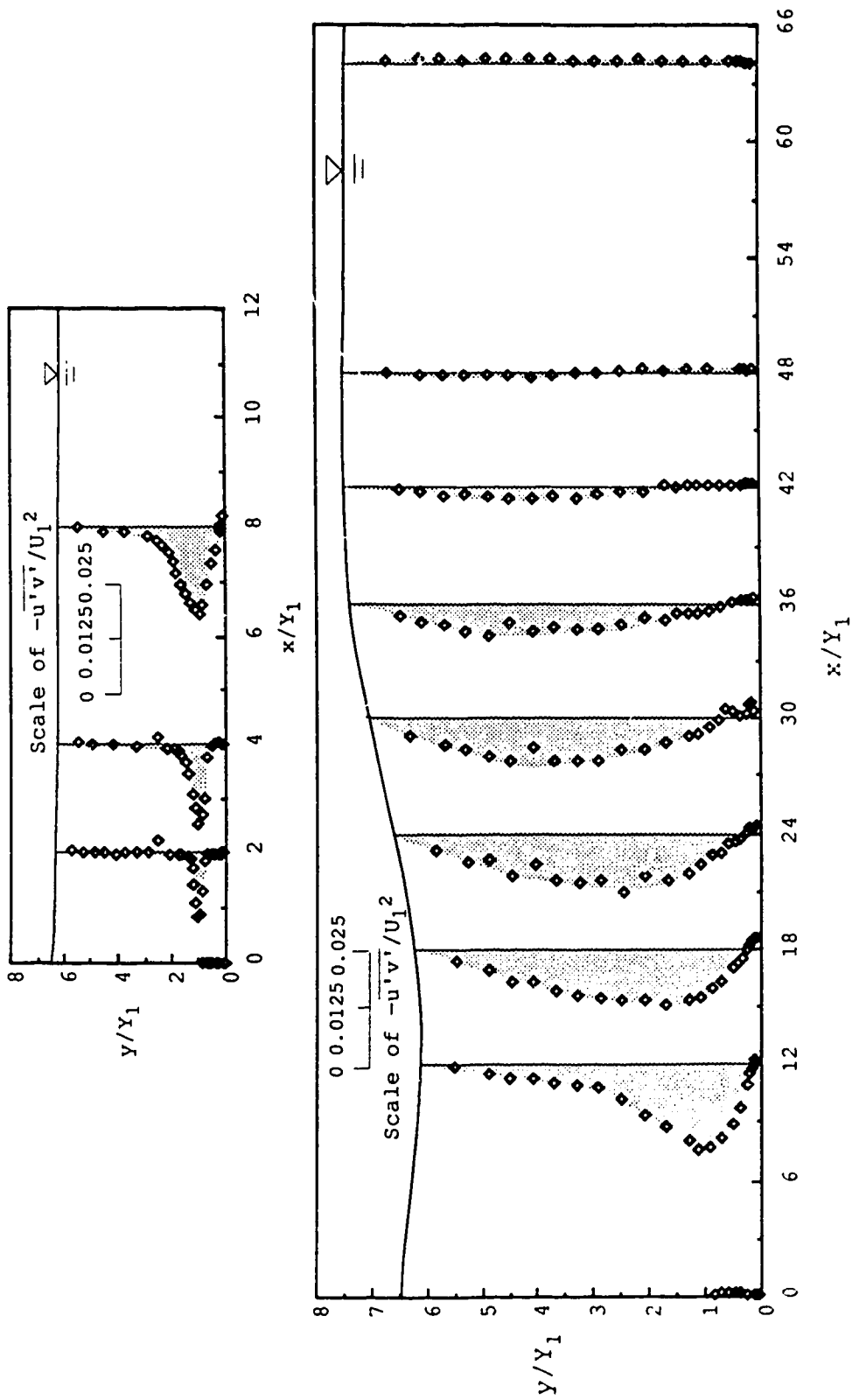


Figure 58. $-\overline{u'v'}/U_1^2$ distribution over the depth at the plane of $z/W=0.36$ for the condition of $F_1=3.19$ and $S=0.85$.

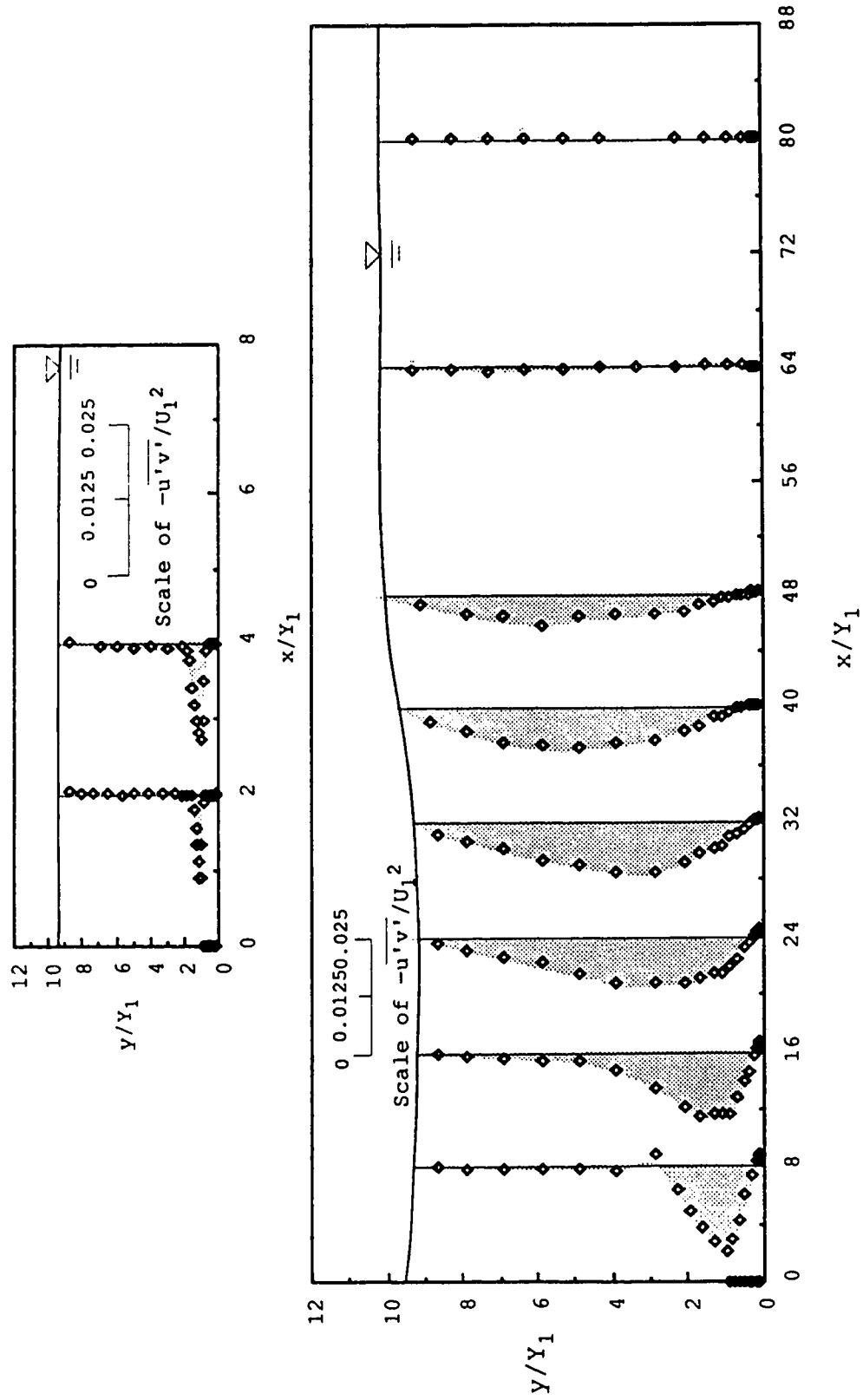


Figure 59. $-\overline{u'v'}/U_1^2$ distribution over the depth at the plane of $z/W=0.36$ for the condition of $F_1=3.01$ and $S=1.69$.

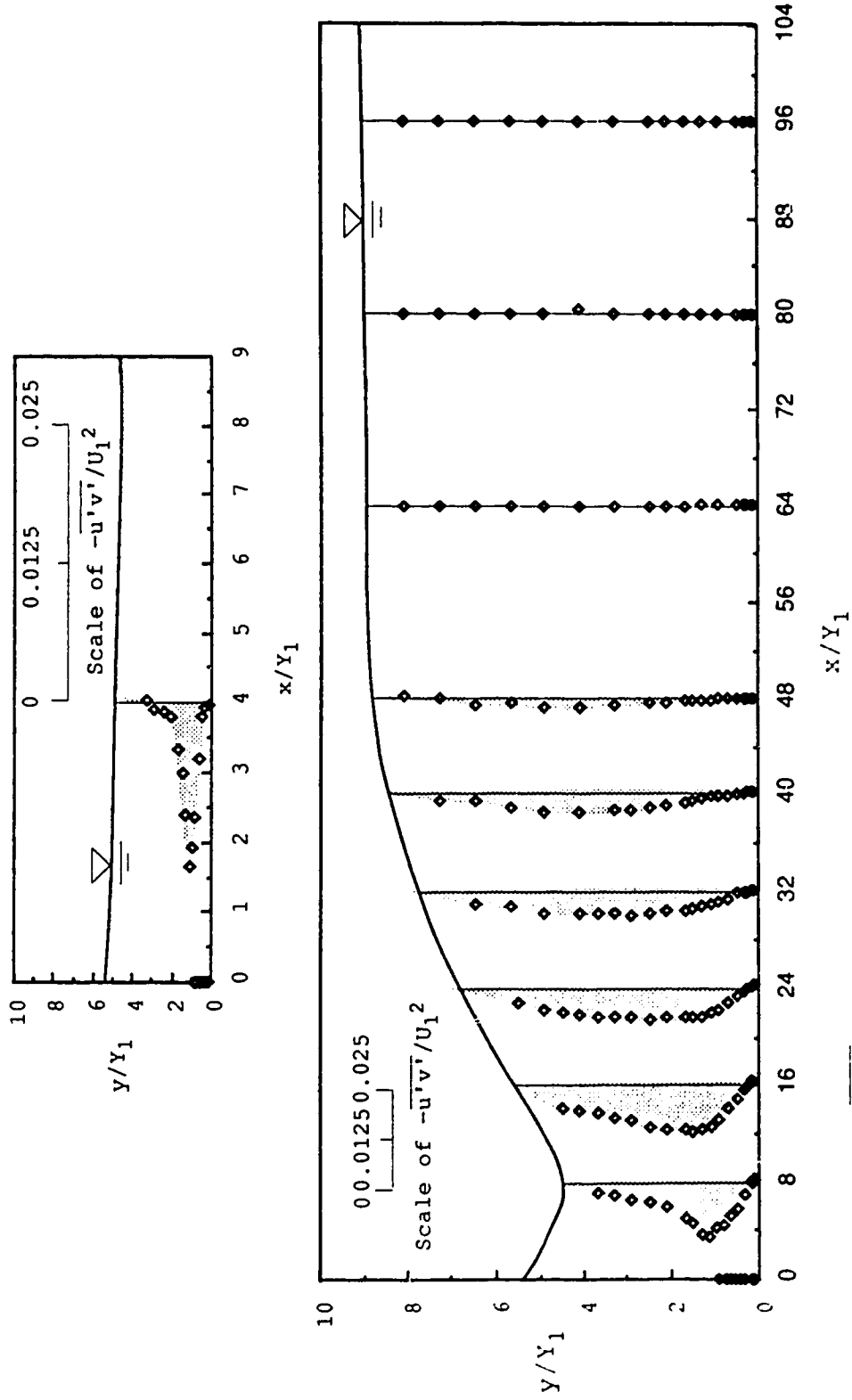


Figure 60. $-\overline{u'v'}/U_1^2$ distribution over the depth at the plane of $z/W=0.36$ for the condition of $F_1=5.61$ and $S=0.22$.

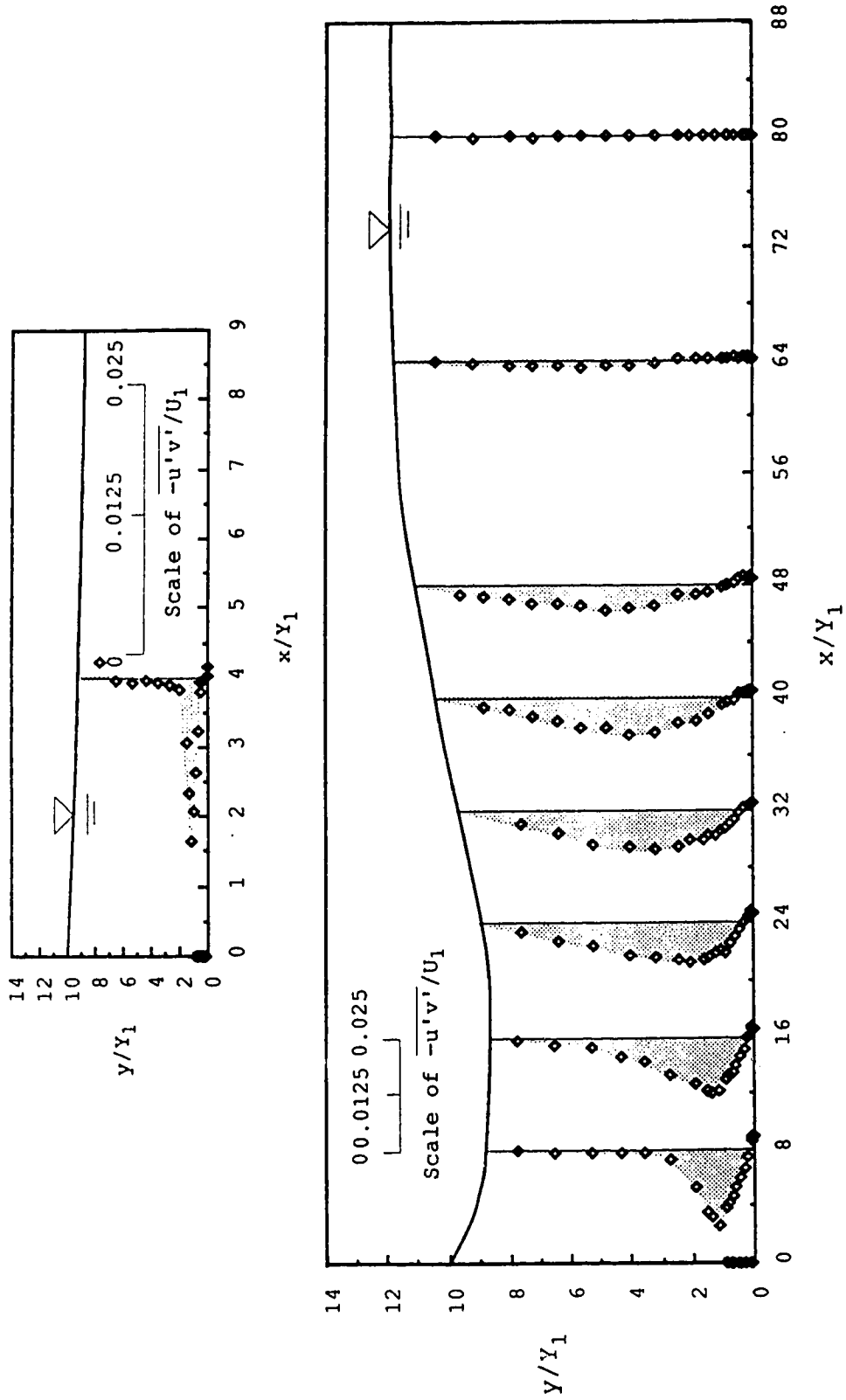


Figure 61. $-\overline{u'v'}/U_1^2$ distribution over the depth at the plane of $z/W=0.36$ for the condition of $F_1=5.49$ and $S=0.63$.

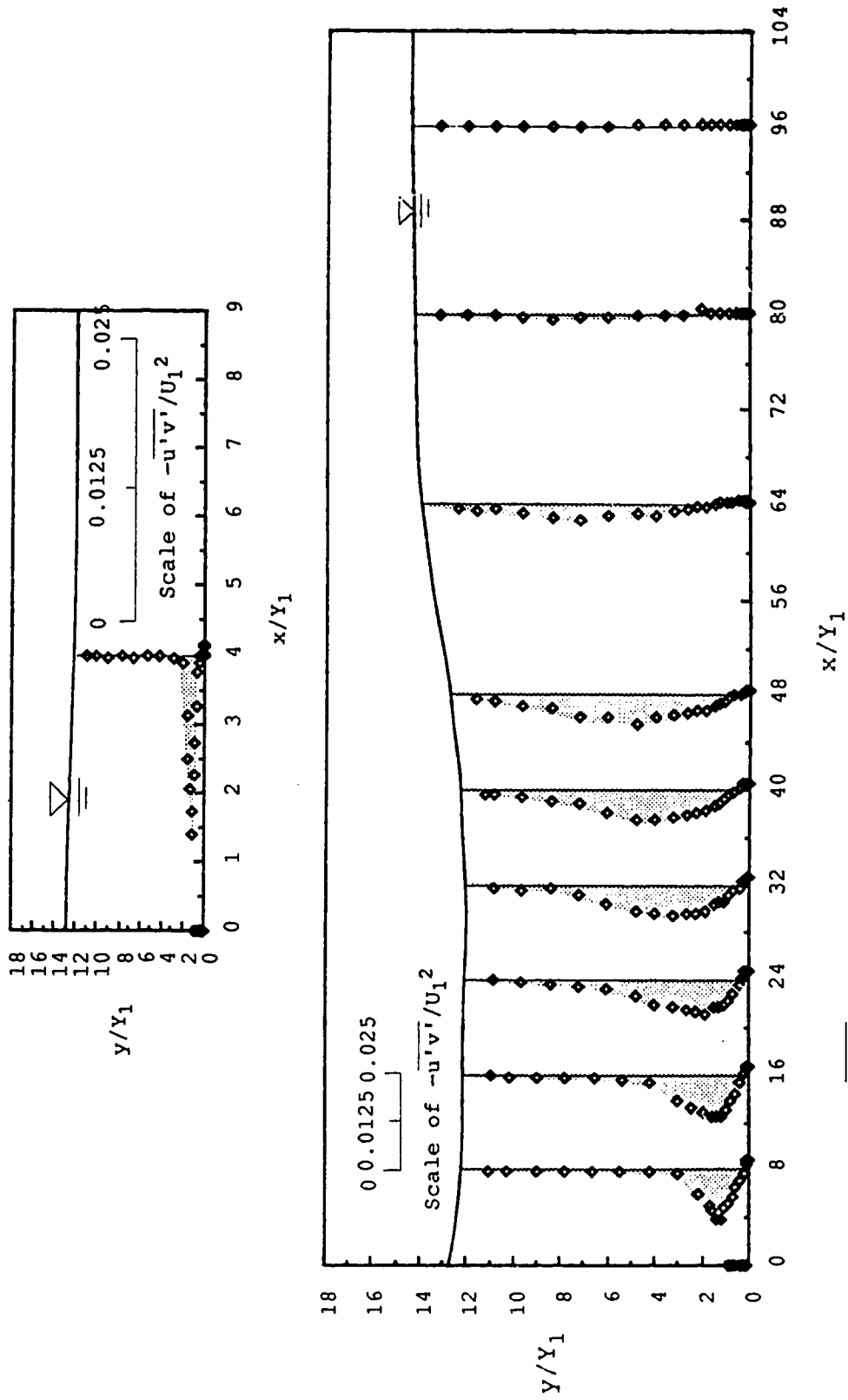


Figure 62. $-\overline{u'v'}/U_1^2$ distribution over the depth at the plane of $z/W=0.36$ for the condition of $F_1=5.43$ and $S=1.01$.

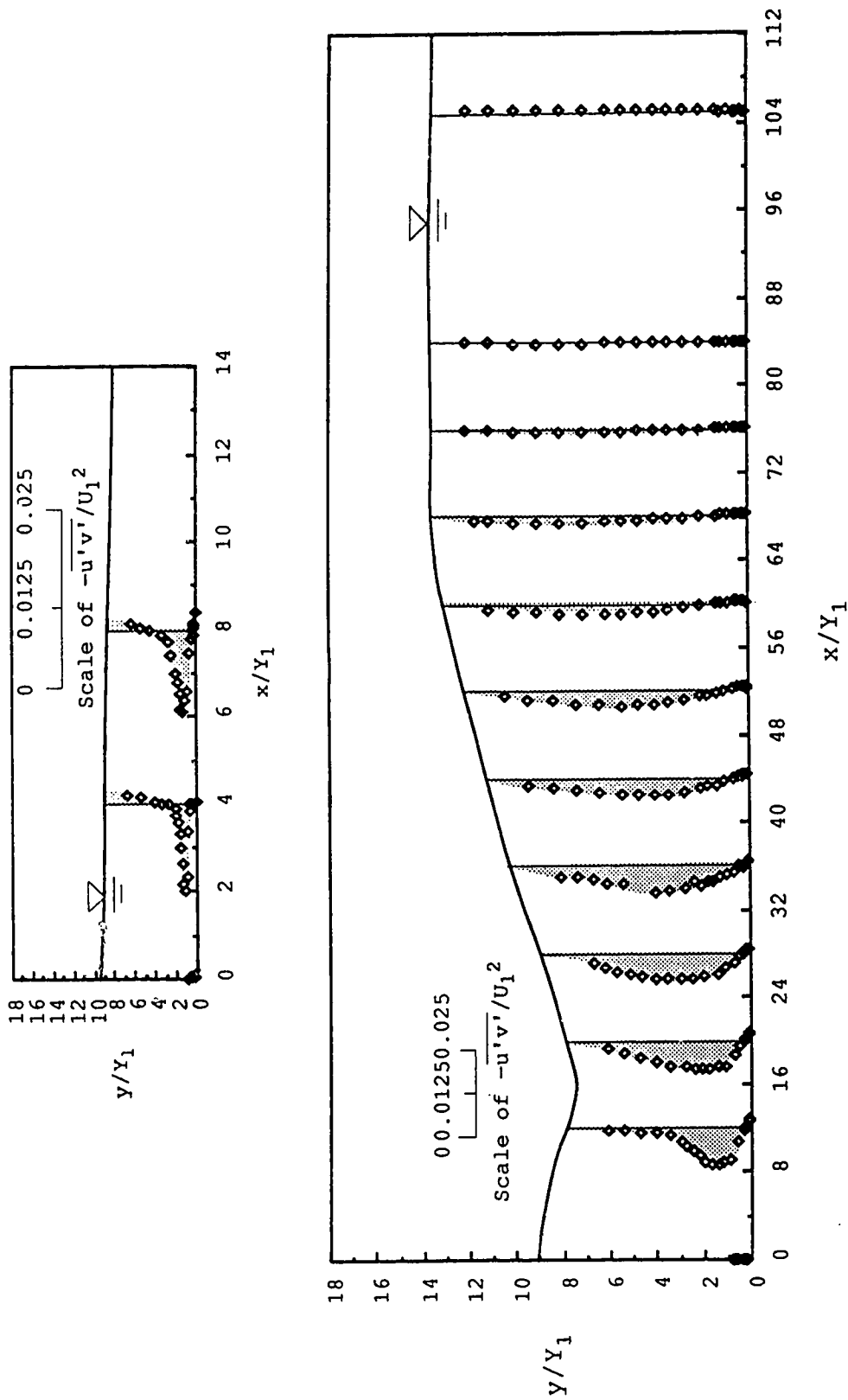


Figure 63. $-\overline{u'v'}/U_1^2$ distribution over the depth at the plane of $z/W=0.36$ for $F_1=8.19$ and $S=0.24$.

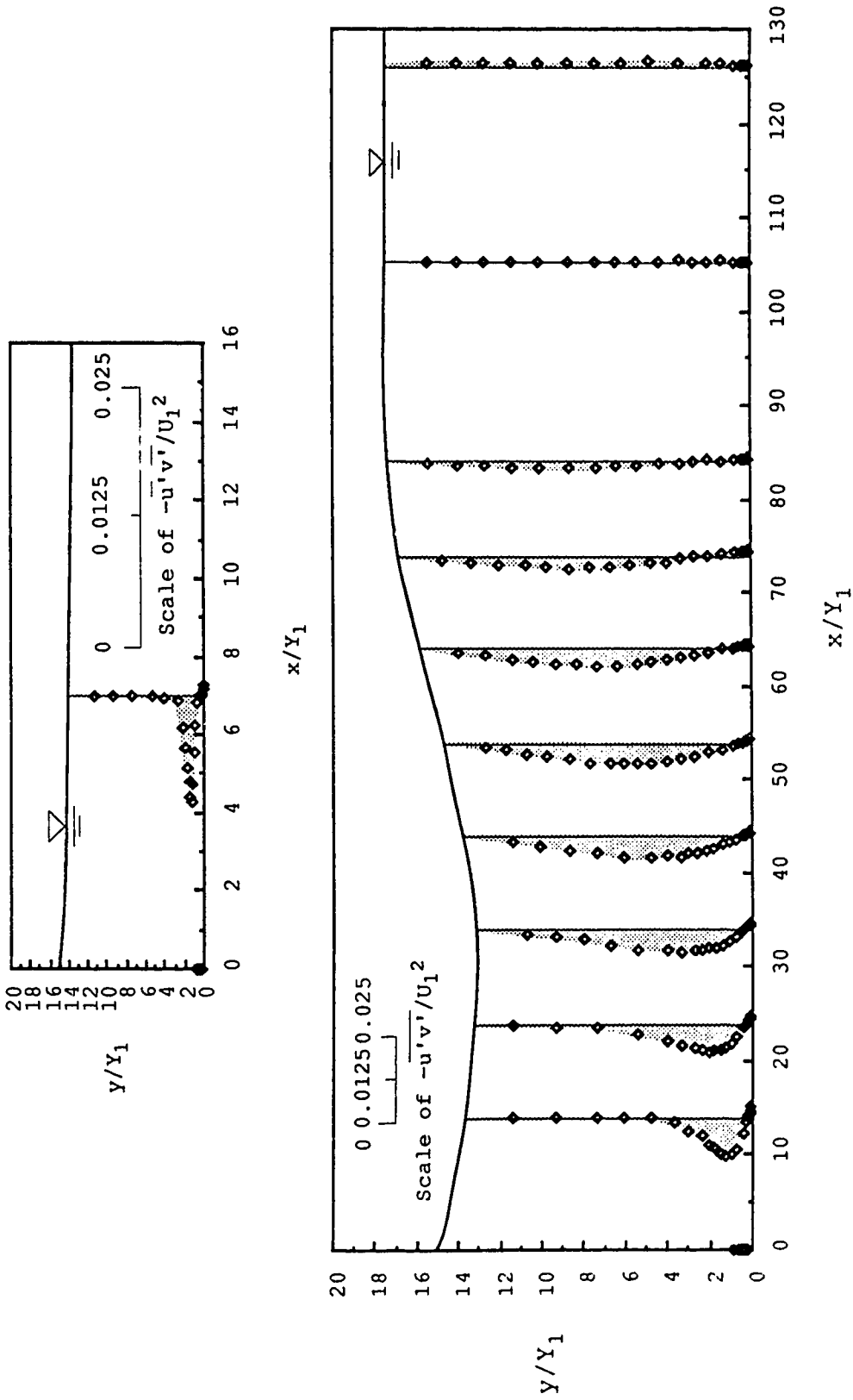


Figure 64. $-\overline{u'v'}/U_1^2$ distribution over the depth at the plane of $z/W=0.36$ for the condition of $F_1=8$ and $S=0.62$.

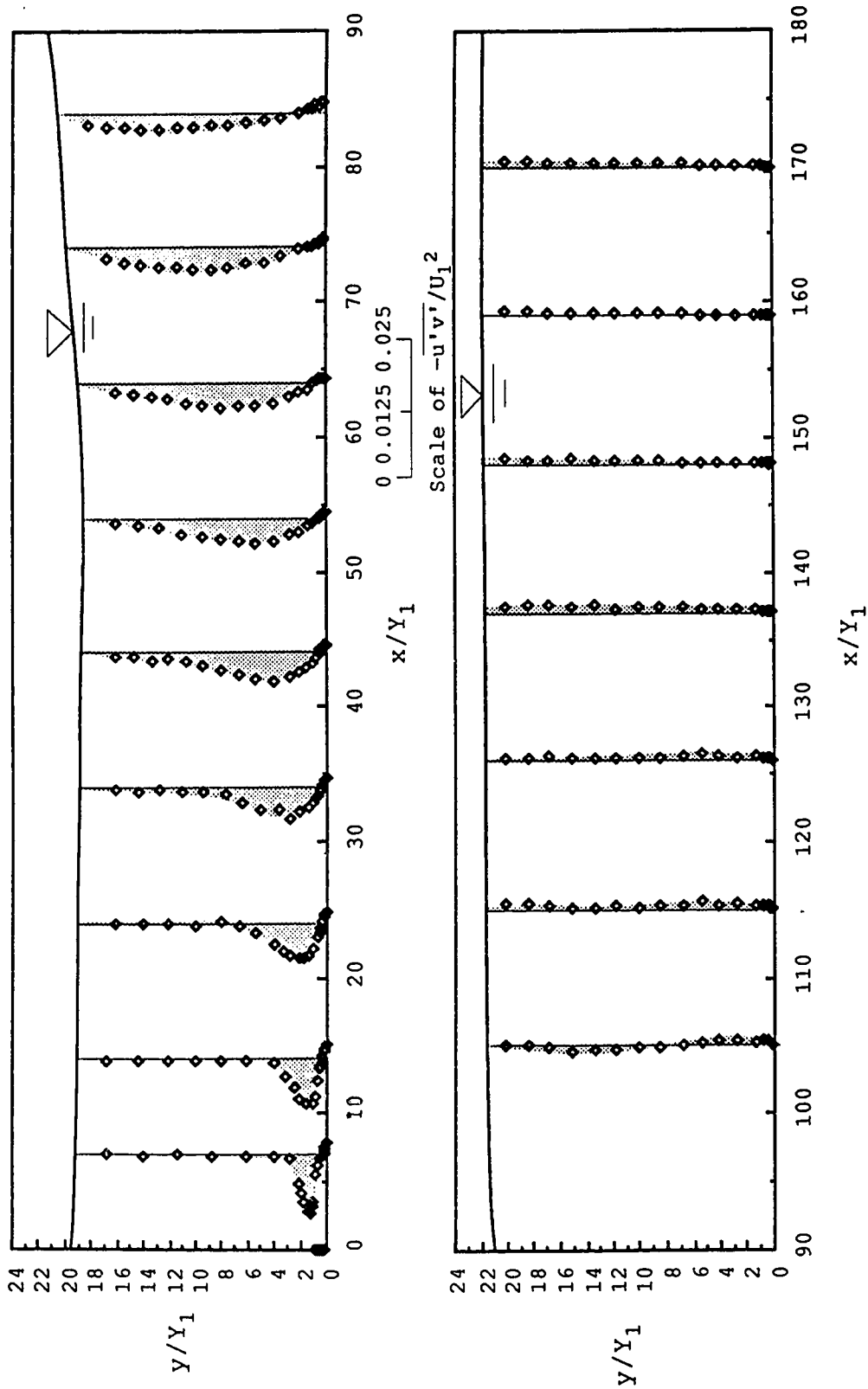


Figure 65. $-\overline{u'v'}/U_1^2$ distribution over the depth at the plane of $z/W=0.36$ for the condition of $F_1=8.11$ and $S=1.00$.

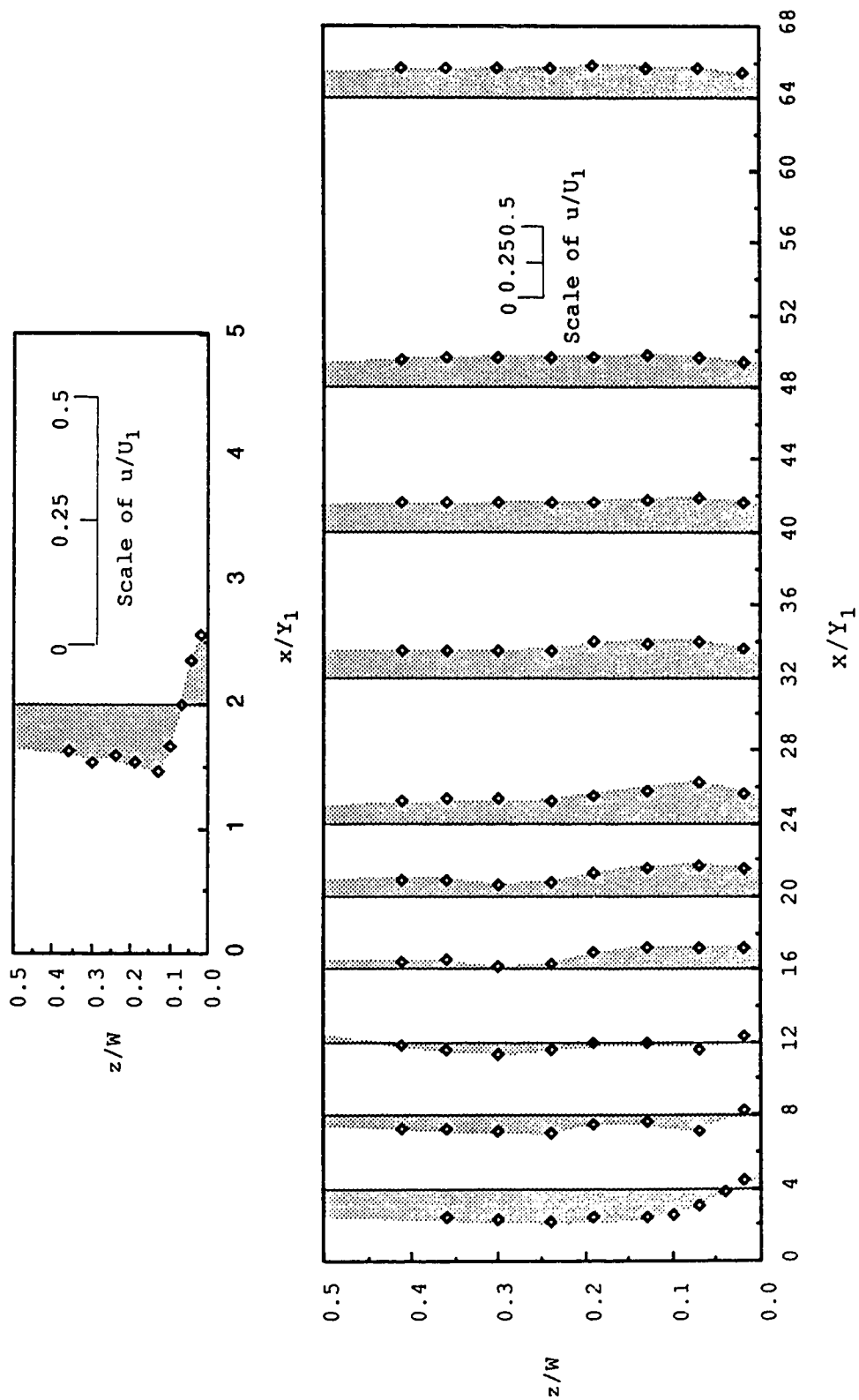


Figure 66. u/U_1 distribution across the channel at the plane of $y/Y_1=2.2$ for the condition of $F_1=3.11$ and $S=0.26$.

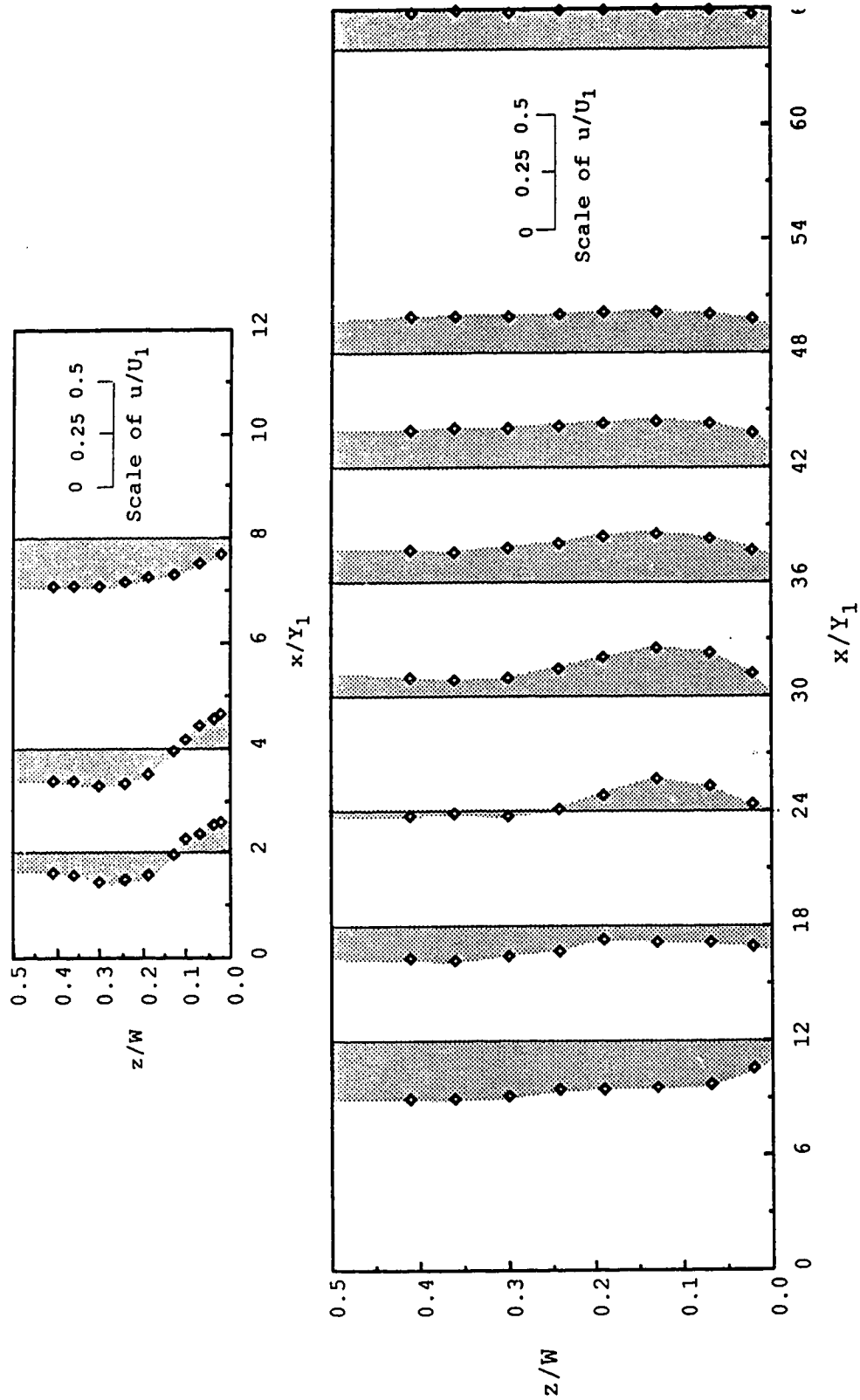


Figure 67. u/U_1 distribution across the channel at the plane of $y/Y_1=3.7$ for the condition of $F_1=3.20$ and $S=0.53$.

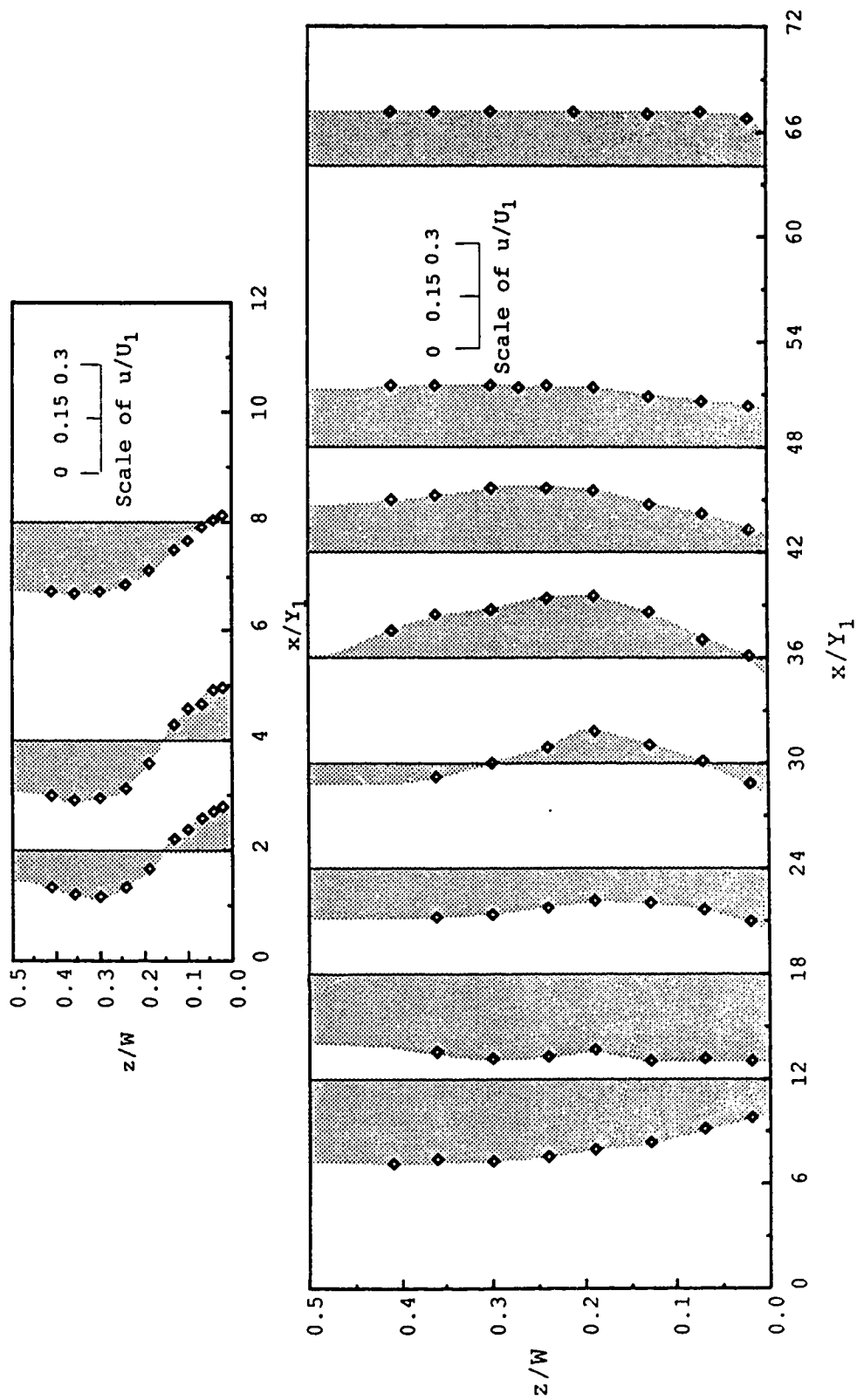


Figure 68. u/U_1 distribution across the channel at the plane of $y/Y_1=5.3$ for the condition of $F_1=3.19$ and $S=0.85$.

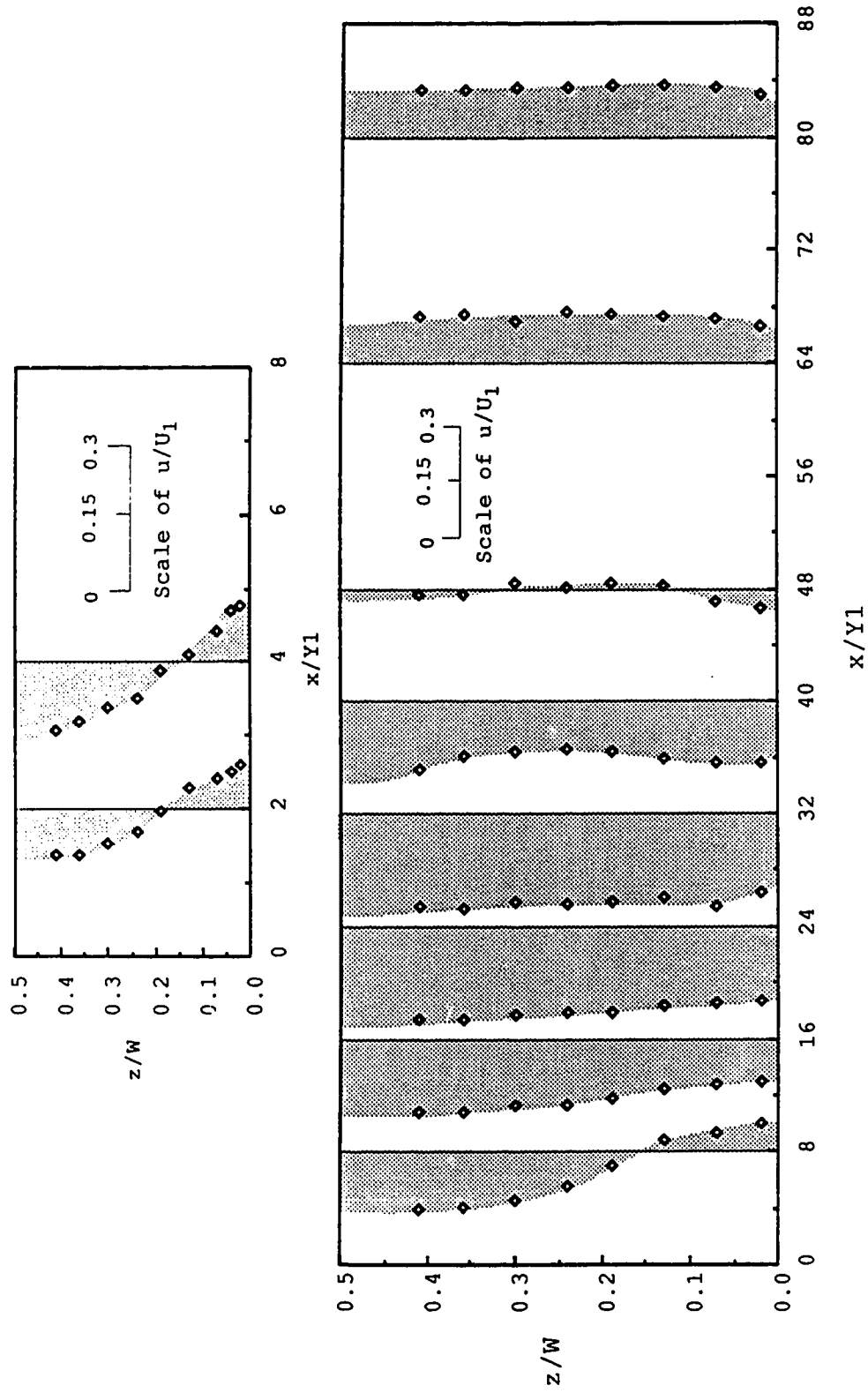


Figure 69. u/U_1 distribution across the channel at the plane of $y/Y_1=8.3$ for the condition of $F_1=3.01$ and $S=1.69$.

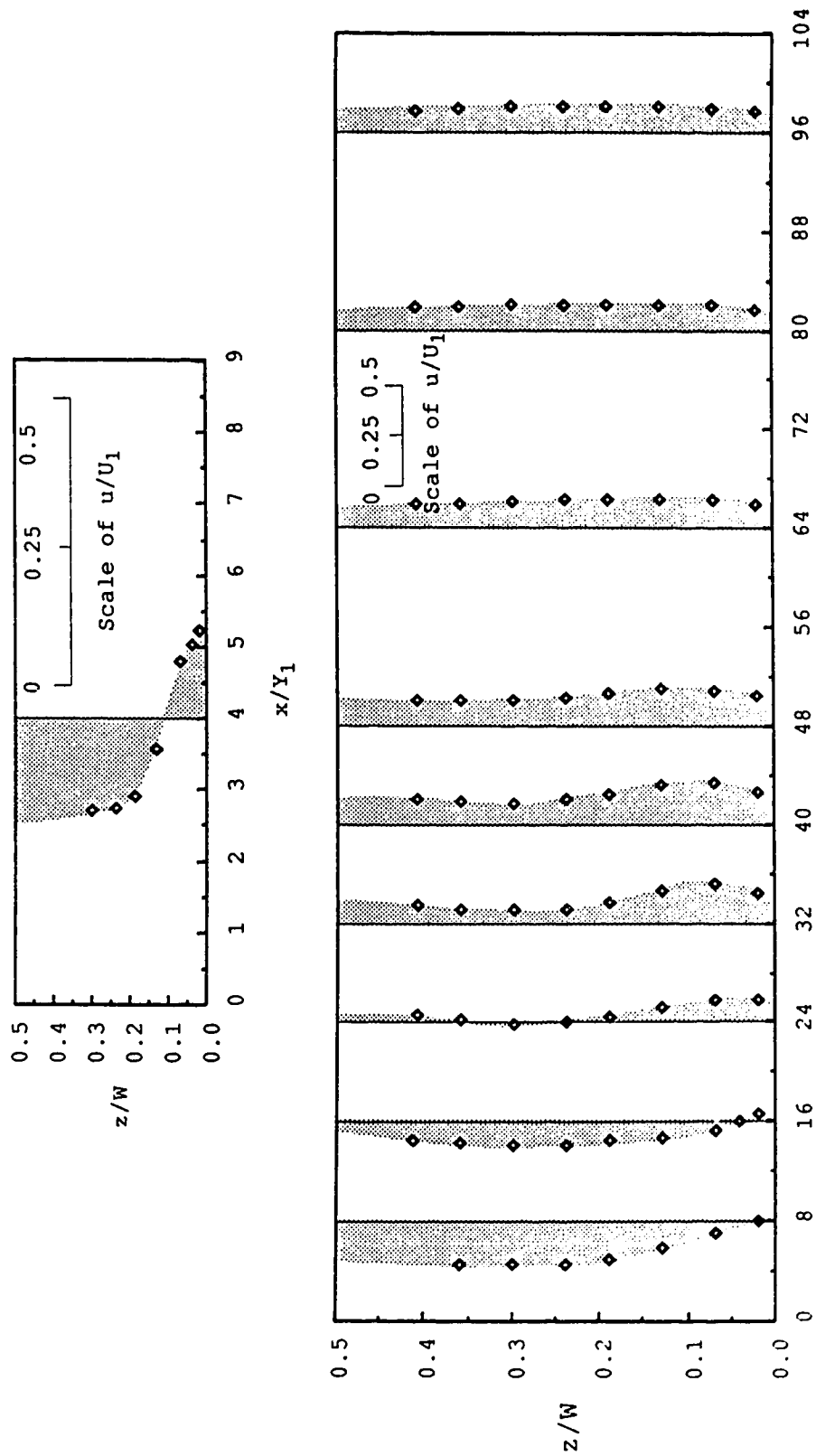


Figure 70. u/U_1 distribution across the channel at the plane of $y/Y_1=3.7$ for the condition of $F_1=5.61$ and $S=0.22$.

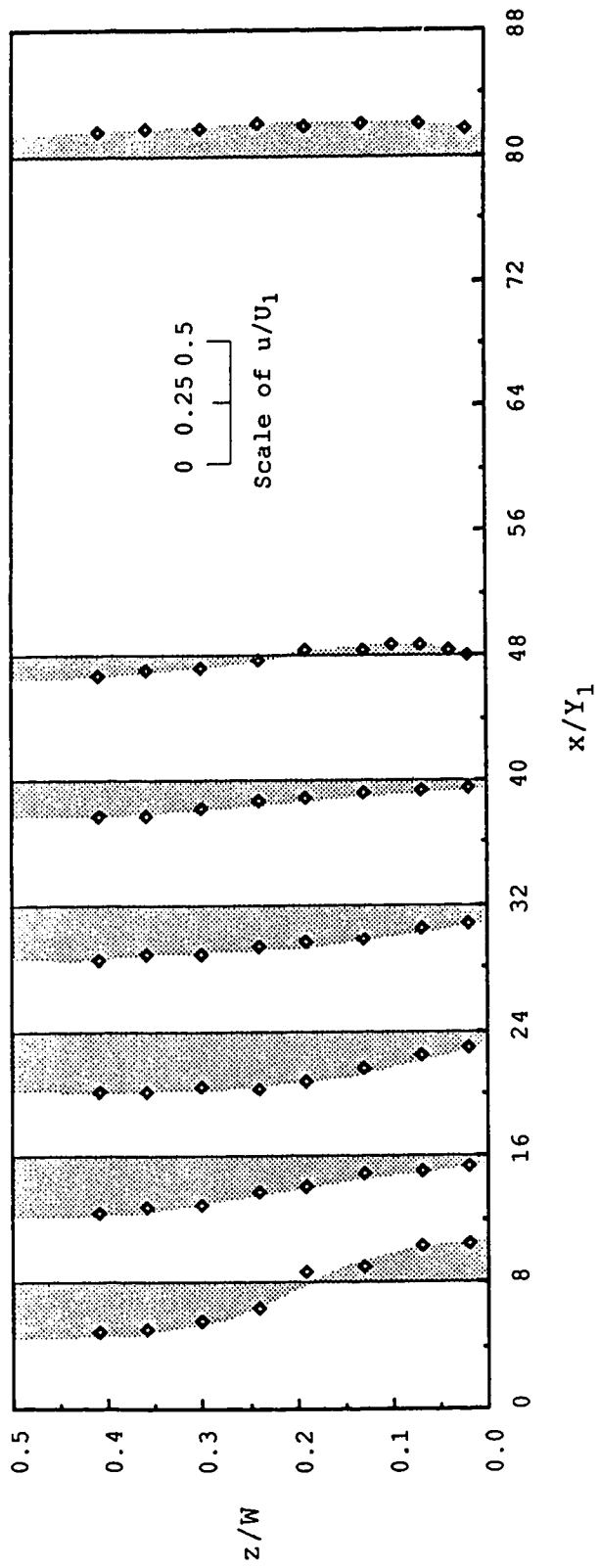


Figure 71. u/U_1 distribution across the channel at the plane of $y/Y_1=7.2$ for the condition of $F_1=5.49$ and $S=0.63$.

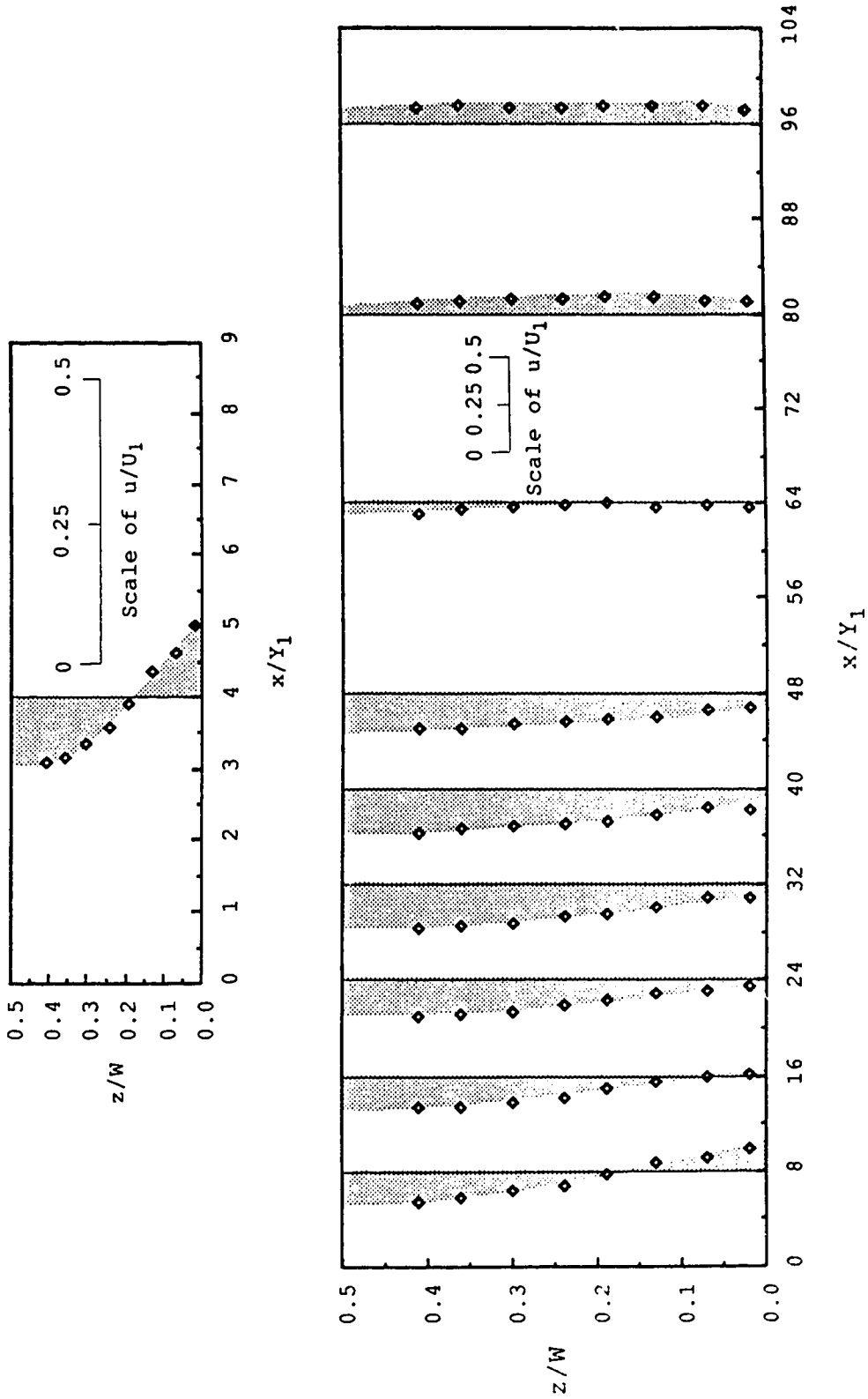


Figure 72. u/U_1 distribution across the channel at the plane of $y/Y_1=10$ for the condition of $F_1=5.43$ and $S=1.01$.

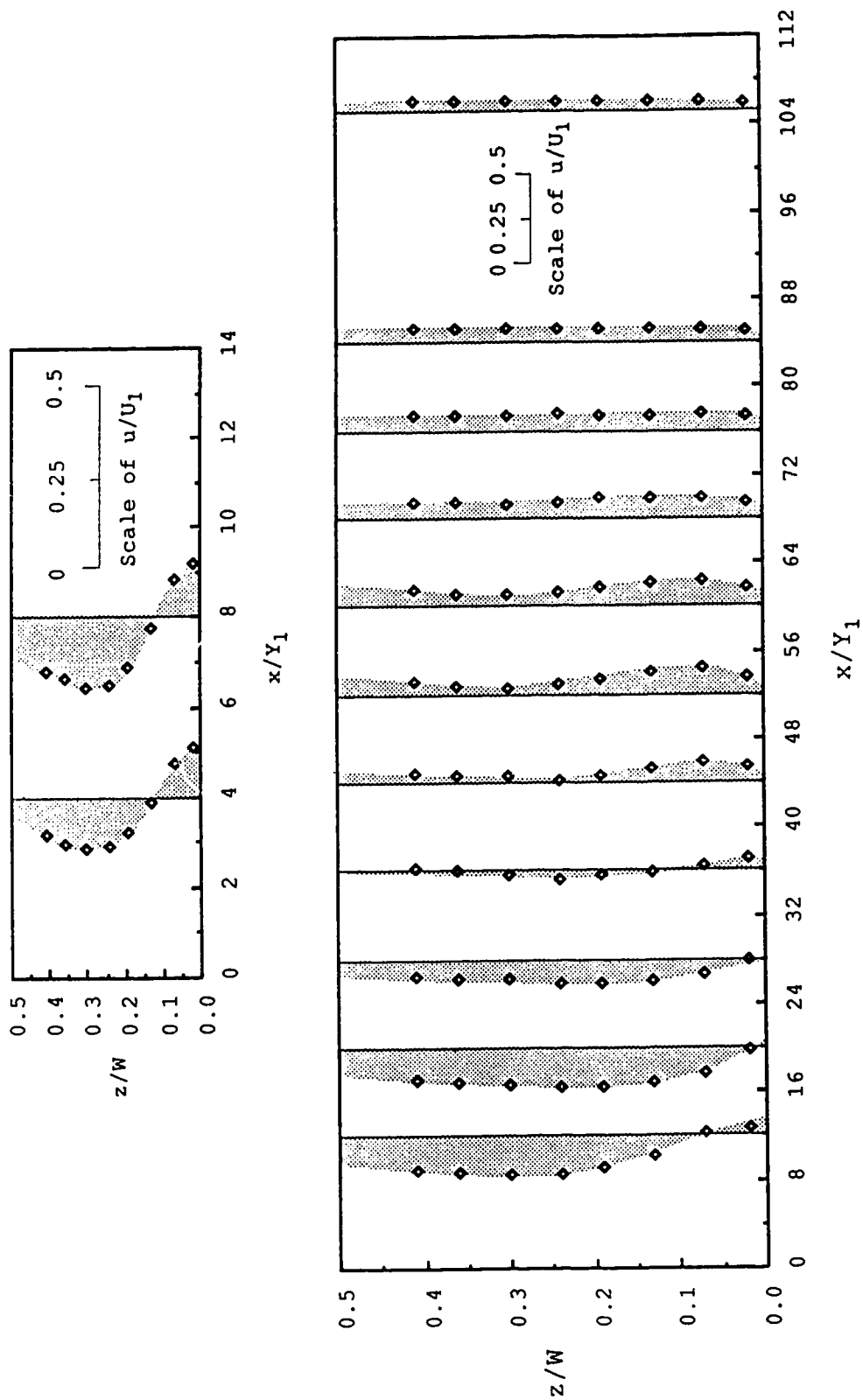


Figure 73. u/U_1 distribution across the channel at the plane of $y/Y_1 = 5.33$ for $F_1 = 8.19$ and $S = 0.24$.

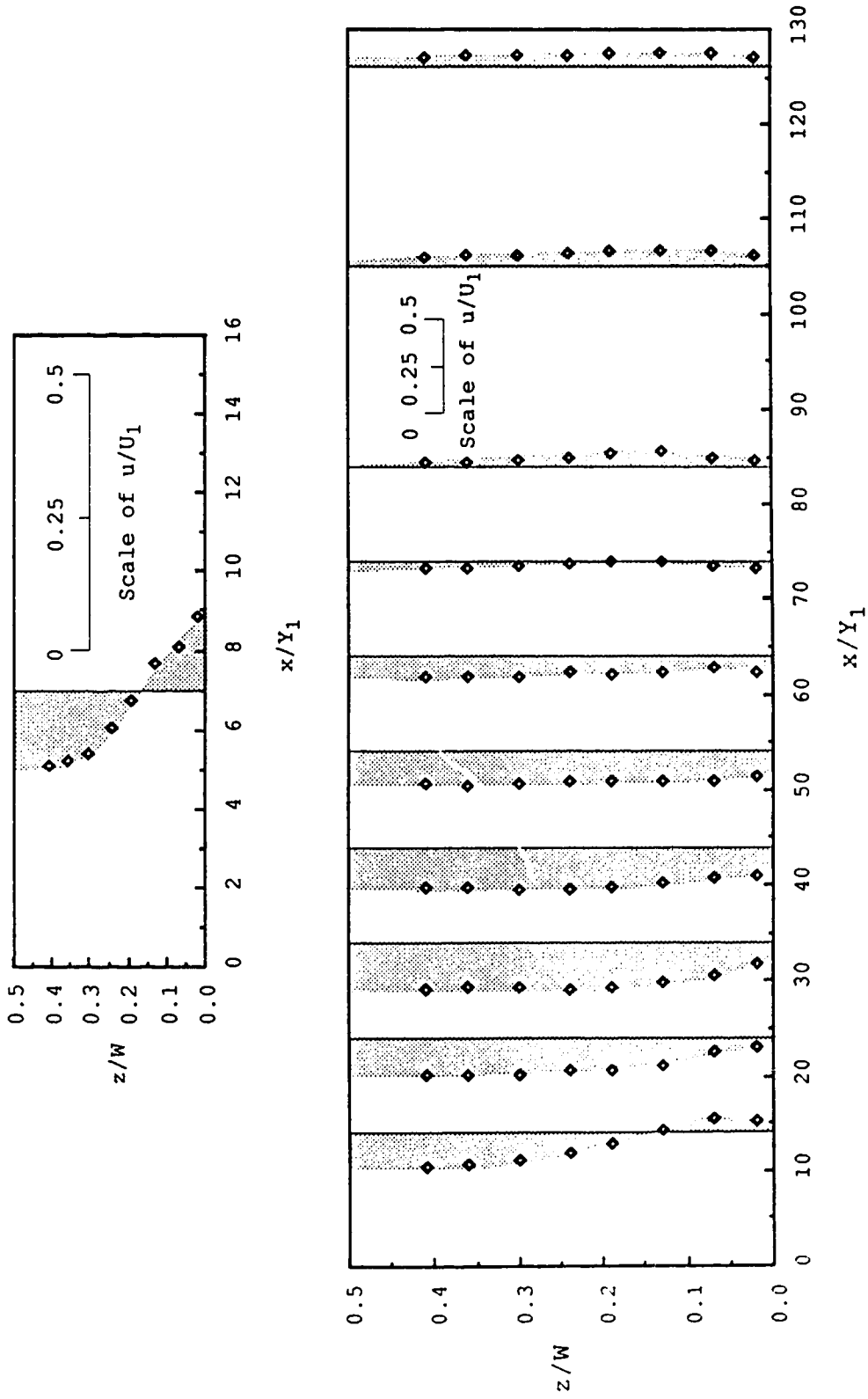


Figure 74. u/U_1 distribution across the channel at the plane of $y/Y_1=10.7$ for the condition of $F_1=8.00$ and $S=0.62$.

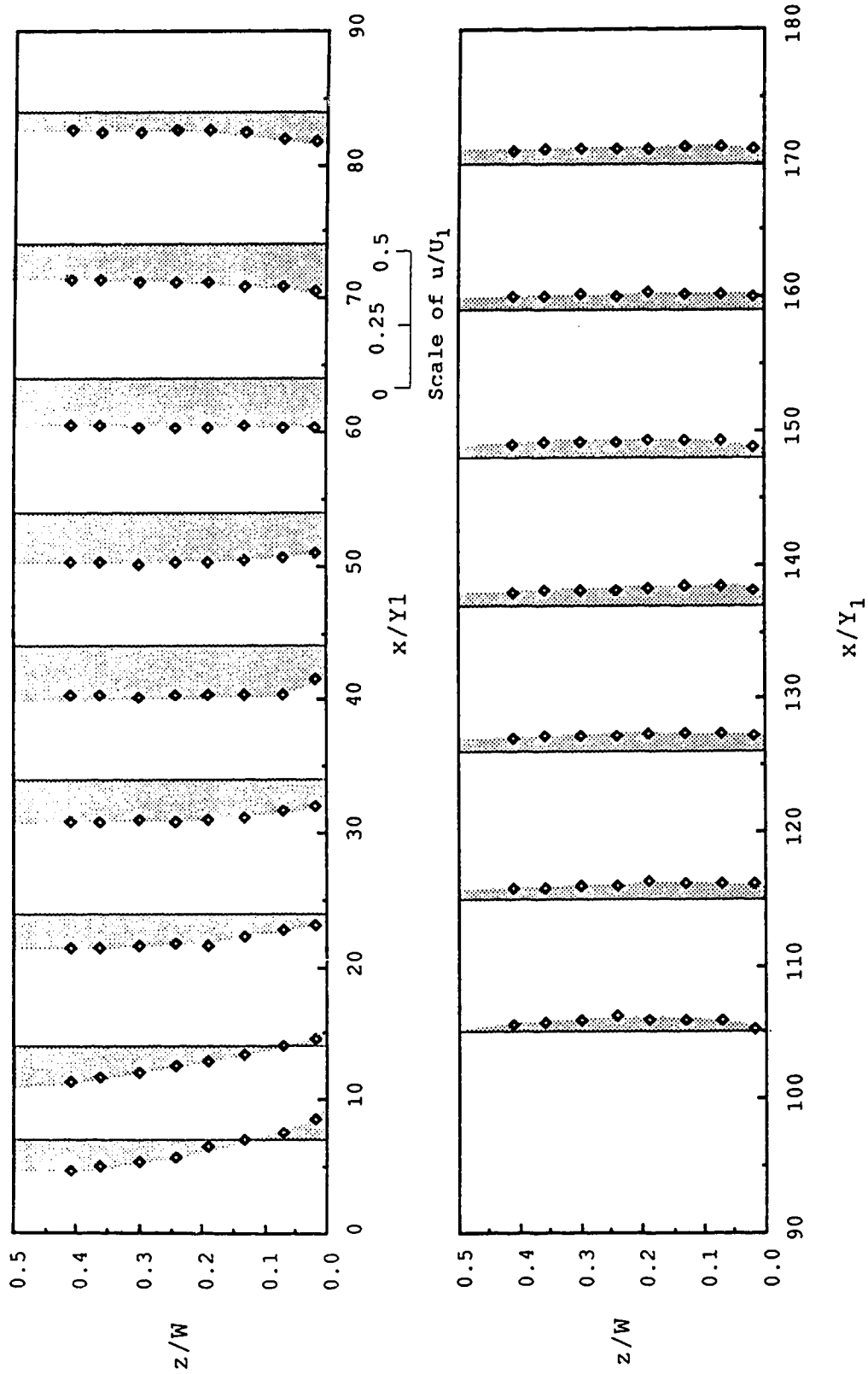


Figure 75. u/U_1 distribution across the channel at the plane of $y/Y_1=15$ for the condition of $F_1=8.11$ and $S=1.00$.

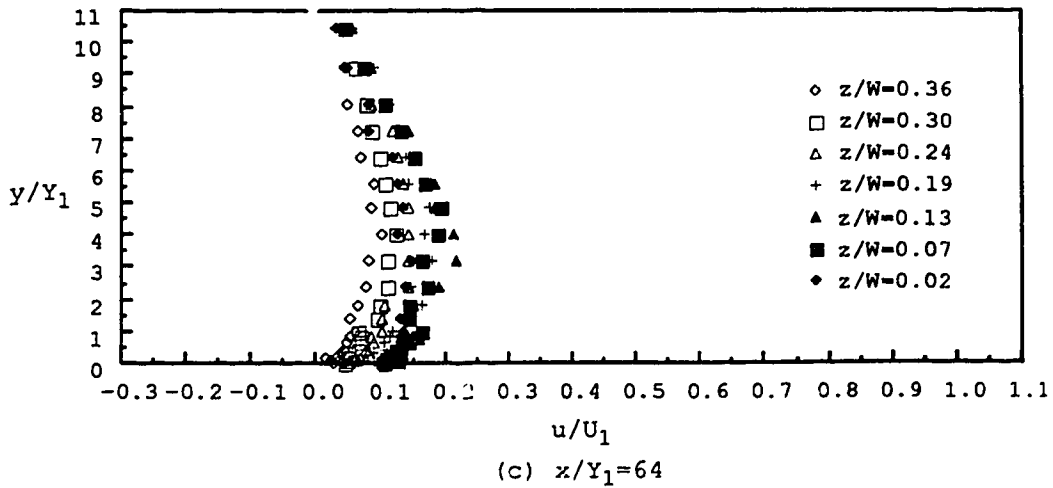
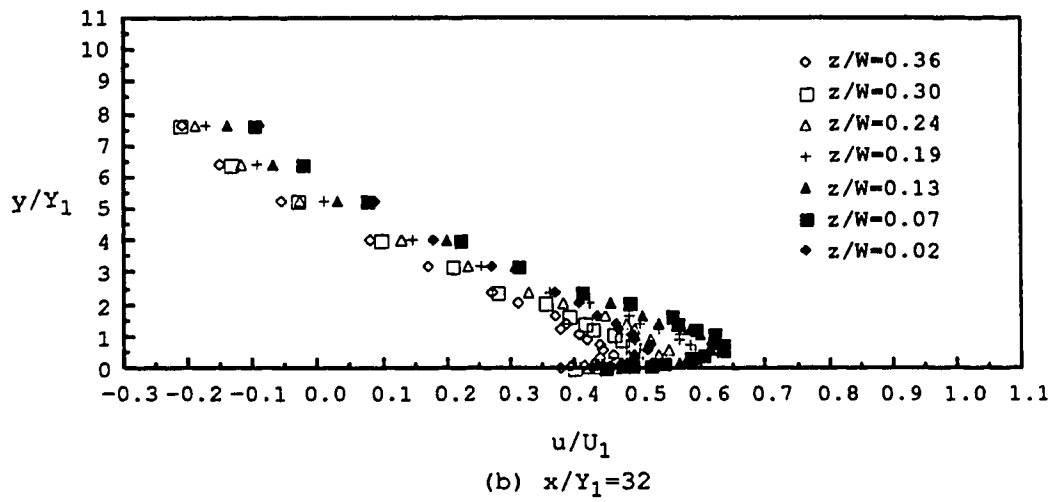
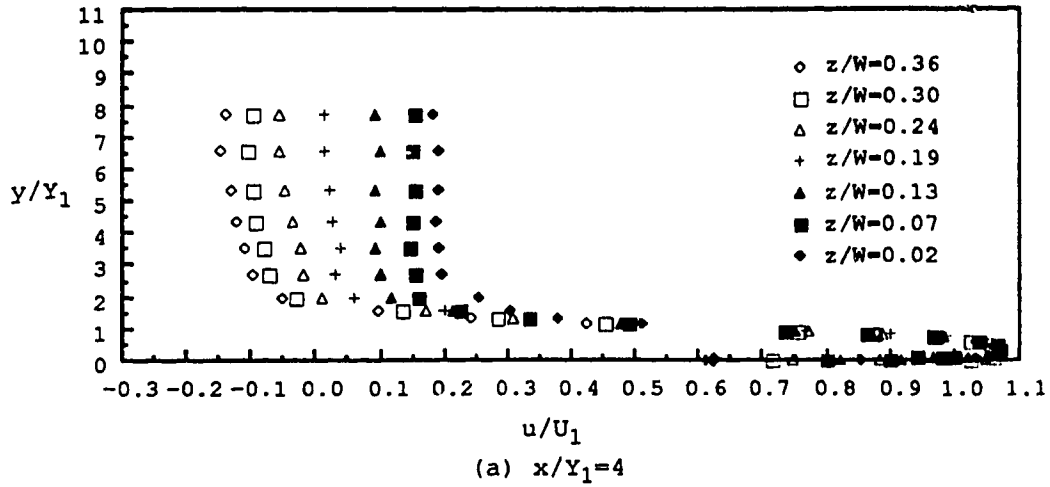


Figure 76. Three dimensional structure of the u velocity for $F_1=5.49$ and $S=0.63$.

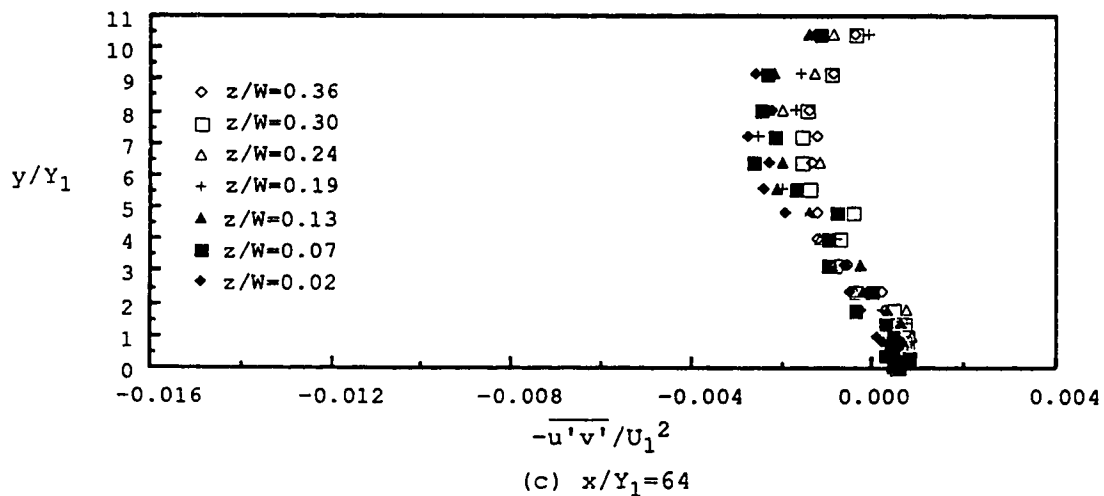
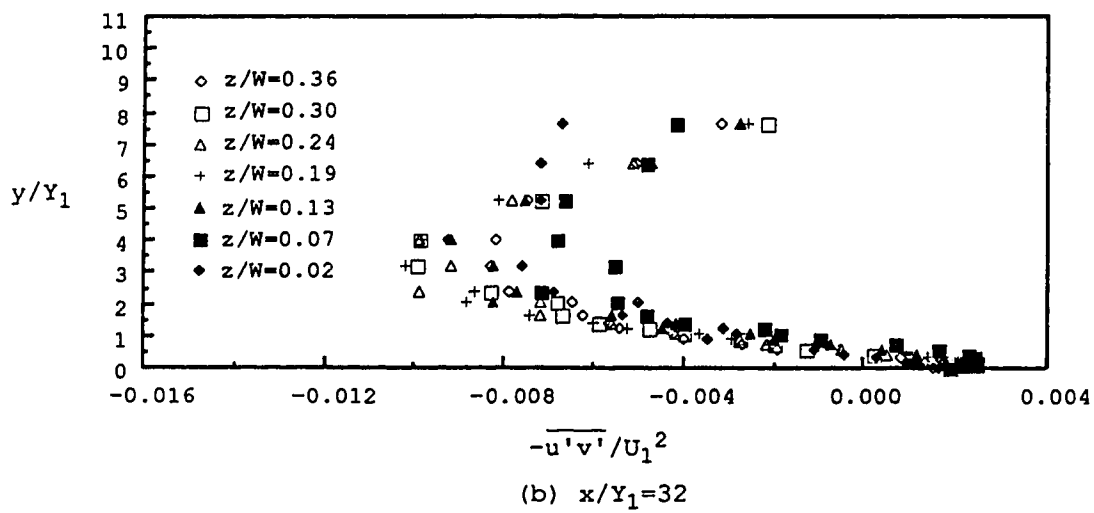
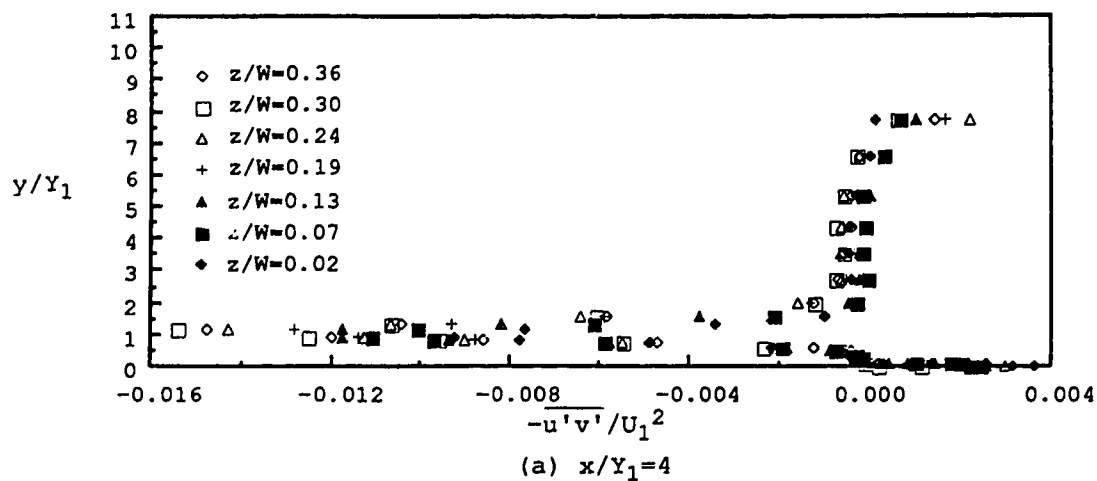


Figure 77. Three dimensional structure of $\overline{-u'v'}$ for $F_1=5.49$ and $S=0.63$.

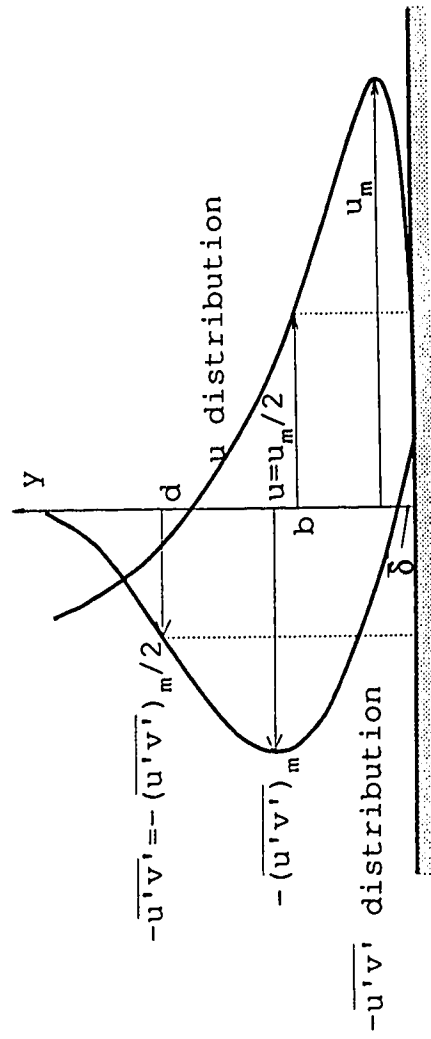


Figure 78. Typical vertical distributions of velocity component u and turbulence shear stress $-\overline{u'v'}$.

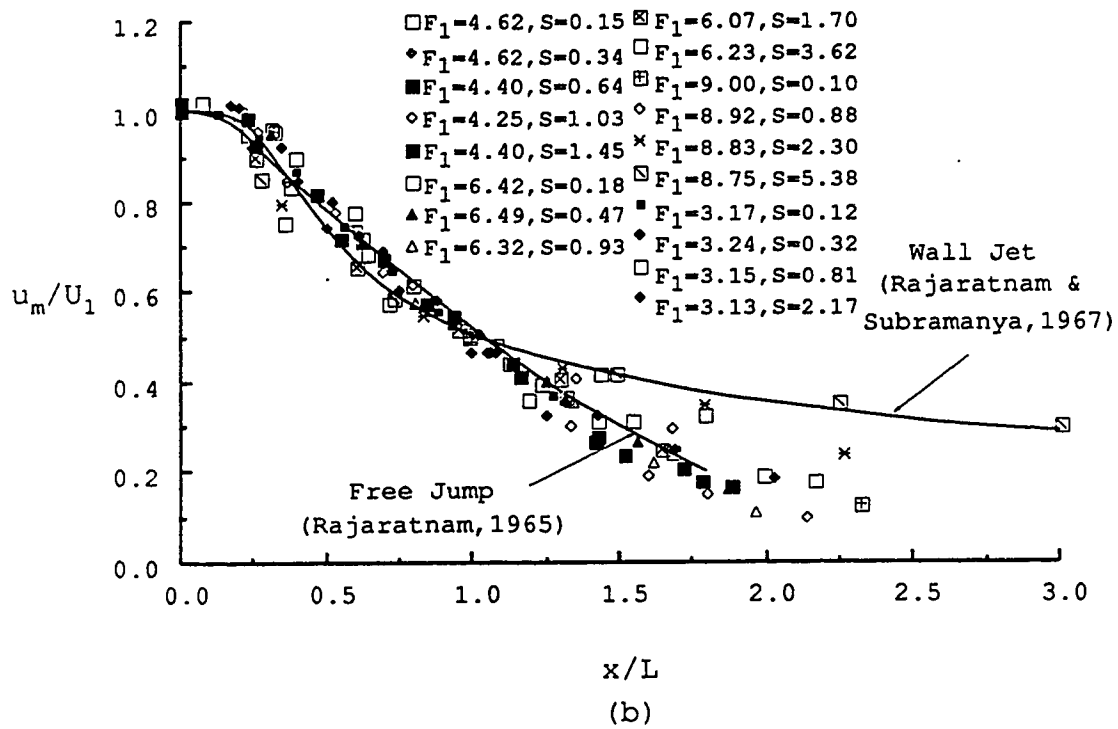
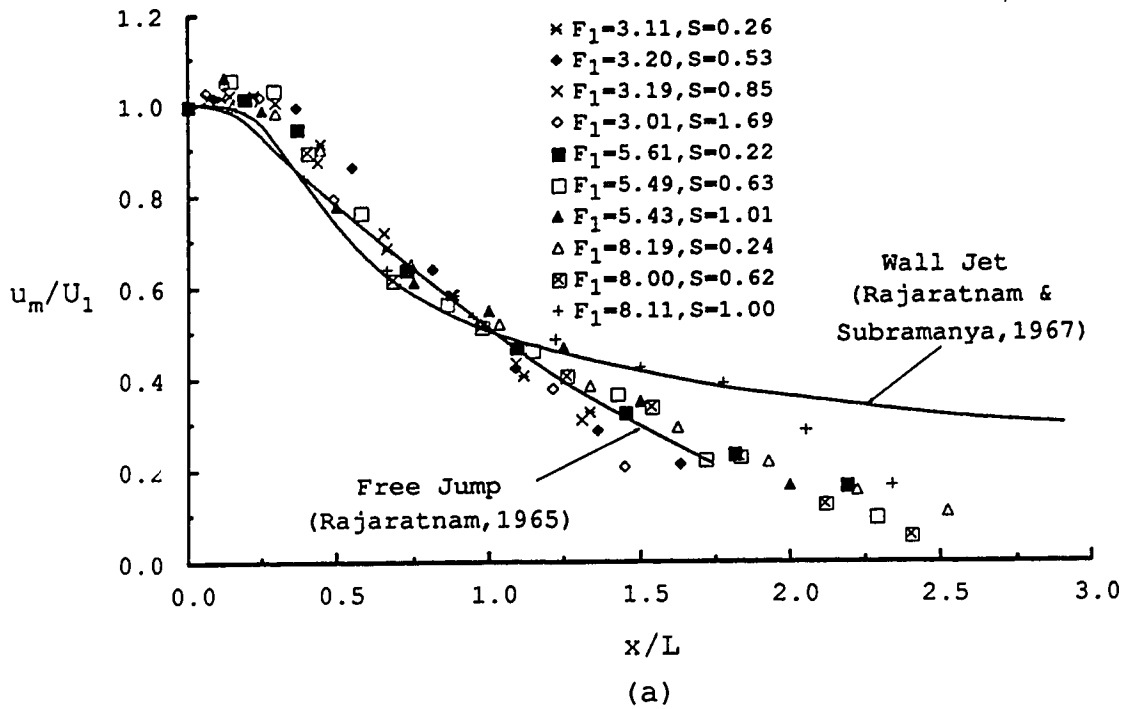


Figure 79. u_m/U_1 vs x/L plots

- (a) Data from the present study;
- (b) Data from Rajaratnam (1976).

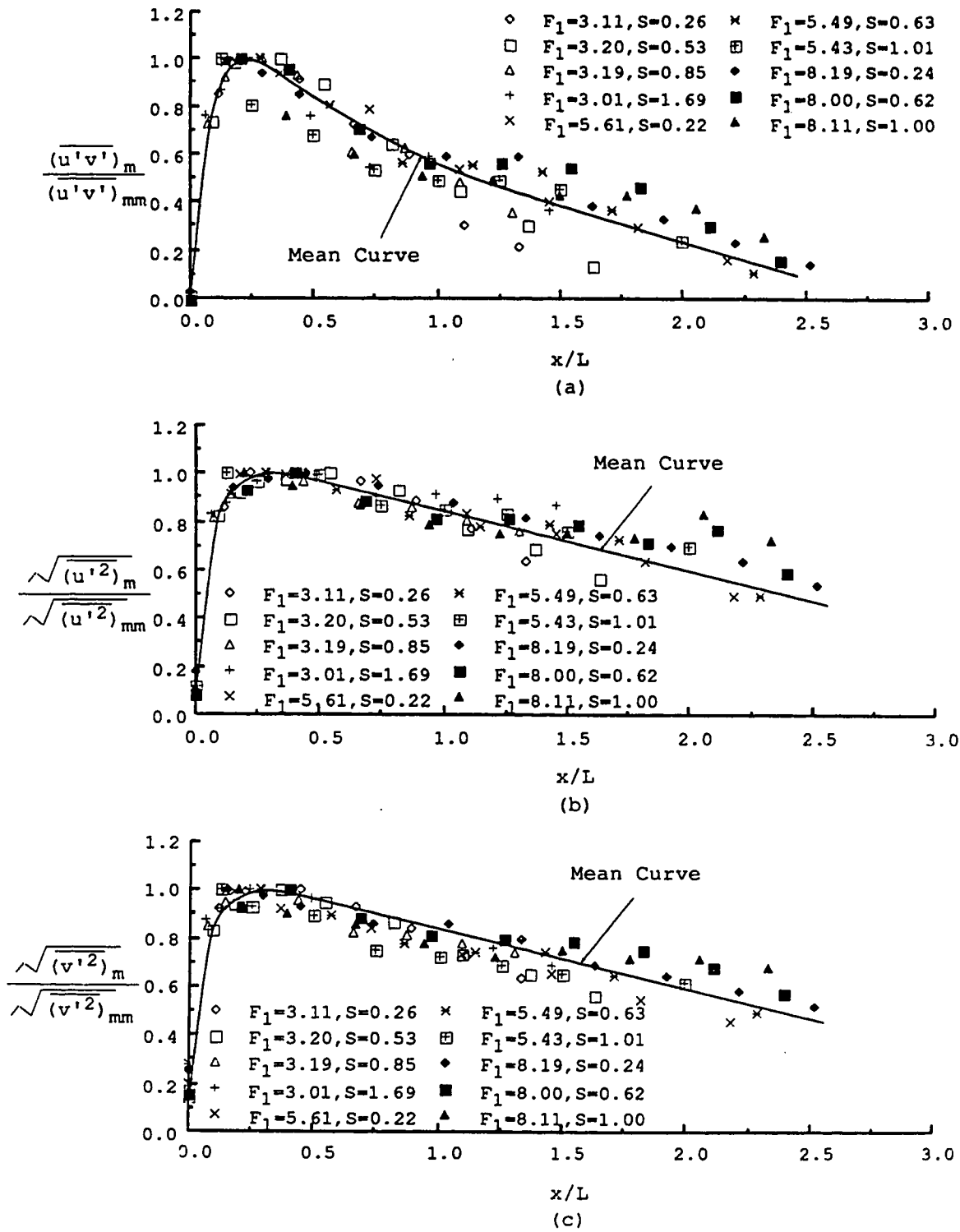


Figure 80. Variation of normalized maximum turbulence shear stress and intensities of a vertical section against x/L .

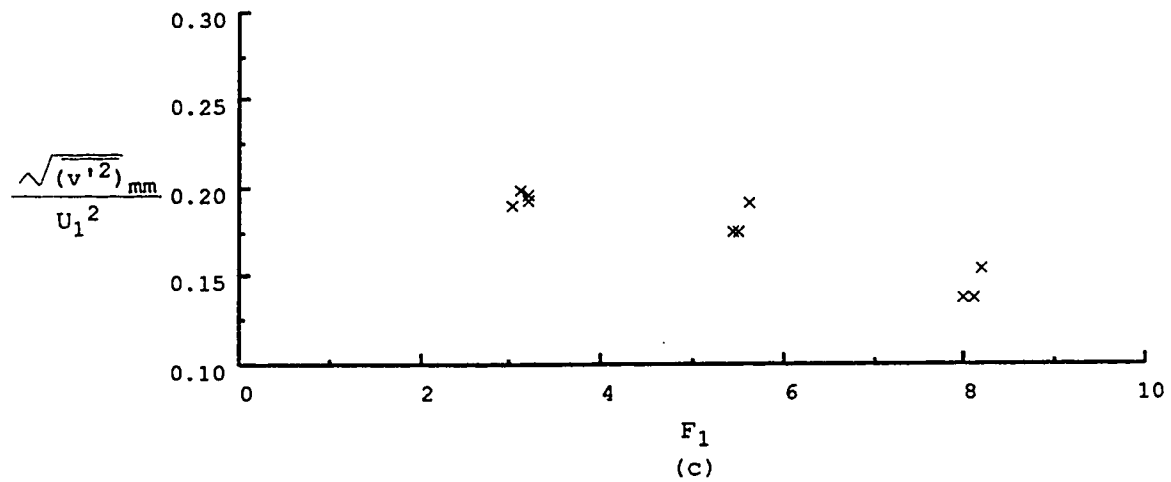
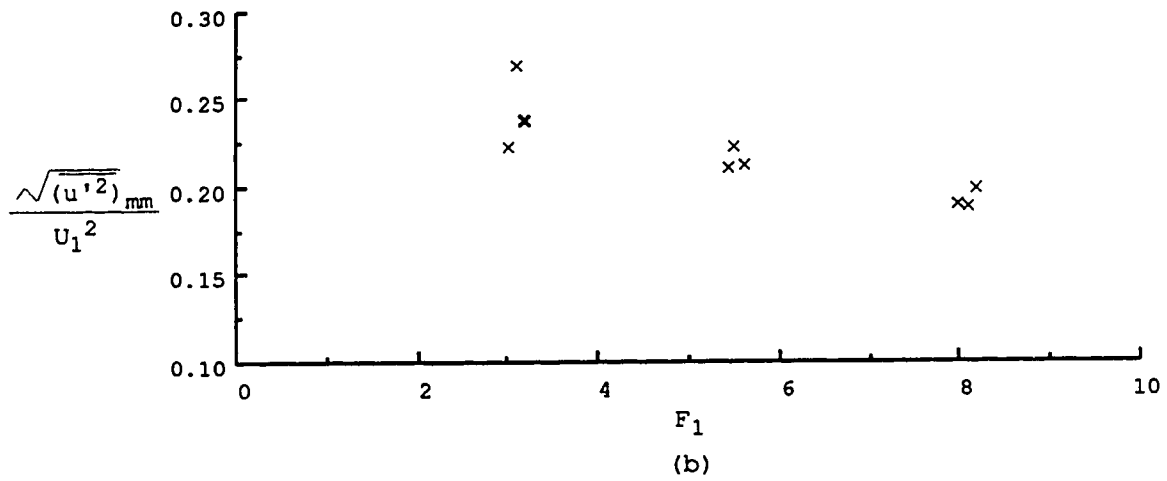
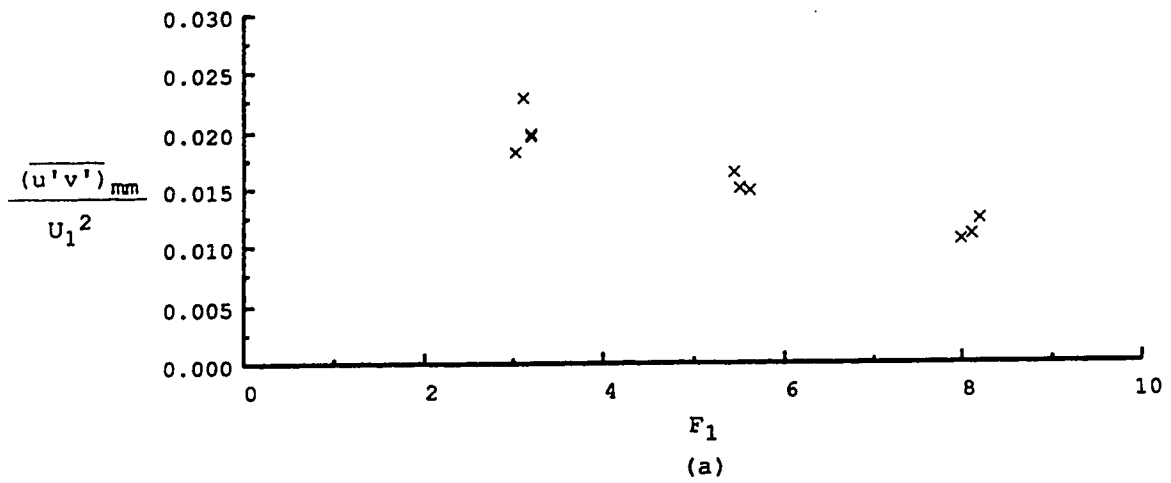


Figure 81. Variation of nondimensionalized maximum turbulence shear stress and intensities against inlet F_1 .

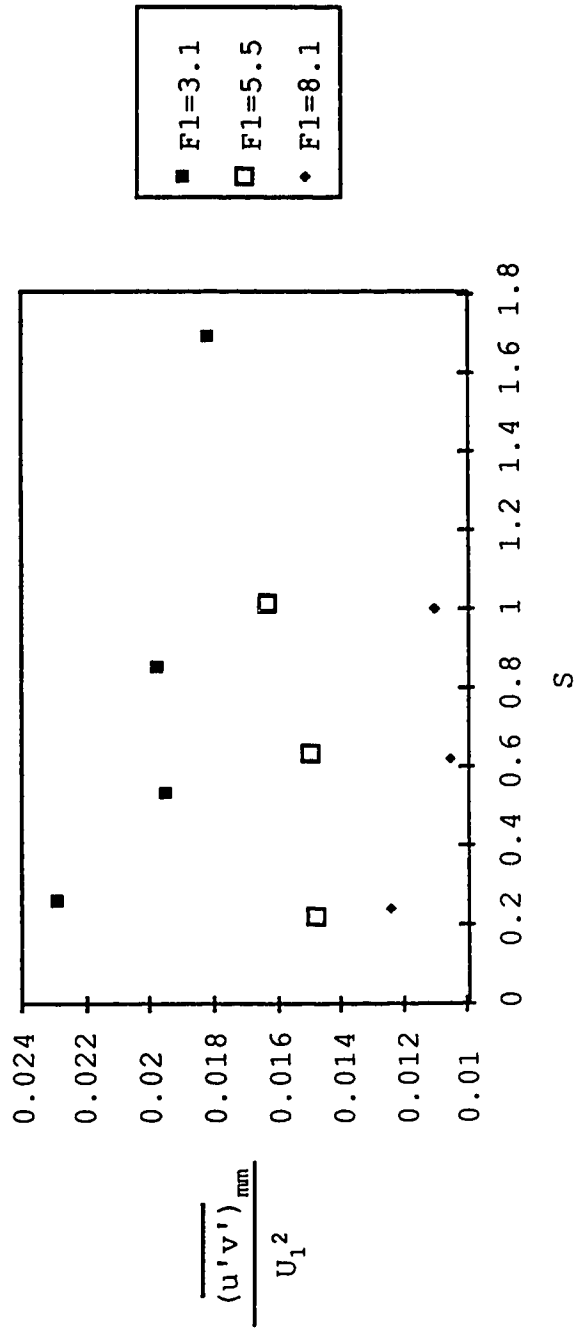


Figure 82. Variation of nondimensionalized maximum shear stresses against submergence factor S.

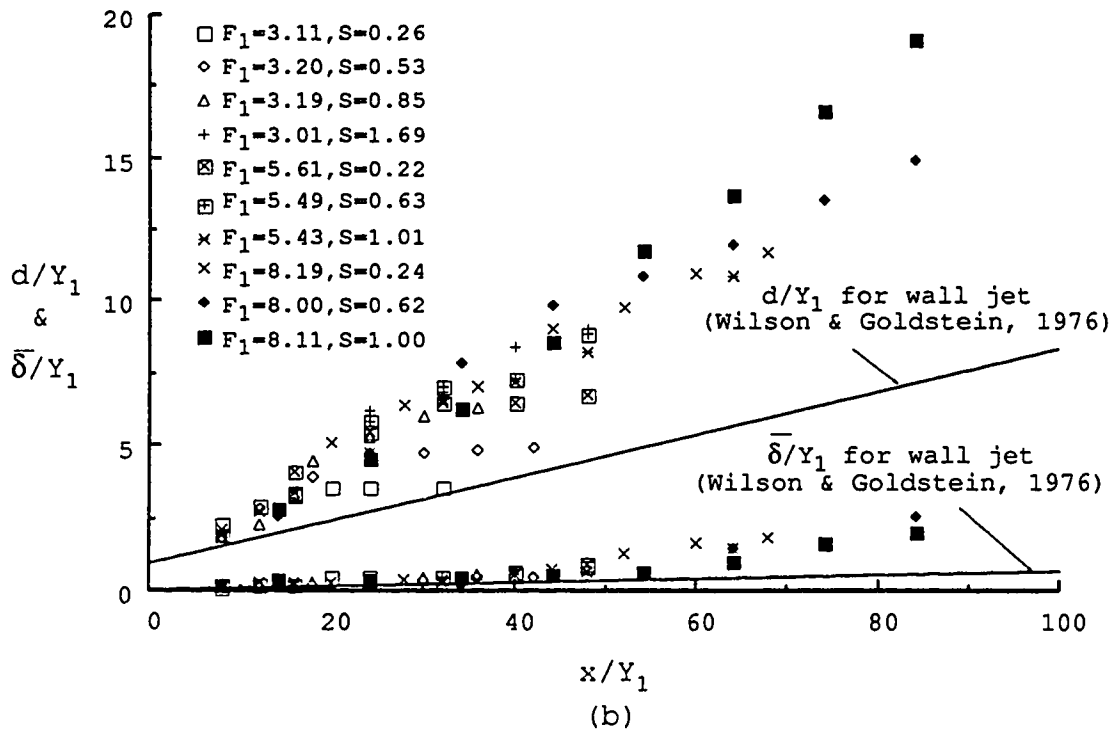
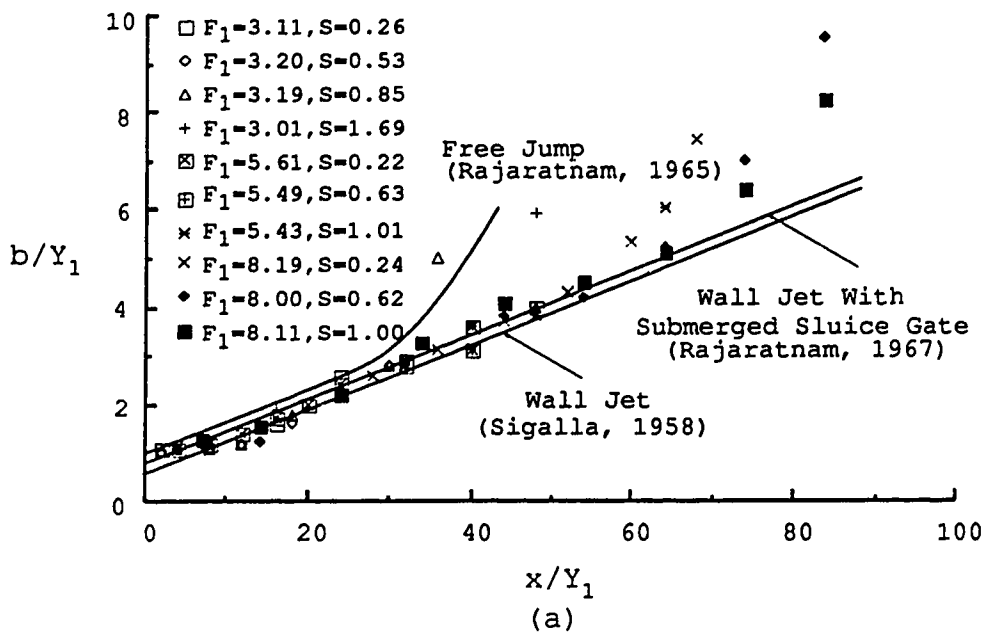


Figure 83. The growth of length scales b/Y_1 , d/Y_1 and $\bar{\delta}/Y_1$ with x/Y_1 .

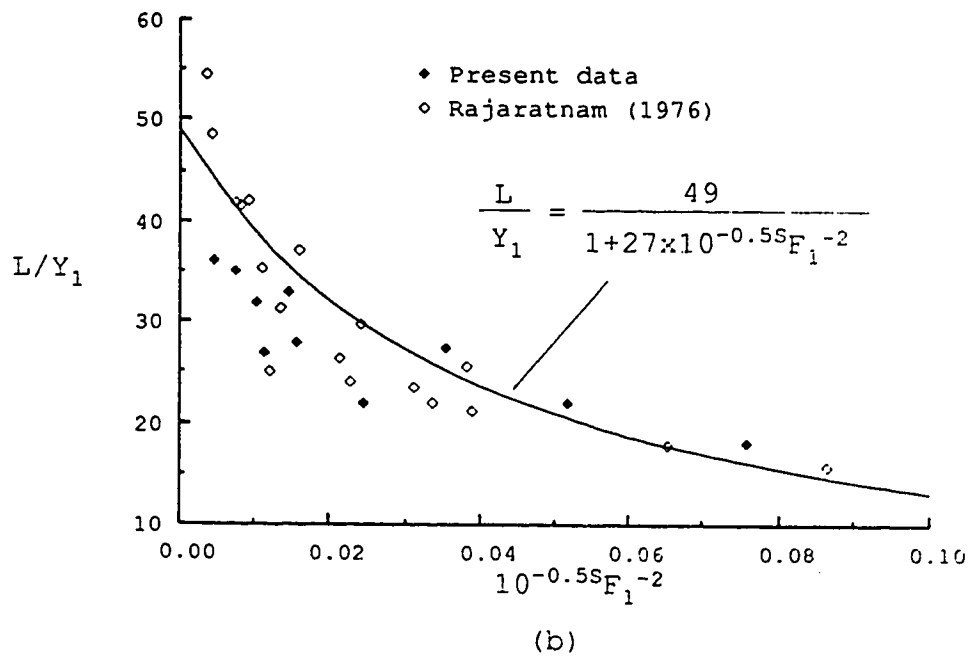
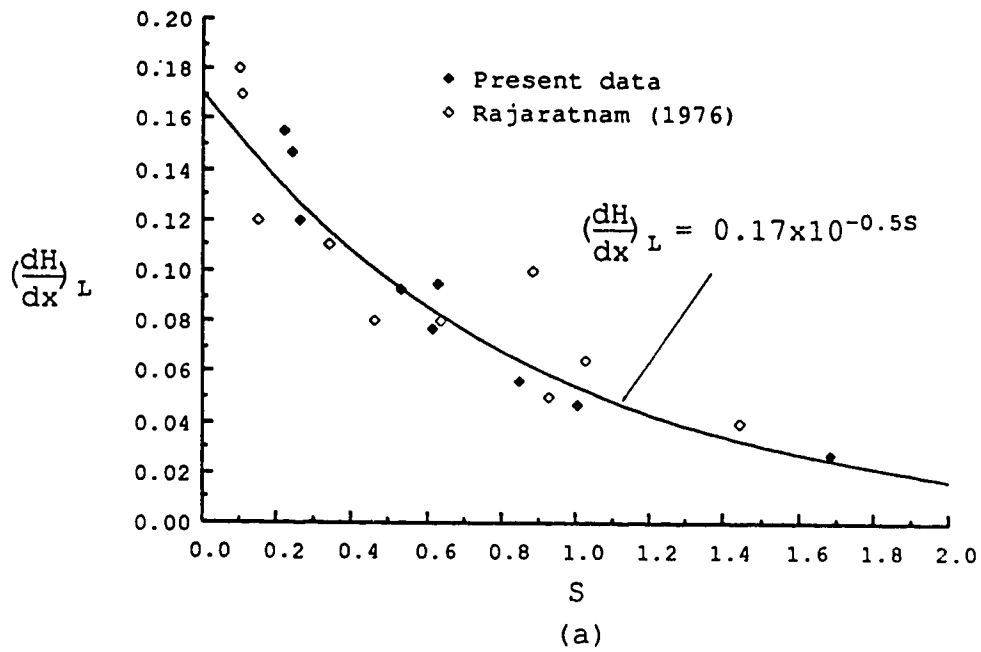


Figure 84. (a) Relationship between $(\frac{dH}{dx})_L$ and S ;
 (b) Relationship between L/Y_1 and F_1 and S .

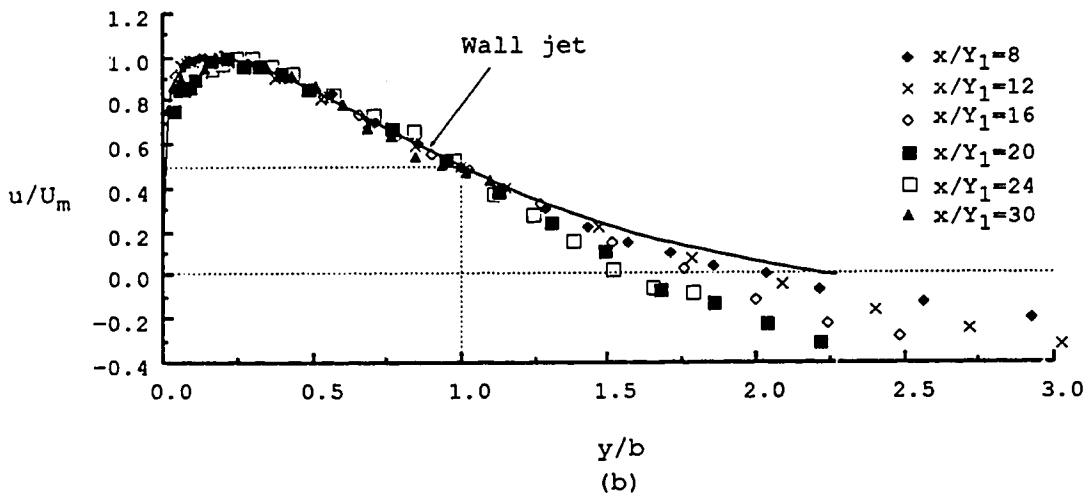
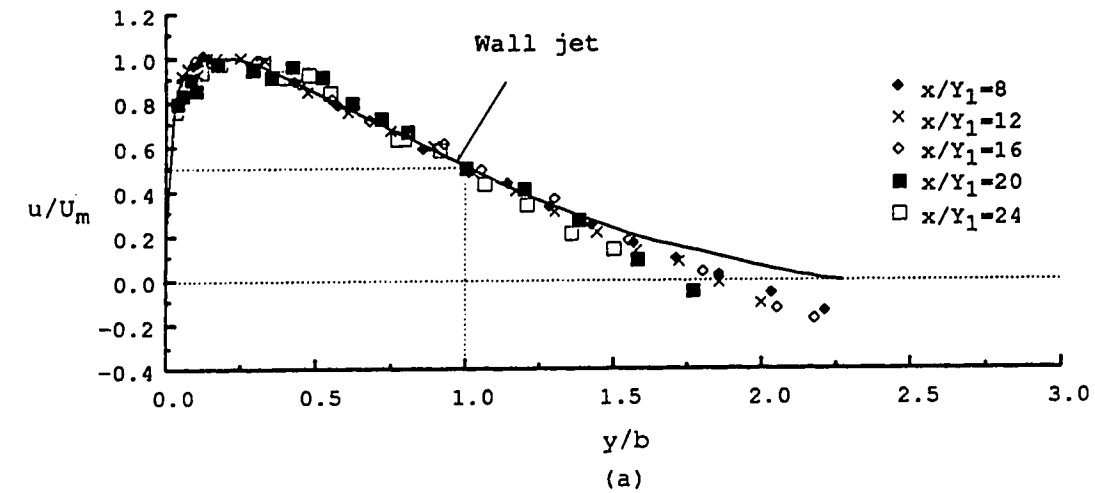


Figure 85. Similarity of velocity profiles in fully developed region for
 (a) $F_1=3.11$ and $S=0.26$;
 (b) $F_1=3.20$ and $S=0.53$.

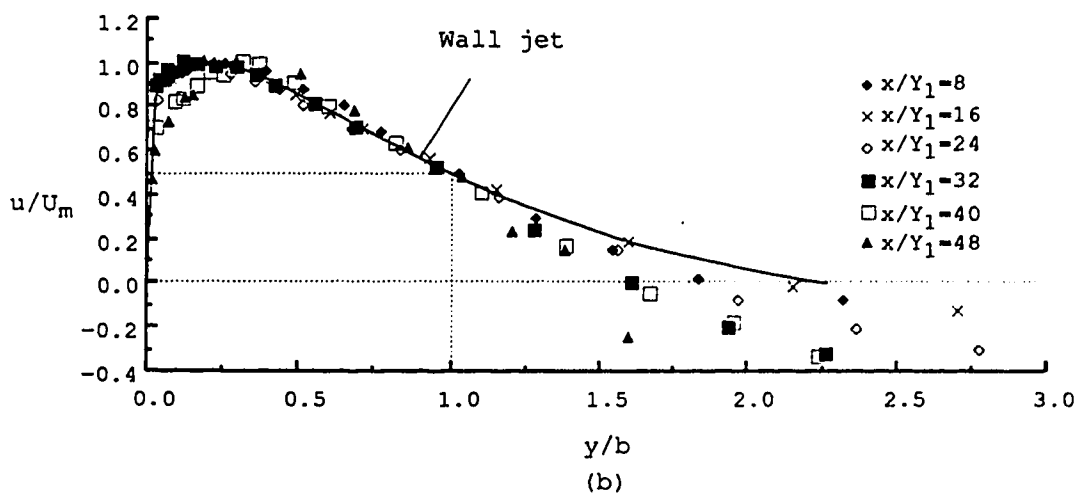
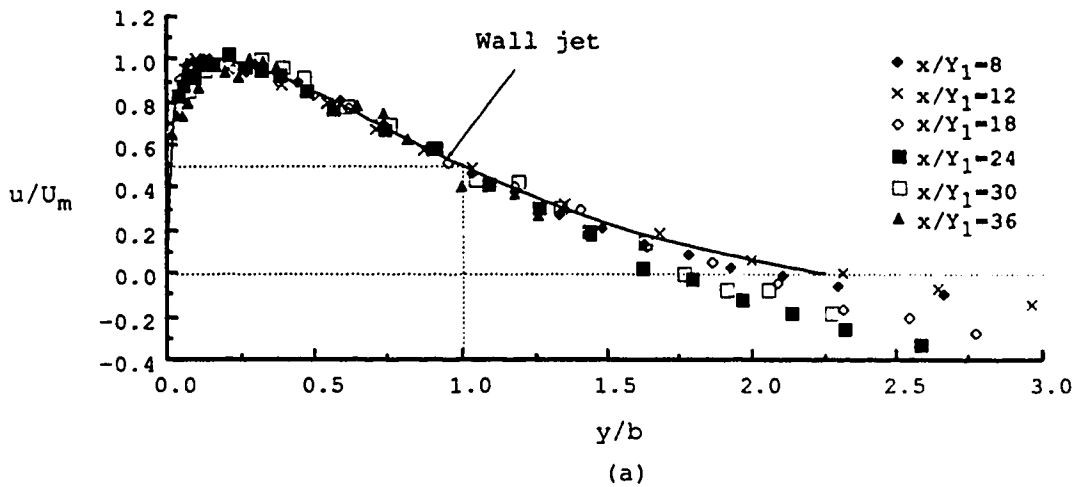


Figure 86. Similarity of velocity profiles in fully developed region for
 (a) $F_1=3.19$ and $S=0.85$;
 (b) $F_1=3.01$ and $S=1.69$.

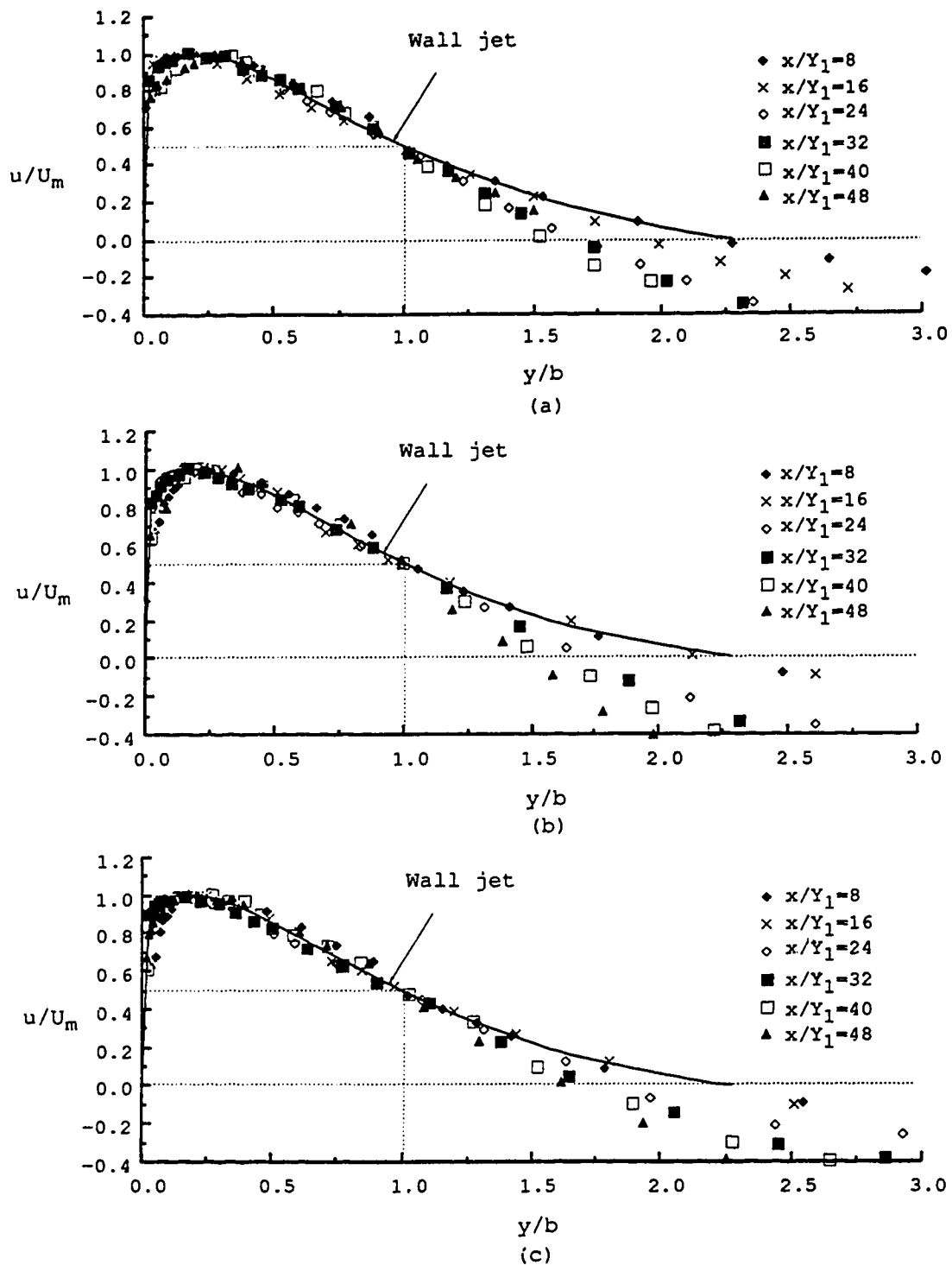


Figure 87. Similarity of velocity profiles
 (a) $F_1=5.61$ and $S=0.22$; (b) $F_1=5.49$ and $S=0.63$;
 (c) $F_1=5.43$ and $S=1.01$.

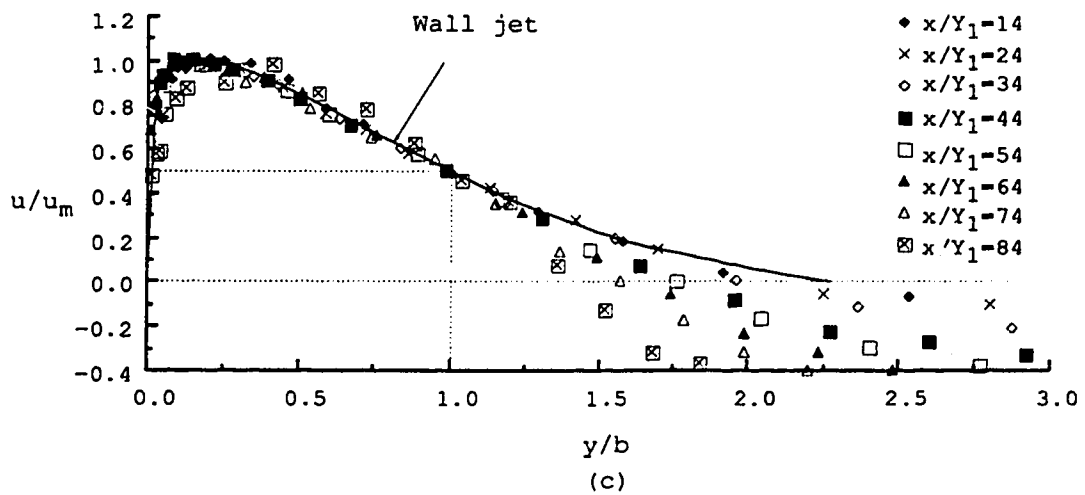
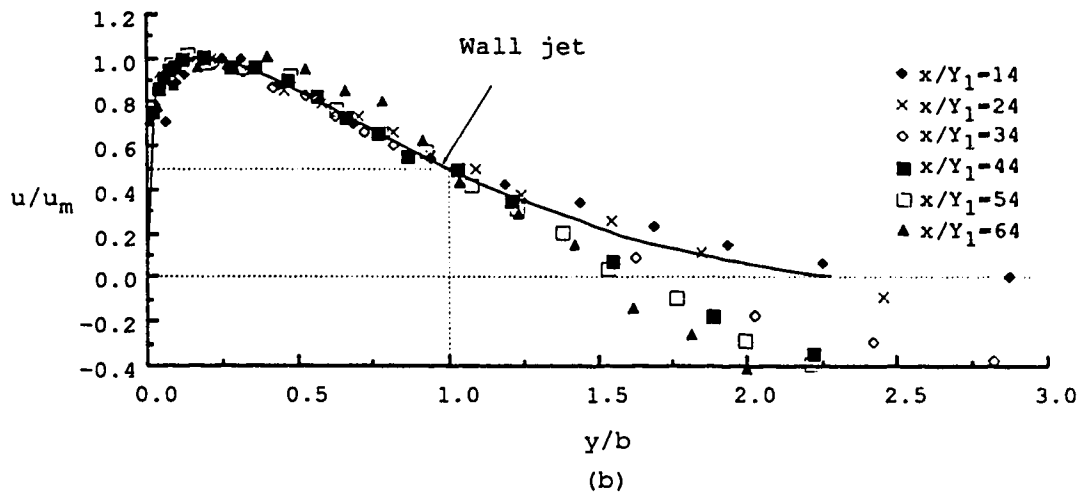
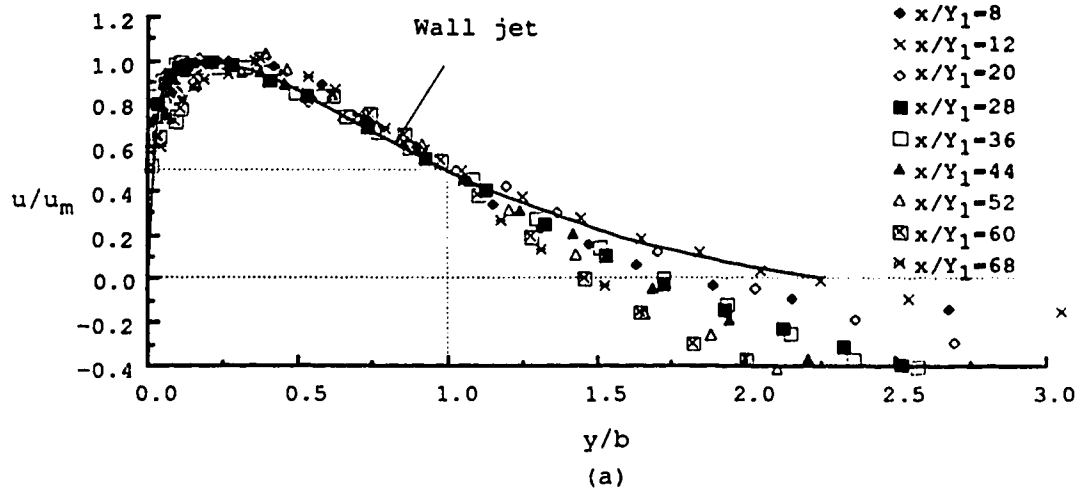


Figure 88. Similarity of velocity profiles in fully developed region for
 (a) $F_1=8.91$ and $S=0.24$; (b) $F_1=8.00$ and $S=0.62$;
 (c) $F_1=8.11$ and $S=1.00$.

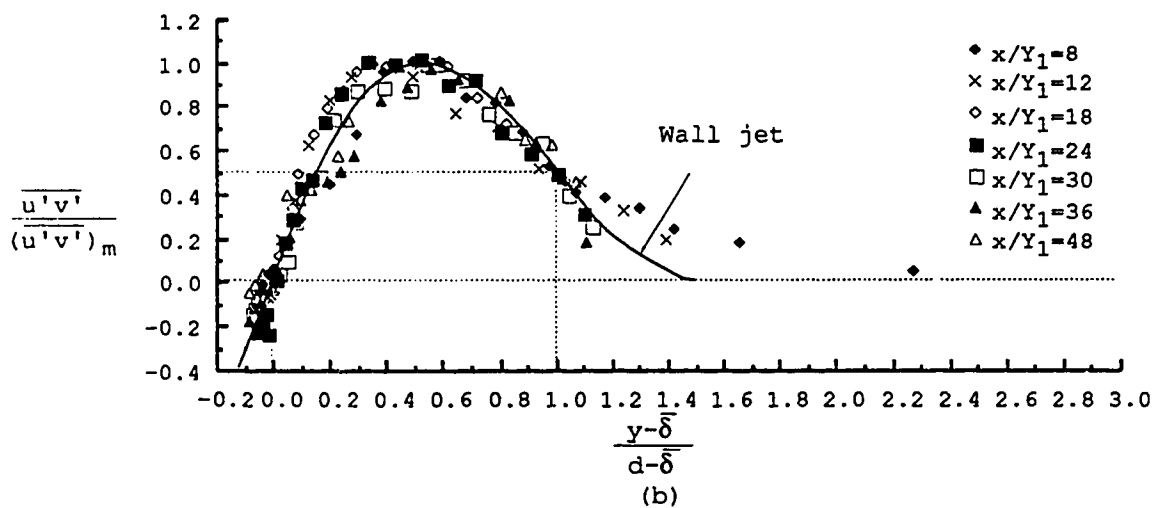
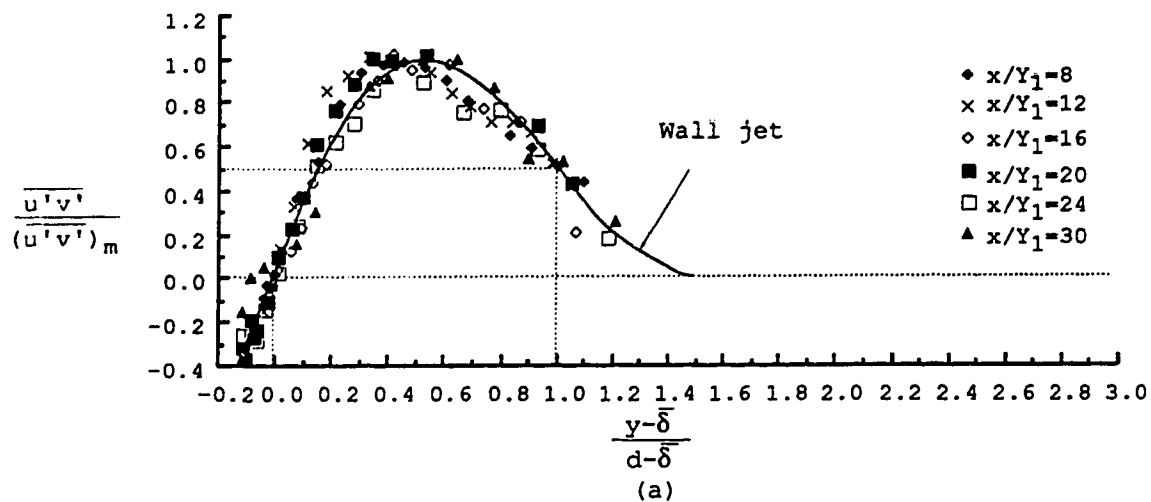


Figure 89. Similarity of turbulence shear stress profiles in fully developed region for
 (a) $F_1=3.11$ and $S=0.26$;
 (b) $F_1=3.20$ and $S=0.53$.

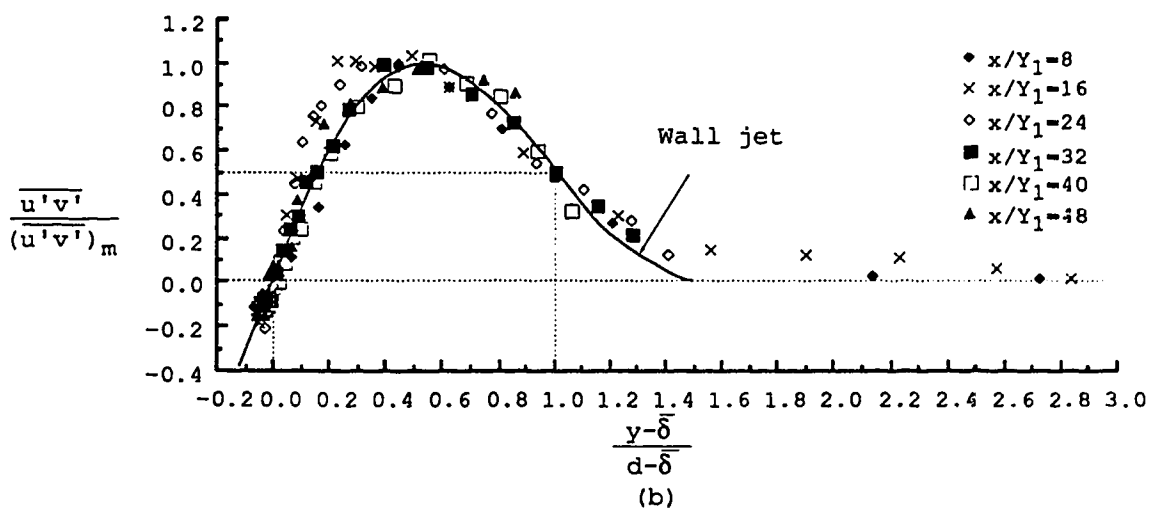
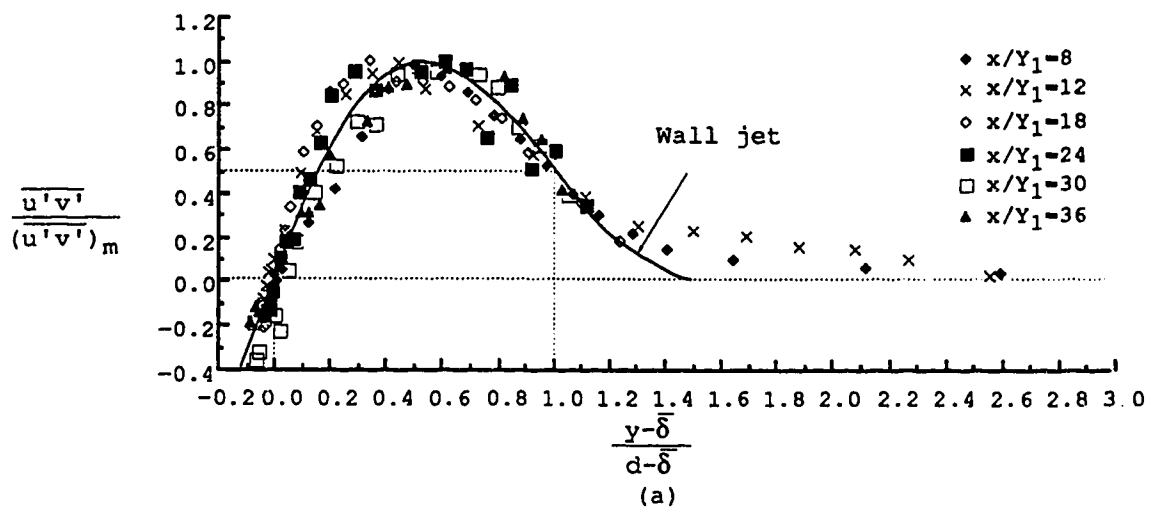


Figure 90. Similarity of turbulence shear stress profiles in fully developed region for
 (a) $F_1=3.19$ and $S=0.85$;
 (b) $F_1=3.01$ and $S=1.69$.

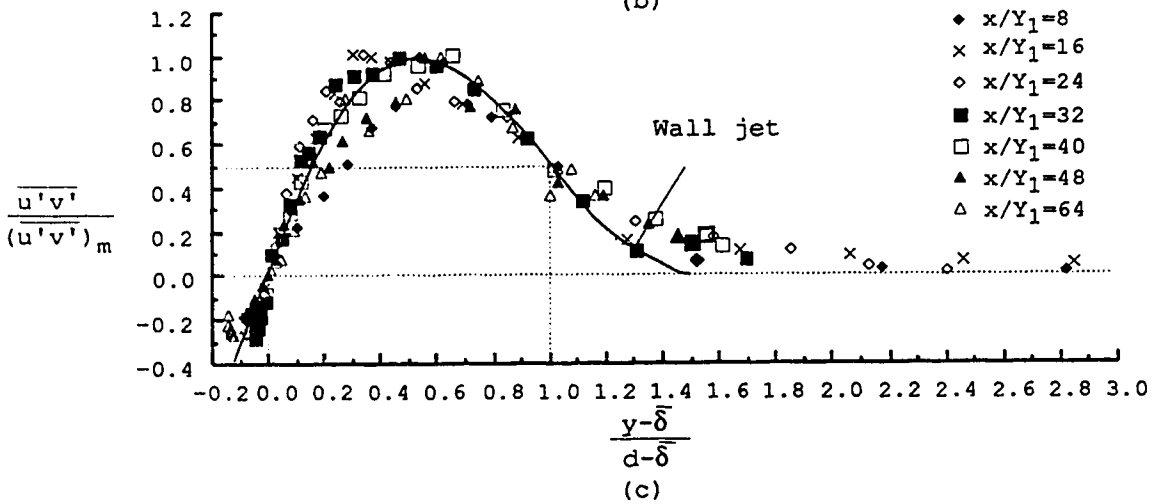
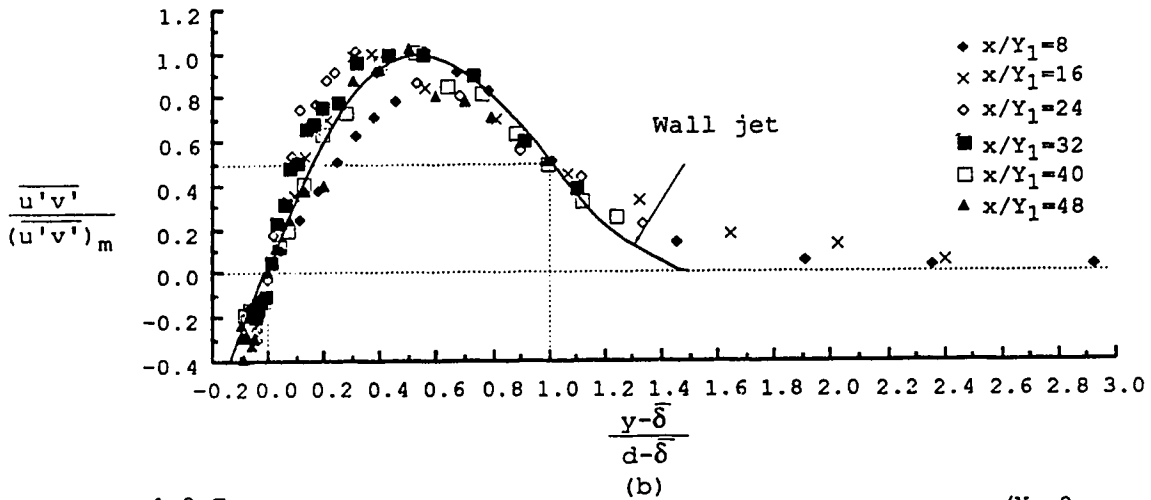
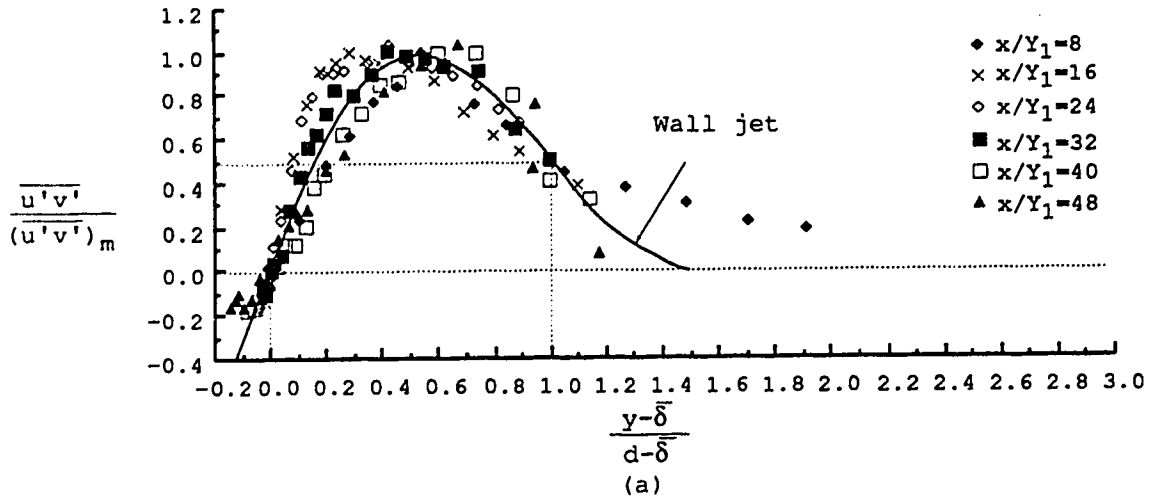


Figure 91. Similarity of turbulence shear stress profiles in fully developed region for (a) $F_1=5.61$ and $S=0.22$; (b) $F_1=5.49$ and $S=0.63$; (c) $F_1=5.43$ and $S=1.01$.

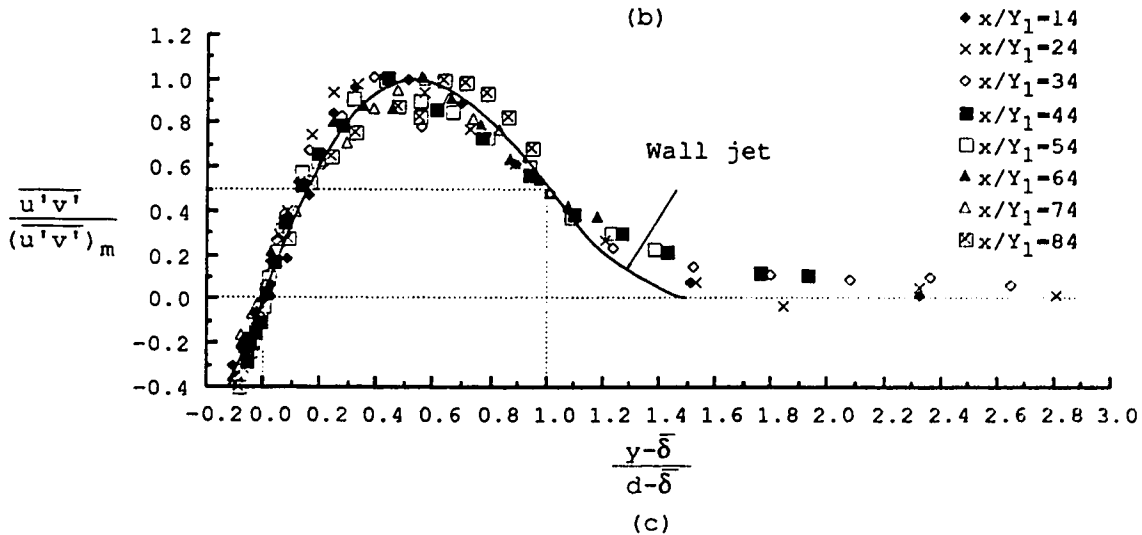
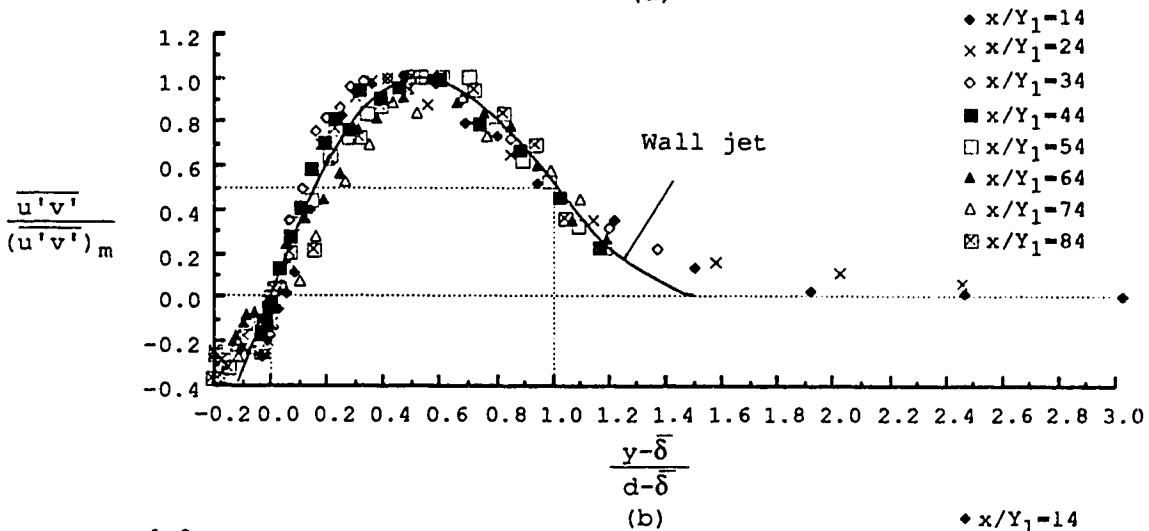
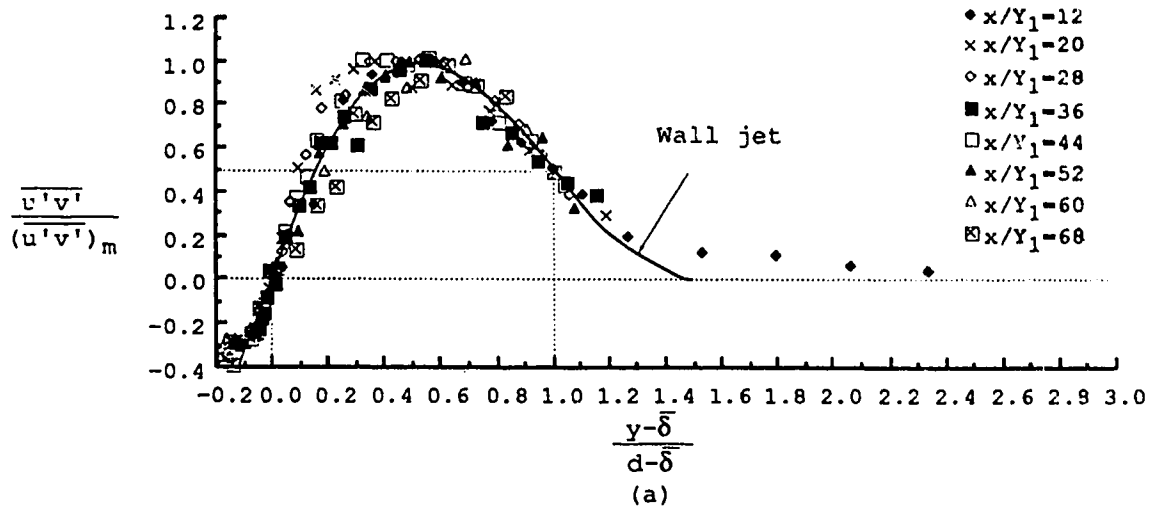


Figure 92. Similarity of turbulence shear stress profiles in fully developed region for
 (a) $F_1=8.91$ and $S=0.24$; (b) $F_1=8.00$ and $S=0.62$;
 (c) $F_1=8.11$ and $S=1.00$.

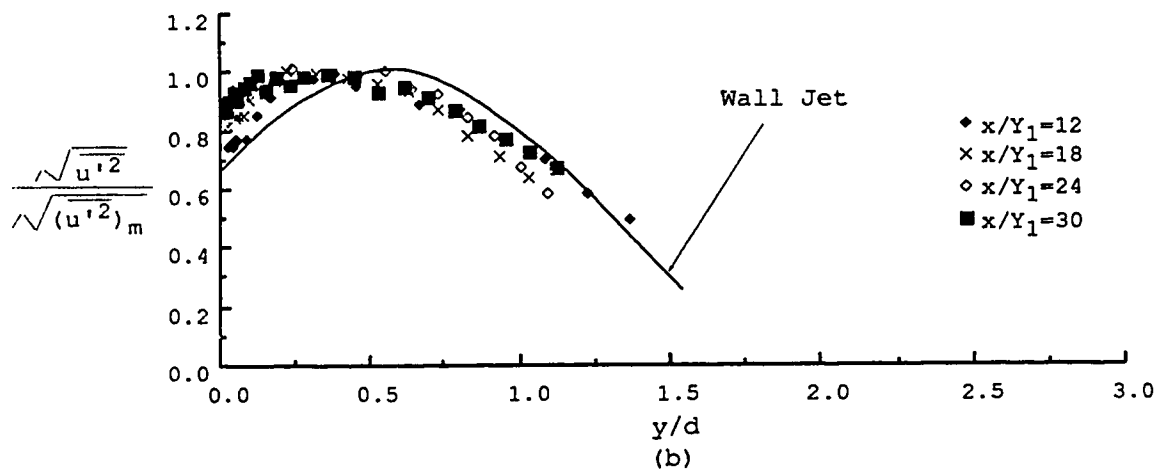
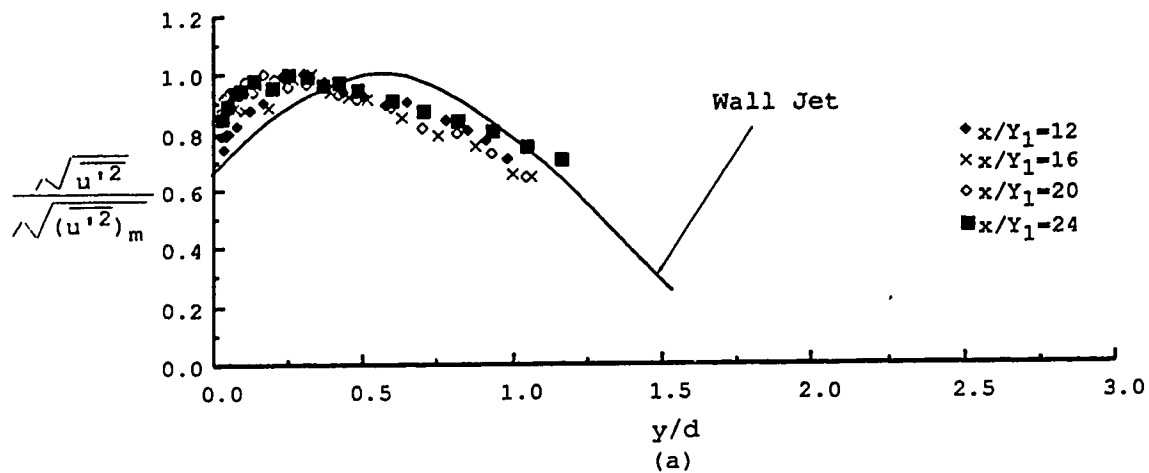


Figure 93. Similarity of longitudinal turbulence intensity profiles in fully developed region for
 (a) $F_1=3.11$ and $S=0.26$;
 (b) $F_1=3.20$ and $S=0.53$.

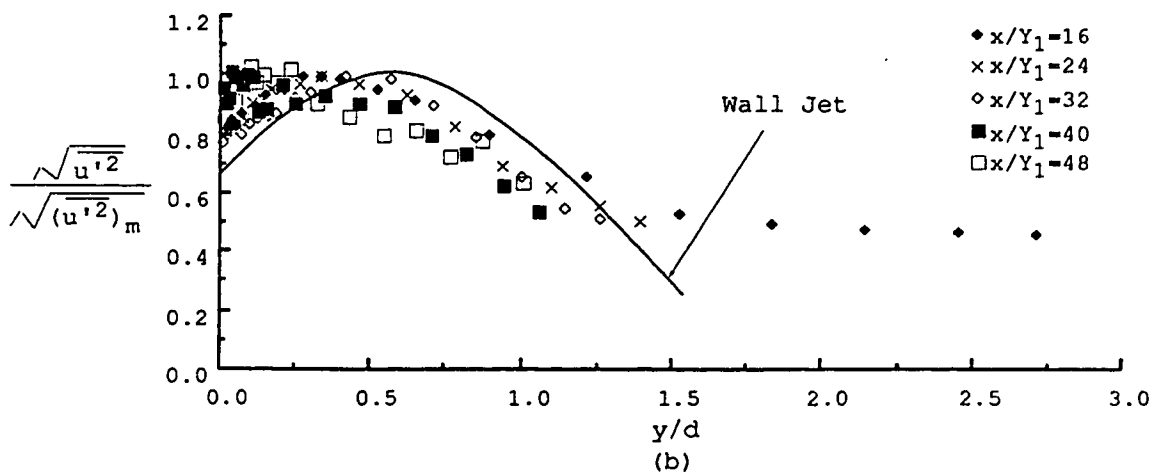
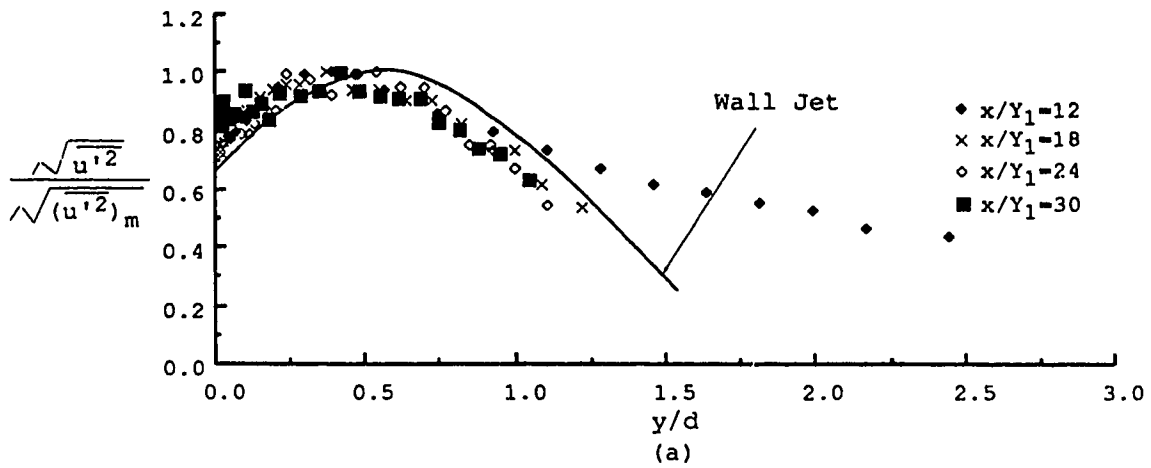


Figure 94. Similarity of longitudinal turbulence intensity profiles in fully developed region for
 (a) $F_1=3.19$ and $S=0.85$;
 (b) $F_1=3.01$ and $S=1.69$.

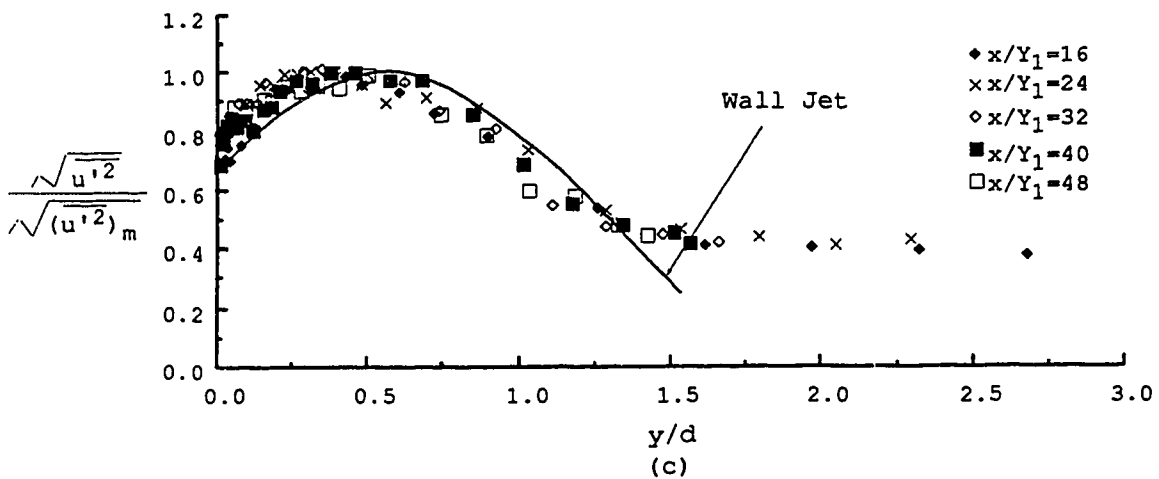
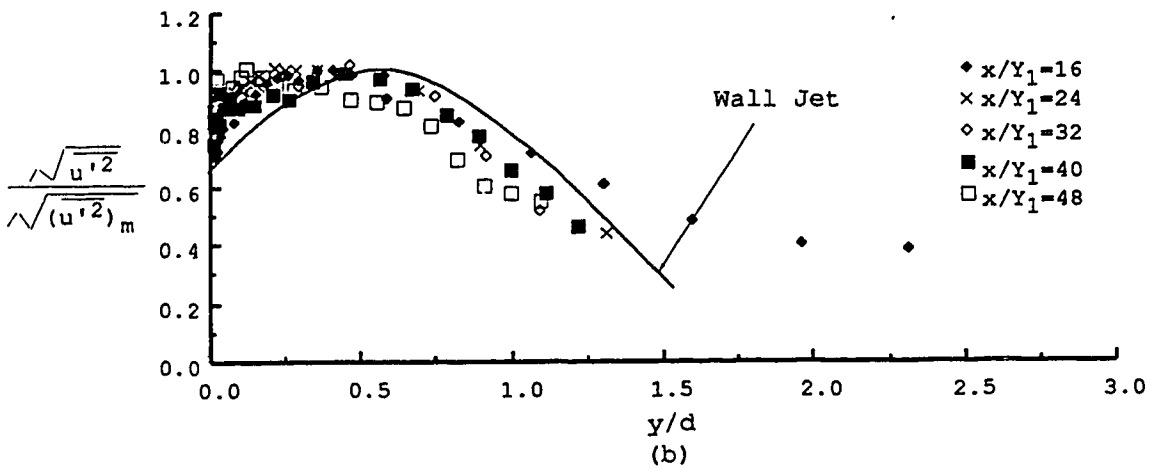
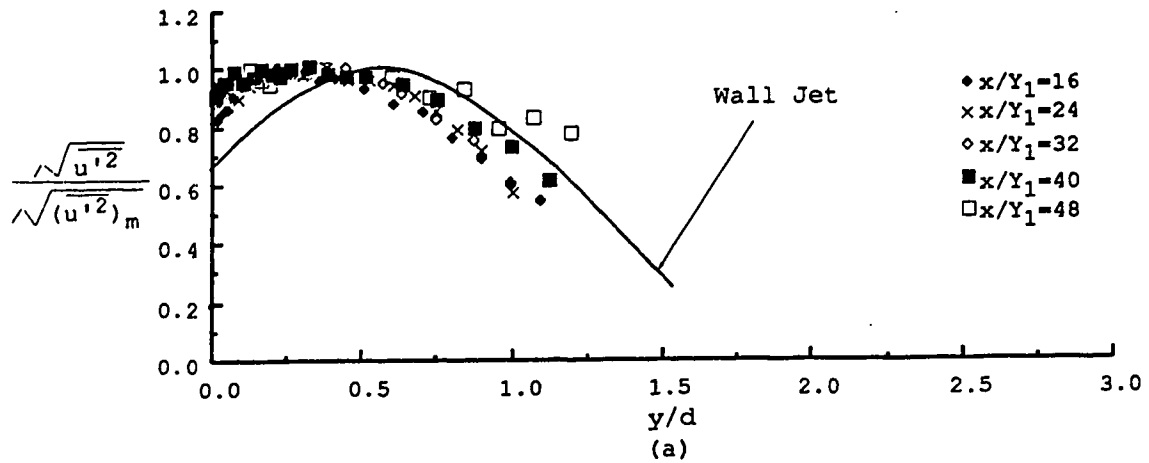


Figure 95. Similarity of longitudinal turbulence intensity profiles in fully developed region for
 (a) $F_1=5.61$ and $S=0.22$; (b) $F_1=5.49$ and $S=0.63$;
 (c) $F_1=5.43$ and $S=1.01$

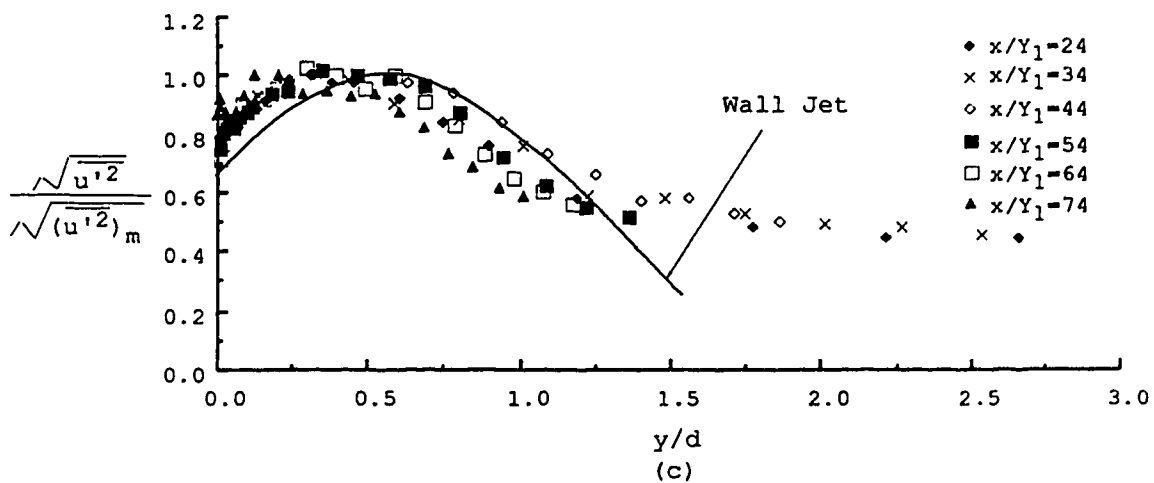
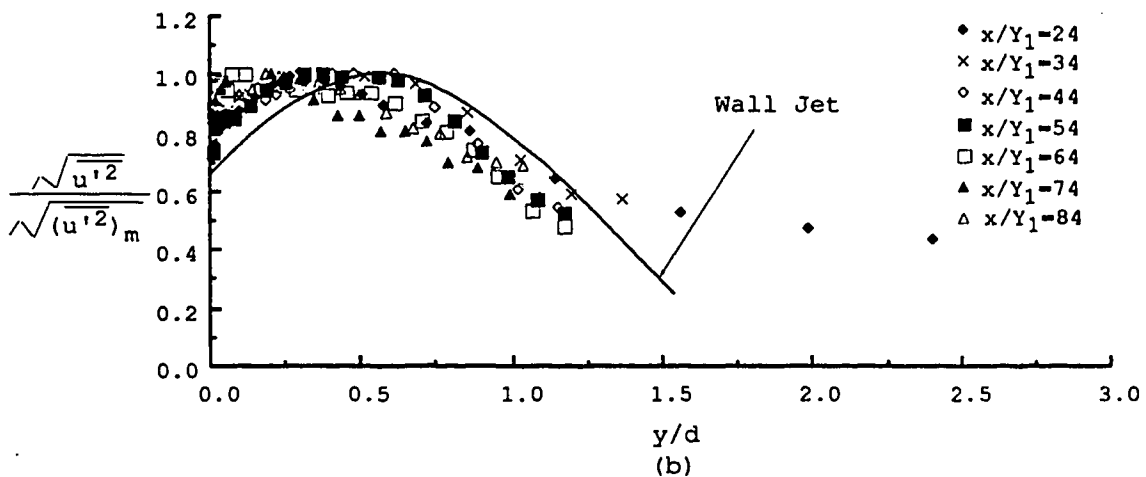
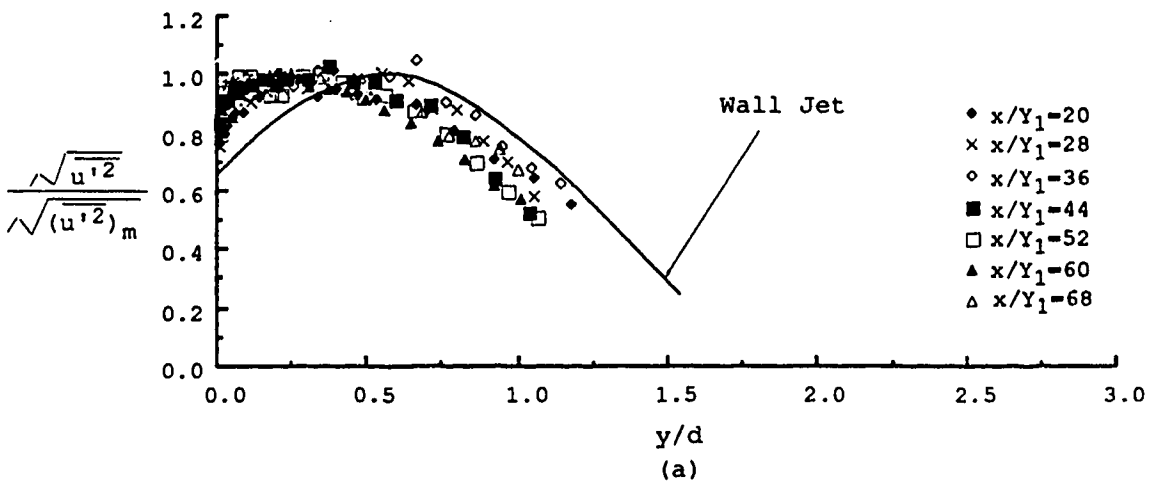


Figure 96. Similarity of longitudinal turbulence intensity profiles in fully developed region for
 (a) $F_1=8.19$ and $S=0.24$; (b) $F_1=8.00$ and $S=0.62$;
 (c) $F_1=8.11$ and $S=1.00$.

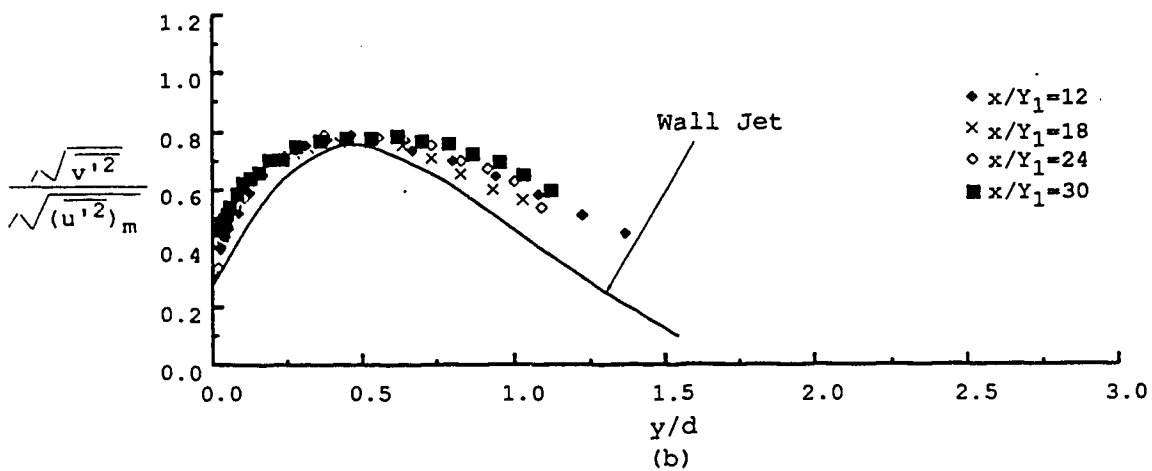
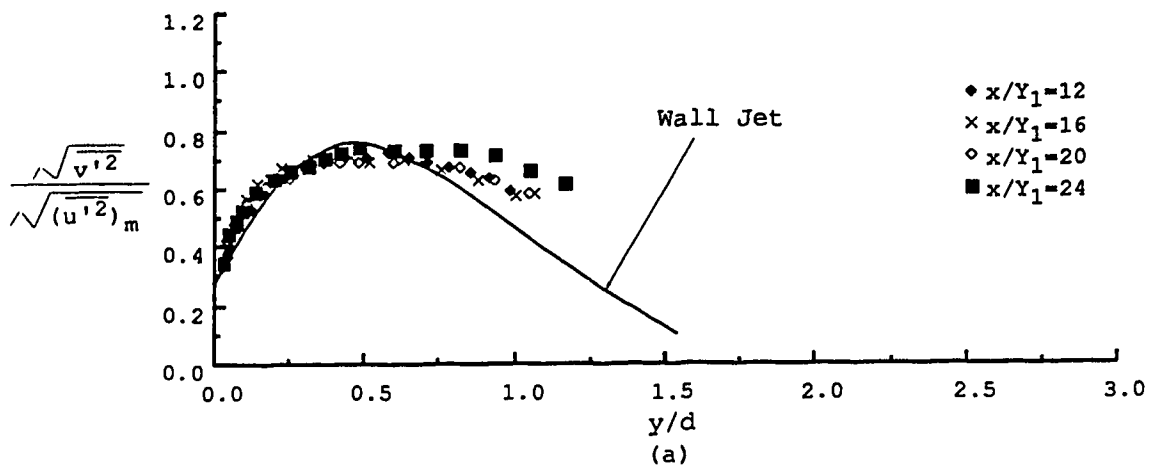


Figure 97. Similarity of vertical turbulence intensity profiles in fully developed region for
 (a) $F_1=3.11$ and $S=0.26$; (b) $F_1=3.20$ and $S=0.53$;
 (c) $F_1=3.19$ and $S=0.85$

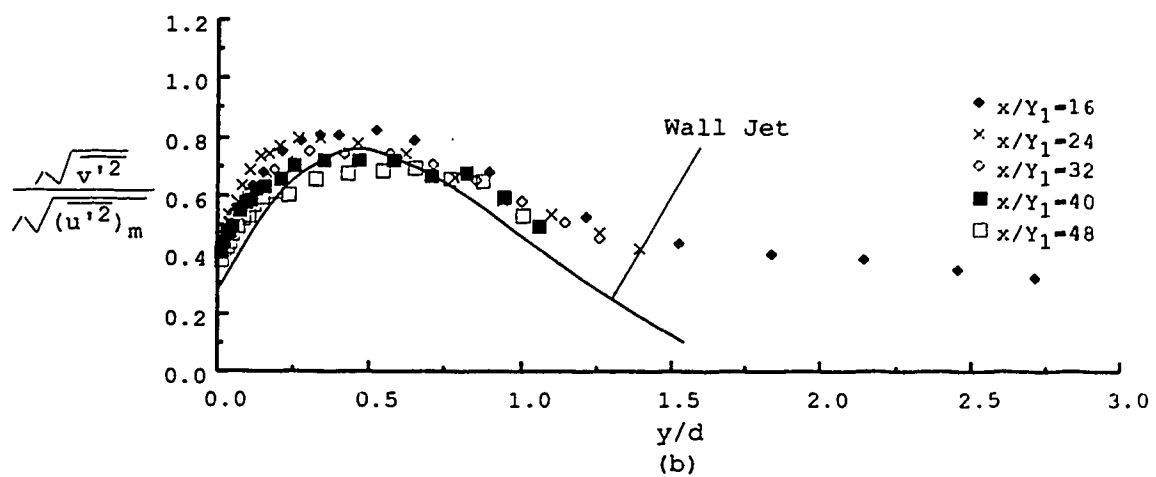
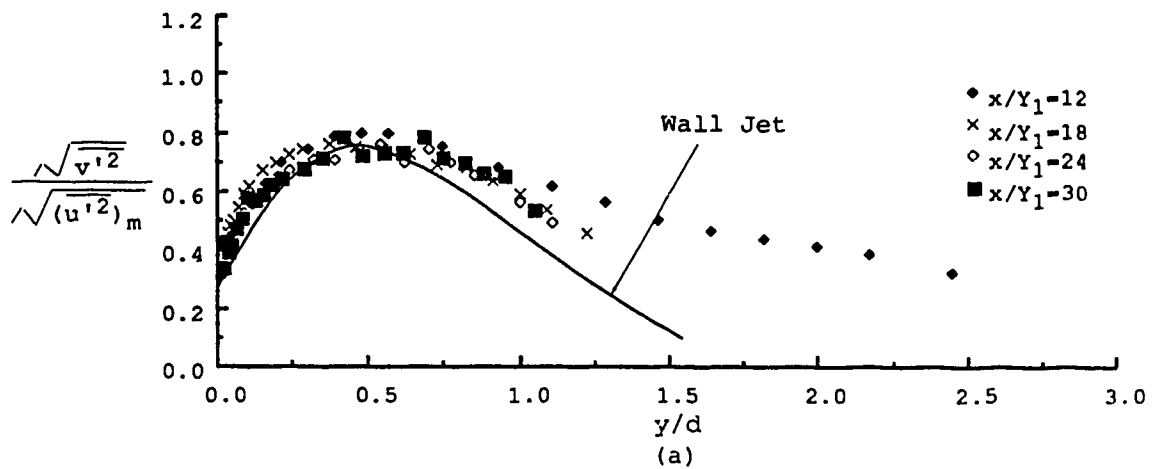


Figure 98. Similarity of vertical turbulence intensity profiles in fully developed region for
 (a) $F_1=3.19$ and $S=0.85$;
 (b) $F_1=3.01$ and $S=1.69$

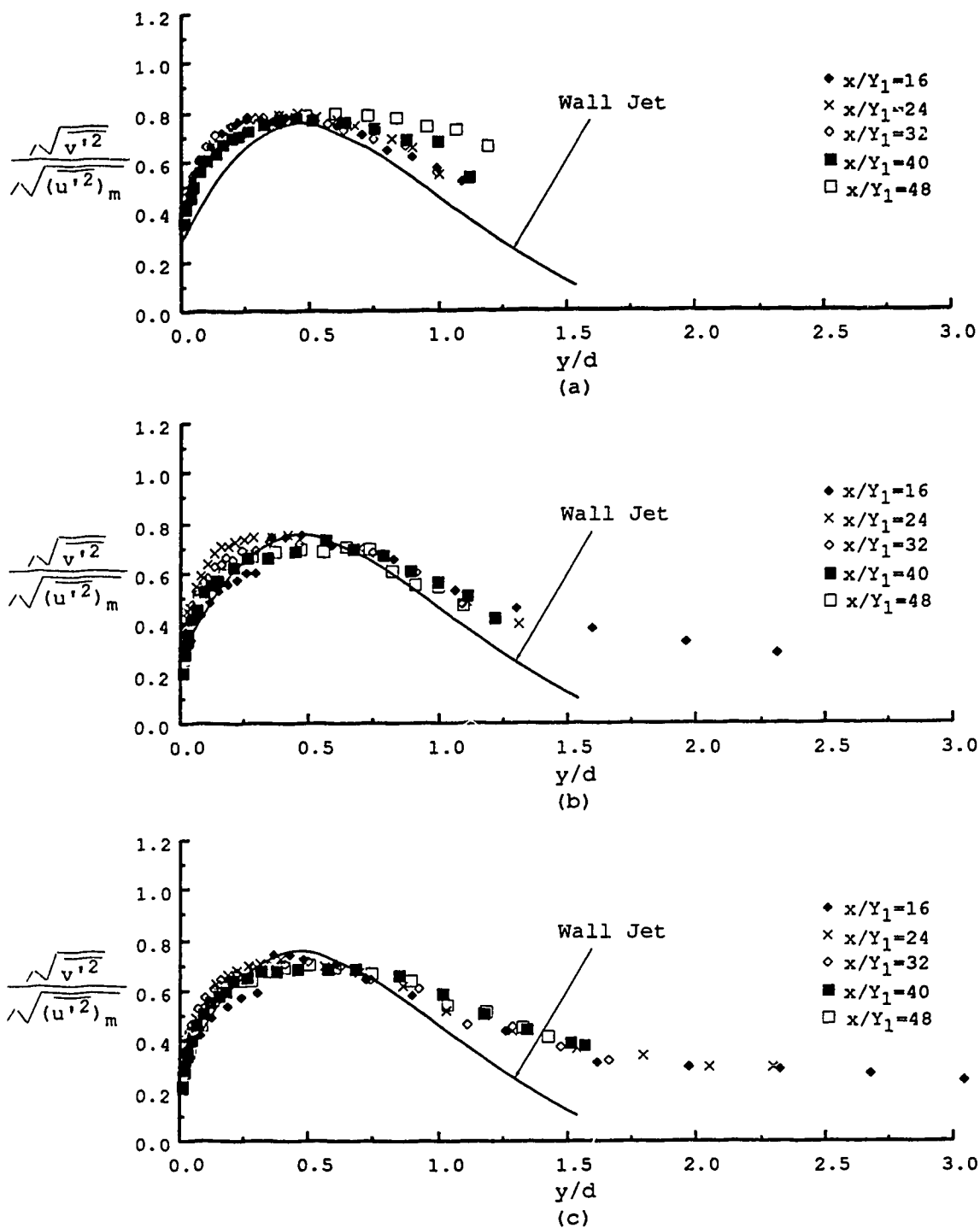


Figure 99. Similarity of vertical turbulence intensity profiles in fully developed region for
 (a) $F_1=5.61$ and $S=0.22$; (b) $F_1=5.49$ and $S=0.63$;
 (c) $F_1=5.43$ and $S=1.01$

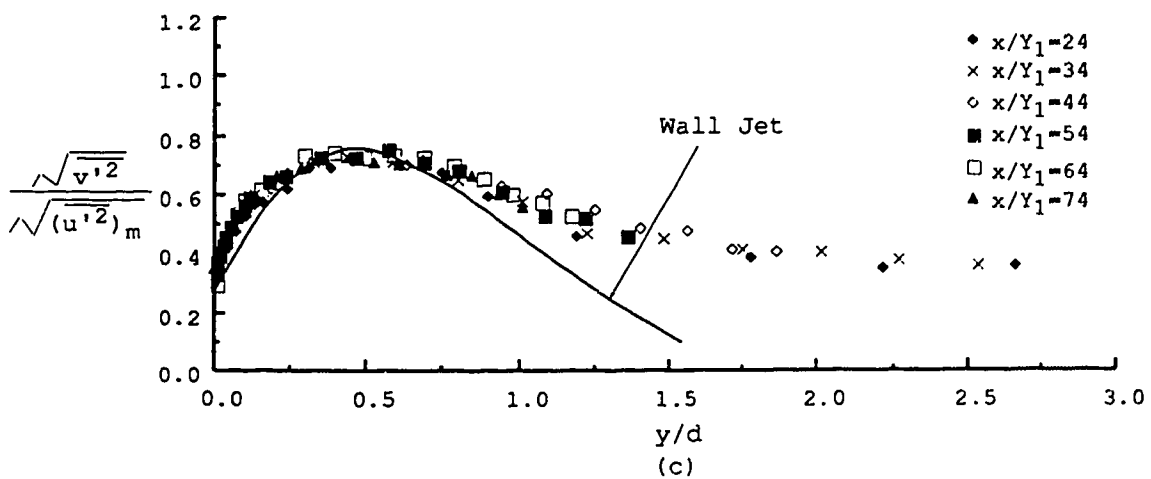
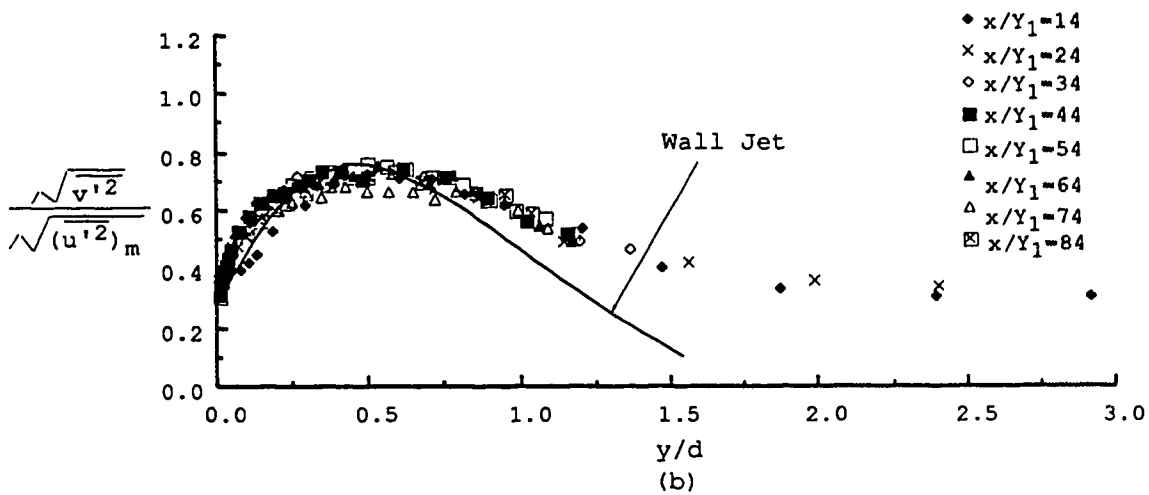
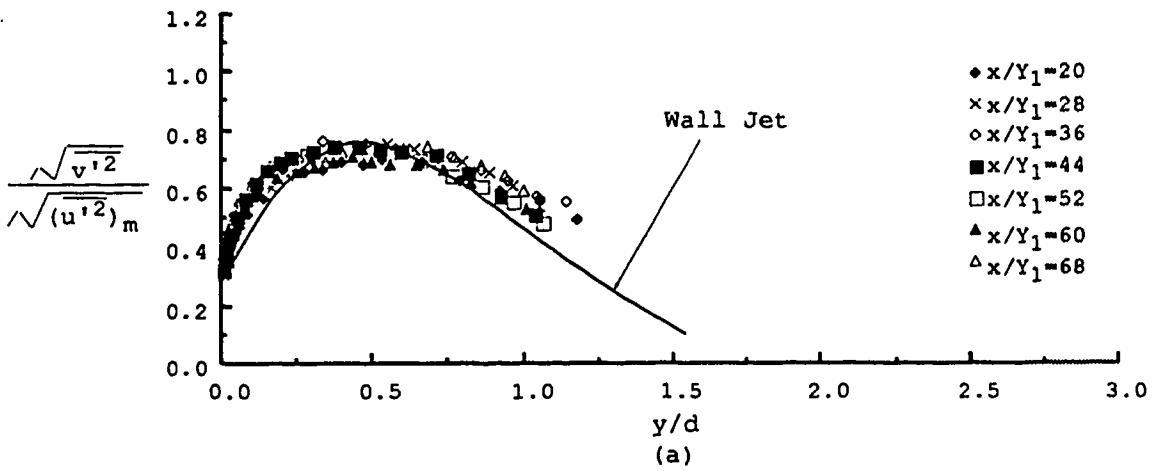


Figure 100. Similarity of vertical turbulence intensity profiles in fully developed region for
 (a) $F_1=8.19$ and $S=0.24$; (b) $F_1=8.00$ and $S=0.62$;
 (c) $F_1=8.11$ and $S=1.00$.

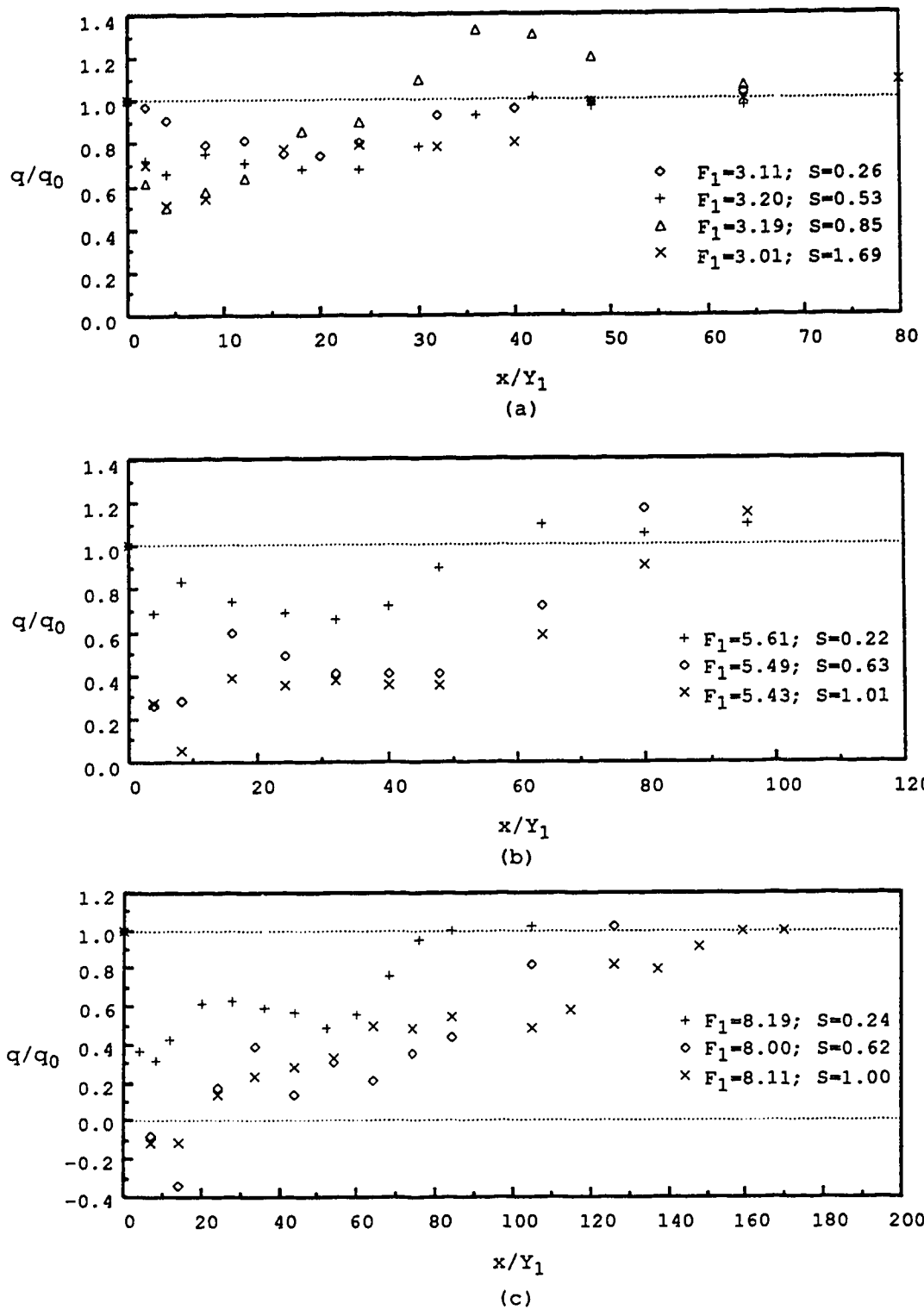


Figure 101. Unit discharge distribution along the jump at the measuring plane of $z/W=0.36$ for all conditions.

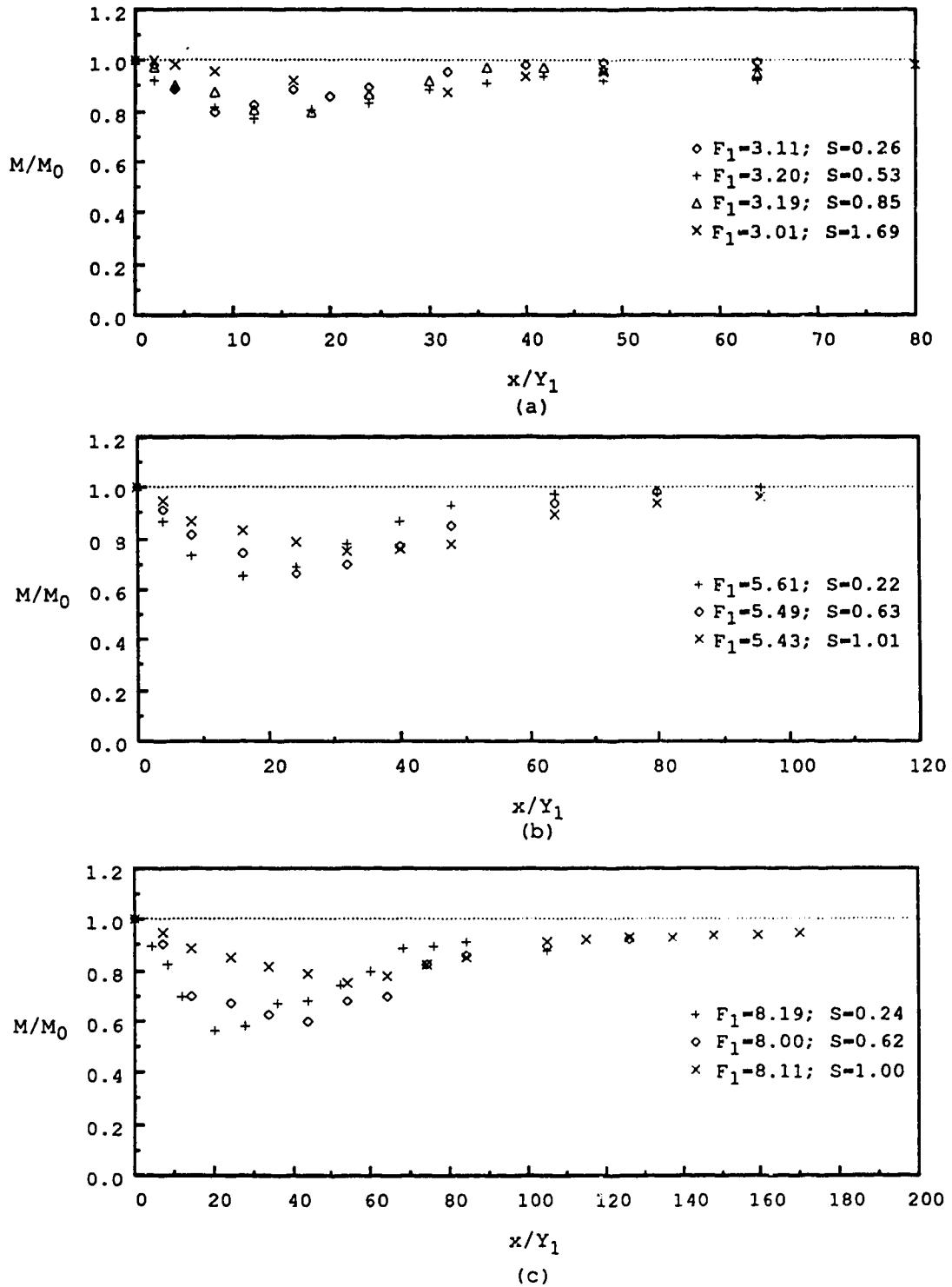


Figure 102. Unit momentum distribution along the jump at the measuring plane of $z/W=0.36$ for all conditions.

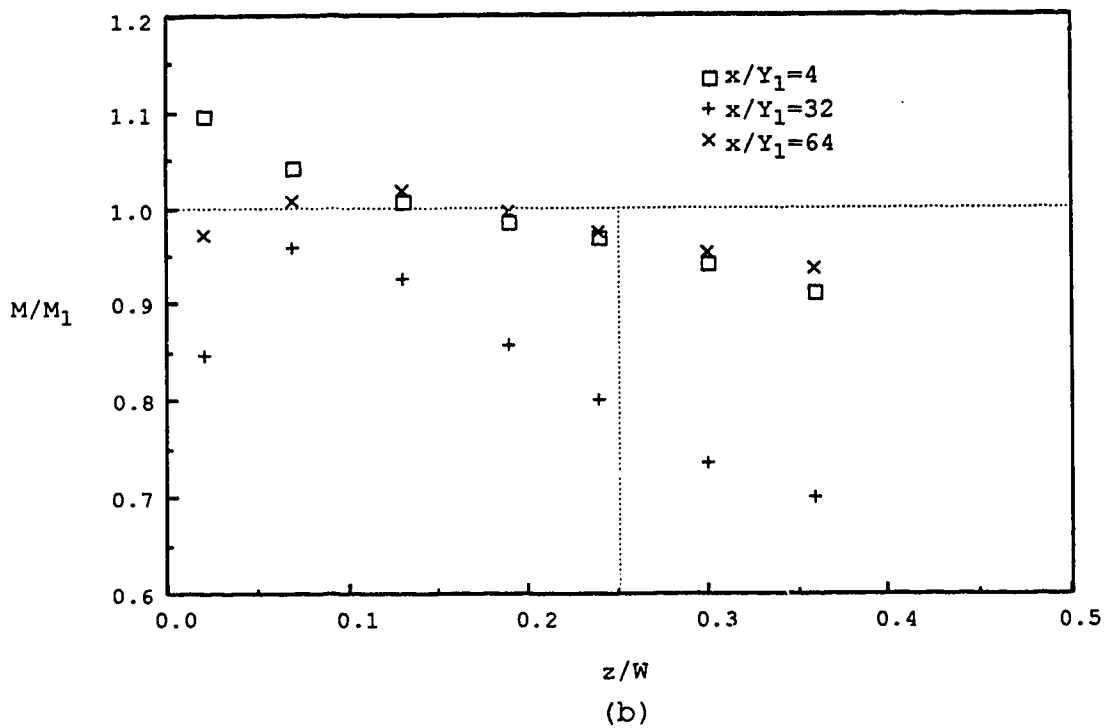
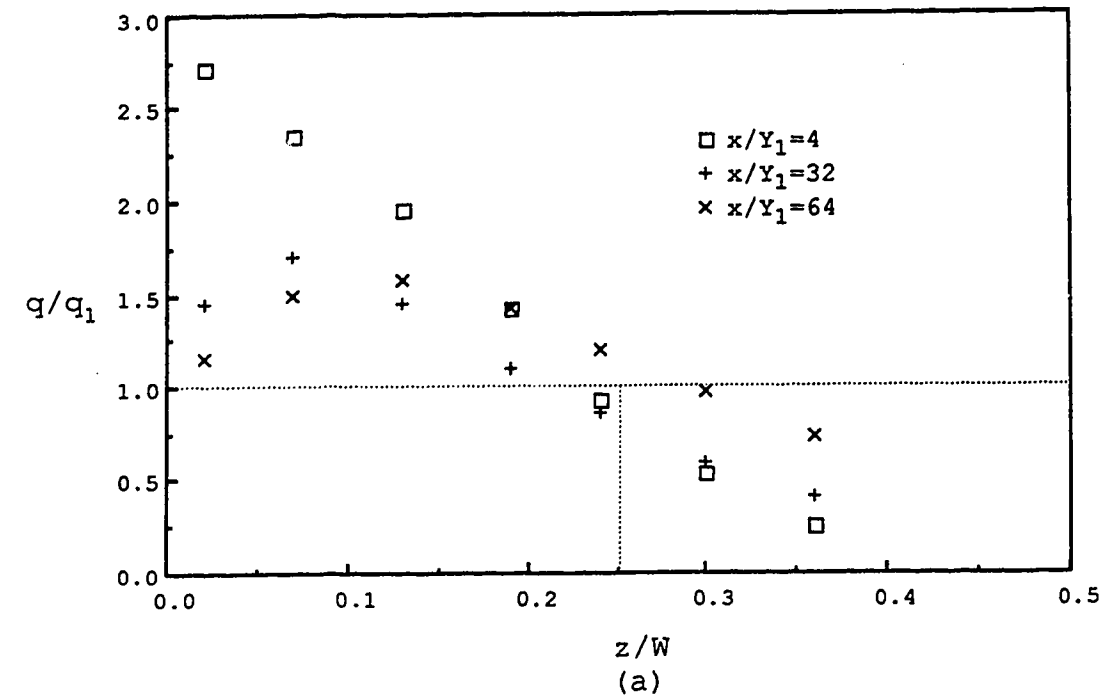


Figure 103. Unit discharge q and unit kinematic momentum flux M distributions across the flume for three cross sections for $F_1=5.49$ and $S=0.63$.

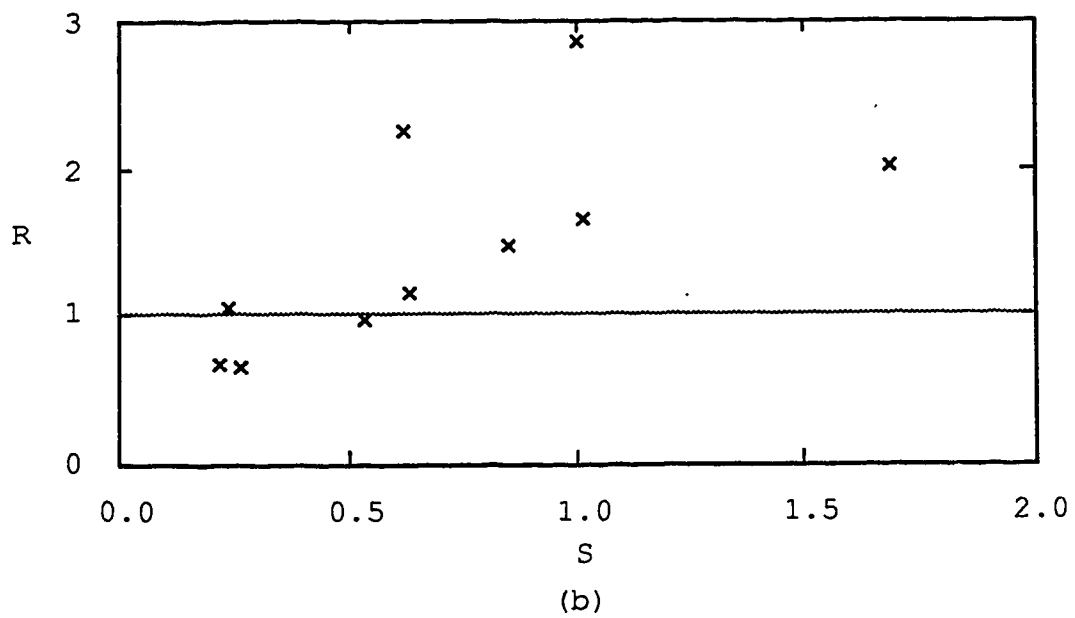
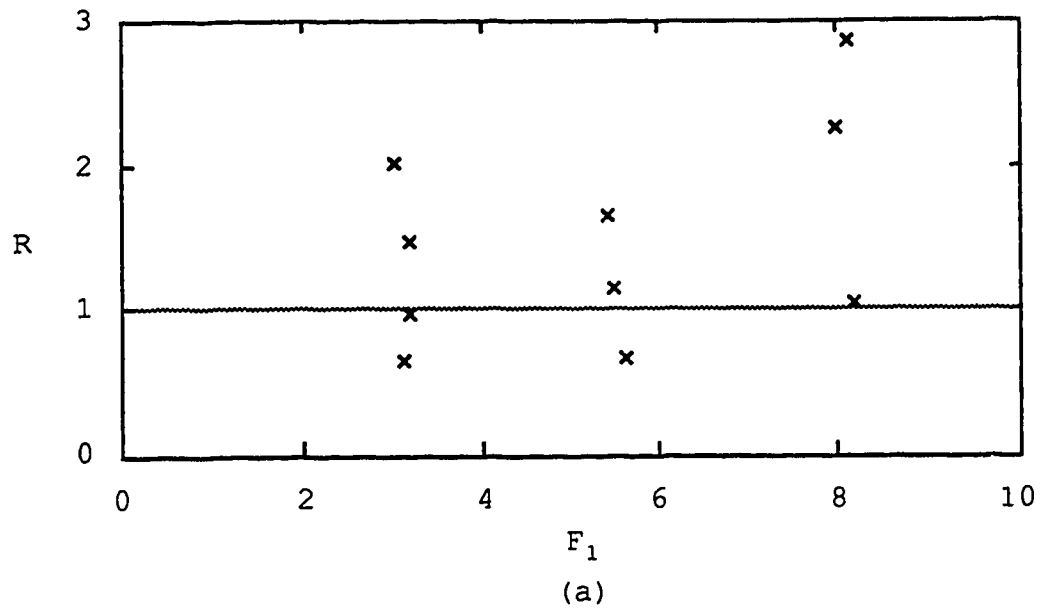


Figure 104. The ratio of predicted roller length over measured roller length vs F_1 and S .

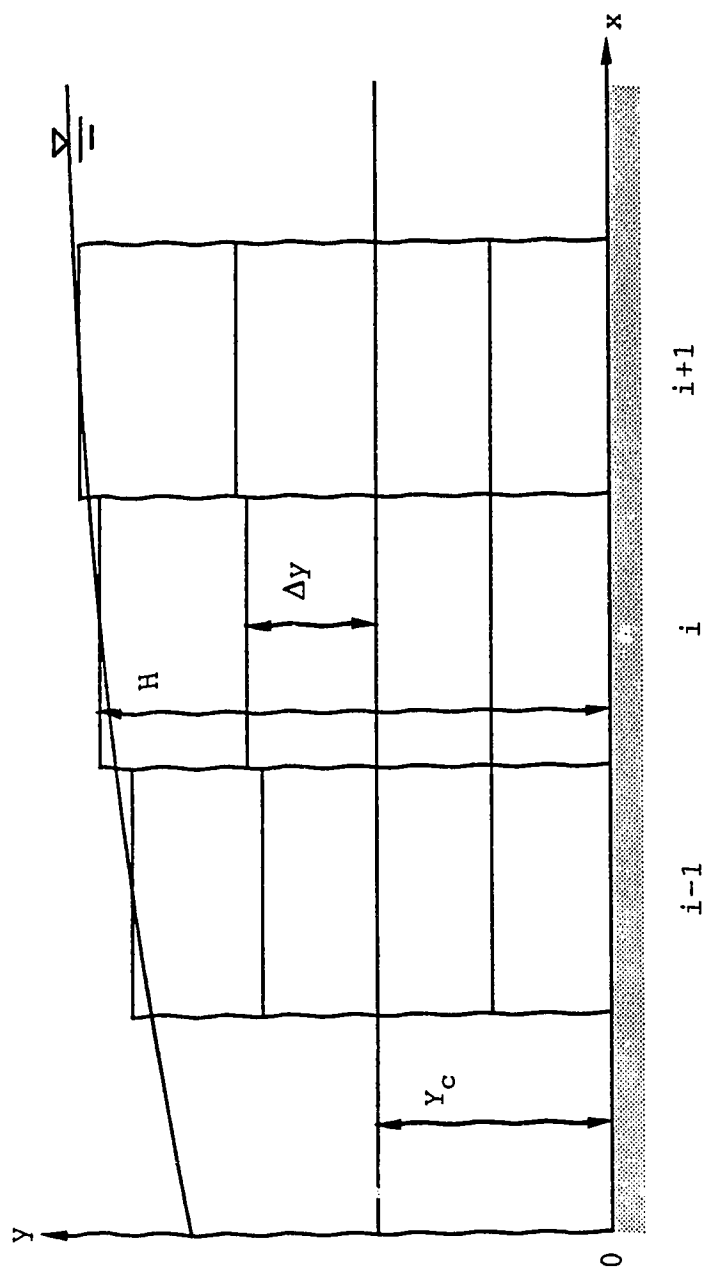


Figure 105. A Typical Discretization of Offset Control Volumes

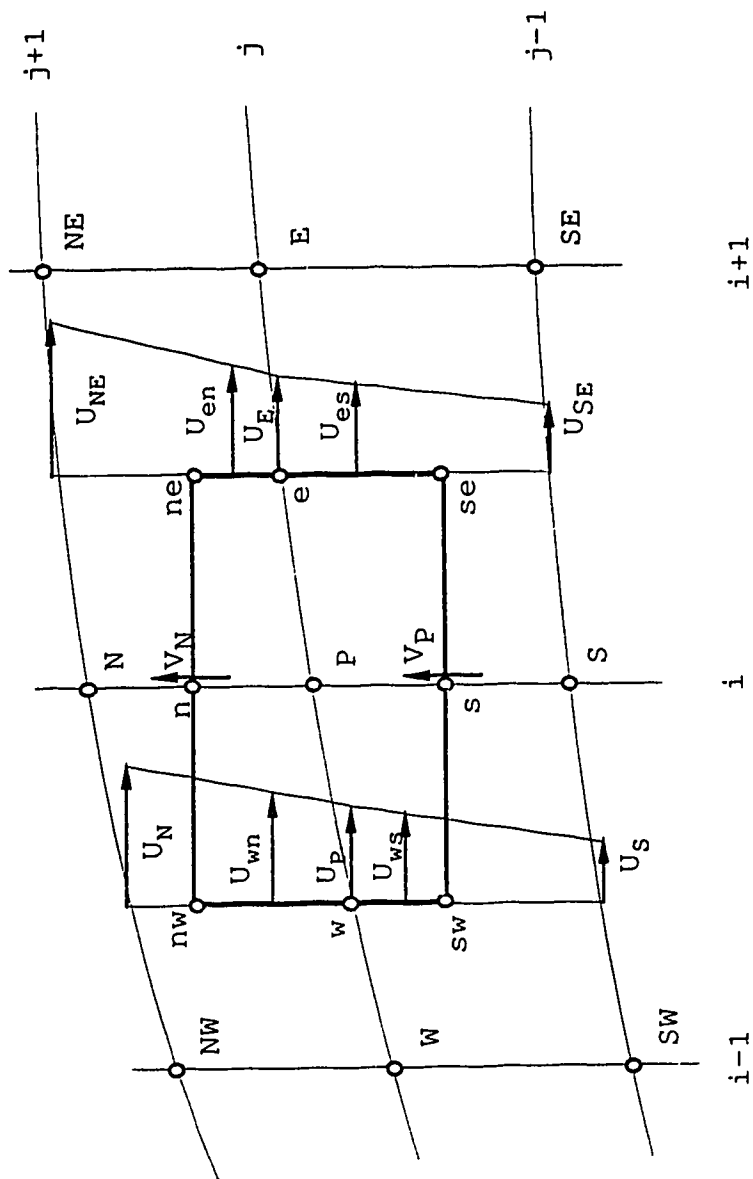


Figure 106. A Typical Control Volume for the Conservation of Mass.

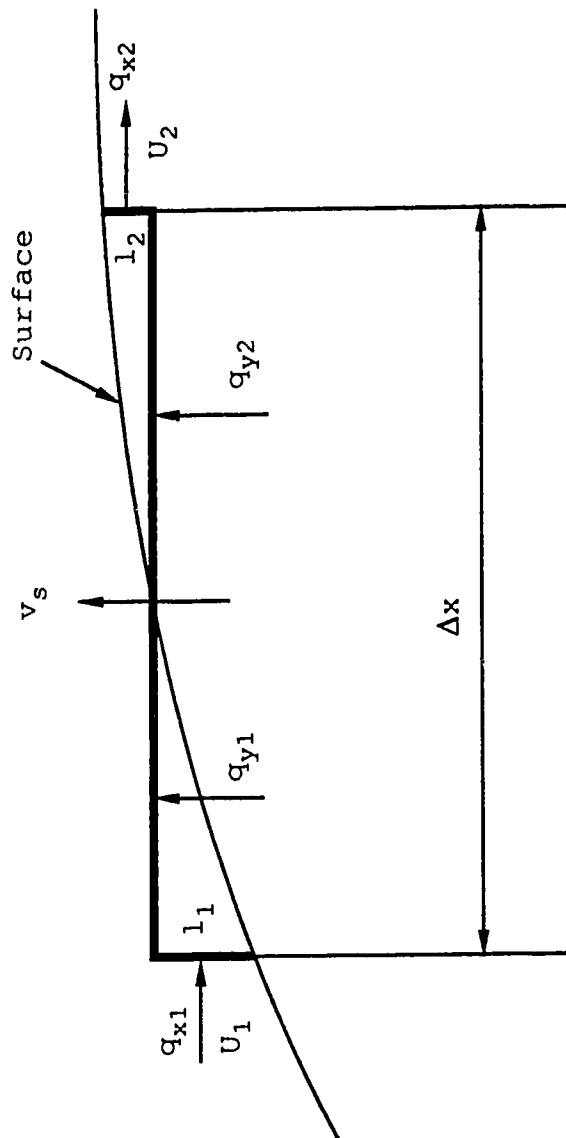


Figure 107. Water Surface Condition for the Conservation of Mass.

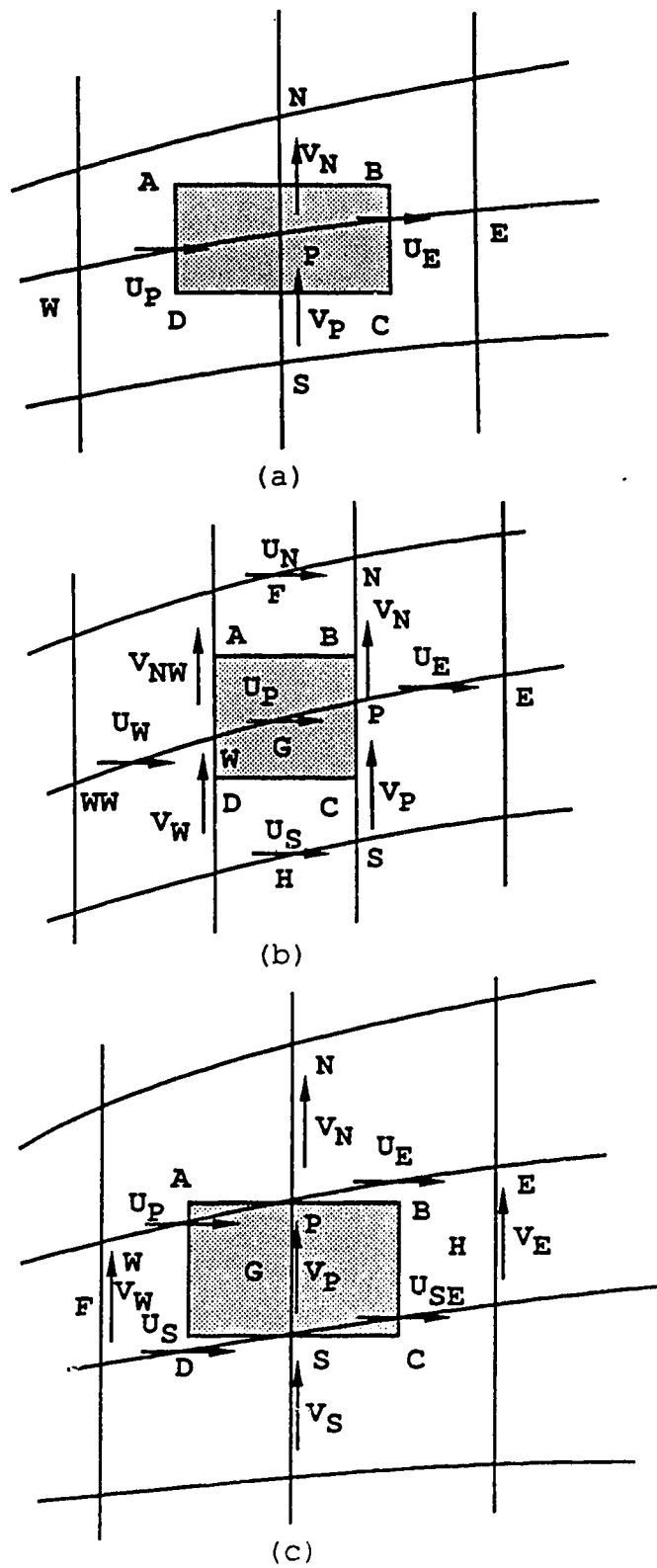


Figure 108. Different control volumes.

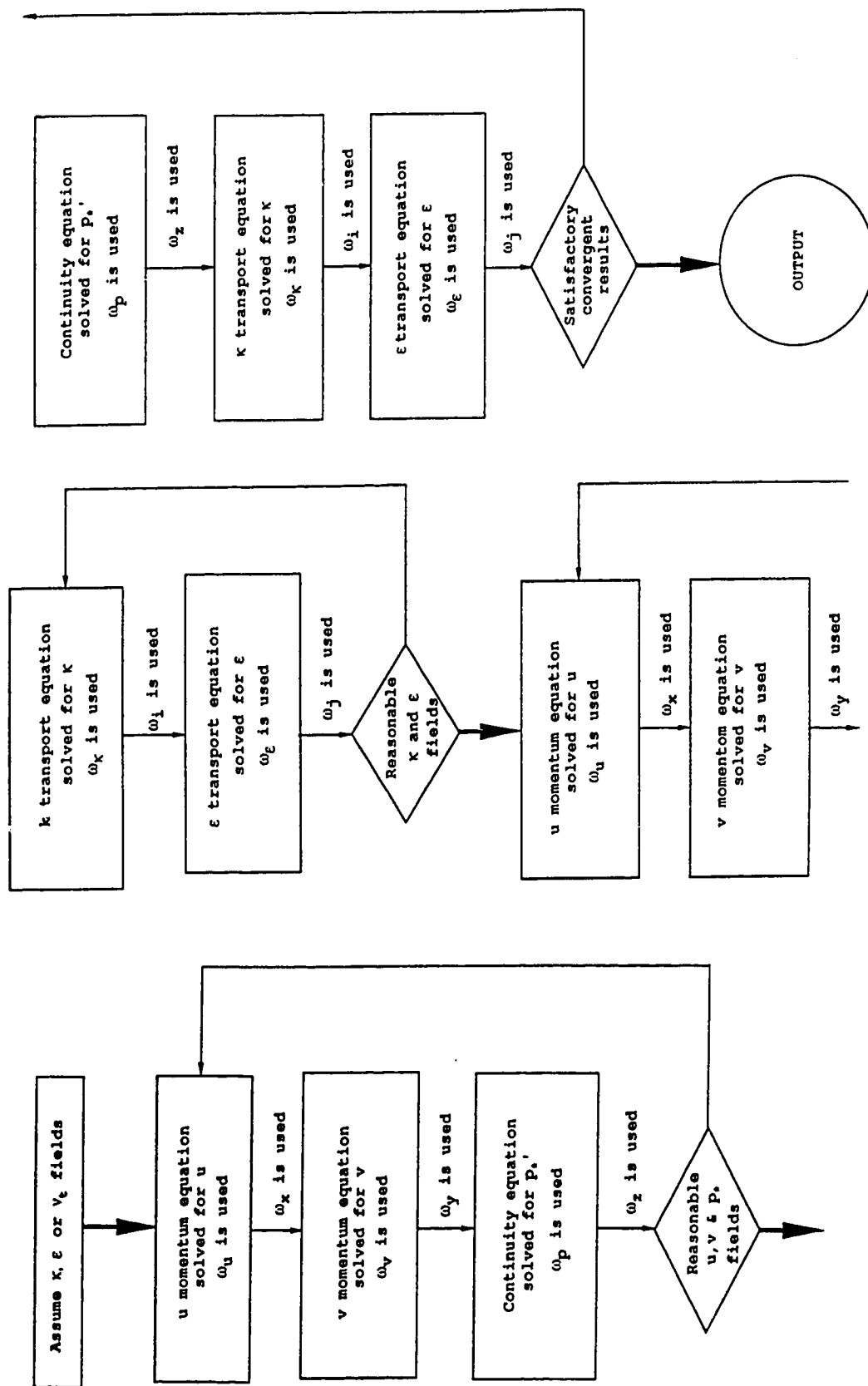


Figure 109. Calculation flow chart.

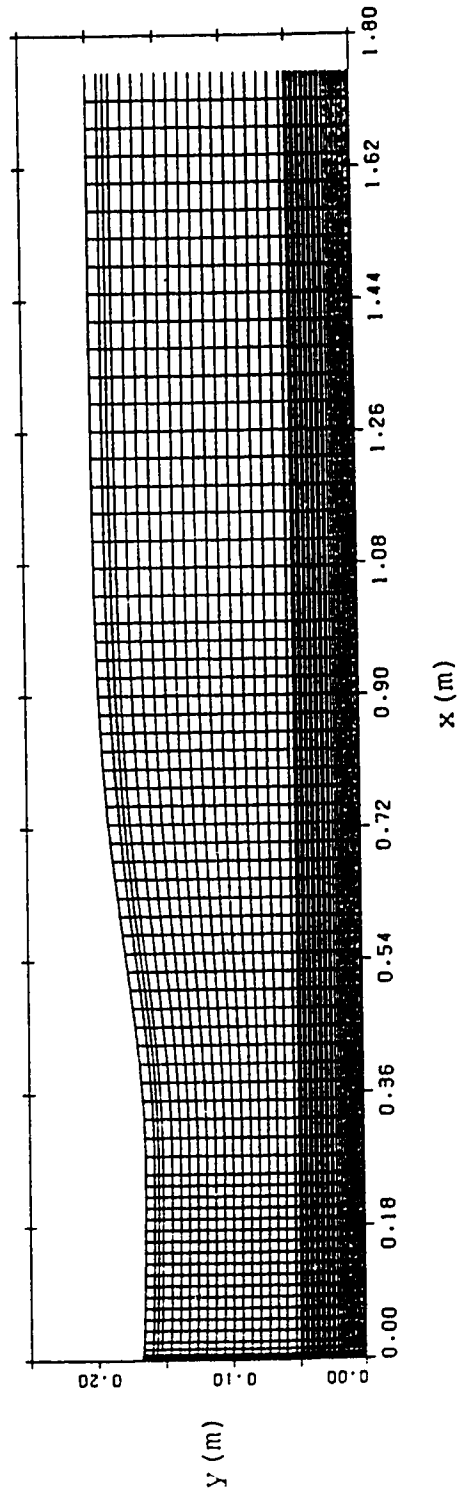


Figure 110. Calculation mesh for $F_1=3.19$ and $S=0.85$.

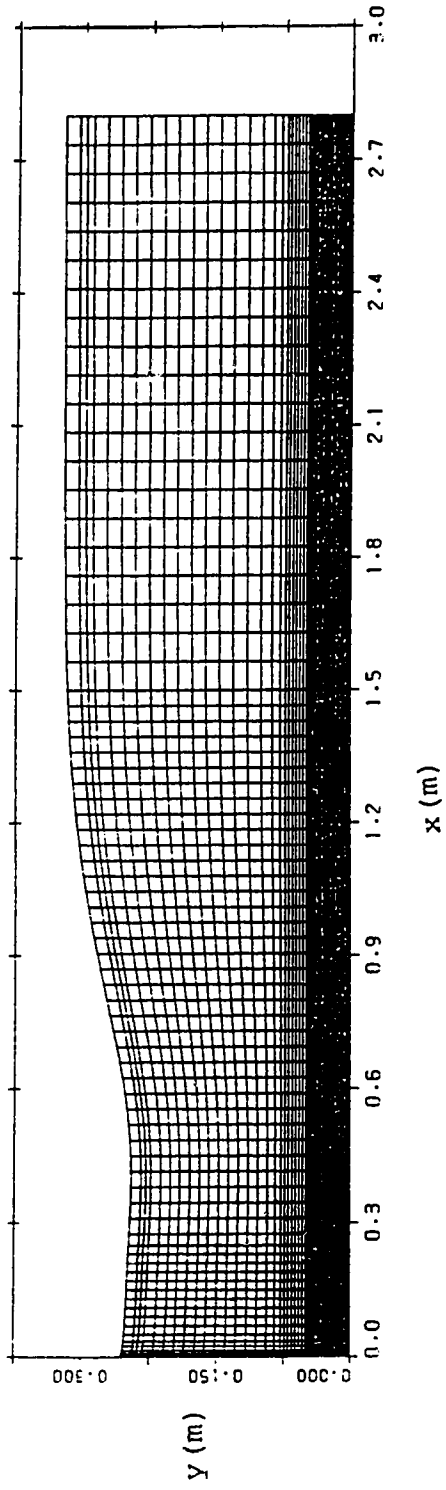


Figure 111. Calculation mesh for $F_1=5.49$ and $S=0.63$.

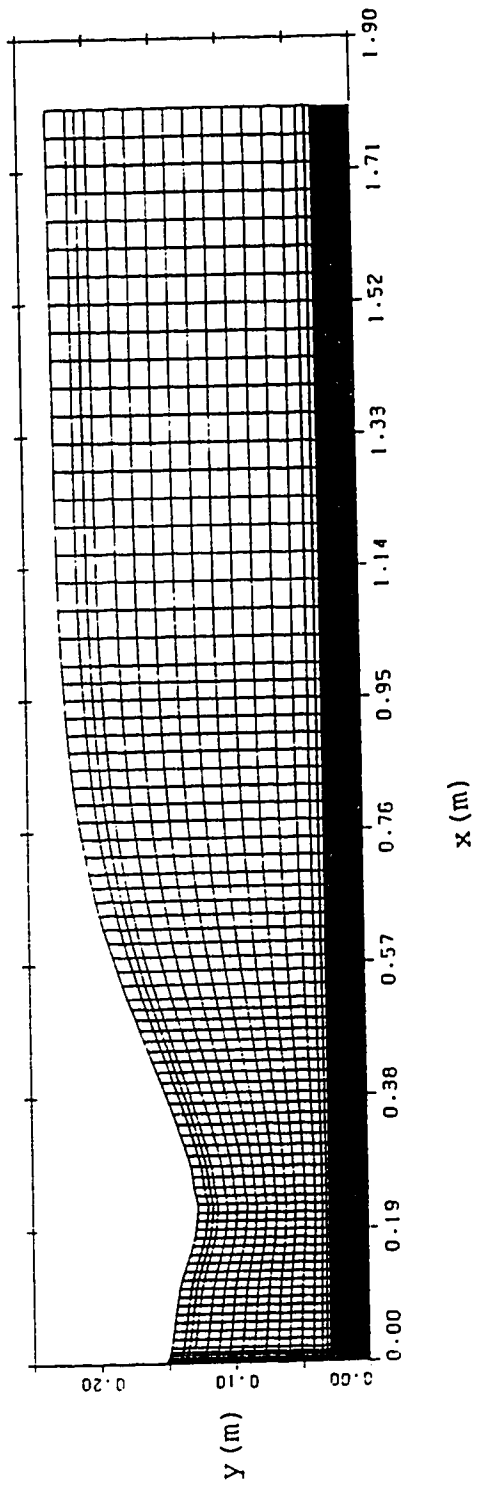


Figure 112. Calculation mesh for $F_1=8.19$ and $S=0.24$.

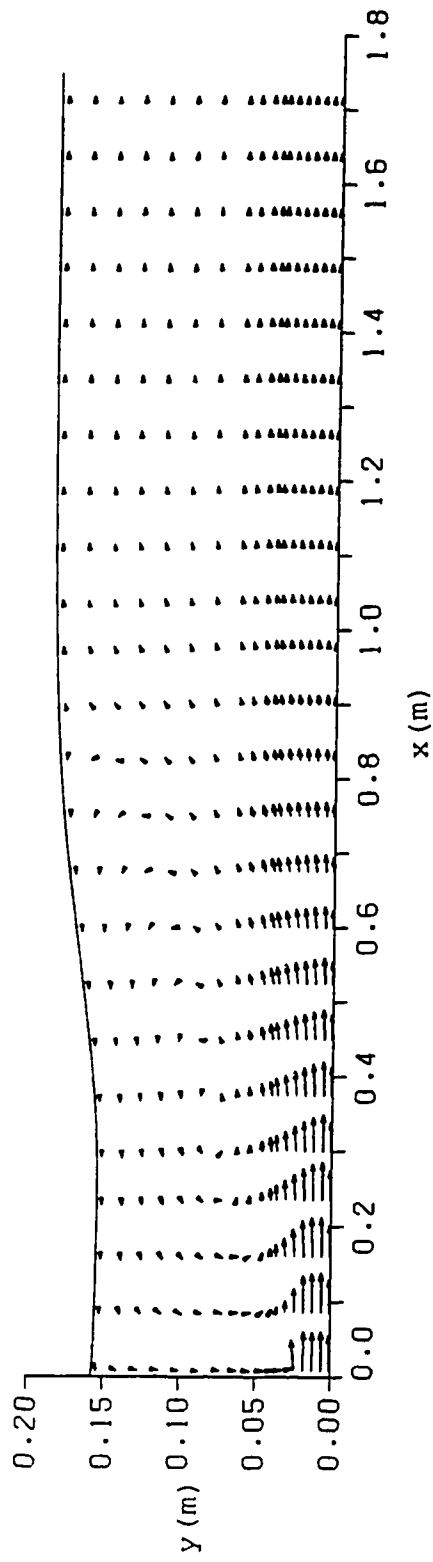


Figure 113. Velocity vector field from numerical calculation for $F_1=3.19$ and $S=0.85$.

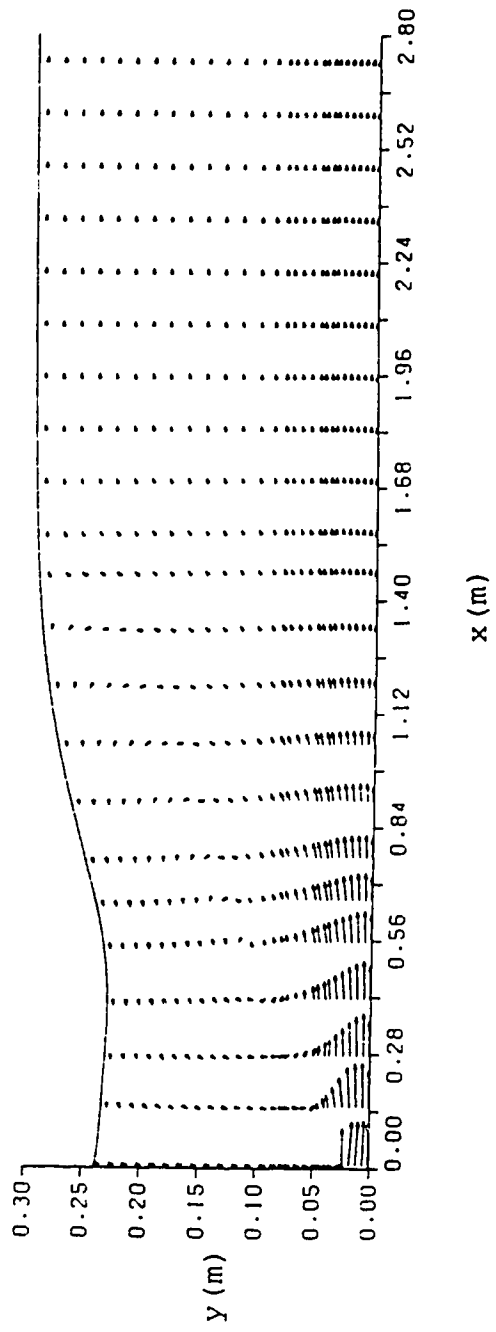


Figure 114. Velocity vector field from numerical calculation for $F_1=5.49$ and $S=0.63$.

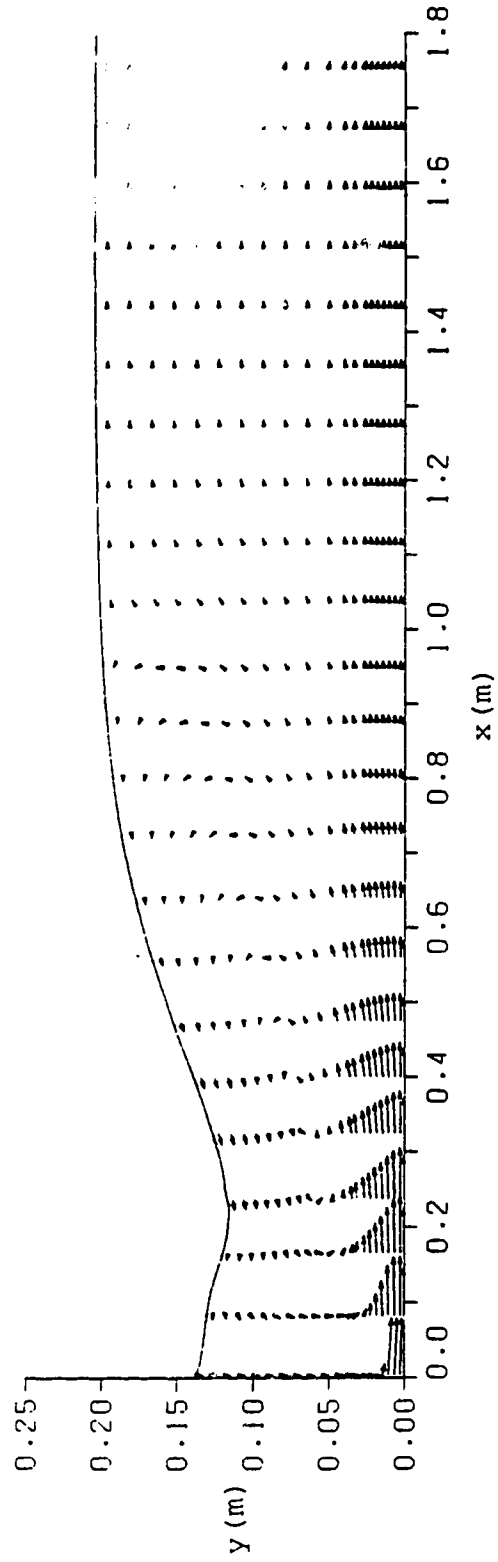


Figure 115. Velocity vector field from numerical calculation for $F_1=8.19$ and $S=0.24$.

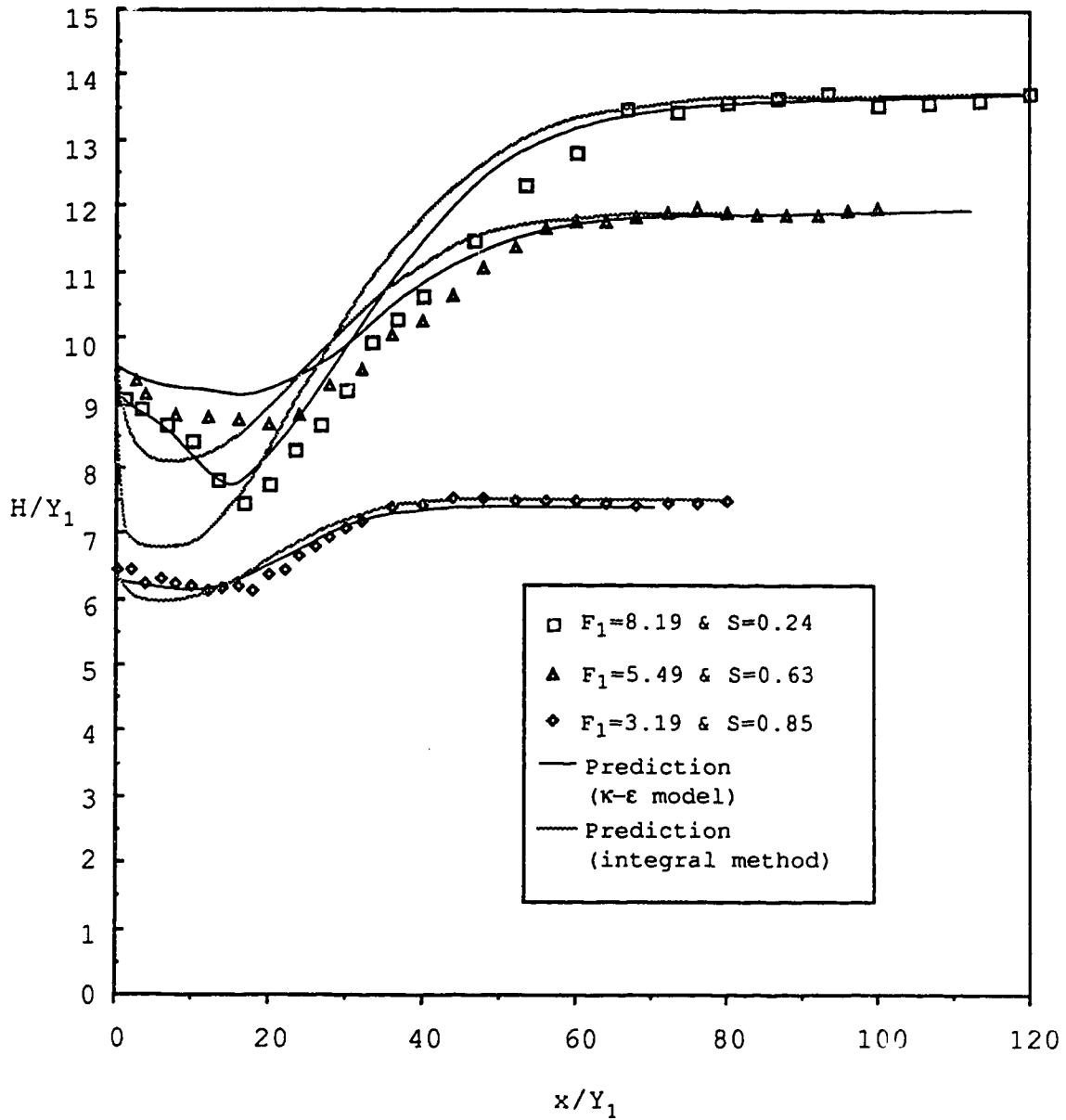
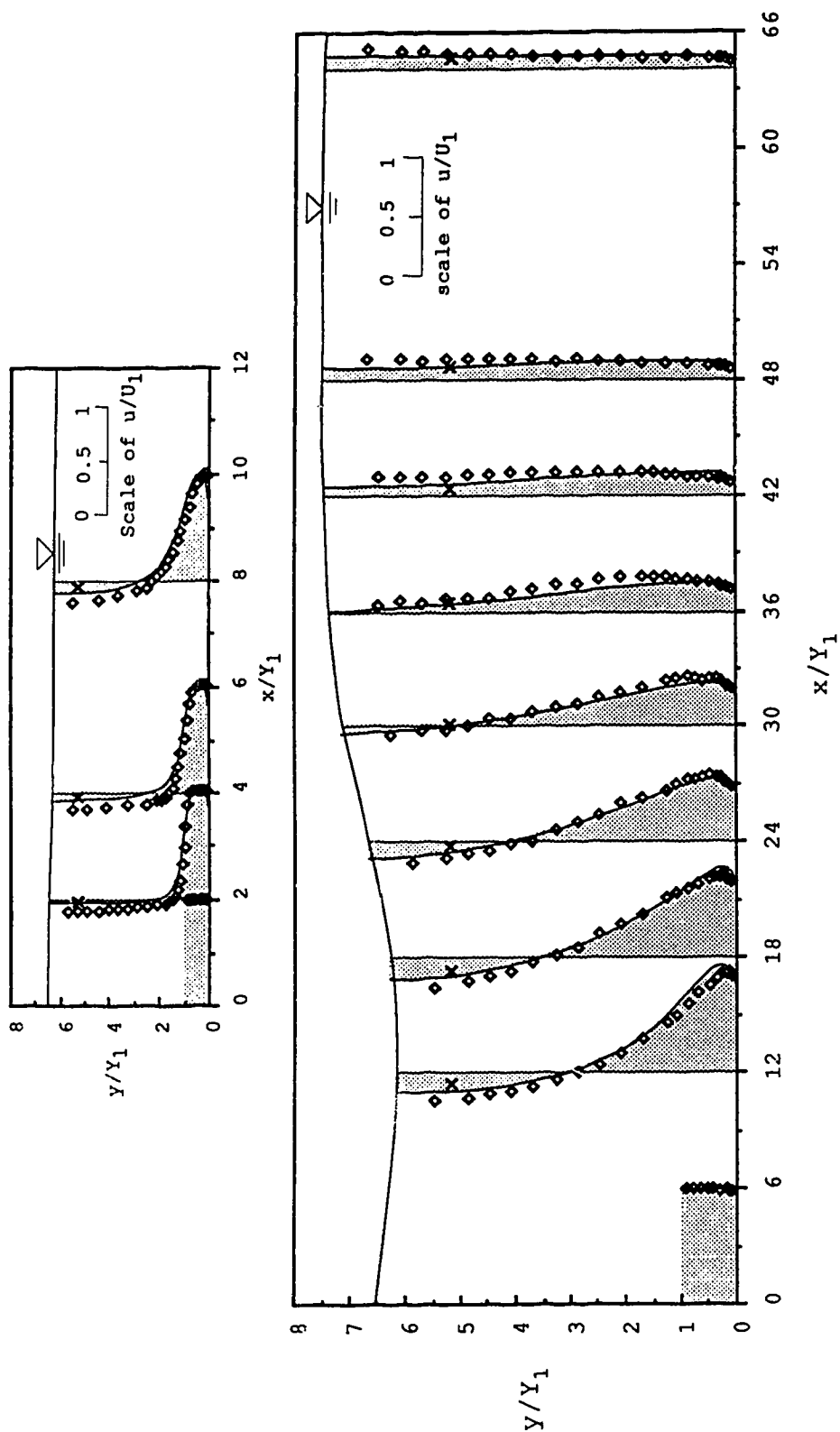


Figure 116. Comparison of water surface profiles from the prediction and experiment.



— Numerical prediction \diamond Experimental data
 x Average flow from experiment

Figure 117. Comparison of longitudinal velocity u/U_1 distribution between the experiment and the prediction for $F_1=3.19$ and $S=0.85$.

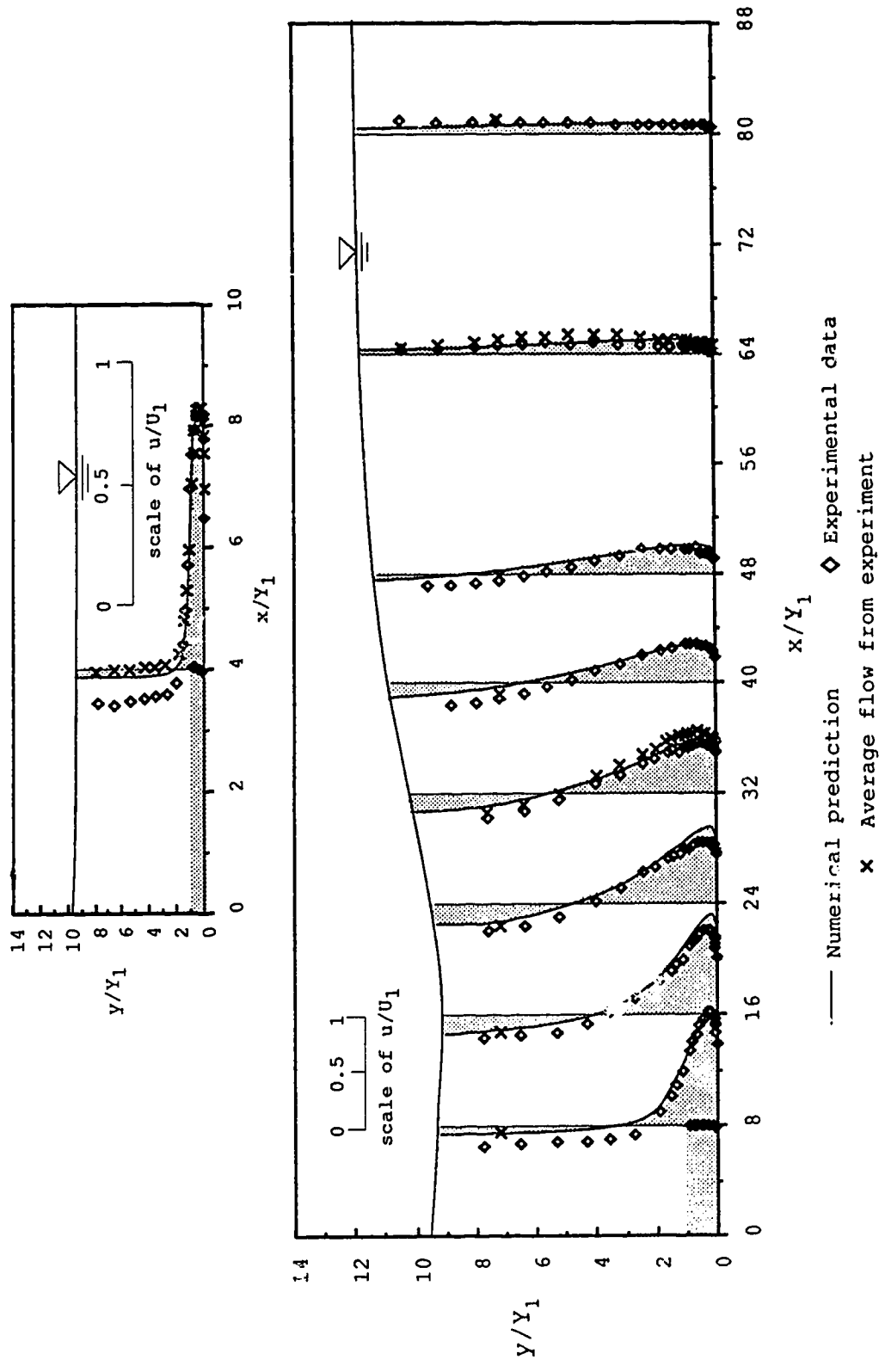


Figure 118. Comparison of longitudinal velocity u/U_1 distribution between the experiment and the prediction for $F_1=5.49$ and $S=0.63$.

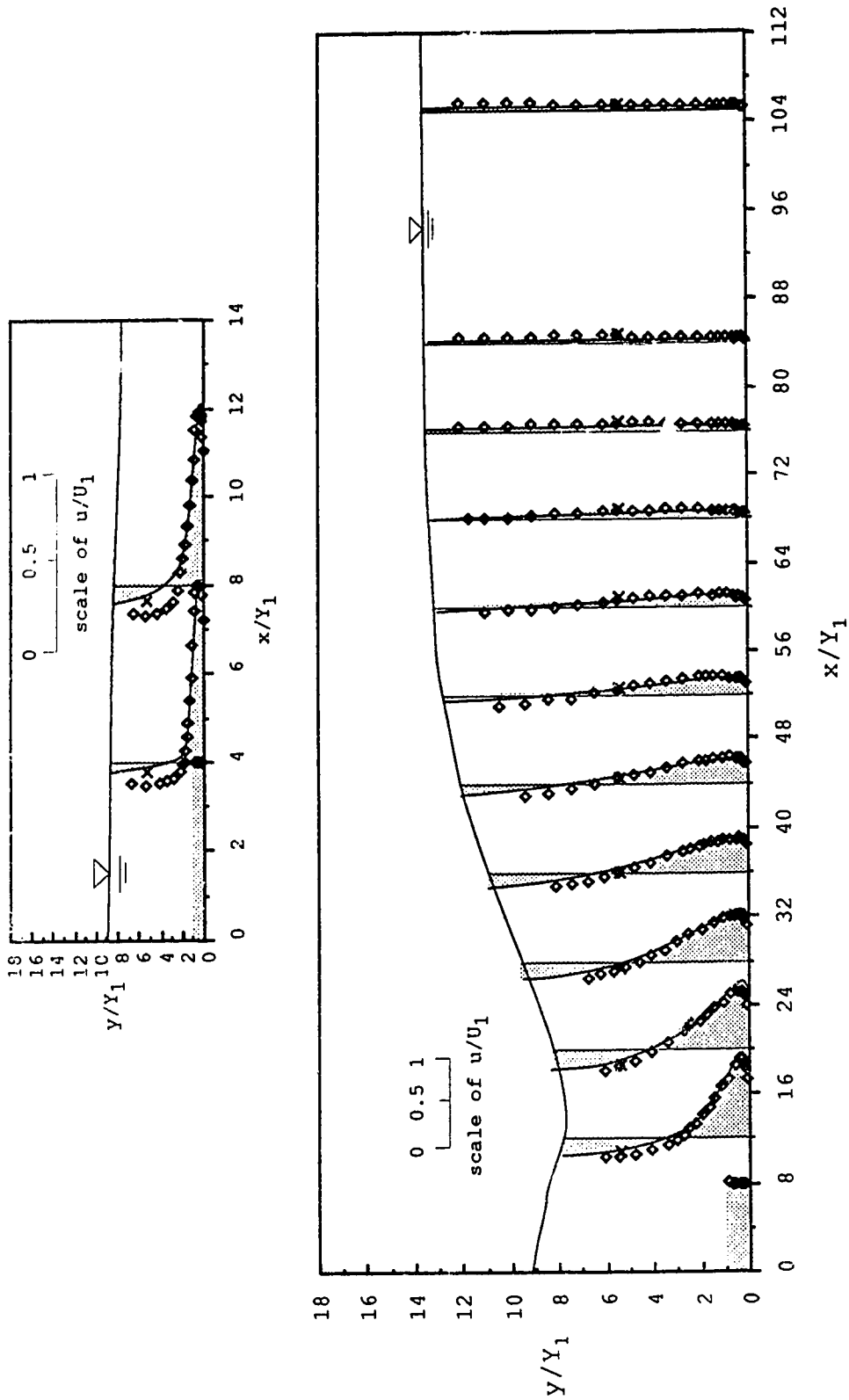


Figure 119. Comparison of longitudinal velocity u/U_1 distribution between the experiment and the prediction for $F_1=8.19$ and $S=0.24$.

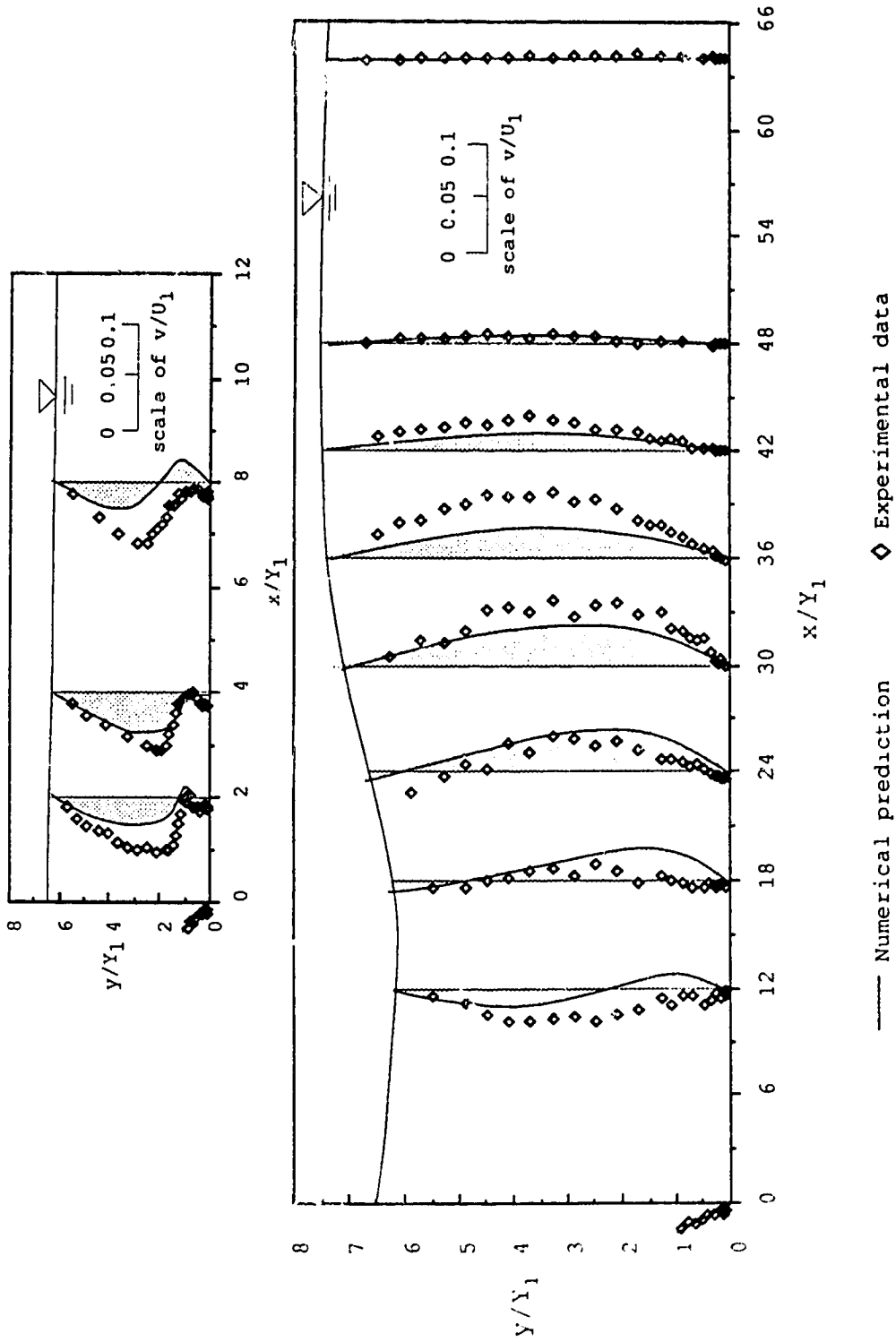


Figure 120. Comparison of vertical velocity v/U_1 distribution between the experiment and the prediction for $F_1=3.19$ and $S=0.85$.

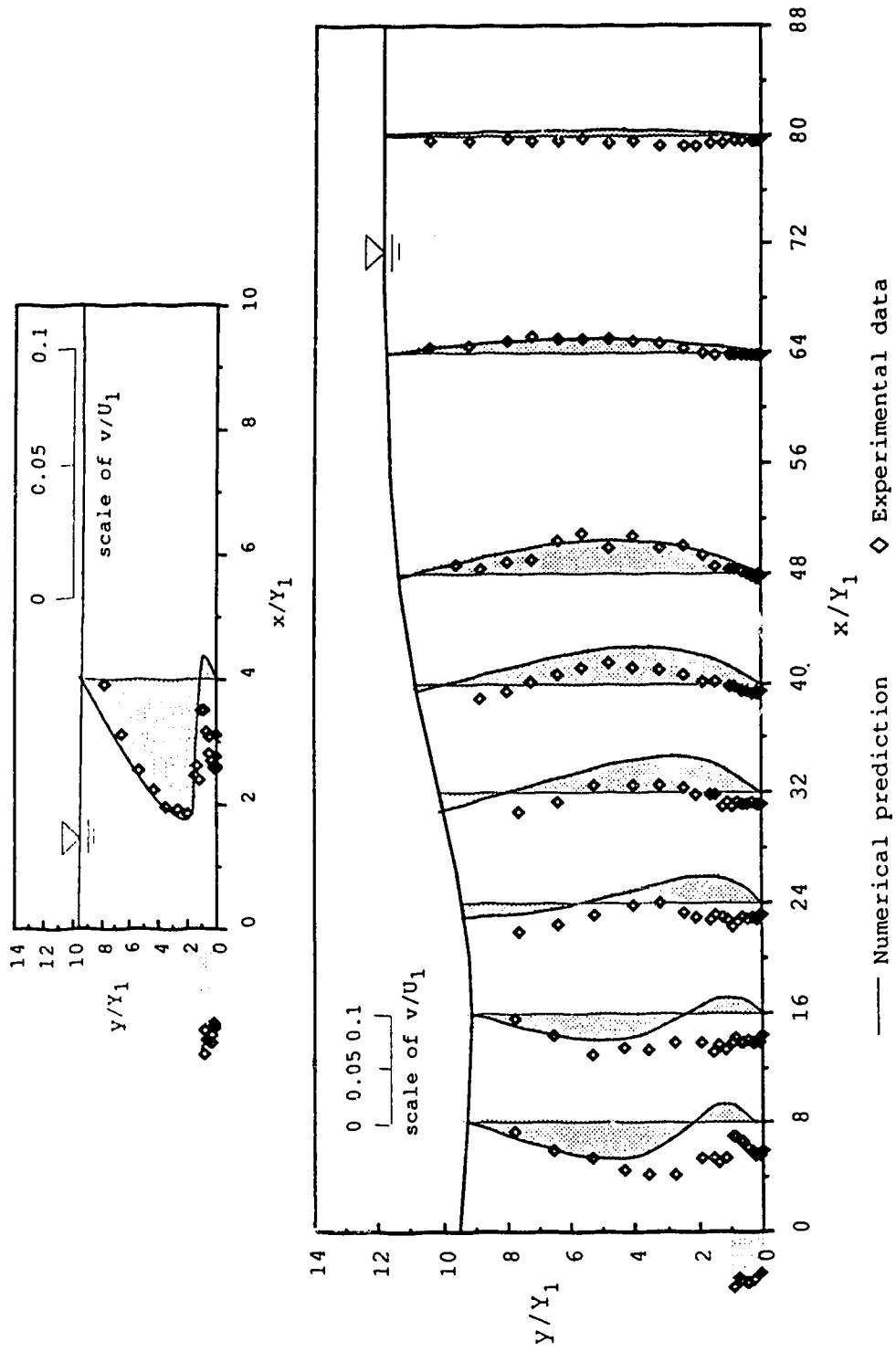


Figure 121. Comparison of vertical velocity v/U_1 distribution between the experiment and the prediction for $F_1=5.49$ and $S=0.63$.

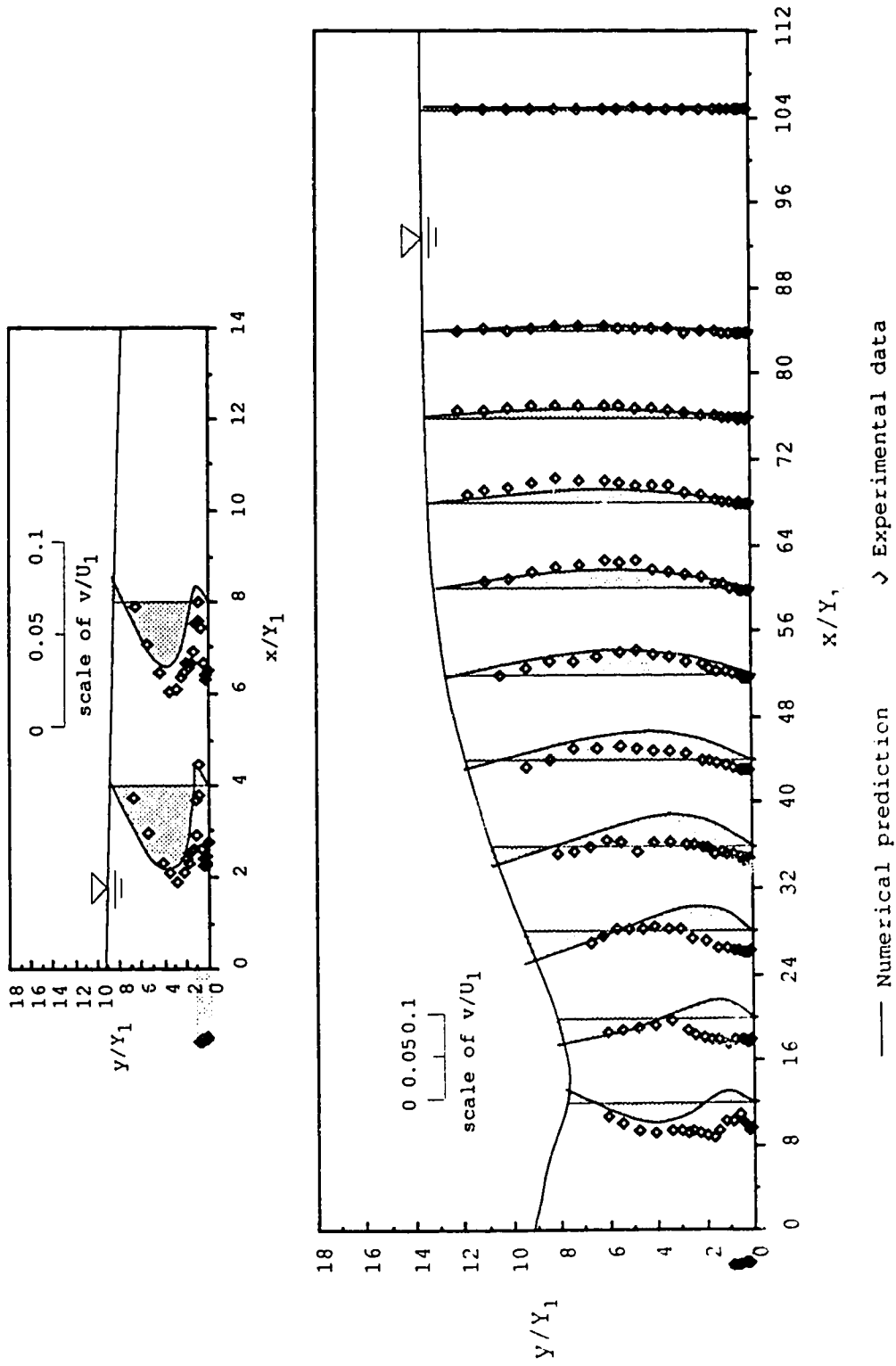


Figure 122. Comparison of vertical velocity v/U_1 distribution between the experiment and the prediction for $F_1=8.19$ and $S=0.24$.

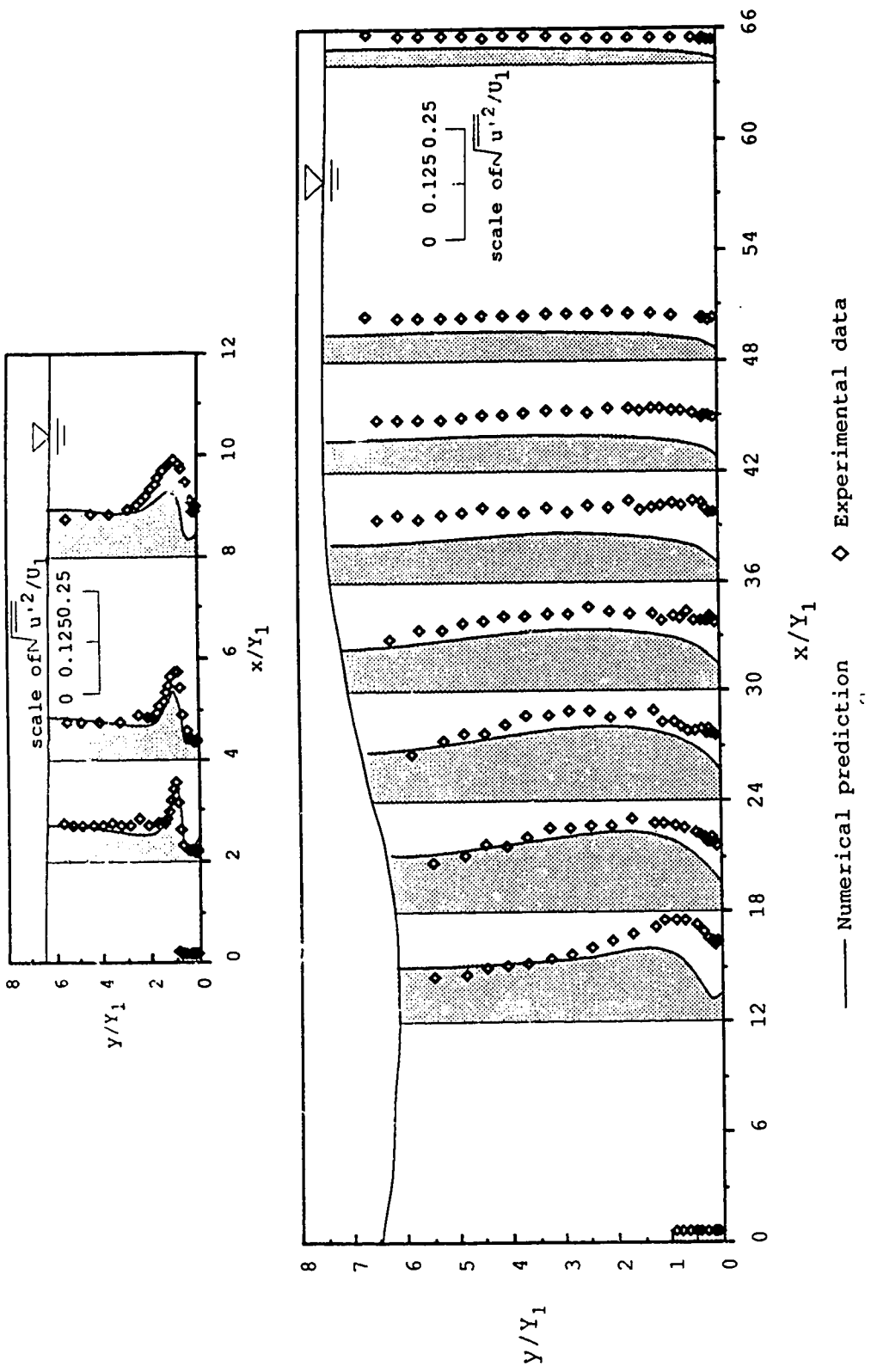


Figure 123. Comparison of $\sqrt{v'^2}/U_1$ distribution along the jump between the experiment and the prediction for $F_1=3.19$ and $S=0.85$.

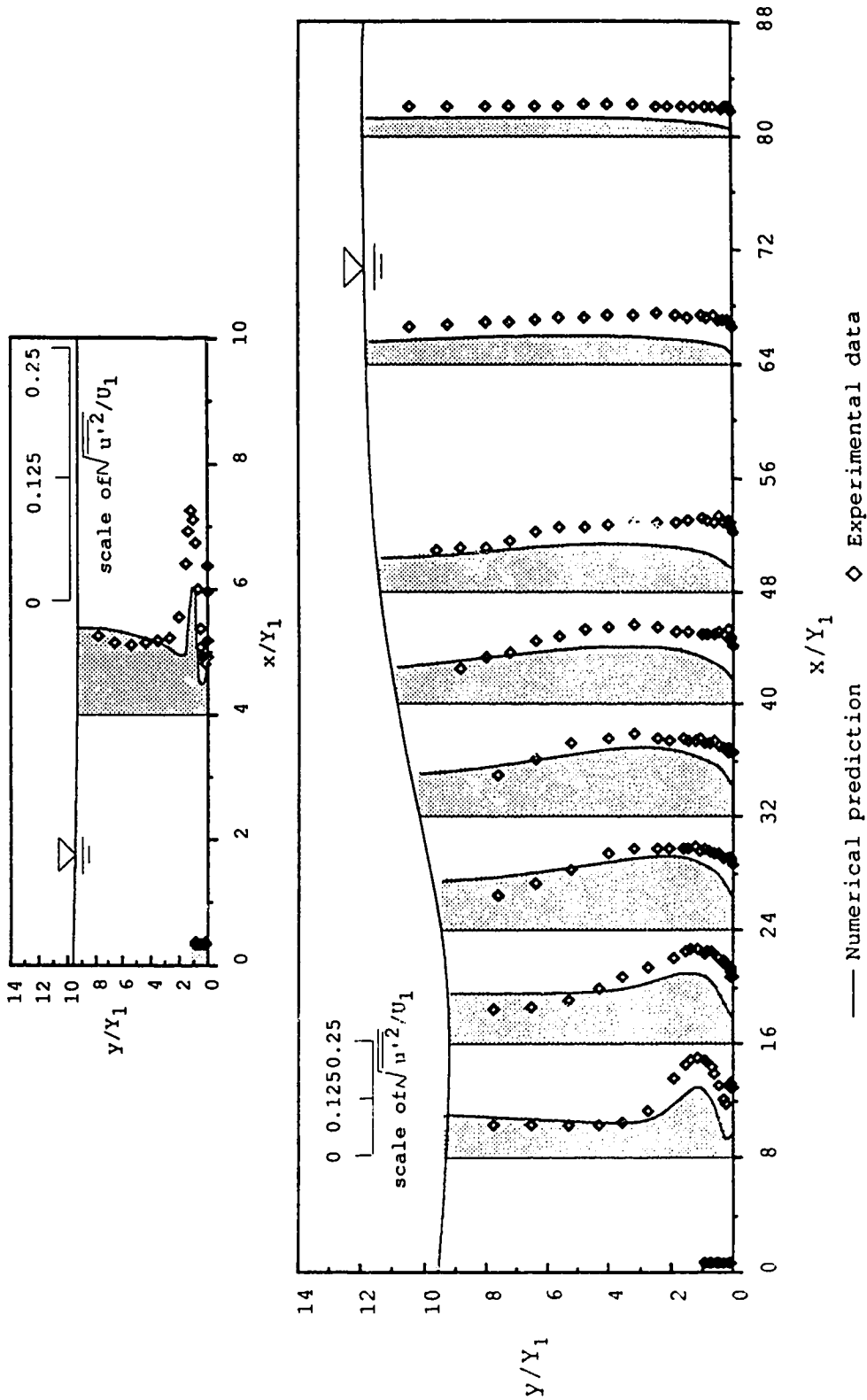


Figure 124. Comparison of $\sqrt{u'^2}/U_1$ distribution along the jump between the experiment and the prediction for $F_1=5.49$ and $S=0.63$.

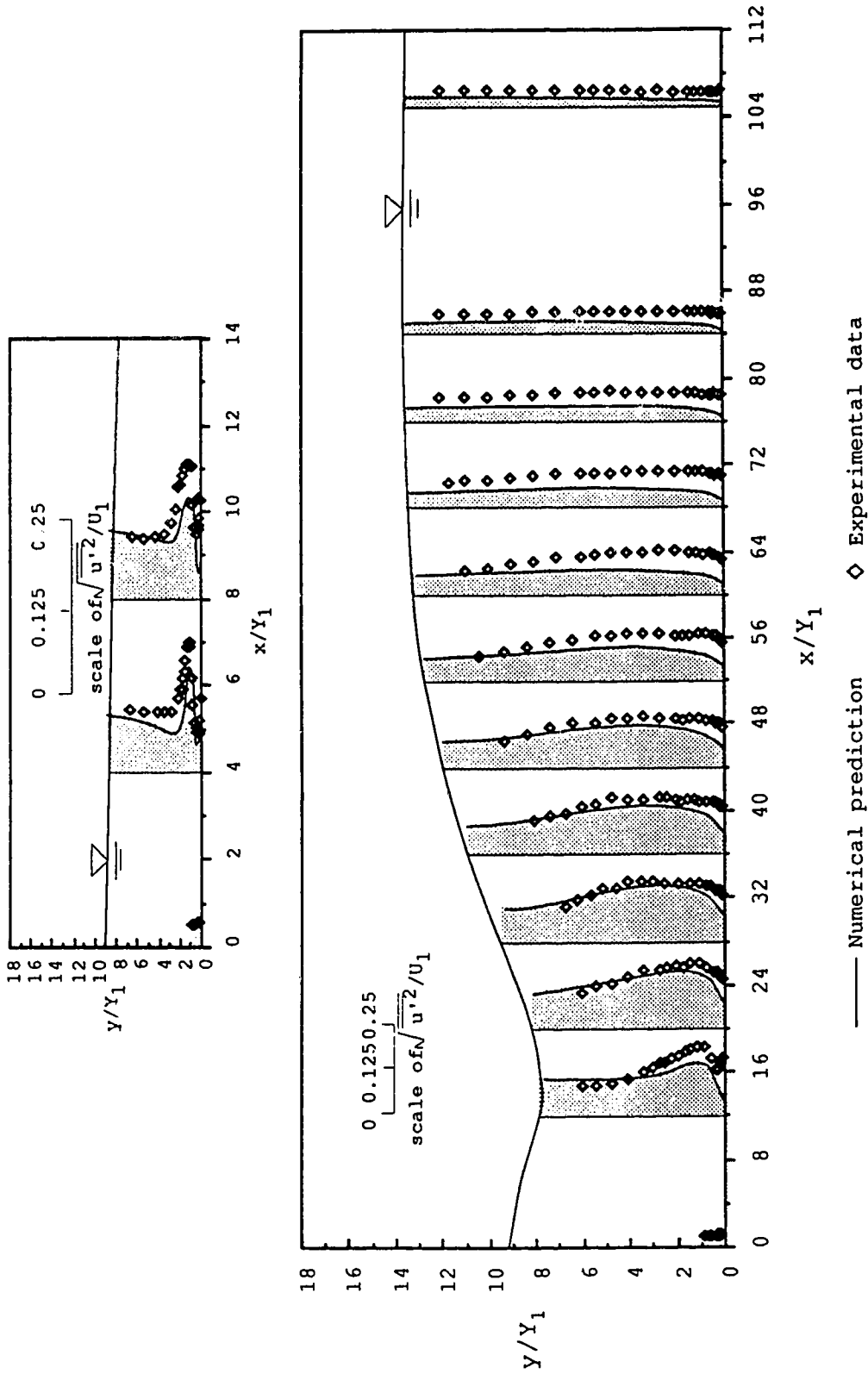


Figure 125. Comparison of $\sqrt{u'^2}/U_1$ distribution along the jump between the experiment and the prediction for $F_1=8.19$ and $S=0.24$.

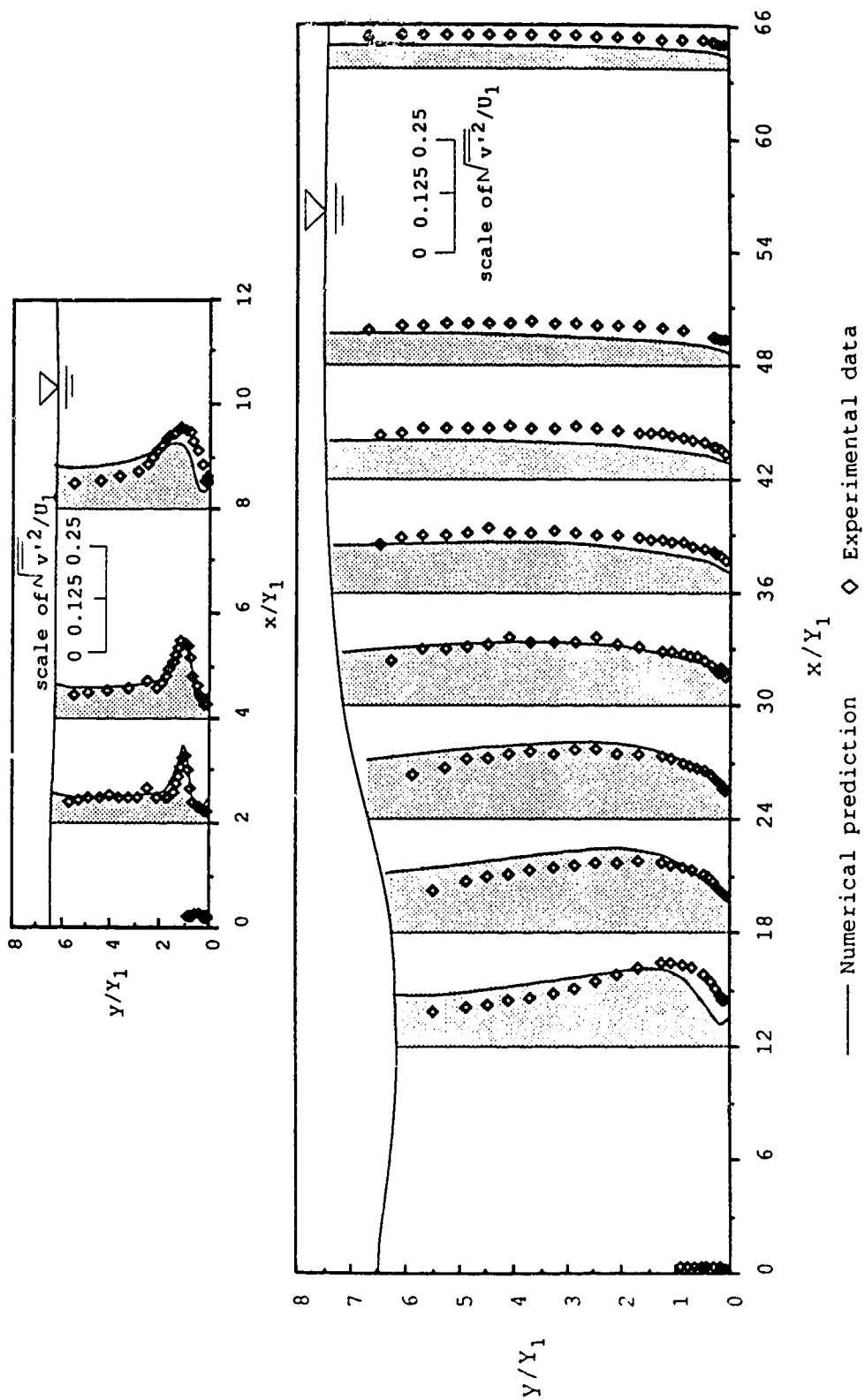


Figure 126. Comparison of $\sqrt{v'^2}/U_1$ distribution along the jump between the experiment and the prediction for $F_1=3.19$ and $S=0.85$.

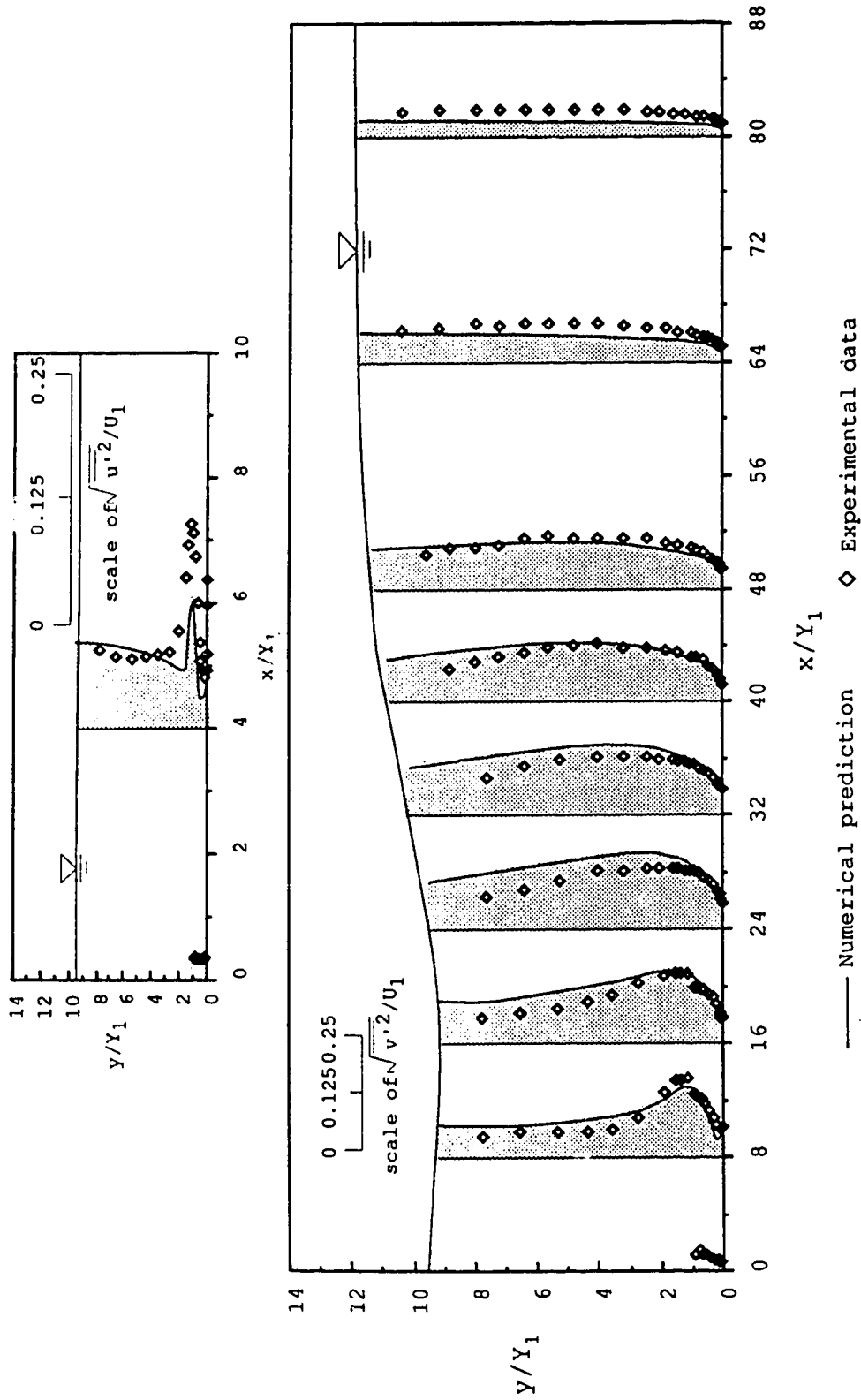


Figure 127. Comparison of $\sqrt{v'^2}/U_1$ distribution along the jump between the experiment and the prediction for $F_r = 5.49$ and $S = 0.63$.

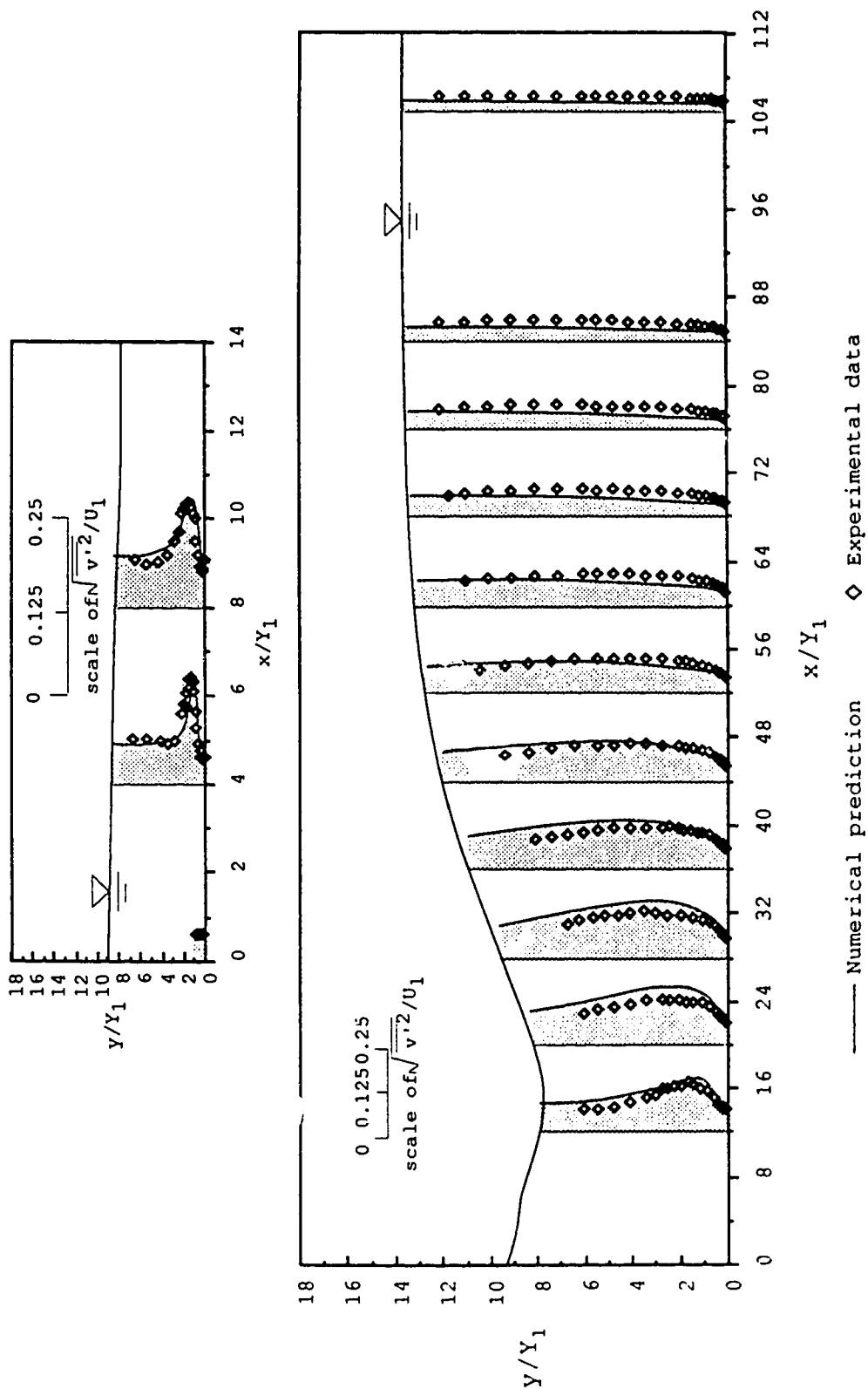


Figure 128. Comparison of $\sqrt{v'^2}/U_1$ distribution along the jump between the experiment and the prediction for $F_1=8.19$ and $S=0.24$.

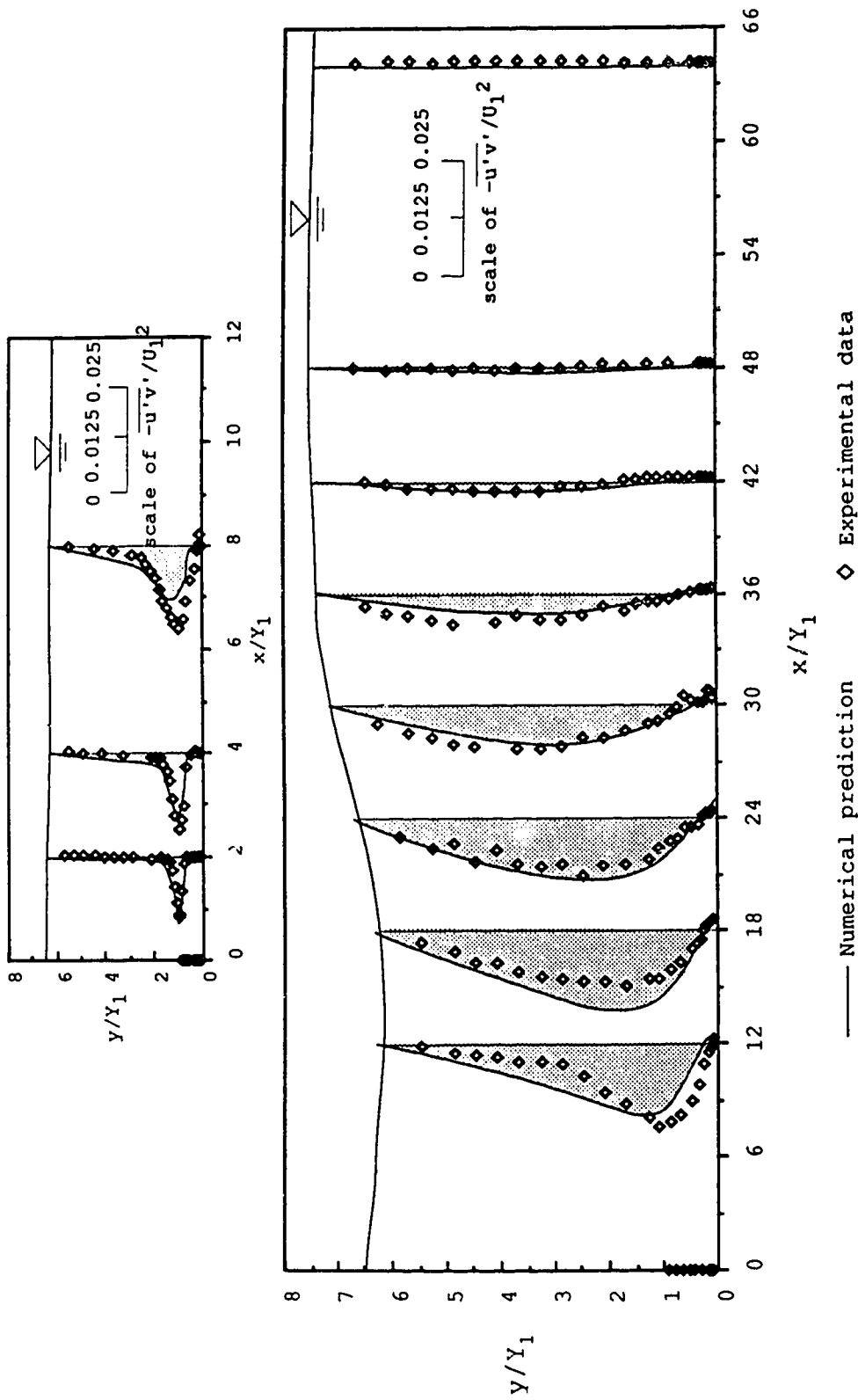


Figure 129. Comparison of $-\overline{u'v'}/U_1^2$ distribution between the experiment and the prediction for $E_1=3.19$ and $S=0.85$.

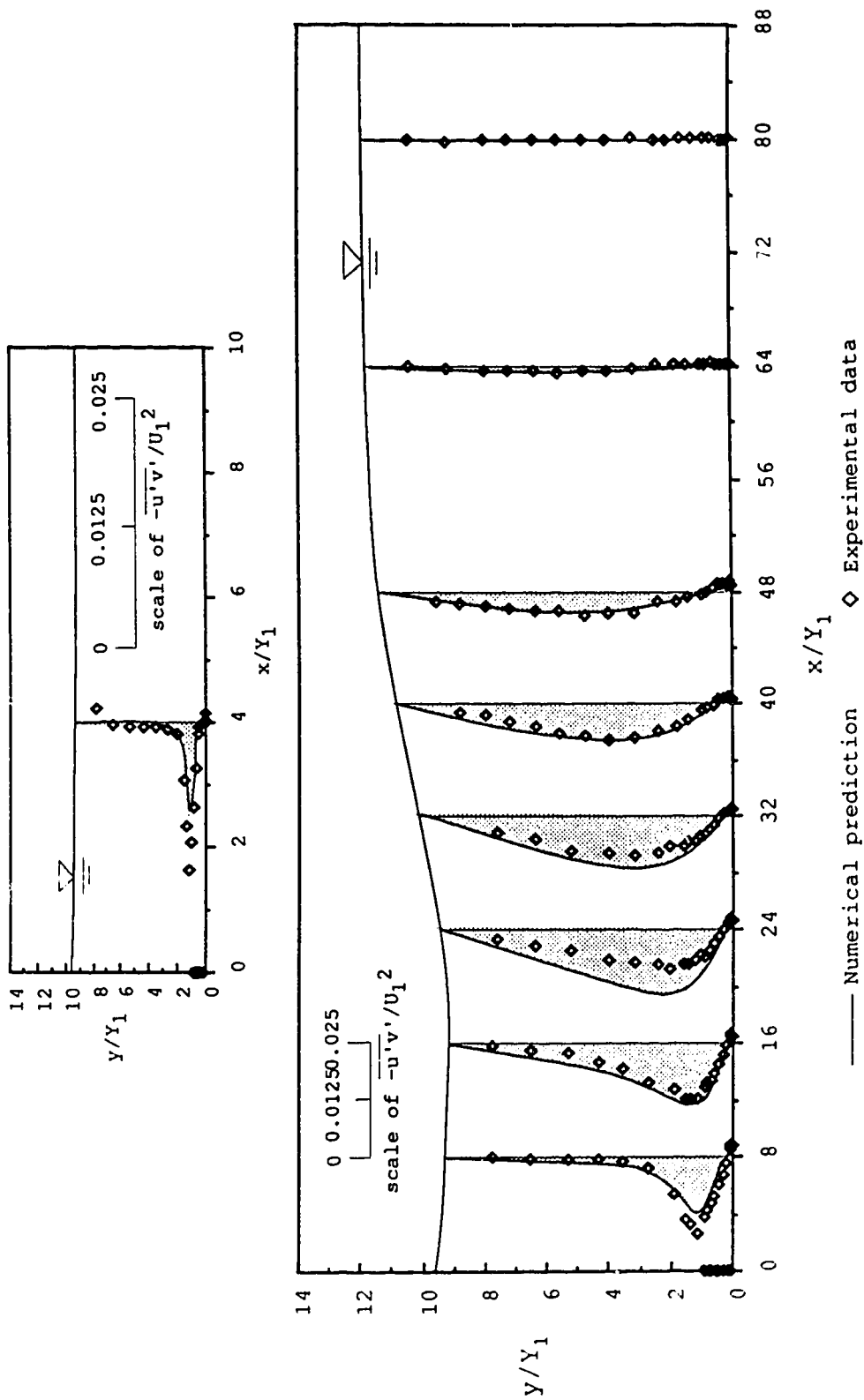


Figure 130. Comparison of $-\overline{u'v'}/U_1^2$ distribution along the jump between the experiment and the prediction for $F_1=5.49$ and $S=0.63$.

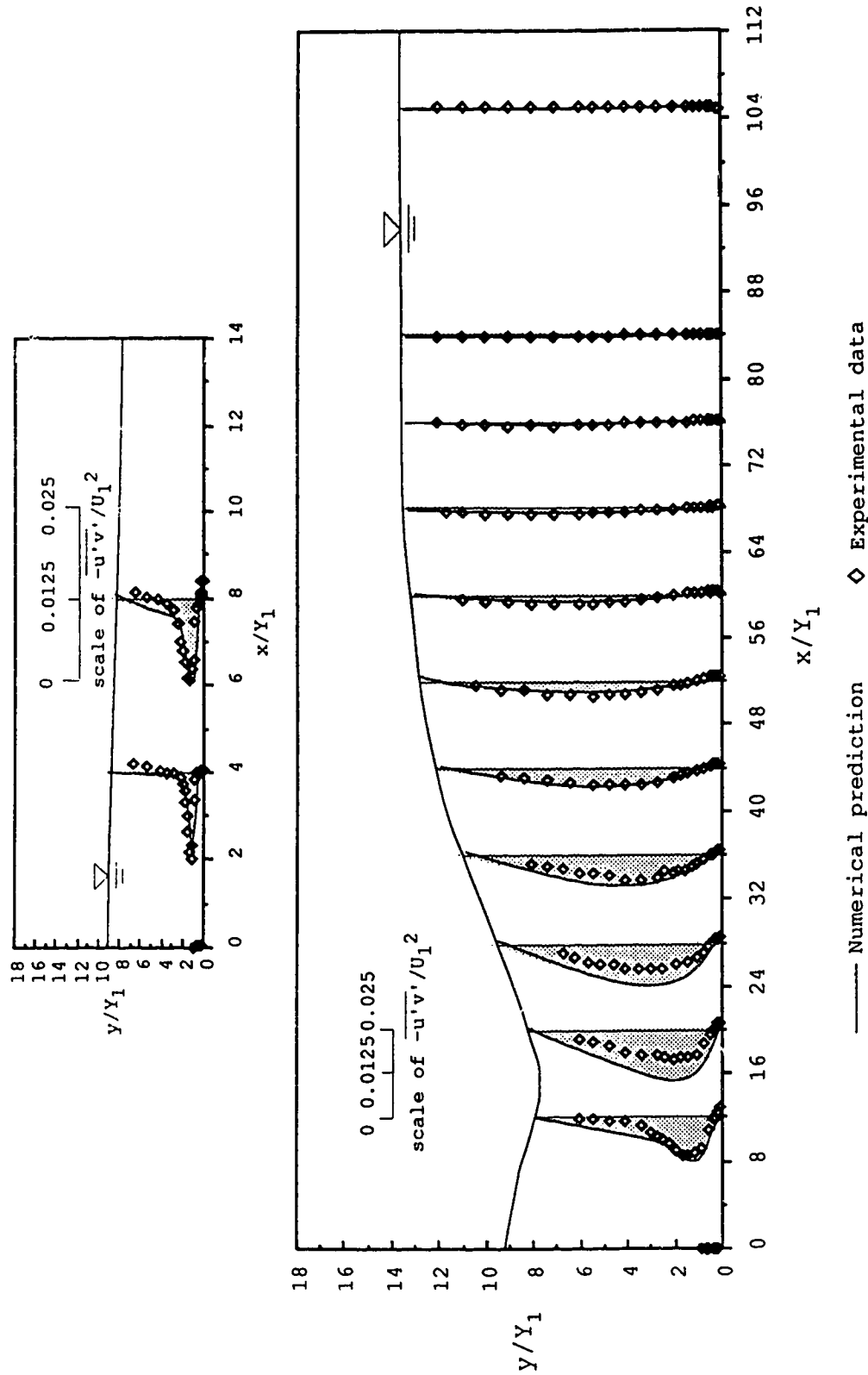


Figure 131. Comparison of $\overline{-u'v'}/U_1^2$ distribution along the jump between the experiment and the prediction for $F_1=8.19$ and $S=0.24$.

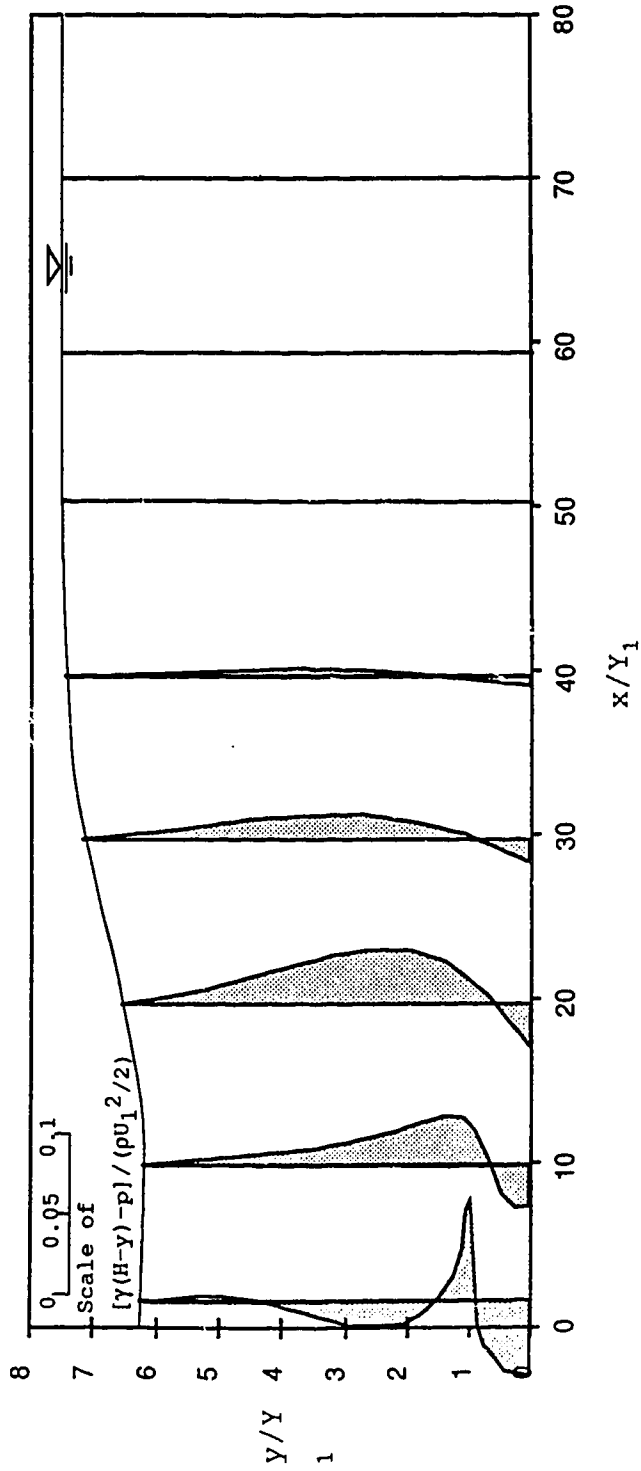


Figure 132. Departure of pressure from hydrostatic distribution along the jump from the numerical prediction for $F_1=3.19$ and $S=0.85$.

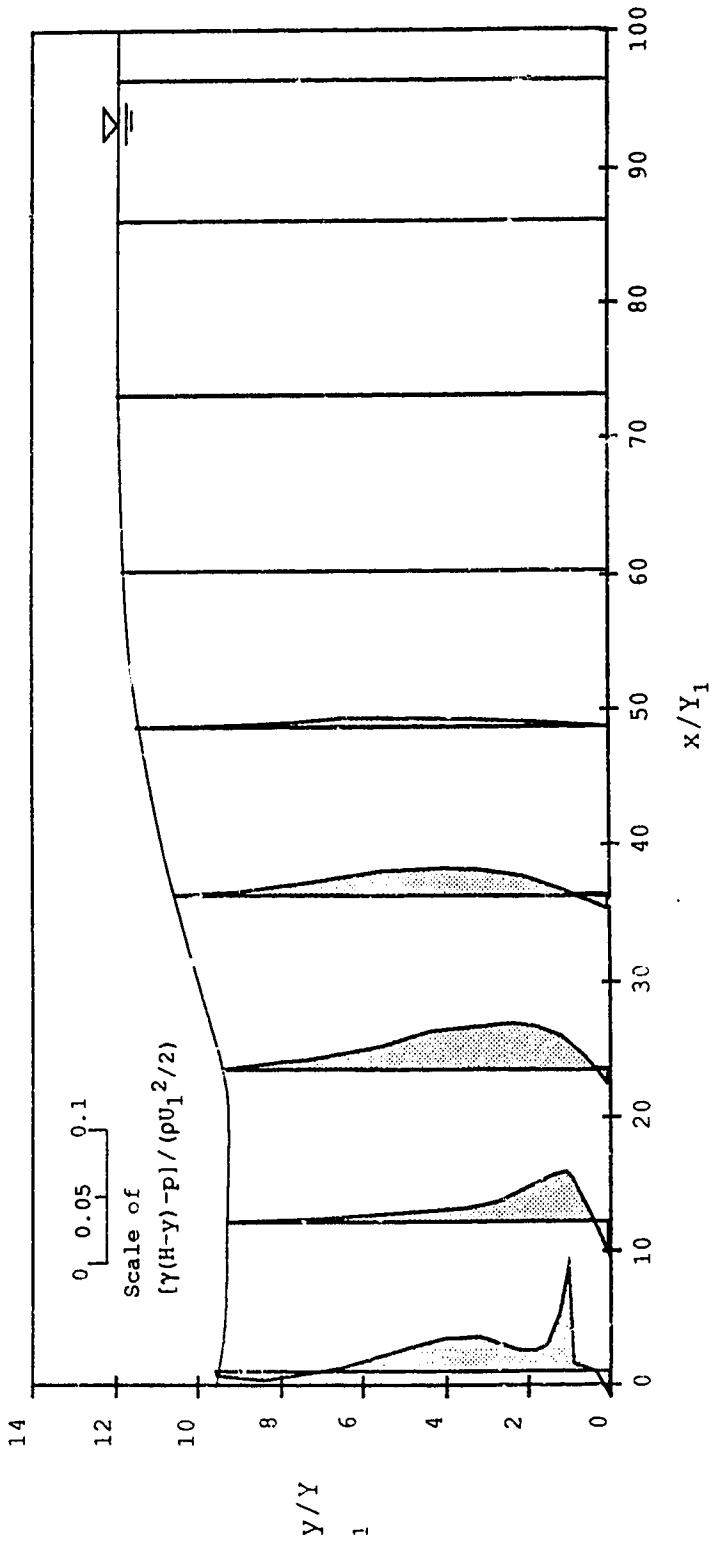


Figure 133. Departure of pressure from hydrostatic distribution along the jump from the numerical prediction for $F_1=5.49$ and $S=0.63$.

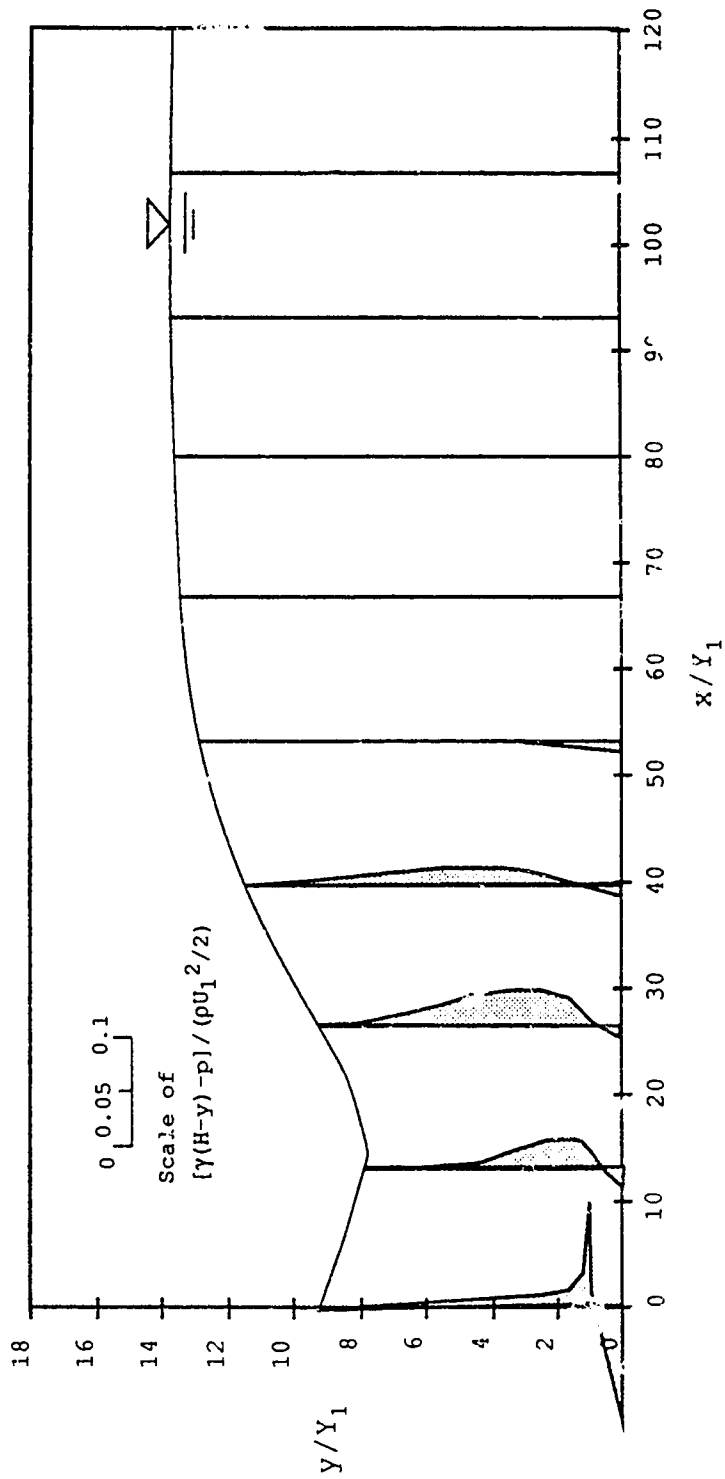
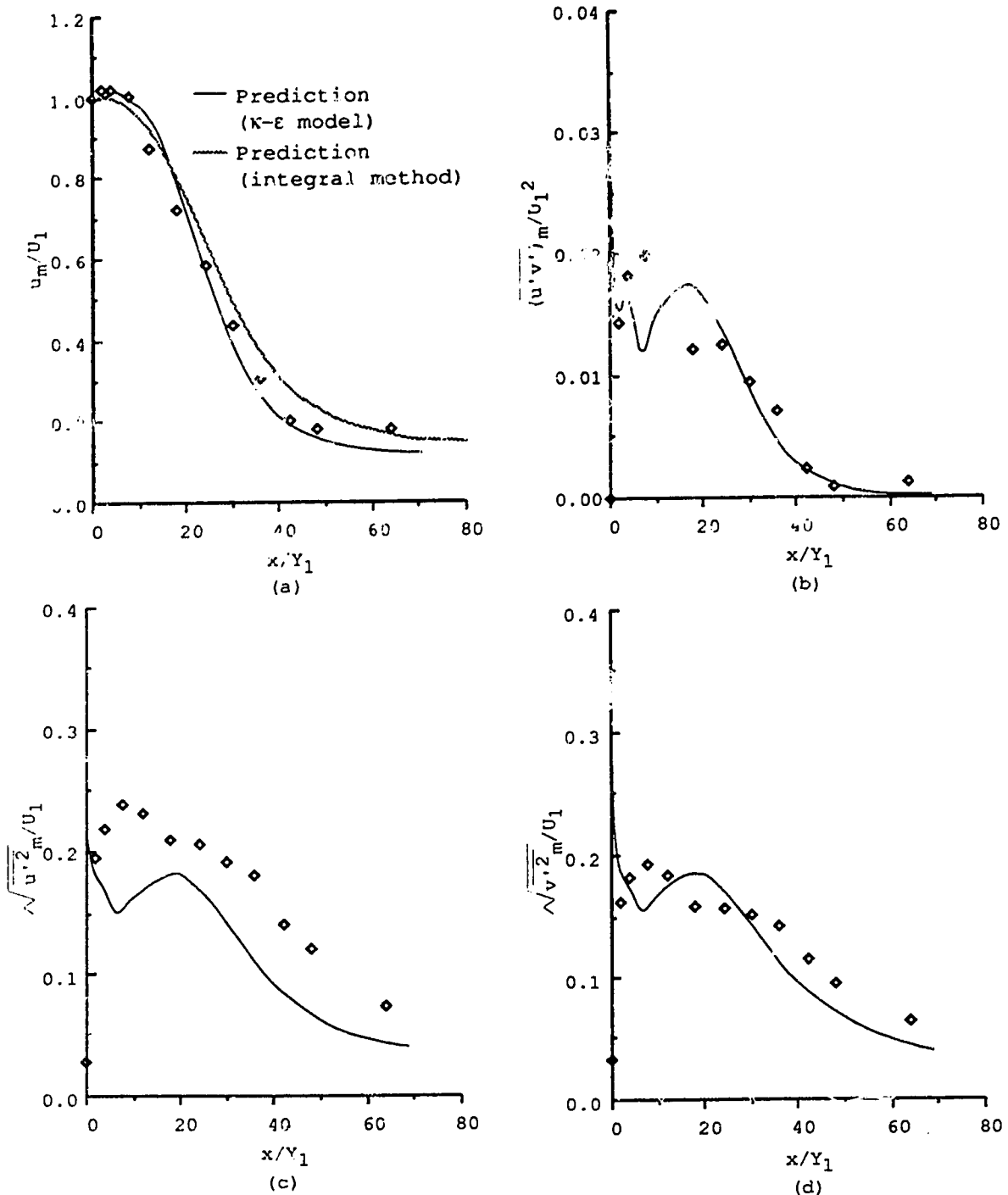


Figure 134. Departure of pressure from hydrostatic distribution along the jump from the numerical prediction for $F_1=8.19$ and $S=0.24$.



— Numerical prediction ◇ Experimental data

Figure 135. Comparison of major flow characteristics between the experiment and the prediction for $F_1=3.19$ and $S=0.85$.
 (a) u_m/U_1 vs x/Y_1 ; (b) $\overline{(u'v')}_m/U_1^2$ vs x/Y_1 ;
 (c) $\sqrt{u'^2}_m/U_1$ vs x/Y_1 ; (d) $\sqrt{v'^2}_m/U_1$ vs x/Y_1 .

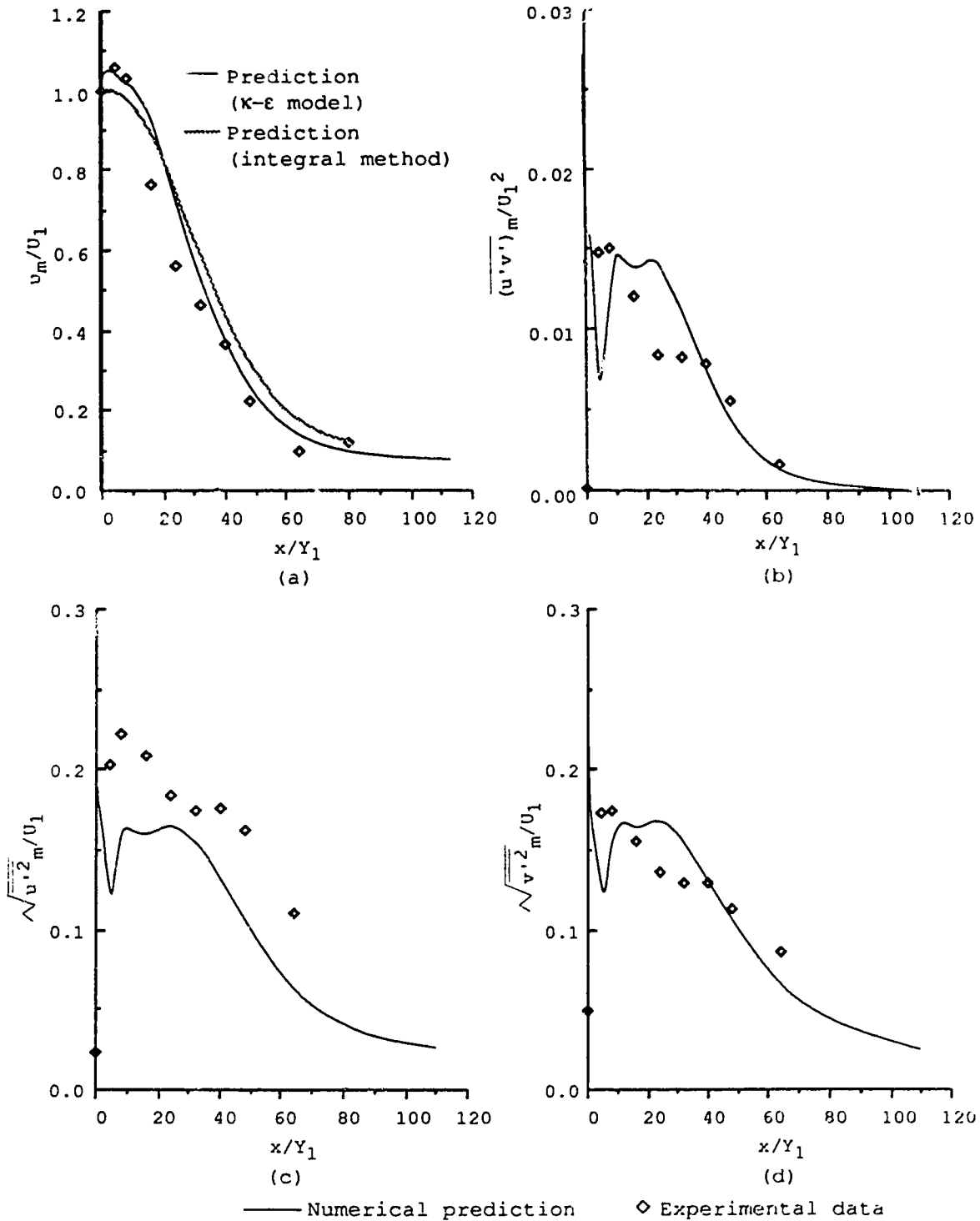


Figure 136. Comparison of major flow characteristics between the experiment and the prediction for $F_1=5.49$ and $S=0.63$.
 (a) u_m/U_1 vs x/Y_1 ; (b) $\overline{(u'v')}_m/U_1^2$ vs x/Y_1 ;
 (c) $\sqrt{\overline{u'^2}}_m/U_1$ vs x/Y_1 ; (d) $\sqrt{\overline{v'^2}}_m/U_1$ vs x/Y_1 .

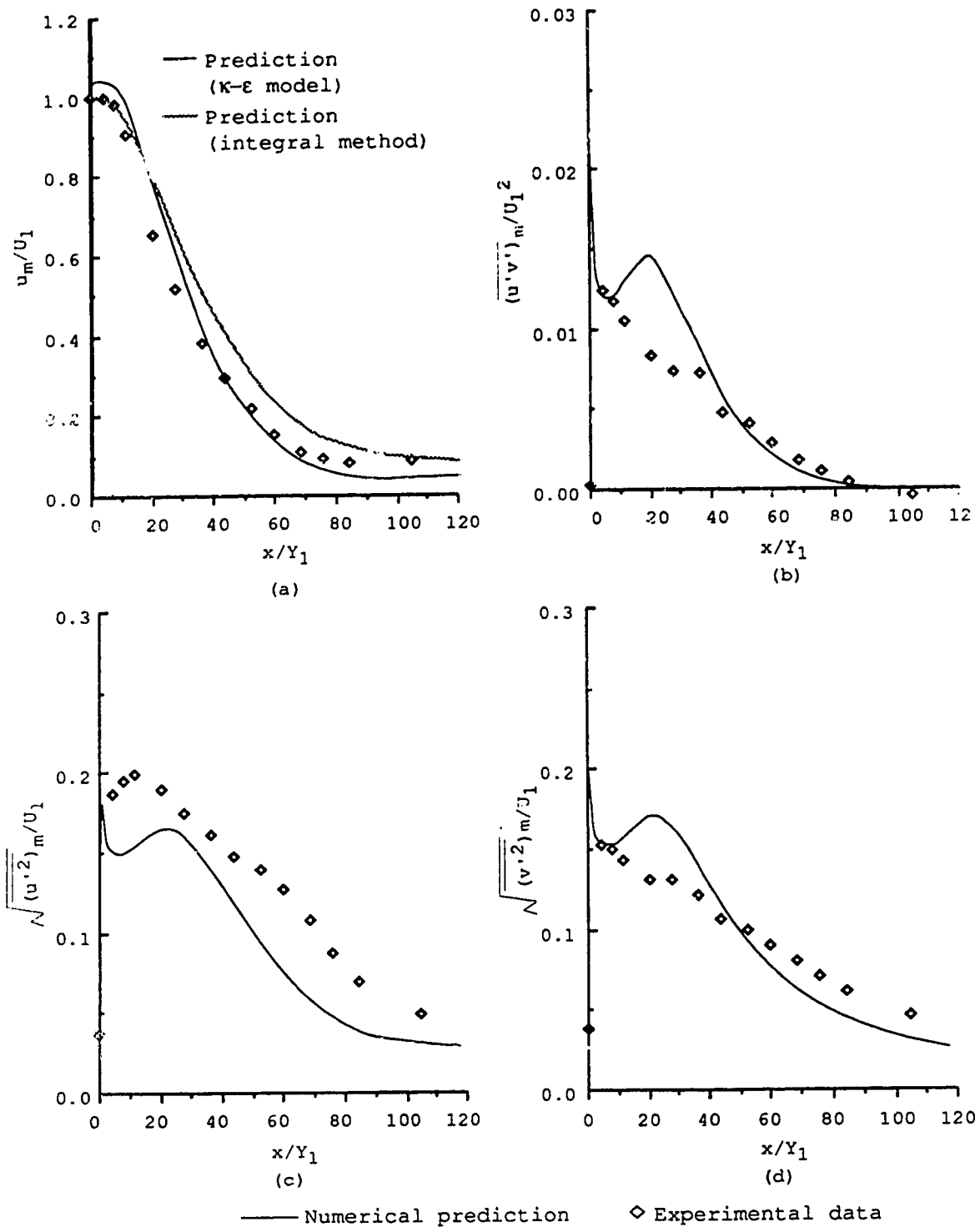


Figure 137. Comparison of major flow characteristics between the experiment and the prediction for $F_1=8.19$ and $S=0.24$.
 (a) u_m/U_1 vs x/Y_1 ; (b) $\overline{(u'v')}_m/U_1^2$ vs x/Y_1 ;
 (c) $\sqrt{\overline{u'^2}}_m/U_1$ vs x/Y_1 ; (d) $\sqrt{\overline{v'^2}}_m/U_1$ vs x/Y_1 .

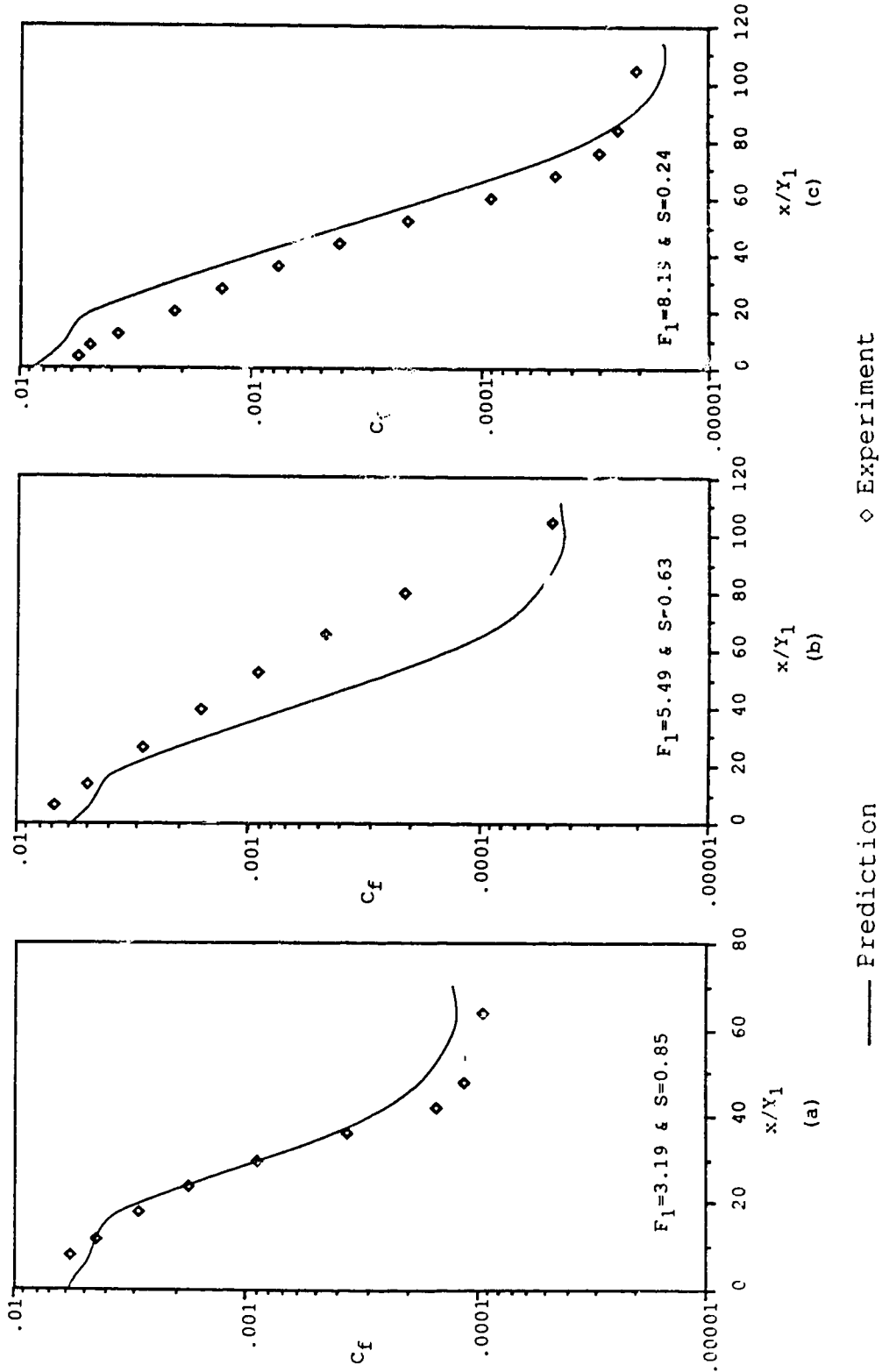


Figure 138. Comparison of shear stress coefficients C_f between the experiment and the prediction.

REFERENCES

- Abdel-Gawad, S. M. and McCorquodale, J. A., 1984, "Modelling submerged radial hydraulic jumps", Proc. Ann. Conf. Can. Soc. Civil Eng., Halifax, Nova Scotia, Canada, pp.711-725.
- Abdul Khader, M. H. and Elango, K., 1974, "Turbulent pressure field beneath a hydraulic jump", Journal of Hydraulic Research, IAHR, 12:4, pp.469-487.
- Task Committee on Turbulence Models in Hydraulic Computations, 1988, "Turbulence modelling of surface water flow and transport: part I to V", Journal of the Hydraulic Engineering, ASCE, Vol.114, No.9, pp.970-1073.
- ASCE Task Force, 1964, "Energy dissipators for spillways and outlet works", Journal of the Hydraulic Division, ASCE, 90:HY1, Proc. Paper 3762, pp.121-147.
- Benim, A. C., and Zinser, W., 1985, "Investigation into the Finite Element Analysis of Confined Turbulent Flows Using a K- ϵ Model of Turbulence", Computer Methods for Applied Mechanics and Engineering, Vol.51, pp.507-523.
- Betchov, R. and Criminale, Jr. W. O., 1967, "Stability of parallel flows", Academic Press. London, 330pp.
- Bowers, C. E. and Tsai, F. Y., 1963, "Fluctuating pressures in spillway stilling basins", Journal of the Hydraulic Division, ASCE, 89:HY1, Paper 3404, pp.1-24.
- Bradley, J. N. and Peterka, A. J., 1957, "The hydraulic design of stilling basins: hydraulic jumps on a horizontal apron (basin I)", Journal of the Hydraulic Division, ASCE, 83:HY5, pp.1-24.
- Buchave, P., George, W. K. and Lumley, J. L., 1979, "The measurement of turbulence with the Laser Doppler Anemometer", Annual Review of Fluid Mechanics, Vol.11, pp.440-503.
- Chow, V.T., 1959, "Open channel hydraulics", McGraw-Hill, New York.

- Durst, F., Melling A. and Whitelaw, J. F., 1976, "Principles and practice of Laser Doppler Anemometry", New York, Academic Press, 405pp.
- Garetto, L. S., Gosman, A. D., Patankar, S. V., and Spalding, D. B., 1972, "Two Calculation Procedures for Steady, Three-dimensional Flows with Recirculation", Proceedings of the Third International Conference on Numerical Methods in Fluid Mechanics, Vol.2, pp.60-68.
- Gartshore, I. S. and Newman, B. G., 1969, "The turbulent wall jet in an arbitrary pressure gradient", Aeronautical Quarterly, pp.25-57.
- George, A. R., 1959, "An investigation of a wall jet in a free stream", Princeton University, Report No.479.
- Gosman, A. D., Khalil, E. E., and Whitelaw, J. H., 1979, "The Calculation of Two-Dimensional Turbulent Recirculating Flows", Turbulent Shear Flows 1, pp.237-255.
- Govinda Rao, N. S. and Rajaratnam N., 1963, "The submerged hydraulic jump", Journal of the Hydraulic Division, ASCE, 89:HY1, pp.139-162.
- Hughes, T. J. R. and Brooks A. N., 1979, "A multidimensional upwind scheme with no crosswind diffusion", in T. J. R. Hughes edition, Finite Element Methods for Convection Dominated Flows, ASCE, AMD-34, New York, pp.19-35.
- Keir, G., Umay, T. E. and Hill, H. M., 1969, "Pressure fluctuations on submerged sluices gate", Journal of the Hydraulic Division, ASCE, 95:HY6, Paper 6875, pp.1781-1791.
- Khalifa, A. M. and McCorquodale, J. A., 1979, "Radial hydraulic jump", Journal of the Hydraulic Division, ASCE, 105:HY9, pp.1065-1078.
- Lakshminarayanan, B., 1986, "Turbulence modelling for complex shear flows", AIAA Journal, Vol.24, No.12, pp.1900-1917.
- Launder, B. E., Reece G. J. and Rodi, W., 1975, "Progress in the development of a Reynolds stress turbulence closure", Journal of Fluid Mechanics, vol.68, pp.537-586.
- Launder, B. E. and Rodi, W., 1981, "The turbulent wall jets", Prog. Aerospace Sci., vol.19, pp.81-128.

- Launder, B. E. and Rodi, W., 1983, "The turbulent wall jet - measurements and modelling", Annual Review of Fluid Mechanics, vol.15, pp.429-459.
- Launder, B. E., and Spalding, D. B., 1972, "Turbulence models and their applications to the prediction of internal flows", Heat Fluid Flow, Vol.2, pp.43-54.
- Launder, B. E., and Spalding, D. B., 1974, "The Numerical Computation of Turbulent Flows", Computer Methods in Applied Mechanics and Engineering, Vol.3, pp.269-289.
- Leonard, B. P., 1979, "A stable and accurate convective modelling procedure based on quadratic upstream interpolation", Journal of Computer Methods for Applied Mechanics and Engineering, Vol.19, pp.59-98.
- Leutheusser, H. J. and Kartha, V. C., 1972, "Effects of inflow condition on hydraulic jump", Journal of the Hydraulic Division, ASCE, 98:HY8, pp.1367-1385.
- Leutheusser, H. J. and Alemn, S., 1979, "Flow separation under hydraulic jump", Journal of Hydraulic Research, IAHR, Vol.17, No.3, pp.193-206.
- Liu, H. K., 1949, "Diffusion of flow from a submerged sluice gate", Thesis presented to the State Univ. of Iowa, Iowa, in partial fulfillment of the requirements for the degree of Master of Science, 45pp.
- Madsen, P. A., and Svendsen, I. A., 1983, "Turbulent Bores and Hydraulic Jumps", Journal of Fluid Mechanics, Vol.129, pp.1-25.
- McCorquodale, J. A., 1986, "Hydraulic jumps and internal flows", in Chapter 6, Encyclopedia of Fluid Mechanics, N.P. Chermisinoff edition, pp.122-173.
- McCorquodale, J. A., and Khalifa, A., 1983, "Internal Flow in a Hydraulic Jump", Journal of the Hydraulic Division, ASCE, 106:HY3, pp.355-367.
- McGuik, J. J., Taylor, A. M. K. P., and Whitelaw, J. H., 1979, "The Assessment of Numerical Diffusion in Upwind Difference Calculations of Turbulent Recirculating Flows", Turbulent Shear Flows I, pp.206-224.

- McLaughlin, D. K., and Tiederman, W. G., 1973, "Biasing correcting for individual realization of laser anemometer measurements in turbulent flows", *Phys. Fluids*, Vol.16, pp.2082-2088.
- Mehrotra, S. C., 1976, "Length of hydraulic jump", *Journal of the Hydraulic Division, ASCE*, 102:HY7, pp.1027-1034.
- Nallasamy, M., 1987, "Turbulence models and their applications to the prediction of internal flows: a review", *Computers and Fluids*, Vol.15, No.2, pp.151-194.
- Narasimhan, S. and Bhargava, V. P., 1976, "Pressure fluctuations in submerged hydraulic jump", *Journal of the Hydraulic Division, ASCE*, 102:HY3, Paper 11004, pp.355-367.
- Narayanan, R., 1975, "Wall Jet Analogy to Hydraulic Jump", *Journal of the Hydraulics Division, ASCE*, 101:HY3, Proceeding paper 11172, pp.347-360.
- Narayanan, R. and Reynolds A. J., 1972, "Reattaching flow downstream of a leaf gate", *Journal of the Hydraulic Division, ASCE*, 98:HY5, Paper 8919, pp.913-934.
- Nece, R. E. and Mahmood, K., 1976, "Boundary shear stress as an index of hydraulic jump performance", *Proc. Sump., Waterways, Harbors Coastal Eng. Div., ASCE, on Inland Waterways for Navigation, Flood Control, and Water Diversions, Vol.2*, pp.978-992.
- Prandtl, L., 1925, "Ober die ansgebildete turbulenz", *ZAMM*, Vol.5, 136pp.
- Rai, M. M., 1984, "Metric-discontinuous zonal grid calculations using the Osher scheme", *Computers and Fluids*, Vol.12, NO.3, pp.161-175.
- Rai, M. M., 1986a, "Application of a conservative zonal scheme to transient and geometrically complex problems", *Computers and Fluids*, Vol.14, No.1, pp.43-58.
- Rai, M. M., 1986b, "An implicit, conservative, zonal-boundary scheme for Euler equation calculations", *Computers and Fluids*, Vol.14, No.3, pp.295-319.

- Rai, M. M., 1986c, "A conservative treatment of zonal boundaries for Euler equation calculations", *Journal of Computational Physics*, Vol.62, pp.472-503.
- Raithby, G. D., 1976, "Skew upstream differencing schemes for problems involving fluid flow", *Journal of Computer Methods for Applied Mechanics and Engineering*, Vol.9, pp.153-164.
- Rajaratnam, N., 1965a, "Submerged hydraulic jump", *Journal of the Hydraulic Division, ASCE*, Vol.91, pp.71-96.
- Rajaratnam, N., 1965b, "The hydraulic jump as a wall jet", *Journal of the Hydraulic Division, ASCE*, 91:HY5, pp.107-132.
- Rajaratnam, N., 1967a, "Hydraulic jumps", in *Advances in Hydroscience*, V.T. Chow, Ed.4, Academic Press, New York, NY, pp.198-280.
- Rajaratnam, N. and Subramanya, K., 1967b, "Diffusion of rectangular wall jets in wider channels", *Journal of Hydraulic Research, IAHR*, Vol.5, pp.281-294.
- Rajaratnam, N., 1968, "Effect of side walls on plane turbulence wall jets", *Journal of Hydraulic Research, IAHR*, 6:4, pp.327-334.
- Rajaratnam, N., 1976a, "Discussion on "pressure fluctuations in submerged jump" by S. Narasimhan and V.P. Bhargava", *Journal of the Hydraulic Division, ASCE*, 102:HY12, pp.1785-1787.
- Rajaratnam, N., 1976b, "Turbulence jets", Elsevier Scientific Co., New York.
- Resch, F. J. and Leutheusser, H.J., 1972, "Reynolds stress measurements in hydraulic jumps", *Journal of Hydraulic Research, IAHR*, 10:4, pp.409-430.
- Resch, F. J., Leutheusser, H. J., and Alemn, S., 1974, "Bubbly two-phase flow in an hydraulic jump", *Journal of the Hydraulic Division, ASCE*, 100:HY1, Proc. Paper 10297, pp.137-150.
- Rodi, W., 1976, "A new algebraic relation for calculation the Reynolds stresses", *ZAMM*, Vol.56, pp.219-221.
- Rodi, W., 1980, "Turbulence models and their application in hydraulics", *State-of-the-Art Paper, IAHR*, 104pp.

- Rouse, J., Siao, T. T. and Nagaratnam, R., 1958, "Turbulence characteristics of the hydraulic jump", Journal of the Hydraulics Division, ASCE, 84:HY1, Pro. Paper 1523, pp.1-30.
- Runchal, A. K., 1972, "Convergence and Accuracy of Three Finite Difference Schemes for a Two-Dimensional Conduction and Convection Problem", International Journal for Numerical Methods in Engineering, Vol.4, pp.541-550.
- Safranez, K., 1929, "Researches relating to the hydraulic jump", in "Bausinginieur" (English translation by D. P. Barnes), Nos. 37 and 38, Bureau of Reclamation Files, Denver, Colorado.
- Sigalla, A., 1958, "Measurement of skin friction in a plane turbulent wall jet", J. Roy. Aero. Soc., vol.62, pp.873-877.
- Smith, C. D., 1976, "Hydraulic design for an outlet structure", Proc. Sump., Waterways, Harbors Coastal Eng. Div., ASCE, on Inland Waterways for Navigation, Flood Control, and Water Diversions, Vol.2, pp.1179-1198.
- Song, C., 1977, "Interfacial boundary condition in transient flows", Proc., Eng. Mech.Div., ASCE, on Advances in Civil Engineering Through Engineering Mechanics, pp.532-534.
- Spalding, D. B., 1972, "A Novel Finite Difference Formulation for Differential Expressions Involving Both First and Second Derivatives", International Journal for Numerical Methods in Engineering, Vol.4, pp.551-559.
- Steffler, P. M., 1984, "Turbulent flow in a curved rectangular channel", Thesis presented to the University of Alberta, Alberta, in partial fulfillment of the requirements for the degree of Doctor of Philosophy, 262pp.
- Steffler, P. M., Rajaratnam, N. and Peterson A. W., 1983, "LDA measurements of mean velocity and turbulence distribution in a smooth rectangular open channel", Water Resources Engineering Report, WRE 83-4, Department of Civil Engineering, University of Alberta, Alberta, 118pp.
- Stepanov, P. M., 1958, "The submerged hydraulic jump (Russian)", Gidrotekhn i Melioratsiya, Moscow

10, (English translation by Israel Programme for Scientific Translations, 1959).

Tailland, A., and Mathieu, J., 1967, "Jet Parietal", Journal de Mecanique, Vol.6, No.1, pp.103-131.

Thompson J. F., Warsi, U. ., and Mastin, C. W., 1982, "Boundary-Fitted Coordinate systems for Numerical Solution of Partial Differential Equations - A Review", Journal of Computational Physics, Vol.47, pp.1-108.

Vassiliev, O. F. and Bukreyev, V. I., 1967, "Statistical characteristics of pressure fluctuations in the region of hydraulic jump", Proc. 12th Congr., Int. Assoc. Hydraul. Res., Vol.2, pp.1-8.

Wilson, J. and Goldstein, R. J., 1976, "Turbulent wall jets with cylindrical streamwise surface curvature", Journal of Fluids Engineering, Trans. ASME, vol 98, pp.550-557.

Wisner, P., 1967, "On the bottom pressure pulsations of the closed conduit and open channel hydraulic jumps", Proc. 12th Congr., Int. Assoc. Hydraul. Res., Vol.2, pp.46-53.

APPENDIX A - FINITE DIFFERENCE EQUATIONS

The finite difference counterparts of governing partial differential equations are listed as follows for further reference. Only the regular treatment of control volumes like Figure 108(a) to (c) is presented herein. Special consideration should be made for the boundary control volumes.

u Momentum Equation

Integrating u momentum equation over the control volume shown in Figure 108(b) yields the following formulas:

$$C_P U_P = C_E U_E + C_W U_W + C_N U_N + C_S U_S + C_\phi \quad (128)$$

where

$$C_E = (B_E + | A_E | + | B_E - | A_E | |) / 2 + A_E \quad (129)$$

$$C_W = (B_W + | A_W | + | B_W - | A_W | |) / 2 + A_W \quad (130)$$

$$C_N = (B_N + | A_N | + | B_N - | A_N | |) / 2 + A_N \quad (131)$$

$$C_S = (B_S + | A_S | + | B_S - | A_S | |) / 2 + A_S \quad (132)$$

$$C_P = C_E + C_W + C_N + C_S \quad (133)$$

$$C_0 = (P_{*W} - P_{*P}) l_{AD}/\rho - 2(\kappa_P - \kappa_W) l_{AD}/3 \quad (134)$$

and

$$A_E = (U_P + U_E) l_{BC}/4 \quad (135)$$

$$B_E = 2v_{tBC} l_{BC}/\Delta x_{WE} \quad (136)$$

$$A_W = (U_P + U_W) l_{AD}/4 \quad (137)$$

$$B_W = 2v_{tAD} l_{AD}/\Delta x_{WWP} \quad (138)$$

$$A_N = (V_{NW} + V_N) l_{AB}/4 \quad (139)$$

$$B_N = v_{tAB} l_{AB}/\Delta y_{FG} \quad (140)$$

$$A_S = (U_P + U_W) l_{DC}/4 \quad (141)$$

$$B_S = v_{tBC} l_{BC}/\Delta y_{GH} \quad (142)$$

v Momentum Equation

Integrating v momentum equation over the control volume shown in Fig.109(c) yields the following formulas:

$$C_P V_P = C_E V_E + C_W V_W + C_N V_N + C_S V_S + C_0 \quad (143)$$

where

$$C_E = (B_E + | A_E | + | B_E - | A_E | |) / 2 + A_E \quad (144)$$

$$C_W = (B_W + | A_W | + | B_W - | A_W | |) / 2 + A_W \quad (145)$$

$$C_N = (B_N + | A_N | + | B_N - | A_N | |) / 2 + A_N \quad (146)$$

$$C_S = (B_S + | A_S | + | B_S - | A_S | |) / 2 + A_S \quad (147)$$

$$C_P = C_E + C_W + C_N + C_S \quad (148)$$

$$C_\phi = (P_{*S} - P_{*P}) l_{AB} / \rho - 2 (\kappa_P - \kappa_S) l_{AB} / 3 \quad (149)$$

and

$$A_E = (U_{SE} + U_E) l_{BC} / 4 \quad (150)$$

$$B_E = 2v_{tBC} l_{BC} / \Delta x_{WE} \quad (151)$$

$$A_W = (U_P + U_S) l_{AD} / 4 \quad (152)$$

$$B_W = 2v_{tAD} l_{AD} / \Delta x_{FG} \quad (153)$$

$$A_N = (V_P + V_N) l_{AB} / 4 \quad (154)$$

$$B_N = v_{tAB} l_{AB} / \Delta y_{NS} \quad (155)$$

$$A_S = (U_P + U_S) l_{DC}/4 \quad (156)$$

$$B_S = v_{\tau DC} l_{DC} / \Delta Y_{PSS} \quad (157)$$

κ Equation

Integrating κ equation over the control volume shown in Figure 108(a) yields the following formulas:

$$C_P K_P = C_E K_E + C_W K_W + C_N K_N + C_S K_S + C_\phi \quad (158)$$

where

$$C_E = (B_E + |A_E| + |B_E - |A_E||) / 2 + A_E \quad (159)$$

$$C_W = (B_W + |A_W| + |B_W - |A_W||) / 2 + A_W \quad (160)$$

$$C_N = (B_N + |A_N| + |B_N - |A_N||) / 2 + A_N \quad (161)$$

$$C_S = (B_S + |A_S| + |B_S - |A_S||) / 2 + A_S \quad (162)$$

$$C_P = C_E + C_W + C_N + C_S \quad (163)$$

$$C_\phi = (G_P - \epsilon_P) l_{AB} l_{AD} \quad (164)$$

and

$$A_E = U_E l_{BC}/2 \quad (165)$$

$$B_E = v_{tBC} l_{BC} / \sigma_K / \Delta x_{EP} \quad (166)$$

$$A_W = U_P l_{AD}/2 \quad (167)$$

$$B_W = v_{tAD} l_{AD} / \sigma_K / \Delta x_{WP} \quad (168)$$

$$A_N = V_N l_{AB}/2 \quad (169)$$

$$B_N = v_{tAB} l_{AB} / \sigma_K / \Delta x_{NP} \quad (170)$$

$$A_S = V_P l_{DC}/2 \quad (171)$$

$$B_S = v_{tDC} l_{DC} / \sigma_K / \Delta x_{PS} \quad (172)$$

ϵ Equation

Integrating ϵ equation over the control volume shown in Figure 108(a) yields the following formulas:

$$C_P \epsilon_P = C_E \epsilon_E + C_W \epsilon_W + C_N \epsilon_N + C_S \epsilon_S + C_\phi \quad (173)$$

where

$$C_E = (B_E + | A_E | + | B_E - | A_E | |) / 2 + A_E \quad (174)$$

$$C_W = (B_W + | A_W | + | B_W - | A_W | |) / 2 + A_W \quad (175)$$

$$C_N = (B_N + | A_N | + | B_N - | A_N | |) / 2 + A_N \quad (176)$$

$$C_S = (B_S + | A_S | + | B_S - | A_S | |) / 2 + A_S \quad (177)$$

$$C_P = C_S + C_W + C_N + C_S \quad (178)$$

$$C_\phi = (C_1 G \varepsilon / \kappa - C_2 \varepsilon^2 / \kappa)_P l_{AB} l_{AD} \quad (179)$$

and

$$A_E = U_E l_{BC} / 2 \quad (180)$$

$$B_E = v_{tBC} l_{BC} / \sigma_E / \Delta x_{EP} \quad (181)$$

$$A_W = U_P l_{AD} / 2 \quad (182)$$

$$B_W = v_{tAD} l_{AD} / \sigma_E / \Delta x_{WP} \quad (183)$$

$$A_N = V_N l_{AB} / 2 \quad (184)$$

$$B_N = v_{tAB} l_{AB} / \sigma_E / \Delta x_{NP} \quad (185)$$

$$A_S = V_P l_{DC} / 2 \quad (186)$$

$$B_S = v_{tDC} l_{DC} / \sigma_\epsilon / \Delta x_{PS} \quad (187)$$

Continuity Equation

Define the pressure correction as:

$$P' = P_{*NEW} - P_{*old} \quad (188)$$

Integrating continuity equation over the control volume shown in Figure 108(a) yields the following formulas:

$$C_P P'_P = C_E P'_E + C_W P'_W + C_N P'_N + C_S P'_S + C_\phi \quad (189)$$

where

$$C_E = A_E^U l_{BC} \quad (190)$$

$$C_W = A_P^U l_{AD} \quad (191)$$

$$C_N = A_N^V l_{AB} \quad (192)$$

$$C_S = A_S^V l_{DC} \quad (193)$$

$$C_P = C_E + C_W + C_N + C_S \quad (194)$$

$$C_\phi = -(U_E - U_P) l_{AD} - (V_N - V_E) l_{AB} \quad (195)$$

where C_0 is evaluated differently for the offset control volumes as explained in the main text and A_E^U , A_P^U , A_N^V and A_S^V are evaluated from the u and v momentum equations.


```

+          DV, H, NS, OMEGAY, TEMP, VREF)
C
CALL PANDM(M, N, X, Y, YP, U, V, ENU, P, PP, OMEGAP, A, B, XL, LEQT1B,
+          MAB, DP, H, AXU, AYV, OMEGAH, DH, NS, PREF)
C
CALL SURFH(M, N, P, H, YP, Y, NS, OMEGAS, DH, HREF)
C
WRITE(6, 1001) K, DU, DV, DP, DH
1001  FORMAT('UVPS-K, DU, DV, DP, DH', I5, 4E12.3)
C
1000  CONTINUE
C
OMEGAK=1.
OMEGAD=1.
OMEGAI=1.
OMEGAJ=1.
DELTAK=1.
DELTAD=1.3
C1=1.43
C2=1.92
TKREF=.1
TDREF=1.
C
CALL PUVXY(M, N, NS, X, Y, YP, H, U, V, UVXY)
C
DO 2000 K=1, 300
C
CALL TDRE(M, N, NS, X, Y, YP, H, U, V, UVXY, TK, TD, TNU, ENU,
+          DELTAD, C1, C2, OMEGAD, DTD, LEQT1B, A, B, XL, MAB,
+          TEMP, OMEGAJ, TDREF, CMU, CK)
C
CALL TKRE(M, N, NS, X, Y, YP, H, U, V, UVXY, TK, TD, TNU, ENU,
+          DELTAK, OMEGAK, DTK, LEQT1B, A, B, XL, MAB, CMU, CNU,
+          TEMP, OMEGAI, TKREF)
C
WRITE(6, 2001) K, DTD, DTK
2001  FORMAT('TKD-K, DTD, DTK', I5, 2E12.3)
C
2000  CONTINUE
C
OMEGAU=.2
OMEGAV=.2
OMEGAP=.2
OMEGAX=.2
OMEGAY=.2
OMEGAH=.2
OMEGAK=.2
OMEGAD=.2
OMEGAI=.2
OMEGAJ=.2
OMEGAS=.1
OMEGAW=.2
TOL=.001
C
DO 3000 K=1, 600
C
CALL UXMOM(M, N, X, Y, YP, U, V, ENU, P, OMEGAU, A, B, XL, LEQT1B, MAB,
+          DU, H, NS, OMEGAX, TEMP, UREF, TK)
C

```

Figure B1 Continued


```

YT=.299
U1=2.72
C
CALL GRID(M,N,X,Y,YP,H,YT)
C
NW=14
CMU=.09
CALL INLET(M,N,U,V,TK,TD,Y,TNU,CMU,U1,Y1,NW)
C
CK=.4
CE=9.
CNU=1.E-6
CALL WALL(M,N,X,Y,U,V,TK,TD,TNU,ENU,Y1,U1,CMU,CE,CNU,CK)
C
CALL GUESS(M,N,U,V,TK,TD,CNU,CMU,H,P,PP,TNU,ENU,U1,X,NW)
C
MAB=72
OMEGAU=.2
OMEGAV=.2
OMEGAP=.2
OMEGAX=.2
OMEGAY=.2
OMEGAH=.2
OMEGAS=.2
UREF=U1
VREF=U1/30.
PREF=YT*9.81E+3
HREF=YT
NS=33
C
DO 1000 K=1,300
C
CALL UXMOM(M,N,X,Y,YP,U,V,ENU,P,OMEGAU,A,B,XL,LEQT1B,MAB,
+          DU,H,NS,OMEGAX,TEMP,UREF)
C
CALL VYMOM(M,N,X,Y,YP,U,V,ENU,P,OMEGAV,A,B,XL,LEQT1B,MAB,
+          DV,H,NS,OMEGAY,TEMP,VREF)
C
CALL PANDM(M,N,X,Y,YP,U,V,ENU,P,PP,OMEGAP,A,B,XL,LEQT1B,
+          MAB,DP,H,AXU,AYV,OMEGAH,DH,NS,PREF)
C
CALL SURFH(M,N,P,H,YP,Y,NS,OMEGAS,DH,HREF)
C
WRITE(6,1001)K,DU,DV,DP,DH
1001  FORMAT('UVPS-K,DU,DV,DP,DH',I5,4E12.3)
C
1000  CONTINUE
C
OMEGAK=.3
OMEGAD=.3
OMEGAI=.3
OMEGAJ=.3
DELTAK=1.
DELTAD=1.3
C1=1.43
C2=1.92
TKREF=.1
TDREF=1.
C

```

Figure B1 Continued

```

CALL PUVXY(M,N,NS,X,Y,YP,H,U,V,UVXY)
C
DO 2000 K=1,300
C
CALL TDRE(M,N,NS,X,Y,YP,H,U,V,UVXY,TK,TD,TNU,ENU,
+ DELTAD,C1,C2,OMEGAD,DTD,LEQT1B,A,B,XL,MAB,
+ TEMP,OMEGAJ,TDREF,CMU,CK)
C
CALL TKEE(M,N,NS,X,Y,YP,H,U,V,UVXY,TK,TD,TNU,ENU,
+ DELTAK,OMEGAK,DTK,LEQT1B,A,B,XL,MAB,CMU,CNU,
+ TEMP,OMEGAI,TKREF)
C
WRITE(6,2001)K,DTD,DTK
2001 FORMAT('TKD-K,DTD,DTK',I5,2E12.3)
C
2000 CONTINUE
C
OMEGAU=.2
OMEGAV=.2
OMEGAP=.2
OMEGAX=.2
OMEGAY=.2
OMEGAH=.2
OMEGAK=.2
OMEGAD=.2
OMEGAI=.2
OMEGAJ=.2
OMEGAS=.01
OMEGAW=.2
C
DO 3000 K=1,800
C
CALL UXMOM(M,N,X,Y,YP,U,V,ENU,P,OMEGAU,A,B,XL,LEQT1B,MAB,
+ DU,H,NS,OMEGAX,TEMP,UREF,TK)
C
CALL VYMOM(M,N,X,Y,YP,U,V,ENU,P,OMEGAV,A,B,XL,LEQT1B,MAB,
+ DV,H,NS,OMEGAY,TEMP,VREF,TK)
C
CALL PANDM(M,N,X,Y,YP,U,V,ENU,P,PP,OMEGAP,A,B,XL,LEQT1B,
+ MAB,DP,H,AXU,AYV,OMEGAH,DH,NS,PREF)
C
CALL PUVXY(M,N,NS,X,Y,YP,H,U,V,UVXY)
C
CALL TDRE(M,N,NS,X,Y,YP,H,U,V,UVXY,TK,TD,TNU,ENU,
+ DELTAD,C1,C2,OMEGAD,DTD,LEQT1B,A,B,XL,MAB,
+ TEMP,OMEGAJ,TDREF,CMU,CK)
C
CALL TKEE(M,N,NS,X,Y,YP,H,U,V,UVXY,TK,TD,TNU,ENU,
+ DELTAK,OMEGAK,DTK,LEQT1B,A,B,XL,MAB,CMU,CNU,
+ TEMP,OMEGAI,TKREF)
C
CALL SURFH(M,N,P,H,YP,Y,NS,OMEGAS,DH,HREF)
C
CALL WALSHR(M,N,X,Y,U,V,TK,TD,CMU,CNU,CE,CK,OMEGAW,DW)
C
WRITE(6,3001)K,DU,DV,DP,DH,DTD,DTK,DW
3001 FORMAT('UVPKD-K,DU,DV,DP,DH,DTD,DTK,DW',I5,7E12.3)
C
3000 CONTINUE

```

Figure B1 Continued

```

C
DO 30 I=1,M
DO 30 J=1,N
WRITE(6,40)I,J,U(I,J),V(I,J),TK(I,J),TD(I,J),TNU(I,J),
+ P(I,J)
40 FORMAT(2I5,6E12.5)
30 CONTINUE
C
DO 51 I=1,M
WRITE(6,61)I,H(I)
61 FORMAT('I,H',I5,E15.5)
51 CONTINUE
C
STOP
END

C
CCCCCCCCCCCCCCCCCCCCCCCCCCCCCCCCCCCCCCCCCCCCCCCCCCCCCCCCCCCC
C
C
C MAIN PROGRAM FOR SERIES S8
C
C
CCCCCCCCCCCCCCCCCCCCCCCCCCCCCCCCCCCCCCCCCCCCCCCCCCCCCCCCCCCC
C
C
EXTERNAL LEQT1B
DOUBLE PRECISION X(90),H(90),Y(45),YP(45),U(90,45),
+ V(90,45),TK(90,45),TD(90,45),P(90,45),
+ TNU(90,45),ENU(90,45),A(90,3),B(90,1),
+ XL(164),UVXY(90,45),PP(90,45),AXU(90,45),
+ AYV(90,45),TEMP(90,45)
C
M=90
N=45
Y1=.015
YT=.206
U1=3.14
C
CALL GRID(M,N,X,Y,YP,H,YT)
C
NW=16
CMU=.09
CALL INLET(M,N,U,V,TK,TD,Y,TNU,CMU,U1,Y1,NW)
C
CK=.4
CE=9.
CNU=1.E-6
CALL WALL(M,N,X,Y,U,V,TK,TD,TNU,ENU,Y1,U1,CMU,CE,CNU,CK)
C
CALL GUESS(M,N,U,V,TK,TD,CNU,CMU,H,P,PP,TNU,ENU,U1,X,NW)
C
MAB=M-2
OMEGAU=.2
OMEGAV=.2
OMEGAP=.1
OMEGAX=.2
OMEGAY=.2
OMEGAH=.1
OMEGAS=.01

```

Figure B1 Continued

```

UREF=U1
VREF=U1/30.
PREF=YT*9.81E+3
HREF=YT
NS=30
C
DO 1000 K=1,300
C
  CALL UXMOM(M,N,X,Y,YP,U,V,ENU,P,OMEGAU,A,B,XL,LEQT1B,MAB,
+           DU,H,NS,OMEGAX,TEMP,UREF)
C
  CALL VYMOM(M,N,X,Y,YP,U,V,ENU,P,OMEGAV,A,B,XL,LEQT1B,MAB,
+           DV,H,NS,OMEGAY,TEMP,VREF)
C
  CALL PANDM(M,N,X,Y,YP,U,V,ENU,P,PP,OMEGAP,A,B,XL,LEQT1B,
+           MAB,DP,H,AXU,AYV,OMEGAH,DH,NS,PREF)
C
  CALL SURFH(M,N,P,H,YP,Y,NS,OMEGAS,DH,HREF)
C
  WRITE(6,1001)K,DU,DV,DP,DH
1001  FORMAT('UVPS-K,DU,DV,DP,DH',I5,4E12.3)
C
1000  CONTINUE
C
  OMEGAK=.1
  OMEGAD=.3
  OMEGAI=.1
  OMEGAJ=.3
  DELTAK=1.
  DELTAD=1.3
  C1=1.43
  C2=1.92
  TKREF=.1
  TDREF=1.
C
  CALL PUVXY(M,N,NS,X,Y,YP,H,U,V,UVXY)
C
DO 2000 K=1,300
C
  CALL TDRE(M,N,NS,X,Y,YP,H,U,V,UVXY,TK,TD,TNU,ENU,
+           DELTAD,C1,C2,OMEGAD,DTD,LEQT1B,A,B,XL,MAB,
+           TEMP,OMEGAJ,TDREF,CMU,CK)
C
  CALL TKEE(M,N,NS,X,Y,YP,H,U,V,UVXY,TK,TD,TNU,ENU,
+           DELTAK,OMEGAK,DTK,LEQT1B,A,B,XL,MAB,CMU,CNU,
+           TEMP,OMEGAI,TKREF)
C
  WRITE(6,2001)K,DTD,DTK
2001  FORMAT('TKD-K,DTD,DTK',I5,2E12.3)
C
3000  CONTINUE
C
  OMEGAU=.2
  OMEGAV=.1
  OMEGAP=.1
  OMEGAX=.2
  OMEGAY=.1
  OMEGAH=.1
  OMEGAK=.1

```

Figure B1 Continued


```

C      THIS SUBROUTINE IS TO INITIALIZE THE GRID MESH.
C
C      SUBROUTINE GRID(M,N,X,Y,YP,H,YT)
C
C      DOUBLE PRECISION X(M),Y(N),YP(N),H(M)
C
C      X(1)=0.
C      X(2)=0.002
C      X(3)=0.004
C      X(4)=0.008
C      X(5)=0.015
C      X(6)=0.025
C
C      DX=.015
C      DO 10 I=7,21
C          X(I)=X(I-1)+DX
10     CONTINUE
C
C      DX=.025
C      DO 20 I=22,51
C          X(I)=X(I-1)+DX
20     CONTINUE
C
C      DX=.0375
C      DO 30 I=52,71
C          X(I)=X(I-1)+DX
30     CONTINUE
C
C      DO 40 I=1,M
C          H(I)=YT
40     CONTINUE
C
C      Y(1)=.001
C      Y(2)=.002
C      DY=.002
C      DO 50 I=3,13
C          Y(I)=Y(I-1)+DY
50     CONTINUE
C
C      Y(14)=.025
C      Y(15)=.026
C      DY=.002
C      DO 60 I=16,27
C          Y(I)=Y(I-1)+DY
60     CONTINUE
C
C      NS=27
C      YP(NS)=0.
C      YP(28)=2./64.
C      DY=4./64.
C      DO 70 J=29,45
C          YP(J)=YP(J-1)+DY
70     CONTINUE
C
C      DO 100 I=1,M
C          WRITE(6,110) I,X(I),H(I)
110     FORMAT('x,h',I4,2E13.4)
100     CONTINUE
C

```

Figure B1 Continued

```

DO 200 J=1,NS
WRITE(6,210)J,Y(J)
210   FORMAT('y',I4,E13.4)
200   CONTINUE
C
DO 300 J=NS+1,N
WRITE(6,210)J,Y(NS)+YP(J)*(YT-Y(NS))
300   CONTINUE
C
RETURN
END

C
C   CCCCCCCCCCCCCCCCCCCCCCCCCCCCCCCCCCCCCCCCCCCCCCCCCCCCC
C   C                               C
C   C   SUBROUTINE GRID FOR S6     C
C   C                               C
C   C   CCCCCCCCCCCCCCCCCCCCCCCCCCCCCCCCCCCCCCCCCCCCCCCCCCCCC
C
C
C   THIS SUBROUTINE IS TO INITIALIZE THE GRID MESH.
C
C   SUBROUTINE  GRID(M,N,X,Y,YP,H,YT)
C
C   DOUBLE PRECISION X(M),Y(N),YP(N),H(M)
C
C   X(1)=0.
C   X(2)=0.002
C   X(3)=0.004
C   X(4)=0.008
C   X(5)=0.015
C   X(6)=0.025
C   X(7)=0.035
C   X(8)=0.050
C
C   DX=.020
C   DO 10 I=9,18
10     X(I)=X(I-1)+DX
C   CONTINUE
C
C   X(19)=.275
C   DX=.035
C   DO 20 I=20,54
20     X(I)=X(I-1)+DX
C   CONTINUE
C
C   DX=.065
C   DO 30 I=55,74
30     X(I)=X(I-1)+DX
C   CONTINUE
C
C   DO 40 I=1,M
40     H(I)=YT
C   CONTINUE
C
C   Y(1)=.001
C   Y(2)=.002
C   DY=.002

```

Figure B1 Continued


```

DO 50 I=3,13
  Y(I)=Y(I-1)+DY
50 CONTINUE
C
  Y(14)=.025
  Y(15)=.026
  DY=.002
  DO 60 I=16,27
    Y(I)=Y(I-1)+DY
60 CONTINUE
C
  DY=.004
  DO 65 I=28,33
    Y(I)=Y(I-1)+DY
65 CONTINUE
C
  NS=33
  YP(NS)=0.
  YP(34)=4./143.
  YP(35)=10./143.
  YP(36)=18./143.
  DY=10./143.
  DO 70 J=37,50
    YP(J)=YP(J-1)+DY
70 CONTINUE
C
  DO 100 I=1,M
    WRITE(6,110) I, X(I), H(I)
110 FORMAT('x,h',I4,2E13.4)
100 CONTINUE
C
  DO 200 J=1,NS
    WRITE(6,210) J, Y(J)
210 FORMAT('y',I4,E13.4)
200 CONTINUE
C
  DO 300 J=NS+1,N
    WRITE(6,210) J, Y(NS)+YP(J)*(YT-Y(NS))
300 CONTINUE
C
RETURN
END

C
C      CCCCCCCCCCCCCCCCCCCCCCCCCCCCCCCCCCCCCCCCCCCCCCCCCCCCCC
C      C                      SUBROUTINE GRID FOR S8          C
C      C
C      C
C      CCCCCCCCCCCCCCCCCCCCCCCCCCCCCCCCCCCCCCCCCCCCCCCCCCCCCC
C
C
C      THIS SUBROUTINE IS TO INITIALIZE THE GRID MESH.
C
C      SUBROUTINE  GRID(M,N,X,Y,YP,H,YT)
C
C      DOUBLE PRECISION X(M),Y(N),YP(N),H(M)
C
C      X(1)=0.
C      X(2)=0.0005

```

Figure B1 Continued

```

X(3)=0.001
X(4)=0.0015
X(5)=0.002
X(6)=0.003
X(7)=0.004
X(8)=0.006
X(9)=0.008
X(10)=0.012
X(11)=0.016
X(12)=0.022
C
DX=.012
DO 10 I=13,31
  X(I)=X(I-1)+DX
10 CONTINUE
C
DX=.015
DO 20 I=32,49
  X(I)=X(I-1)+DX
20 CONTINUE
C
DX=.020
DO 30 I=50,58
  X(I)=X(I-1)+DX
30 CONTINUE
C
DX=.025
DO 32 I=59,70
  X(I)=X(I-1)+DX
32 CONTINUE
C
DX=.040
DO 34 I=71,90
  X(I)=X(I-1)+DX
34 CONTINUE
C
DO 40 I=1,M
  H(I)=YT
40 CONTINUE
C
Y(1)=.0005
Y(2)=.001
DY=.001
DO 50 I=3,15
  Y(I)=Y(I-1)+DY
50 CONTINUE
C
Y(16)=.015
Y(17)=.016
DY=.001
DO 60 I=18,29
  Y(I)=Y(I-1)+DY
60 CONTINUE
Y(30)=.030
C
NS=30
YP(NS)=0.
YP(31)=2./83.5
YP(32)=5./83.5

```

Figure B1 Continued

```

YP(33)=10./83.5
DY=7./83.5
DO 70 J=34,45
  YP(J)=YP(J-1)+DY
70 CONTINUE
C
  DO 100 I=1,M
    WRITE(6,110) I,X(I),H(I)
110   FORMAT('x,h',I4,2E13.4)
100 CONTINUE
C
  DO 200 J=1,NS
    WRITE(6,210) J,Y(J)
210   FORMAT('y',I4,E13.4)
200 CONTINUE
C
  DO 300 J=NS+1,N
    WRITE(6,210) J,Y(NS)+YP(J)*(YT-Y(NS))
300 CONTINUE
C
RETURN
END

C
C      CCCCCCCCCCCCCCCCCCCCCCCCCCCCCCCCCCCCCCCCCCCCCCCCCCCCCCCCC
C      C
C      C              SUBROUTINE INLET              C
C      C
C      CCCCCCCCCCCCCCCCCCCCCCCCCCCCCCCCCCCCCCCCCCCCCCCCCCCCCCCCC
C
C
C      THIS SUBROUTINE IS TO INITIALIZE THE INLET CONDITION.
C
C      SUBROUTINE INLET(M,N,U,V,TK,TD,Y,TNU,CMU,U1,Y1,NW)
C
C      DOUBLE PRECISION U(M,N),V(M,N),TK(M,N),TD(M,N),Y(N),TNU(N,M)
C
C      UP=.04*U1
C      TKO=1.5*UP**2
C      TDO=.8*UP**3/Y1
C      TNUO=CMU*TKO**2/TDO
C
C      DO 10 J=1,NW-1
C      U(1,J)=U1+1.4*(Y(J)-Y1/2.)
C      V(1,J)=-1.8*Y(J)
C      TK(1,J)=TKO
C      TD(1,J)=TDO
C      TNU(1,J)=TNUO
10 CONTINUE
C
C      DO 20 J=NW,N
C      U(1,J)=.0
C      V(1,J)=.0
C      TK(1,J)=.0
C      TD(1,J)=.0
C      TNU(1,J)=.0
20 CONTINUE
V(1,NW)=-1.8*Y(NW)

```

Figure B1 Continued

```

C
RETURN
END

C
CCCCCCCCCCCCCCCCCCCCCCCCCCCCCCCCCCCCCCCCCCCC
C
C          SUBROUTINE WALL          C
C
C          CCCCCCCCCCCCCCCCCCCCCCCCCCCCCCCCCCCCCCCCCCCCC
C
C
THIS SUBROUTINE IS TO EVALUATE THE WALL BOUNDARY CONDITION.
C
SUBROUTINE WALL(M,N,X,Y,U,V,TK,TD,TNU,ENU,Y1,U1,CMU,CE,CNU,
+          CK)
C
DOUBLE PRECISION X(M),Y(N),U(M,N),V(M,N),TK(M,N),TD(M,N),
+          TNU(M,N),ENU(M,N)
C
DO 10 I=2,M
  IF(X(I)/Y1.GE.50.)GO TO 11
  CF=.0059*(.0001/.0059)**(X(I)/Y1/50.)
GO TO 12
11  CF=.0001
12  USTAR=SQRT(CF/2.)*U1
  TK(I,1)=USTAR**2/SQRT(CMU)
  TD(I,1)=USTAR**3/CK/Y(1)
  U(I,1)=USTAR/CK*DLOG(CE*Y(1)*USTAR/CNU)
  V(I,1)=0.
  TNU(I,1)=CMU*TK(I,1)**2/TD(I,1)
  ENU(I,1)=TNU(I,1)+CNU
10  CONTINUE
C
RETURN
END

C
CCCCCCCCCCCCCCCCCCCCCCCCCCCCCCCCCCCCCCCCCCCC
C
C          SUBROUTINE GUESS          C
C
C          CCCCCCCCCCCCCCCCCCCCCCCCCCCCCCCCCCCCCCCCCCCCC
C
C
THIS SUBROUTINE IS TO GUESS THE UNKNOWNNS.
C
SUBROUTINE GUESS(M,N,U,V,TK,TD,CNU,CMU,H,P,PP,TNU,ENU,U1,X,
+          NW)
C
DOUBLE PRECISION U(M,N),V(M,N),TK(M,N),TD(M,N),H(M),X(M),
+          P(M,N),PP(M,N),TNU(M,N),ENU(M,N)
C
TK0=.6
TDO=40.
DO 10 I=2,M
  DO 20 J=2,N
    U(I,J)=U1/2.

```

Figure B1 Continued

```

      IF (J.GT.NW)U(I,J)=-U1/5.
      IF (X(I).GT.X(M)/2.)U(I,J)=U1*25./187.
      V(I,J)=-.01
      IF (J.GT.NW)V(I,J)=-.01
      IF (J.EQ.N-1)V(I,J)=.0
      TK(I,J)=TKO
      TD(I,J)=TDO
20     CONTINUE
10     CONTINUE
C
      DO 30 I=1,M
      DO 40 J=1,N
      P(I,J)=9.81E+3*H(I)
      IF (TK(I,J).NE.0.)GO TO 50
      TNU(I,J)=.0
      ENU(I,J)=CNU
      GO TO 40
50     TNU(I,J)=CMU*TK(I,J)**2/TD(I,J)
      ENU(I,J)=TNU(I,J)+CNU
40     CONTINUE
30     CONTINUE
C
      DO 60 I=1,M
      DO 60 J=1,N
      PP(I,J)=.0
60     CONTINUE
C
      RETURN
      END

C
C      CCCCCCCCCCCCCCCCCCCCCCCCCCCCCCCCCCCCCCCCCCCCCCCCCCCCCCCCC
C      C                                                                 C
C      C          SUBROUTINE UXMOM                                     C
C      C                                                                 C
C      C      CCCCCCCCCCCCCCCCCCCCCCCCCCCCCCCCCCCCCCCCCCCCCCCCCCCCCCCCC
C
C
C      THIS SUBROUTINE IS TO EVALUATE VELOCITY U.
C      MAB=MAX(M,N)-2
C
C      SUBROUTINE  UXMOM(M,N,X,Y,YP,U,V,ENU,P,OMEGAU,A,B,XL,LEQT1B,
+      MAB,DU,H,NS,OMEGAX,TEMP,UREF,TK)
C
C      EXTERNAL LEQT1B
C      DOUBLE PRECISION U(M,N),V(M,N),ENU(M,N),X(M),Y(N),YP(N),
+      A(MAB,3),B(MAB,1),P(M,N),XL(2*MAB),H(M),
+      TEMP(M,N),TK(M,N)
C
      DO 1 I=2,M
      DO 1 J=2,N
      TEMP(I,J)=U(I,J)
1     CONTINUE
C
C-----
C      SWEEP IN X DIRECTION
C-----
C

```

Figure B1 Continued

```

DO 10 J=2,N-2
  IF(J.GE.NS)GO TO 11
  AX=(Y(J+1)-Y(J-1))/2.
C
11 DO 20 I=2,M-1
  IF(J.LT.NS)GO TO 21
  HAV=(H(I-1)+H(I))/2.-Y(NS)
  DO 22 JJ=NS+1,N
  Y(JJ)=Y(NS)+YP(JJ)*HAV
22 CONTINUE
  AX=(Y(J+1)-Y(J-1))/2.
21 AY=X(I)-X(I-1)
C
  IF(I.GT.2)GO TO 30
  CL=(X(2)-X(1))/2.
  CU=U(1,J)
  BW=ENU(1,J)*AX/CL
  AW=CU*AX/2.
  IF(CU*CL/ENU(1,J).GT.1.)BW=.0
  GO TO 40
C
30 CL=(X(I)-X(I-2))/2.
  CU=(U(I,J)+U(I-1,J))/2.
  BW=ENU(I-1,J)*AX/CL
  AW=CU*AX/2.
C
40 CL=(X(I+1)-X(I-1))/2.
  CU=(U(I,J)+U(I+1,J))/2.
  BE=ENU(I,J)*AX/CL
  AE=CU*AX/2.
C
  CL=Y(J+1)-Y(J)
  CU=(V(I-1,J+1)+V(I,J+1))/2.
  CENU=(ENU(I,J)+ENU(I,J+1)+ENU(I-1,J)+ENU(I-1,J+1))/4.
  BN=CENU*AY/CL
  AN=CU*AY/2.
C
  CL=Y(J)-Y(J-1)
  CU=(V(I-1,J)+V(I,J))/2.
  CENU=(ENU(I,J)+ENU(I-1,J)+ENU(I-1,J-1)+ENU(I,J-1))/4.
  BS=CENU*AY/CL
  AS=CU*AY/2.
C
  STURB=-2./3.*(TK(I,J)-TK(I-1,J))*AX
  IF(I.EQ.2)STURB=0.
C
  CE=(BE+ABS(AE)+ABS(BE-ABS(AE)))/2.-AE
  CW=(BW+ABS(AW)+ABS(BW-ABS(AW)))/2.+AW
  IF(I.EQ.2)CW=2.*AW+BW
  CN=(BN+ABS(AN)+ABS(BN-ABS(AN)))/2.-AN
  CS=(BS+ABS(AS)+ABS(BS-ABS(AS)))/2.+AS
  CP=CE+CW+CN+CS
  CE=CE/CP
  CW=CW/CP
  CN=CN/CP
  CS=CS/CP
  CH=AX/1.E+3*(P(I-1,J)-P(I,J))/CP
  CH=CH+STURB/CP
C

```

Figure B1 Continued

```

      IF(I.GT.2)GO TO 50
      A(I-1,1)=.0
      A(I-1,2)=1.
      A(I-1,3)=-CE
      B(I-1,1)=-CW*U(I-1,J)+CN*U(I,J+1)+CS*U(I,J-1)+CH
      GO TO 20
50     IF(I.EQ.M-1)GO TO 60
      A(I-1,1)=-CW
      A(I-1,2)=1.
      A(I-1,3)=-CE
      B(I-1,1)=-CN*U(I,J+1)+CS*U(I,J-1)+CH
      GO TO 20
60     A(I-1,1)=-CW
      A(I-1,2)=1.
      A(I-1,3)=.0
      B(I-1,1)=-CN*U(I,J+1)+CS*U(I,J-1)+CH+CE*U(I+1,J)
C
20     CONTINUE
C
      CALL LEQT1B(A,M-2,1,1,MAB,B,1,MAB,0,XL,IER)
      DO 70 I=2,M-1
        U(I,J)=(1.-OMEGAU)*U(I,J)+OMEGAU*B(I-1,1)
70     CONTINUE
      U(M,J)=U(M-1,J)
C
      IF(J.NE.N-2)GO TO 10
      DO 80 I=2,M
        U(I,N-1)=U(I,N-2)
        U(I,N)=U(I,N-3)
80     CONTINUE
C
10     CONTINUE
C-----
C     SWEEP IN Y DIRECTION
C-----
C
      DO 110 I=2,M-1
      AY=X(I)-X(I-1)
      HAV=(H(I-1)+H(I))/2.-Y(NS)
      DO 111 JJ=NS+1,N
        Y(JJ)=Y(NS)+YP(JJ)*HAV
111    CONTINUE
C
      DO 120 J=2,N-2
      AX=(Y(J+1)-Y(J-1))/2.
C
      IF(I.GT.2)GO TO 130
      CL=(X(2)-X(1))/2.
      CU=U(1,J)
      BW=ENU(1,J)*AX/CL
      AW=CU*AX/2.
      IF(CU*CL/ENU(1,J).GT.1.)BW=.0
      GO TO 140
C
130    CL=(X(I)-X(I-2))/2.
      CU=(U(I,J)+U(I-1,J))/2.
      BW=ENU(I-1,J)*AX/CL
      AW=CU*AX/2.

```

Figure B1 Continued

```

C
140 CL=(X(I+1)-X(I-1))/2.
    CU=(U(I,J)+U(I+1,J))/2.
    BE=ENU(I,J)*AX/CL
    AE=CU*AX/2.
C
    CL=Y(J+1)-Y(J)
    CU=(V(I-1,J+1)+V(I,J+1))/2.
    CENU=(ENU(I,J)+ENU(I,J+1)+ENU(I-1,J)+ENU(I-1,J+1))/4.
    BN=CENU*AY/CL
    AN=CU*AY/2.
C
    CL=Y(J)-Y(J-1)
    CU=(V(I-1,J)+V(I,J))/2.
    CENU=(ENU(I,J)+ENU(I-1,J)+ENU(I-1,J-1)+ENU(I,J-1))/4.
    BS=CENU*AY/CL
    AS=CU*AY/2.
C
    STURB=-2./3.*(TK(I,J)-TK(I-1,J))*AX
    IF(I.EQ.2)STURB=0.
C
    CE=(BE+ABS(AE)+ABS(BE-ABS(AE)))/2.-AE
    CW=(BW+ABS(AW)+ABS(BW-ABS(AW)))/2.+AW
    IF(I.EQ.2)CW=2.*AW+BW
    CN=(BN+ABS(AN)+ABS(BN-ABS(AN)))/2.-AN
    CS=(BS+ABS(AS)+ABS(BS-ABS(AS)))/2.+AS
    CP=CE+CW+CN+CS
    CE=CE/CP
    CW=CW/CP
    CN=CN/CP
    CS=CS/CP
    CH=AX/1.E+3*(P(I-1,J)-P(I,J))/CP
    CH=CH+STURB/CP
C
    IF(J.GT.2)GO TO 150
    A(J-1,1)=.0
    A(J-1,2)=1.
    A(J-1,3)=-CN
    B(J-1,1)=CW*U(I-1,J)+CE*U(I+1,J)+CS*U(I,J-1)+CH
    GO TO 120
150 IF(J.EQ.N-2)GO TO 160
    A(J-1,1)=-CS
    A(J-1,2)=1.
    A(J-1,3)=-CN
    B(J-1,1)=CE*U(I+1,J)+CW*U(I-1,J)+CH
    GO TO 120
160 A(J-1,1)=-CS
    A(J-1,2)=1.
    A(J-1,3)=.0
    B(J-1,1)=CE*U(I+1,J)+CW*U(I-1,J)+CH+CN*U(I,J+1)
C
120 CONTINUE
C
    CALL LEQT1B(A,N-3,1,1,MAB,B,1,MAB,0,XL,IER)
    DO 170 J=2,N-2
    IF(I.EQ.2.AND.J.EQ.2)DU=.0
    UO=U(I,J)
    U(I,J)=(1.-OMEGAU)*U(I,J)+OMEGAU*B(J-1,1)
    DU=ABS(U(I,J)-UO)+DU

```

Figure B1 Continued


```

170    CONTINUE
      U(I,N-1)=U(I,N-2)
      U(I,N)=U(I,N-3)
C
      IF(I.NE.M-1)GO TO 110
      DO 180 J=2,N
        U(M,J)=U(M-1,J)
180    CONTINUE
C
110    CONTINUE
C
      DU=DU/(N-3)/(M-2)
      DU=DU/UREF
C
      DO 2 I=2,M
        DO 2 J=2,N
          U(I,J)=(1.-OMEGAX)*TEMP(I,J)+OMEGAX*U(I,J)
2      CONTINUE
C
      RETURN
      END

C          CCCCCCCCCCCCCCCCCCCCCCCCCCCCCCCCCCCCCCCCCCCCCCCCCC
C          C
C          C          SUBROUTINE VYMOM          C
C          C
C          C          CCCCCCCCCCCCCCCCCCCCCCCCCCCCCCCCCCCCCCCCCCCCCCCCCC
C
C
C      THIS SUBROUTINE IS TO EVALUATE VELOCITY V.
C      MAB=MAX(M,N)-2
C
C      SUBROUTINE  VYMOM(M,N,X,Y,YP,U,V,ENU,P,OMEGAV,A,B,XL,LEQT1B,
+      MAB,DV,H,NS,OMEGAY,TEMP,VREF,TK)
C
C      EXTERNAL LEQT1B
C      DOUBLE PRECISION U(M,N),V(M,N),ENU(M,N),X(M),Y(N),YP(N),
+      A(MAB,3),B(MAB,1),P(M,N),XL(2*MAB),H(M),
+      TEMP(M,N),TK(M,N)
C
C      DO 1 I=2,M
        DO 1 J=2,N
          TEMP(I,J)=V(I,J)
1      CONTINUE
C
      DO 5 I=2,M-1
        DY1=(H(I)-H(I-1))/2.
        DY2=(H(I+1)-H(I))/2.
        DX=(X(I+1)-X(I-1))/2.
        V(I,N-1)=(U(I+1,N-2)*DY2+U(I,N-2)*DY1)/DX
5      CONTINUE
C
C-----
C          SWEEP IN X DIRECTION
C-----
C
      DO 10 J=2,N-2
        IF(J.GE.NS)GO TO 11

```

Figure B1 Continued

```

      AX=Y(J)-Y(J-1)
C
11 DO 20 I=2,M-1
      IF(J.LT.NS)GO TO 21
      HAV=H(I)-Y(NS)
      DO 22 JJ=NS+1,N
        Y(JJ)=Y(NS)+YP(JJ)*HAV
22      CONTINUE
      AX=Y(J)-Y(J-1)
21      AY=(X(I+1)-X(I-1))/2.
C
      CL=X(I+1)-X(I)
      CU=(U(I+1,J)+U(I+1,J-1))/2.
      CENU=(ENU(I,J)+ENU(I,J-1)+ENU(I+1,J)+ENU(I+1,J-1))/4.
      BE=CENU*AX/CL
      AE=CU/2.*AX
C
      CL=X(I)-X(I-1)
      CU=(U(I,J)+U(I,J-1))/2.
      CENU=(ENU(I,J)+ENU(I,J-1)+ENU(I-1,J)+ENU(I-1,J-1))/4.
      BW=CENU*AX/CL
      AW=CU/2.*AX
C
      CL=(Y(J+1)-Y(J-1))/2.
      CU=(V(I,J+1)+V(I,J))/2.
      CENU=ENU(I,J)
      BN=CENU*AY/CL
      AN=CU/2.*AY
C
      IF(J.GT.2)GO TO 30
      CL=(Y(2)-Y(1))/2.
      CU=V(I,1)
      GO TO 40
30      CL=(Y(J)-Y(J-2))/2.
      CU=(V(I,J)+V(I,J-1))/2.
40      CENU=ENU(I,J-1)
      BS=CENU*AY/CL
      AS=CU/2.*AY
C
      STURB=-2./3.*(TK(I,J)-TK(I,J-1))*AY
      IF(J.EQ.2)STURB=0.
C
      CN=(BN+ABS(AN)+ABS(BN-ABS(AN)))/2.-AN
      CS=(BS+ABS(AS)+ABS(BS-ABS(AS)))/2.+AS
      CE=(BE+ABS(AE)+ABS(BE-ABS(AE)))/2.-AE
      CW=(BW+ABS(AW)+ABS(BW-ABS(AW)))/2.+AW
      CP=CE+CW+CN+CS
      CE=CE/CP
      CW=CW/CP
      CN=CN/CP
      CS=CS/CP
      CH=AY/1.E+3*(P(I,J-1)-P(I,J))/CP
      CH=CH+STURB/CP
C
      IF(I.GT.2)GO TO 50
      A(I-1,1)=.0
      A(I-1,2)=1.
      A(I-1,3)=-CE
      B(I-1,1)=CW*V(I-1,J)+CN*V(I,J+1)+CS*V(I,J-1)+CH

```

Figure B1 Continued

```

      GO TO 20
50    IF(I.EQ.M-1)GO TO 60
      A(I-1,1)=-CW
      A(I-1,2)=1.
      A(I-1,3)=-CE
      B(I-1,1)=S*V(I,J+1)+CS*V(I,J-1)+CH
      GO TO 20
60    A(I-1,1)=-CW
      A(I-1,2)=1.-CE
      A(I-1,3)=.0
      B(I-1,1)=CN*V(I,J+1)+CS*V(I,J-1)+CH
C
20    CONTINUE
C
      CALL LEQT1B(A,M-2,1,1,MAB,B,1,MAB,0,XL,IER)
      DO 70 I=2,M-1
        V(I,J)=(1.-OMEGAV)*V(I,J)+OMEGAV*B(I-1,1)
70    CONTINUE
      V(M,J)=V(M-1,J)
C
      IF(J.NE.N-2)GO TO 10
      DO 80 I=2,M-1
        V(I,N)=V(I,N-2)
80    CONTINUE
C
10    CONTINUE
C
-----
C      SWEEP IN Y DIRECTION
-----
C
      DO 110 I=2,M-1
        AY=(X(I+1)-X(I-1))/2.
        HAV=H(I)-Y(NS)
        DO 111 JJ=NS+1,N
          Y(JJ)=Y(NS)+YP(JJ)*HAV
111    CONTINUE
C
      DO 120 J=2,N-2
        AX=Y(J)-Y(J-1)
C
        CL=X(I+1)-X(I)
        CU=(U(I+1,J)+U(I+1,J-1))/2.
        CENU=(ENU(I,J)+ENU(I,J-1)+ENU(I+1,J)+ENU(I+1,J-1))/4.
        BE=CENU*AX/CL
        AE=CU/2.*AX
C
        CL=X(I)-X(I-1)
        CU=(U(I,J)+U(I,J-1))/2.
        CENU=(ENU(I,J)+ENU(I,J-1)+ENU(I-1,J)+ENU(I-1,J-1))/4.
        BW=CENU*AX/CL
        AW=CU/2.*AX
C
        CL=(Y(J+1)-Y(J-1))/2.
        CU=(V(I,J+1)+V(I,J))/2.
        CENU=ENU(I,J)
        BN=CENU*AY/CL
        AN=CU/2.*AY
C

```

Figure B1 Continued

```

IF(J.GT.2)GO TO 130
  CL=(Y(2)-Y(1))/2.
  CU=V(I,1)
  GO TO 140
130  CL=(Y(J)-Y(J-2))/2.
      CU=(V(I,J)+V(I,J-1))/2.
140  CENU=ENU(I,J-1)
      BS=CENU*AY/CL
      AS=CU/2.*AY
C
      STURB=-2./3.*(TK(I,J)-TK(I,J-1))*AY
      IF(J.EQ.2)STURB=0.
C
      CN=(BN+ABS(AN)+ABS(BN-ABS(AN)))/2.-AN
      CS=(BS+ABS(AS)+ABS(BS-ABS(AS)))/2.+AS
      CE=(BE+ABS(AE)+ABS(BE-ABS(AE)))/2.-AE
      CW=(BW+ABS(AW)+ABS(BW-ABS(AW)))/2.+AW
      CP=CE+CW+CN+CS
      CE=CE/CP
      CW=CW/CP
      CN=CN/CP
      CS=CS/CP
      CH=AY/1.E+3*(P(I,J-1)-P(I,J))/CP
      CH=CH+STURB/CP
C
      IF(J.GT.2)GO TO 150
          A(J-1,1)=.0
          A(J-1,2)=1.
          A(J-1,3)=-CN
          B(J-1,1)=CE*V(I+1,J)+CW*V(I-1,J)+CS*V(I,J-1)+CH
          GO TO 120
150  IF(J.EQ.N-2)GO TO 160
          A(J-1,1)=-CS
          A(J-1,2)=1.
          A(J-1,3)=-CN
          B(J-1,1)=CE*V(I+1,J)+CW*V(I-1,J)+CH
          GO TO 120
160  A(J-1,1)=-CS
          A(J-1,2)=1.
          A(J-1,3)=.0
          B(J-1,1)=CE*V(I+1,J)+CW*V(I-1,J)+CN*V(I,J+1)+CH
C
120  CONTINUE
C
      CALL LEQT1B(A,N-3,1,1,MAB,B,1,MAB,0,XL,IER)
      DO 170 J=2,N-2
          IF(I.EQ.2.AND.J.EQ.2)DV=.0
          VO=V(I,J)
          V(I,J)=(1.-OMEGAV)*V(I,J)+OMEGAV*B(J-1,1)
          DV=ABS(V(I,J)-VO)+DV
170  CONTINUE
          V(I,N)=V(I,N-2)
C
          IF(I.NE.M-1)GO TO 110
          DO 180 J=2,N
              V(M,J)=V(M-1,J)
180  CONTINUE
C
110  CONTINUE

```

Figure B1 Continued

```

C      DV=DV/(N-3)/(M-2)
C      DV=DV/VREF
C
C      DO 2 I=2,M
C          DO 2 J=2,N
C              V(I,J)=(1.-OMEGAY)*TEMP(I,J)+OMEGAY*V(I,J)
2      CONTINUE
C
C      RETURN
C      END

C      CCCCCCCCCCCCCCCCCCCCCCCCCCCCCCCCCCCCCCCCCCCCCCCCCCCCCC
C      C
C      C          SUBROUTINE PANDM
C      C
C      C      CCCCCCCCCCCCCCCCCCCCCCCCCCCCCCCCCCCCCCCCCCCCCCCCCCCCCC
C
C      THIS SUBROUTINE IS TO EVALUATE PRESSURE CORRECTION.
C      MAB=MAX(M,N)-2
C
C      SUBROUTINE PANDM(M,N,X,Y,YP,U,V,ENU,P,PP,OMEGAP,A,B,XL,LEQT1B,
+          MAB,DP,H,AXU,AYV,OMEGAH,DH,NS,PREF)
C
C      EXTERNAL LEQT1B
C      DOUBLE PRECISION U(M,N),V(M,N),ENU(M,N),X(M),Y(N),YP(N),
+          A(MAB,3),B(MAB,1),PP(M,N),P(M,N),XL(2*MAB),
+          H(M),AXU(M,N),AYV(M,N)
C
C      -----
C      EVALUATE THE COEFFICIENTS FOR SOLUTIONS
C      -----
C
C      ----- EVALUATE AXU FROM X-MOMENTUM EQUATION-----
C
C      DO 10 J=2,N-2
C          IF(J.GE.NS)GO TO 11
C          AX=(Y(J+1)-Y(J-1))/2.
C
C      DO 20 I=2,M-1
11      IF(J.LT.NS)GO TO 21
C          HAV=(H(I-1)+H(I))/2.-Y(NS)
C          DO 22 JJ=NS+1,N
C              Y(JJ)=Y(NS)+YP(JJ)*HAV
22      CONTINUE
C          AX=(Y(J+1)-Y(J-1))/2.
21      AY=X(I)-X(I-1)
C
C          IF(I.GT.2)GO TO 30
C          CL=(X(2)-X(1))/2.
C          CU=U(1,J)
C          BW=ENU(1,J)*AX/CL
C          AW=CU*AX/2.
C          IF(CU*CL/ENU(1,J).GT.1.)BW=.0
C          GO TO 40
C
C      30      CL=(X(I)-X(I-2))/2.

```

Figure B1 Continued

```

      CU=(U(I,J)+U(I-1,J))/2.
      BW=ENU(I-1,J)*AX/CL
      AW=CU*AX/2.
C
40      CL=(X(I+1)-X(I-1))/2.
      CU=(U(I,J)+U(I+1,J))/2.
      BE=ENU(I,J)*AX/CL
      AE=CU*AX/2.
C
      CL=Y(J+1)-Y(J)
      CU=(V(I-1,J+1)+V(I,J+1))/2.
      CENU=(ENU(I,J)+ENU(I,J+1)+ENU(I-1,J)+ENU(I-1,J+1))/4.
      BN=CENU*AY/CL
      AN=CU*AY/2.
C
      CL=Y(J)-Y(J-1)
      CU=(V(I-1,J)+V(I,J))/2.
      CENU=(ENU(I,J)+ENU(I-1,J)+ENU(I-1,J-1)+ENU(I,J-1))/4.
      BS=CENU*AY/CL
      AS=CU*AY/2.
C
      CE=(BE+ABS(AE)+ABS(BE-ABS(AE)))/2.-AE
      CW=(BW+ABS(AW)+ABS(BW-ABS(AW)))/2.+AW
      IF(I.EQ.2)CW=2.*AW+BW
      CN=(BN+ABS(AN)+ABS(BN-ABS(AN)))/2.-AN
      CS=(BS+ABS(AS)+ABS(BS-ABS(AS)))/2.+AS
      CP=CE+CW+CN+CS
      AXU(I,J)=AX/1.E+3/CP
C
20      CONTINUE
10      CONTINUE
C
C----- EVALUATE AYV FROM Y-MOMENTUM EQUATION-----
C
      DO 110 J=2,N-1
      IF(J.GE.NS)GO TO 111
      AX=Y(J)-Y(J-1)
C
111      DO 120 I=2,M-1
      IF(J.LT.NS)GO TO 121
      HAV=H(I)-Y(NS)
      DO 122 JJ=NS+1,N
      Y(JJ)=Y(NS)+YP(JJ)*HAV
122      CONTINUE
      AX=Y(J)-Y(J-1)
121      AY=(X(I+1)-X(I-1))/2.
C
      CL=X(I+1)-X(I)
      CU=(U(I+1,J)+U(I+1,J-1))/2.
      CENU=(ENU(I,J)+ENU(I,J-1)+ENU(I+1,J)+ENU(I+1,J-1))/4.
      BE=CENU*AX/CL
      AE=CU/2.*AX
C
      CL=X(I)-X(I-1)
      CU=(U(I,J)+U(I,J-1))/2.
      CENU=(ENU(I,J)+ENU(I,J-1)+ENU(I-1,J)+ENU(I-1,J-1))/4.
      BW=CENU*AX/CL
      AW=CU/2.*AX
C

```

Figure B1 Continued

```

CL=(Y(J+1)-Y(J-1))/2.
CU=(V(I,J+1)+V(I,J))/2.
CENU=ENU(I,J)
BN=CENU*AY/CL
AN=CU/2.*AY
C
IF(J.GT.2)GO TO 130
  CL=(Y(2)-Y(1))/2.
  CU=V(I,1)
  GO TO 140
130 CL=(Y(J)-Y(J-2))/2.
    CU=(V(I,J)+V(I,J-1))/2.
140 CENU=ENU(I,J-1)
    BS=CENU*AY/CL
    AS=CU/2.*AY
C
CN=(BN+ABS(AN)+ABS(BN-ABS(AN)))/2.-AN
CS=(BS+ABS(AS)+ABS(BS-ABS(AS)))/2.+AS
CE=(BE+ABS(AE)+ABS(BE-ABS(AE)))/2.-AE
CW=(BW+ABS(AW)+ABS(BW-ABS(AW)))/2.+AW
CP=CE+CW+CN+CS
AYV(I,J)=AY/1.E+3/CP
C
120 CONTINUE
110 CONTINUE
C
C=====
C SOLVE CONTINUITY EQUATION FOR PRESSURE CORRECTION
C THREE TIMES OF DOUBLE SWEEP
C-----
C
DO 1000 K=1,3
C
C-----
C SWEEP IN X DIRECTION
C-----
C
DO 310 J=1,N-2
C
C::::::::::::::::::::::::::::::::::::::::::::::::::
C THIS IS THE SPECIAL TREATMENT WHEN Y=0 (ON THE BOTTOM WALL)
C.....
C
IF(J.GT.1)GO TO 311
  AX=Y(2)/2.
  DO 312 I=2,M-2
    AY=(X(I+1)-X(I-1))/2.
    CE=AXU(I+1,2)*AX/4.
    CW=AXU(I,2)*AX/4.
    CS=-AYV(I,2)*AY
    CP=CE+CW+CS
    CH=-3./4.*(U(I+1,1)-U(I,1))*AX+V(I,1)*AY-
    + (U(I+1,2)-U(I,2))*AX/4.-V(I,2)*AY
    PPI1=(CP*PP(I,2)-CE*PP(I+1,2)-CW*PP(I-1,2)-CH)/CS
    PP(I,1)=(1.-OMEGAP)*PP(I,1)+OMEGAP*PPI1
312 CONTINUE
GO TO 310
C
C::::::::::::::::::::::::::::::::::::::::::::::::::

```

Figure B1 Continued

```

C      THIS IS THE REGULAR TREATMENT FOR THE INTERIOR GRIDS
C.....
C
311      IF(J.GE.NS)GO TO 314
          AX=(Y(J+1)-Y(J-1))/2.
314      DO 320 I=1,M-2
          IF(J.LT.NS)GO TO 321
          HAV=H(I)-Y(NS)
          DO 322 JJ=NS+1,N
              Y(JJ)=Y(NS)+YP(JJ)*HAV
322      CONTINUE
          AX=(Y(J+1)-Y(J-1))/2.
321      IF(I.GT.1)AY=(X(I+1)-X(I-1))/2.
          IF(I.EQ.1)AY=(X(2)-X(1))/2.
C
          IF(I.GT.1)GO TO 323
          CW=-AXU(2,J)*AX
          CN=AYV(2,J+1)*AY/4.
          CS=AYV(2,J)*AY/4.
          CH=-U(2,J)*AX-(V(2,J+1)-V(2,J))*AY/4.+U(1,J)*AX-3./4
+          *(V(1,J+1)-V(1,J))*AY-(CN+CS)*PP(2,J)
          CP=CW
          CW=CW/CP
          CN=CN/CP
          CS=CS/CP
          CH=CH/CP
          GO TO 324
C
323      CE=AX*AXU(I+1,J)
          CW=AX*AXU(I,J)
          CN=AY*AYV(I,J+1)
          CS=AY*AYV(I,J)
          CP=CE+CW+CN+CS
C
          IF(J.GE.NS)GO TO 331
          CH=- (AX*(U(I+1,J)-U(I,J))+AY*(V(I,J+1)-V(I,J)))
          GO TO 332
331      HAV1=H(I-1)-Y(NS)
          HAV2=H(I)-Y(NS)
          HAV3=H(I+1)-Y(NS)
          IF(J.GT.NS)GO TO 333
          YSW=Y(J-1)
          YS=Y(J-1)
          YSE=Y(J-1)
          YW=Y(J)
          YC=Y(J)
          YE=Y(J)
          YNW=Y(NS)+YP(J+1)*HAV1
          YN=Y(NS)+YP(J+1)*HAV2
          YNE=Y(NS)+YP(J+1)*HAV3
          GO TO 334
333      IF(J.GT.NS+1)GO TO 335
          YSW=Y(J-1)
          YS=Y(J-1)
          YSE=Y(J-1)
          YW=Y(NS)+YP(J)*HAV1
          YC=Y(NS)+YP(J)*HAV2
          YE=Y(NS)+YP(J)*HAV3
          YNW=Y(NS)+YP(J+1)*HAV1

```

Figure B1 Continued


```

      YN=Y(NS)+YP(J+1)*HAV2
      YNE=Y(NS)+YP(J+1)*HAV3
      GO TO 334
335   YSW=Y(NS)+YP(J-1)*HAV1
      YS=Y(NS)+YP(J-1)*HAV2
      YSE=Y(NS)+YP(J-1)*HAV3
      YW=Y(NS)+YP(J)*HAV1
      YC=Y(NS)+YP(J)*HAV2
      YE=Y(NS)+YP(J)*HAV3
      YNW=Y(NS)+YP(J+1)*HAV1
      YN=Y(NS)+YP(J+1)*HAV2
      YNE=Y(NS)+YP(J+1)*HAV3
C
334   DY1=((YC+YW)-(YC+YS))/2.
      U1=U(I,J)+(U(I,J-1)-U(I,J))/(YC+YW-YS-YSW)*DY1
      DY2=((YC+YN)-(YC+YW))/2.
      U2=U(I,J)+(U(I,J+1)-U(I,J))/(YNW+YN-YC-YW)*DY2
      DY3=((YC+YN)-(YC+YE))/2.
      U3=U(I+1,J)+(U(I+1,J+1)-U(I+1,J))/(YN+YNE-YC-YE)*DY3
      DY4=((YC+YE)-(YC+YS))/2.
      U4=U(I+1,J)+(U(I+1,J-1)-U(I+1,J))/(YC+YE-YS-YSE)*DY4
      CH=-(U3*DY3+U4*DY4-U1*DY1-U2*DY2+AY*(V(I,J+1)-V(I,J)))
C
332   CE=CE/CP
      CW=CW/CP
      CN=CN/CP
      CS=CS/CP
      CH=CH/CP
324   IF(I.GT.1)GO TO 330
      A(I,1)=.0
      A(I,2)=1.
      A(I,3)=-1.
      B(I,1)=-CN*PP(2,J+1)+CS*PP(2,J-1)+CH)
      GO TO 320
330   IF(I.EQ.M-2)GO TO 340
      A(I,1)=-CW
      A(I,2)=1.
      A(I,3)=-CE
      B(I,1)=CN*PP(I,J+1)+CS*PP(I,J-1)+CH
      GO TO 320
340   A(I,1)=-CW
      A(I,2)=1.
      A(I,3)=.0
      B(I,1)=CN*PP(I,J+1)+CS*PP(I,J-1)+CE*PP(I+1,J)+CH
C
320   CONTINUE
C
C::::::::::::::::::::::::::::::::::::::::::::::::::::::::::
C   SOLVE THE CONTINUITY EQUATION FOR THE PRESSURE CORRECTION
C.....
C
      CALL LEQT1B(A,M-2,1,1,MAB,B,1,MAB,0,XL,IER)
      DO 380 I=1,M-2
        PP(I,J)=(1.-OMEGAP)*PP(I,J)+OMEGAP*B(I,1)
380   CONTINUE
C
      IF(J.EQ.2)PP(1,1)=PP(1,2)
C
      IF(J.NE.N-2)GO TO 310

```

Figure B1 Continued

```

          DO 390 I=1,M-2
            PP(I,N-1)=PP(I,N-2)
            PP(I,N)=PP(I,N-3)
390      CONTINUE
C
C:.....
C
310      CONTINUE
C
C -----
C      SWEEP IN Y DIRECTION
C -----
C
          DO 410 I=1,M-2
C
C:.....
C      THIS IS THE SPECIAL TREATMENT WHEN X=0 (VERTICAL WALL)
C:.....
C
          IF(I.GT.1)GO TO 412
            AY=(X(2)-X(1))/2.
            HAV=H(1)+(H(2)-H(1))/4.-Y(NS)
            DO 415 JJ=NS+1,N
              Y(JJ)=Y(NS)+YP(JJ)*HAV
415      CONTINUE
C
          DO 413 J=2,N-2
            AX=(Y(J+1)-Y(J-1))/2.
            CW=-AXU(2,J)*AX
            CN=AYV(2,J+1)*AY/4.
            CS=AYV(2,J)*AY/4.
            CH=-U(2,J)*AX-(V(2,J+1)-V(2,J))*AY/4.+U(1,J)*AX-3./4
            + * (V(1,J+1)-V(1,J))*AY
            CP=CW+CN+CS
            PP1J=(CP*PP(2,J)-CN*PP(2,J+1)-CS*PP(2,J-1)-CH)/CW
            PP(1,J)=(1.-OMEGAP)*PP(1,J)+OMEGAP*PP1J
413      CONTINUE
            PP(1,1)=PP(1,2)
            PP(1,N-1)=PP(1,N-2)
            PP(1,N)=PP(1,N-3)
            GO TO 410
C
C:.....
C      THIS IS THE REGULAR TREATMENT FOR THE INTERIOR GRID POINTS
C:.....
C
412      AY=(X(I+1)-X(I-1))/2.
            HAV=H(I)-Y(NS)
            DO 411 JJ=NS+1,N
              Y(JJ)=Y(NS)+YP(JJ)*HAV
411      CONTINUE
C
          DO 420 J=1,N-2
C
          IF(J.GT.1)GO TO 421
            AX=Y(2)/2.
            CE=AXU(I+1,2)*AX/4.
            CW=AXU(I,2)*AX/4.
            CS=-AYV(I,2)*AY

```

Figure B1 Continued

```

CP=CS
CH=-3./4.* (U(I+1,1)-U(I,1))*AX+V(I,1)*AY-
+ (U(I+1,2)-U(I,2))*AX/4.-V(I,2)*AY-(CE+CW)*PP(I,2)
CE=CE/CP
CW=CW/CP
CS=CS/CP
CH=CH/CP
GO TO 422

C
421 AX=(Y(J+1)-Y(J-1))/2.
    CE=AX*AXU(I+1,J)
    CW=AX*AXU(I,J)
    CN=AY*AYV(I,J+1)
    CS=AY*AYV(I,J)
    CP=CE+CW+CN+CS

C
    IF(J.GE.NS)GO TO 431
    CH--(AX*(U(I+1,J)-U(I,J))+AY*(V(I,J+1)-V(I,J)))
    GO TO 432
431 HAV1=H(I-1)-Y(NS)
    HAV2=H(I)-Y(NS)
    HAV3=H(I+1)-Y(NS)
    IF(J.GT.NS)GO TO 433
    YSW=Y(J-1)
    YS=Y(J-1)
    YSE=Y(J-1)
    YW=Y(J)
    YC=Y(J)
    YE=Y(J)
    YNW=Y(NS)+YP(J+1)*HAV1
    YN=Y(NS)+YP(J+1)*HAV2
    YNE=Y(NS)+YP(J+1)*HAV3
    GO TO 434
433 IF(J.GT.NS+1)GO TO 435
    YSW=Y(J-1)
    YS=Y(J-1)
    YSE=Y(J-1)
    YW=Y(NS)+YP(J)*HAV1
    YC=Y(NS)+YP(J)*HAV2
    YE=Y(NS)+YP(J)*HAV3
    YNW=Y(NS)+YP(J+1)*HAV1
    YN=Y(NS)+YP(J+1)*HAV2
    YNE=Y(NS)+YP(J+1)*HAV3
    GO TO 434
435 YSW=Y(NS)+YP(J-1)*HAV1
    YS=Y(NS)+YP(J-1)*HAV2
    YSE=Y(NS)+YP(J-1)*HAV3
    YW=Y(NS)+YP(J)*HAV1
    YC=Y(NS)+YP(J)*HAV2
    YE=Y(NS)+YP(J)*HAV3
    YNW=Y(NS)+YP(J+1)*HAV1
    YN=Y(NS)+YP(J+1)*HAV2
    YNE=Y(NS)+YP(J+1)*HAV3

C
434 DY1=((YC+YW)-(YC+YS))/2.
    U1=U(I,J)+(U(I,J-1)-U(I,J))/(YC+YW-YS-YSW)*DY1
    DY2=((YC+YN)-(YC+YW))/2.
    U2=U(I,J)+(U(I,J+1)-U(I,J))/(YNW+YN-YC-YW)*DY2
    DY3=((YC+YN)-(YC+YE))/2.

```

Figure B1 Continued

```

      U3=U(I+1,J)+(U(I+1,J+1)-U(I+1,J))/(YN+YNE-YC-YE)*DY3
      DY4=((YC+YE)-(YC+YS))/2.
      U4=U(I+1,J)+(U(I+1,J-1)-U(I+1,J))/(YC+YE-YS-YSE)*DY4
      CH=-(U3*DY3+U4*DY4-U1*DY1-U2*DY2+AY*(V(I,J+1)-V(I,J)))
C
432      CE=CE/CP
      CW=CW/CP
      CN=CN/CP
      CS=CS/CP
      CH=CH/CP
C
422      IF(J.GT.1)GO TO 430
      A(J,1)=.0
      A(J,2)=1.
      A(J,3)=-1.
      B(J,1)=- (CW*PP(I-1,2)+CE*PP(I+1,2)+CH)
      GO TO 420
430      IF(J.EQ.N-2)GO TO 440
      A(J,1)=-CS
      A(J,2)=1.
      A(J,3)=-CN
      B(J,1)=CE*PP(I+1,J)+CW*PP(I-1,J)+CH
      GO TO 420
440      A(J,1)=-CS-CN
      A(J,2)=1.
      A(J,3)=.0
      B(J,1)=CE*PP(I+1,N-1)+CW*PP(I-1,N-1)+CH
C
420      CONTINUE
C
C::::::::::::::::::::::::::::::::::::::::::::::::::::::::::::::::::
C      SOLVE THE EQUATION
C.....
C
      CALL LEQT1B(A,N-2,1,1,MAB,B,1,MAB,0,XL,IER)
      DO 450 J=1,N-2
      PP(I,J)=(1.-OMEGAP)*PP(I,J)+OMEGAP*B(J,1)
450      CCNTINUE
      PP(I,N-1)=PP(I,N-2)
      PP(I,N)=PP(I,N-3)
C
C::::::::::::::::::::::::::::::::::::::::::::::::::::::::::::::::::
C
410      CONTINUE
C
1000     CONTINUE
C
C-----
C      RELAX THE PRESSURE CORRECTION
C      EVALUATE THE NEW VELOCITY FIELD FOR RE-SOLUTION OF MTM-EQN.
C      SUMMARIZE THE TOTAL PRESSURE CORRECTION FOR CRITERIOR CHECK.
C      RE-ZERO THE PRESSURE CORRECTION FOR RE-SOLUTION OF C-EQN.
C-----
C
      DO 500 I=1,M-2
      DO 600 J=1,N
      P(I,J)=P(I,J)+OMEGAH*PP(I,J)
600      CONTINUE
500      CONTINUE

```

Figure B1 Continued

```

C
DO 700 I=2,M-1
DO 800 J=2,N-2
  U(I,J)=U(I,J)+AXU(I,J)*(PP(I-1,J)-PP(I,J))*OMEGA
  V(I,J)=V(I,J)+AYV(I,J)*(PP(I,J-1)-PP(I,J))*OMEGA
800 CONTINUE
C
  U(I,N-1)=U(I,N-2)
  U(I,N)=U(I,N-3)
  V(I,N)=V(I,N-2)
  DY1=(H(I)-H(I-1))/2.
  DY2=(H(I+1)-H(I))/2.
  DX=(X(I+1)-X(I-1))/2.
  V(I,N-1)=(U(I+1,N-2)*DY2+U(I,N-2)*DY1)/DX
C
  IF(I.NE.M-1)GO TO 700
DO 750 J=2,N
  U(M,J)=U(M-1,J)
  V(M,J)=V(M-1,J)
750 CONTINUE
C
700 CONTINUE
C
DP=.0
DO 850 I=1,M-2
DO 850 J=1,N-2
  DP=ABS(PP(I,J))+DP
850 CONTINUE
DP=DP/(N-2)/(M-2)
DP=DP/PREF
C
DO 900 I=1,M
DO 900 J=1,N
  PP(I,J)=.0
900 CONTINUE
C
RETURN
END

C
CCCCCCCCCCCCCCCCCCCCCCCCCCCCCCCCCCCCCCCCCCCC
C
C          SUBROUTINE SURFH          C
C
C          C          C
C
CCCCCCCCCCCCCCCCCCCCCCCCCCCCCCCCCCCCCCCCCCCC
C
C
C THIS SUBROUTINE IS TO CORRECT THE SURFACE PROFILE AND
C CHANGE THE GRIDS FOR NEXT ITERATION.
C
C SUBROUTINE SURFH(M,N,P,H,YP,Y,NS,OMEGA, DH, HREF)
C
C DOUBLE PRECISION P(M,N),H(M),YP(N),Y(N)
C
C DH=0.
DO 10 I=1,M-2
  HAV=H(I)-Y(NS)
  DY1=H(I)-YP(N-2)*HAV-Y(NS)
  DY2=(YP(N-2)-YP(N-3))*HAV

```

Figure B1 Continued

```

      PSURF=P(I,N-2)+(P(I,N-2)-P(I,N-3))*DY1/DY2
      HNEW=PSURF/9.81E+3
      HOLD=H(I)
      H(I)=(1.-OMEGAS)*HOLD+OMEGAS*HNEW
      DH=ABS(H(I)-HOLD)+DH
10    CONTINUE
C
      DH=DH/(M-2)
      DH=DH/HREF
C
      RETURN
      END

C
C      CCCCCCCCCCCCCCCCCCCCCCCCCCCCCCCCCCCCCCCCCCCCCCCCCCCCCC
C      C
C      C          SUBROUTINE PUVXY          C
C      C
C      CCCCCCCCCCCCCCCCCCCCCCCCCCCCCCCCCCCCCCCCCCCCCCCCCCCCCC
C
C      THIS SUBROUTINE IS TO EVALUATE THE VELOCITY GRADIENTS
C      FOR THE EVALUATION OF TURBULENCE PRODUCTION.
C
C      SUBROUTINE PUVXY(M,N,NS,X,Y,YP,H,U,V,UVXY)
C
C      DOUBLE PRECISION X(M),Y(N),YP(N),H(M),U(M,N),V(M,N),
+      UVXY(M,N)
C
C      DO 10 I=2,M-1
C      AY=(X(I+1)-X(I-1))/2.
C      HAV=H(I)-Y(NS)
C      DO 11 JJ=NS+1,N
C      Y(JJ)=Y(NS)+YP(JJ)*HAV
11    CONTINUE
C
C      DO 20 J=2,N-2
C      AX=(Y(J+1)-Y(J-1))/2.
C      DUDX=(U(I+1,J)-U(I,J))/AY
C      DVDY=(V(I,J+1)-V(I,J))/AX
C      DUDY=((U(I,J+1)+U(I+1,J+1)+U(I,J)+U(I+1,J))/4.-
+      (U(I,J)+U(I+1,J)+U(I,J-1)+U(I+1,J-1))/4.)/AX
C      DVDX=((V(I+1,J+1)+V(I+1,J)+V(I,J+1)+V(I,J))/4.-
+      (V(I,J+1)+V(I,J)+V(I-1,J+1)+V(I-1,J))/4.)/AY
C      UVXY(I,J)=2.*(DUDX**2+DVDY**2)+(DUDY+DVDX)**2
20    CONTINUE
C
10    CONTINUE
C
      RETURN
      END

C
C      CCCCCCCCCCCCCCCCCCCCCCCCCCCCCCCCCCCCCCCCCCCCCCCCCCCCCC
C      C
C      C          SUBROUTINE TDRE          C
C      C
C      CCCCCCCCCCCCCCCCCCCCCCCCCCCCCCCCCCCCCCCCCCCCCCCCCCCCCC

```

Figure B1 Continued

```

C
C
C   THIS SUBROUTINE IS TO EVALUATE TURBULENCE KINETIC
C   ENERGY, DISSIPATION RATE AND TURBULENCE VISCOSITY.
C   MAB=MAX(M,N)-2
C
C   SUBROUTINE TDRE(M,N,NS,X,Y,YP,H,U,V,UVXY,TK,TD,TNU,ENU,
+   DELTAD,C1,C2,OMEGA,D,DTD,LEQT1B,A,B,XL,MAB,
+   TEMP,OMEGAJ,TDREF,CMU,CK)
C
C   EXTERNAL LEQT1B
C   DOUBLE PRECISION X(M),Y(N),YP(N),H(M),U(M,N),V(M,N),
+   UVXY(M,N),TK(M,N),TD(M,N),TNU(M,N),
+   ENU(M,N),A(MAB,3),B(MAB,1),XL(2*MAB),
+   TEMP(M,N)
C
C   DO 1 I=2,M
C     DO 1 J=2,N
C       TEMP(I,J)=TD(I,J)
1     CONTINUE
C
C   DO 5 I=2,M
C     HAV=H(I)-Y(NS)
C     YF=H(I)-YP(N-2)*HAV
C     TD(I,N-2)=(TK(I,N-2)*SQRT(CMU))**1.5/CK/YF
C     CONTINUE
C
C-----
C   SWEEP IN X DIRECTION
C-----
C
C   DO 10 J=2,N-2
C     IF(J.GE.NS)GO TO 11
C     AX=(Y(J+1)-Y(J-1))/2.
C
11   DO 20 I=2,M-1
C     IF(J.LT.NS)GO TO 21
C     HAV=H(I)-Y(NS)
C     DO 22 JJ=NS+1,N
C       Y(JJ)=Y(NS)+YP(JJ)*HAV
22   CONTINUE
C     AX=(Y(J+1)-Y(J-1))/2.
21   AY=(X(I+1)-X(I-1))/2.
C
C     CL=X(I+1)-X(I)
C     CU=U(I+1,J)
C     CENU=(ENU(I+1,J)+ENU(I,J))/2./DELTAD
C     BE=CENU*AX/CL
C     AE=CU/2.*AX
C
C     CL=X(I)-X(I-1)
C     CU=U(I,J)
C     CENU=(ENU(I,J)+ENU(I-1,J))/2./DELTAD
C     BW=CENU*AX/CL
C     AW=CU/2.*AX
C
C     CL=Y(J+1)-Y(J)
C     CU=V(I,J+1)
C     CENU=(ENU(I,J)+ENU(I,J+1))/2./DELTAD

```

Figure B1 Continued

```

BN=CENU*AY/CL
AN=CU/2.*AY
C
CL=Y(J)-Y(J-1)
CU=V(I,J)
CENU=(ENU(I,J)+ENU(I,J-1))/2./DELTAD
BS=CENU*AY/CL
AS=CU/2.*AY
C
CE=(BE+ABS(AE)+ABS(BE-ABS(AE)))/2.-AE
CW=(BW+ABS(AW)+ABS(BW-ABS(AW)))/2.+AW
CN=(BN+ABS(AN)+ABS(BN-ABS(AN)))/2.-AN
CS=(BS+ABS(AS)+ABS(BS-ABS(AS)))/2.+AS
CO=C2*TD(I,J)*AX*AY/TK(I,J)
CP=CE+CW+CN+CS+CO
CE=CE/CP
CW=CW/CP
CN=CN/CP
CS=CS/CP
CH=C1*TNU(I,J)*UVXY(I,J)*TD(I,J)*AX*AY/TK(I,J)/CP
C
IF(I.GT.2)GO TO 30
  A(I-1,1)=.0
  A(I-1,2)=1.
  A(I-1,3)=-CE
  B(I-1,1)=CW*TD(I-1,J)+CN*TD(I,J+1)+CS*TD(I,J-1)+CH
  GO TO 20
30 IF(I.EQ.M-1)GO TO 40
  A(I-1,1)=-CW
  A(I-1,2)=1.
  A(I-1,3)=-CE
  B(I-1,1)=CN*TD(I,J+1)+CS*TD(I,J-1)+CH
  GO TO 20
40 A(I-1,1)=-CW
  A(I-1,2)=1.-CE
  A(I-1,3)=.0
  B(I-1,1)=CN*TD(I,J+1)+CS*TD(I,J-1)+CH
C
20 CONTINUE
C
CALL LEQT1B(A,M-2,1,1,MAB,B,1,MAB,0,XL,IER)
DO 50 I=2,M-1
  TD(I,J)=(1.-OMEGAD)*TD(I,J)+OMEGAD*B(I-1,1)
  IF(TD(I,J).LE..0)TD(I,J)=1.E-3
50 CONTINUE
  TD(M,J)=TD(M-1,J)
C
IF(J.NE.N-2)GO TO 10
  DO 60 I=2,M
    TD(I,N)=TD(I,N-3)
    TD(I,N-1)=TD(I,N-2)
60 CONTINUE
C
10 CONTINUE
C
-----
C SWEEP IN Y DIRECTION
-----
C

```

Figure B1 Continued


```

DO 110 I=2,M-1
  AY=(X(I+1)-X(I-1))/2.
  HAV=H(I)-Y(NS)
  DO 111 JJ=NS+1,N
    Y(JJ)=Y(NS)+YP(JJ)*HAV
111  CONTINUE
  C
  DO 120 J=2,N-2
    AX=(Y(J+1)-Y(J-1))/2.
  C
    CL=X(I+1)-X(I)
    CU=U(I+1,J)
    CENU=(ENU(I+1,J)+ENU(I,J))/2./DELTAD
    BE=CENU*AX/CL
    AE=CU/2.*AX
  C
    CL=X(I)-X(I-1)
    CU=U(I,J)
    CENU=(ENU(I,J)+ENU(I-1,J))/2./DELTAD
    BW=CENU*AX/CL
    AW=CU/2.*AX
  C
    CL=Y(J+1)-Y(J)
    CU=V(I,J+1)
    CENU=(ENU(I,J)+ENU(I,J+1))/2./DELTAD
    BN=CENU*AY/CL
    AN=CU/2.*AY
  C
    CL=Y(J)-Y(J-1)
    CU=V(I,J)
    CENU=(ENU(I,J)+ENU(I,J-1))/2./DELTAD
    BS=CENU*AY/CL
    AS=CU/2.*AY
  C
    CE=(BE+ABS(AE)+ABS(BE-ABS(AE)))/2.-AE
    CW=(BW+ABS(AW)+ABS(BW-ABS(AW)))/2.+AW
    CN=(BN+ABS(AN)+ABS(BN-ABS(AN)))/2.-AN
    CS=(BS+ABS(AS)+ABS(BS-ABS(AS)))/2.+AS
    CO=C2*TD(I,J)*AX*AY/TK(I,J)
    CP=CE+CW+CN+CS+CO
    CE=CE/CP
    CW=CW/CP
    CN=CN/CP
    CS=CS/CP
    CH=C1*TNU(I,J)*UVXY(I,J)*TD(I,J)*AX*AY/TK(I,J)/CP
  C
    IF(J.GT.2)GO TO 130
    A(J-1,1)=.0
    A(J-1,2)=1.
    A(J-1,3)=-CN
    B(J-1,1)=CW*TD(I-1,J)+CE*TD(I+1,J)+CS*TD(I,J-1)+CH
    GO TO 120
130  IF(J.EQ.N-2)GO TO 140
    A(J-1,1)=-CS
    A(J-1,2)=1.
    A(J-1,3)=-CN
    B(J-1,1)=CE*TD(I+1,J)+CW*TD(I-1,J)+CH
    GO TO 120
140  A(J-1,1)=-CS

```

Figure B1 Continued

```

      A(J-1,2)=1.-CN
      A(J-1,3)=.0
      B(J-1,1)=CE*TD(I+1,J)+CW*TD(I-1,J)+CH
C
120  CONTINUE
C
      CALL LEQT1B(A,N-3,1,1,MAB,B,1,MAB,0,XL,IER)
      DO 150 J=2,N-2
        IF(I.EQ.2.AND.J.EQ.2)DTD=.0
        TDO=TD(I,J)
        TD(I,J)=(1.-OMEGAD)*TD(I,J)+OMEGAD*B(J-1,1)
        IF(TD(I,J).LE.0.)TD(I,J)=1.E-3
        DTD=ABS(TD(I,J)-TDO)+DTD
150  CONTINUE
      TD(I,N)=TD(I,N-3)
      TD(I,N-1)=TD(I,N-2)
C
      IF(I.NE.M-1)GO TO 110
      DO 160 J=2,N
        TD(M,J)=TD(M-1,J)
160  CONTINUE
C
110  CONTINUE
C
      DTD=DTD/(N-3)/(M-2)
      DTD=DTD/TDREF
C
      DO 2 I=2,M
        DO 2 J=2,N
          TD(I,J)=(1.-OMEGAJ)*TEMP(I,J)+OMEGAJ*TD(I,J)
2    CONTINUE
C
      RETURN
      END

C          CCCCCCCCCCCCCCCCCCCCCCCCCCCCCCCCCCCCCCCCCCCCC
C          C                                                    C
C          C          SUBROUTINE TKEE          C
C          C                                                    C
C          C          CCCCCCCCCCCCCCCCCCCCCCCCCCCCCCCCCCCCCCCCCCCCC
C
C
C          THIS SUBROUTINE IS TO EVALUATE TURBULENCE KINETIC
C          ENERGY, DISSIPATION RATE AND TURBULENCE VISCOSITY.
C          MAB=MAX(M,N)-2
C
C          SUBROUTINE  TKEE(M,N,NS,X,Y,YP,H,U,V,UVXY,TK,TD,TNU,ENU,
+          DELTAK,OMEGAK,DTK,LEQT1B,A,B,XL,MAB,
+          CMU,CNU,TEMP,OMEGAI,TKREF)
C
C          EXTERNAL LEQT1B
C          DOUBLE PRECISION X(M),Y(N),YP(N),H(M),U(M,N),V(M,N),
+          UVXY(M,N),TK(M,N),TD(M,N),TNU(M,N),
+          ENU(M,N),A(MAB,3),B(MAB,1),XL(2*MAB),
+          TEMP(M,N)
C
      DO 1 I=2,M
        DO 1 J=2,N

```

Figure B1 Continued

```

      TEMP(I,J)=TK(I,J)
1     CONTINUE
C
C-----
C     SWEEP IN X DIRECTION
C-----
C
      DO 10 J=2,N-2
        IF(J.GE.NS)GO TO 11
        AX=(Y(J+1)-Y(J-1))/2.
C
11     DO 20 I=2,M-1
        IF(J.LT.NS)GO TO 21
        HAV=H(I)-Y(NS)
        DO 22 JJ=NS+1,N
          Y(JJ)=Y(NS)+YP(JJ)*HAV
22     CONTINUE
        AX=(Y(J+1)-Y(J-1))/2.
21     AY=(X(I+1)-X(I-1))/2.
C
        CL=X(I+1)-X(I)
        CU=U(I+1,J)
        CENU=(ENU(I+1,J)+ENU(I,J))/2./DELTAK
        BE=CENU*AX/CL
        AE=CU/2.*AX
C
        CL=X(I)-X(I-1)
        CU=U(I,J)
        CENU=(ENU(I,J)+ENU(I-1,J))/2./DELTAK
        BW=CENU*AX/CL
        AW=CU/2.*AX
C
        CL=Y(J+1)-Y(J)
        CU=V(I,J+1)
        CENU=(ENU(I,J)+ENU(I,J+1))/2./DELTAK
        BN=CENU*AY/CL
        AN=CU/2.*AY
C
        CL=Y(J)-Y(J-1)
        CU=V(I,J)
        CENU=(ENU(I,J)+ENU(I,J-1))/2./DELTAK
        BS=CENU*AY/CL
        AS=CU/2.*AY
C
        CE=(BE+ABS(AE)+ABS(BE-ABS(AE)))/2.-AE
        CW=(BW+ABS(AW)+ABS(BW-ABS(AW)))/2.+AW
        CN=(BN+ABS(AN)+ABS(BN-ABS(AN)))/2.-AN
        CS=(BS+ABS(AS)+ABS(BS-ABS(AS)))/2.+AS
        CP=CE+CW+CN+CS
        CE=CE/CP
        CW=CW/CP
        CN=CN/CP
        CS=CS/CP
        CH=(TNU(I,J)*UVXY(I,J)-TD(I,J))*AX*AY/CP
C
        IF(I.GT.2)GO TO 30
        A(I-1,1)=.0
        A(I-1,2)=1.
        A(I-1,3)=-CE

```

Figure B1 Continued

```

      B(I-1,1)=CW*TK(I-1,J)+CN*TK(I,J+1)+CS*TK(I,J-1)+CH
      GO TO 20
30    IF(I.EQ.M-1)GO TO 40
      A(I-1,1)=-CW
      A(I-1,2)=1.
      A(I-1,3)=-CE
      B(I-1,1)=CN*TK(I,J+1)+CS*TK(I,J-1)+CH
      GO TO 20
40    A(I-1,1)=-CW
      A(I-1,2)=1.-CE
      A(I-1,3)=.0
      B(I-1,1)=CN*TK(I,J+1)+CS*TK(I,J-1)+CH
C
20    CONTINUE
C
      CALL LEQT1B(A,M-2,1,1,MAB,B,1,MAB,0,XL,IER)
      DO 50 I=2,M-1
        TK(I,J)=(1.-OMEGAK)*TK(I,J)+OMEGAK*B(I-1,1)
        IF(TK(I,J).LE.0.)TK(I,J)=1.E-3
50    CONTINUE
      TK(M,J)=TK(M-1,J)
C
      IF(J.NE.N-2)GO TO 10
      DO 60 I=2,M
        TK(I,N)=TK(I,N-3)
        TK(I,N-1)=TK(I,N-2)
60    CONTINUE
C
10    CONTINUE
C
-----
C    SWEEP IN Y DIRECTION
-----
C
      DO 110 I=2,M-1
        AY=(X(I+1)-X(I-1))/2.
        HAV=H(I)-Y(NS)
        DO 111 JJ=NS+1,N
          Y(JJ)=Y(NS)+YP(JJ)*HAV
111    CONTINUE
C
      DO 120 J=2,N-2
        AX=(Y(J+1)-Y(J-1))/2.
C
        CL=X(I+1)-X(I)
        CU=U(I+1,J)
        CENU=(ENU(I+1,J)+ENU(I,J))/2./DELTAK
        BE=CENU*AX/CL
        AE=CU/2.*AX
C
        CL=X(I)-X(I-1)
        CU=U(I,J)
        CENU=(ENU(I,J)+ENU(I-1,J))/2./DELTAK
        BW=CENU*AX/CL
        AW=CU/2.*AX
C
        CL=Y(J+1)-Y(J)
        CU=V(I,J+1)
        CENU=(ENU(I,J)+ENU(I,J+1))/2./DELTAK

```

Figure B1 Continued

```

BN=CENU*AY/CL
AN=CU/2.*AY
C
CL=Y(J)-Y(J-1)
CU=V(I,J)
CENU=(ENU(I,J)+ENU(I,J-1))/2./DELTAK
BS=CENU*AY/CL
AS=CU/2.*AY
C
CE=(BE+ABS(AE)+ABS(BE-ABS(AE)))/2.-AE
CW=(BW+ABS(AW)+ABS(BW-ABS(AW)))/2.+AW
CN=(BN+ABS(AN)+ABS(BN-ABS(AN)))/2.-AN
CS=(BS+ABS(AS)+ABS(BS-ABS(AS)))/2.+AS
CP=CE+CW+CN+CS
CE=CE/CP
CW=CW/CP
CN=CN/CP
CS=CS/CP
CH=(TNU(I,J)*UVXY(I,J)-TD(I,J))*AX*AY/CP
C
IF(J.GT.2)GO TO 130
A(J-1,1)=.0
A(J-1,2)=1.
A(J-1,3)=-CN
B(J-1,1)=CW*TK(I-1,J)+CE*TK(I+1,J)+CS*TK(I,J-1)+CH
GO TO 120
130 IF(J.EQ.N-2)GO TO 140
A(J-1,1)=-CS
A(J-1,2)=1.
A(J-1,3)=-CN
B(J-1,1)=CE*TK(I+1,J)+CW*TK(I-1,J)+CH
GO TO 120
140 A(J-1,1)=-CS
A(J-1,2)=1.-CN
A(J-1,3)=.0
B(J-1,1)=CE*TK(I+1,J)+CW*TK(I-1,J)+CH
C
120 CONTINUE
C
CALL LEQT1B(A,N-3,1,1,MAB,B,1,MAB,0,XL,IER)
DO 150 J=2,N-2
IF(I.EQ.2.AND.J.EQ.2)DTK=.0
TKO=TK(I,J)
TK(I,J)=(1.-OMEGAK)*TK(I,J)+OMEGAK*B(J-1,1)
IF(TK(I,J).LE..0)TK(I,J)=1.E-3
DTK=ABS(TK(I,J)-TKO)+DTK
150 CONTINUE
TK(I,N)=TK(I,N-3)
TK(I,N-1)=TK(I,N-2)
C
IF(I.NE.M-1)GO TO 110
DO 160 J=2,N
TK(M,J)=TK(M-1,J)
160 CONTINUE
C
110 CONTINUE
C
DTK=DTK/(N-3)/(M-2)
DTK=DTK/TKREF

```

Figure B1 Continued


```
TDOLD=TD(I,1)
TD(I,1)=USTAR**3/CK/Y(1)
DTDW=ABS((TD(I,1)-TDOLD)/TD(I,1))
C
UOLD=UC1
UC1=USTAR/CK*DLOG(CE*Y(1)*USTAR/CNU)
DUW=ABS((UC1-UOLD)/UC1)
U(I,1)=(UW1+UC1)/2.
UW1=UC1
C
DWMAX=AMAX1(DTKW,DTDW,DUW)
DW=DW+DWMAX
C
10 CONTINUE
C
U(M,1)=U(M-1,1)
TK(M,1)=TK(M-1,1)
TD(M,1)=TD(M-1,1)
DW=DW/(M-2)
C
DO 20 I=2,M-1
  AX=Y(1)
  AY=(X(I+1)+X(I-1))/2.
  V(I,1)=AX/AY/2.*(U(I,1)-U(I+1,1))
20 CONTINUE
V(M,1)=V(M-1,1)
C
RETURN
END
```

Figure B1 Continued

APPENDIX C - ORDINARY DIFFERENTIAL EQUATIONS OF SIM

The set of ordinary differential equations for SIM (Strip Integral Method) is in the following form as discussed in Part Three of this thesis.

$$A_i \frac{dH}{dx} + B_i \frac{d\delta}{dx} + C_i \frac{du_\infty}{dx} + D_i \frac{du_m}{dx} = E_i \quad (i=1,2,3,4) \quad (123)$$

The coefficients A_i , B_i , C_i , D_i and E_i are functions of the unknowns H , δ , u_∞ and u_m . These functions are listed as the following.

$$A_1 = u_s + CJ2 \frac{2}{\sqrt{c}} u_t \quad (196)$$

$$B_1 = -\frac{u_m}{8} + u_t [1 - e^{-c} - CJ2 \frac{2}{\sqrt{c}}] \quad (197)$$

$$C_1 = (H - \delta) \left\{ \frac{CI2}{\sqrt{c}} - 1 \right\} \quad (198)$$

$$D_1 = \frac{7}{8} \delta + CI2 \frac{H-\delta}{\sqrt{c}} \quad (199)$$

$$E_1 = 0 \quad (200)$$

$$A_2 = g\delta \quad (201)$$

$$B_2 = -\frac{7}{72} u_m^2 \quad (202)$$

$$C_2 = 0 \quad (203)$$

$$D_2 = \frac{49}{72} u_m \delta \quad (204)$$

$$E_2 = - \frac{\tau_0}{\rho} \quad (205)$$

$$A_3 = - CJ1 \frac{4}{\sqrt{c}} u_\infty u_t + CJ3 \sqrt{\frac{2}{c}} u_t^2 - CJ1 \frac{2}{\sqrt{c}} u_* u_t + \frac{g}{\sqrt{8c}} (H-\delta) \quad (206)$$

$$B_3 = u_\infty u_t [CJ1 \frac{4}{\sqrt{c}} - 2(1-e^{-0.125})] + u_t^2 (1-e^{-0.25}-CJ3 \sqrt{\frac{2}{c}}) u_* u_t (CJ1 \frac{2}{\sqrt{c}} - 1 + e^{-0.125}) + \frac{1}{8} u_m (u_* - u_m) \quad (207)$$

$$C_3 = \frac{2u_\infty}{\sqrt{c}} (H-\delta) \left(\frac{1}{\sqrt{8}} - CI1 \right) + \frac{u_t}{\sqrt{c}} (H-\delta) (\sqrt{2} CI3 - 2CI1) + \frac{u_*}{\sqrt{c}} (H-\delta) \left(\frac{1}{\sqrt{8}} - CI1 \right) \quad (208)$$

$$D_3 = \frac{1}{\sqrt{c}} (H-\delta) (\sqrt{2} CI3 u_t - 2CI1 u_\infty - CI1 u_*) + \frac{7}{8} \delta (u_m - u_*) \quad (209)$$

$$E_3 = -(0.019x)^2 \frac{c}{2} \left(\frac{u_t}{H-\delta} \right)^2 e^{-0.25} \quad (210)$$

$$A_4 = u_s^2 + g(H-\delta) - CJ2 \frac{4}{\sqrt{c}} u_\infty u_t + CJ4 \sqrt{\frac{2}{c}} u_t^2 \quad (211)$$

$$B_4 = - \frac{1}{8} u_m^2 + u_\infty u_t [CJ2 \frac{4}{\sqrt{c}} - 2(1-e^{-c})] + u_t^2 (1 - e^{-2c} - CJ4 \sqrt{\frac{2}{c}}) \quad (212)$$

$$C_4 = 2u_\infty (H-\delta) \left(1 - \frac{CI2}{\sqrt{c}} \right) + \frac{u_t}{\sqrt{c}} (H-\delta) (\sqrt{2} CI4 - 2CI2) \quad (213)$$

$$D_4 = \frac{7}{8} \delta u_m + \frac{1}{\sqrt{c}} (H-\delta) (\sqrt{2} CI4 u_t - 2CI2 u_\infty) \quad (214)$$

$$E_4 = 0 \quad (215)$$

The inlet condition is given by the following two equations to solve for u_∞ and H at the end of the potential core.

$$U_1 Y_1 = \frac{7}{8} u_m \delta + (H - \delta) \left(\frac{CI2}{\sqrt{c}} u_t - u_\infty \right) \quad (216)$$

$$\begin{aligned} \frac{1}{2} \gamma (Y_s^2 - H^2) - 6 Y_1 \tau_0 &= \rho \frac{7}{8} u_m^2 \delta - \rho U_1^2 Y_1 \\ + \rho (H - \delta) (u_\infty^2 - 2 u_\infty u_t \frac{CI2}{\sqrt{c}} + \frac{CI4}{\sqrt{c}} u_t^2) & \end{aligned} \quad (217)$$

For all the equations above CI_i and CJ_i ($i=1,2,3,4$) are constant integrals given by the following.

$$CI1 = \int_0^{1/\sqrt{8}} \exp(-z^2) dz \quad (218)$$

$$CJ1 = \int_0^{1/\sqrt{8}} z^2 \exp(-z^2) dz \quad (219)$$

$$CI2 = \int_0^{\sqrt{c}} \exp(-z^2) dz \quad (220)$$

$$CJ2 = \int_0^{\sqrt{c}} z^2 \exp(-z^2) dz \quad (221)$$

$$CI3 = \int_0^{1/2} \exp(-z^2) dz \quad (222)$$

$$CJ3 = \int_0^{1/2} z^2 \exp(-z^2) dz \quad (223)$$

$$CI4 = \int_0^{\sqrt{2c}} \exp(-z^2) dz \quad (224)$$

APPENDIX D - COMPUTER PROGRAM OF SIM

```

$DEBUG
C
C THE FOLLOWING IS THE MAIN PROGRAM FOR PREDICTING THE
C MAIN FLOW PARAMETERS OF A SUBMERGED JUMP
C
C DECLARE VARIABLES
C
  CHARACTER*20 FIN,FOUT
  DOUBLE PRECISION C,ZUPPER,CJ1,CJ2,CJ3,CJ4,CI1,CJ1,CJ2,CJ3,CI4,CJ4
  DOUBLE PRECISION U1,Y1,HS,UINF,H,DELTA,UM,YT
  DOUBLE PRECISION XDIST,A(4,5),X(4),DX,DYT
C
C INPUT DATA
C
  WRITE(*,'(A)') ' ENTER THE INPUT FILENAME: '
  READ(*,'(A)')FIN
  WRITE(*,'(A)') ' ENTER THE OUTPUT FILENAME: '
  READ(*,'(A)')FOUT
  OPEN(5,FILE=FIN)
  OPEN(6,FILE=FOUT)
  READ(5,*)U1,Y1,HS,C,OMEGA,YT
C
  DX=.002
  KCOUNT=0
  ZUPPER=1./DSQRT(B.)
  CALL INTEGR(ZUPPER,CI1,CJ1)
  ZUPPER=DSQRT(C)
  CALL INTEGR(ZUPPER,CI2,CJ2)
  ZUPPER=.5
  CALL INTEGR(ZUPPER,CI3,CJ3)
  ZUPPER=DSQRT(2.*C)
  CALL INTEGR(ZUPPER,CI4,CJ4)
100 XDIST=6.*Y1
  CALL INLET(C,U1,Y1,HS,UINF,H,DELTA,UM,OMEGA,CI2,CI4)
C
  KCOUNT=KCOUNT+1
  WRITE(*,*)KCOUNT
C
  DO 10 I=1,1000
    CALL COEFF(XDIST,C,UM,DELTA,UINF,H,A,
+           CI1,CJ1,CI2,CJ2,CI3,CJ3,CI4,CJ4)
    CALL SOLVE(A,X)
    XDIST=XDIST+DX
    H=H+X(1)*DX
    DELTA=DELTA+X(2)*DX
    UINF=UINF+X(3)*DX
    UM=UM+X(4)*DX

```

Figure D1 SIM Program Listing

```

10  CONTINUE
    IF(DABS(H-YT).GT..001)THEN
        DYT=YT-H
        HS=HS+DYT*.5
        GO TO 100
    ENDIF
C
    XDIST=4.*Y1
    WRITE(6,2000)HS
2000 FORMAT('FINAL SOLUTION WITH HS=',E12.4)
    CALL INLET(C,U1,Y1,HS,UINF,H,DELTA,UM,OMEGA,C12,C14)
    WRITE(6,1000)XDIST,H,DELTA,UINF,UM
1000 FORMAT('X,H,DELTA,UINF,UM',5E12.4)
    DO 20 I=1,1000
        CALL COEFF(XDIST,C,UM,DELTA,UINF,H,A,
+             C11,CJ1,C12,CJ2,C13,CJ3,C14,CJ4)
        CALL SOLVE(A,X)
        XDIST=XDIST+DX
        H=H+X(1)*DX
        DELTA=DELTA+X(2)*DX
        UINF=UINF+X(3)*DX
        UM=UM+X(4)*DX
        WRITE(6,1000)XDIST,H,DELTA,UINF,UM
20  CONTINUE
C
    STOP
    END
C
C THIS SUBROUTINE NUMERICALLY INTEGRATES TWO FUNCTIONS
C GIVEN THE UPPER LIMIT WITH A LOWER LIMIT OF ZERO
C
    SUBROUTINE INTEGR(ZUPPER,OUT1,OUT2)
C
    DOUBLE PRECISION ZUPPER,OUT1,OUT2,
+             DZ,Z,ZTWO,VAL1,VAL2
C
    NDEVID=10000
    DZ=ZUPPER/FLOAT(NDEVID)
    Z=DZ/2.
    OUT1=0.
    OUT2=0.
    DO 10 I=1,NDEVID
        ZTWO=Z*Z
        VAL1=DEXP(-ZTWO)
        VAL2=VAL1*ZTWO
        OUT1=OUT1+VAL1*DZ
        OUT2=OUT2+VAL2*DZ
        Z=Z+DZ
10  CONTINUE

```

Figure D1 Continued

```

C
  RETURN
  END

C
C THIS SUBROUTINE ESTABLISHES THE INITIAL CONDITION AT THE END OF
C THE POTENTIAL CORE USING INFORMATION OF U1, Y1, C AND QUESSED HS
C
  SUBROUTINE INLET(C,U1,Y1,HS,UINF,H,DELTA,UM,OMEGA,CI2,CI4)
C
  DOUBLE PRECISION C,U1,Y1,HS,UINF,H,
+      DELTA,UM,TO,HOLD,UT,DH,CI2,CI4
C
  DELTA=5.*SQRT(4.D-6*Y1/U1)
  UM=U1
  TO=.0424D+3*UM*UM/2./((UM*DELTA*1.D+6)**.25)
C
C START THE ITERATION
C
  HOLD=HS
10  UINF=(-CI2*UM/DSQRT(C)+(U1*Y1-7./8.*DELTA*UM)/(HOLD-DELTA))/
+      (CI2/DSQRT(C)-1.)
  UT=UINF+UM
  HNEW=DELTA+1.D-3*(9.807D+3/2.*(HS*HS-HOLD*HOLD)-
+      7.D+3/9.*UM*UM*DELTA+1.D+3*U1*U1*Y1-4.*TO*Y1)/
+      (UINF*UINF-2.*CI2*UINF*UT/DSQRT(C)+
+      CI4/DSQRT(2.*C)*UT*UT)
  DH=DABS((HNEW-HOLD)/HS)
C   WRITE(6,1000)UINF,HNEW,DELTA,TO,DH
C1000 FORMAT('UINF,HNEW,DELTA,TO,DH',5E10.3)
  IF(DH.GT.1.D-6)THEN
    HOLD=HNEW*OMEGA+HOLD*(1.-OMEGA)
    GO TO 10
  ENDIF
  H=HNEW
C
  RETURN
  END

C
C THIS SUBROUTINE CALCULATES THE COEFFICIENTS OF THE MATRIX [A] IN
C PREPARATION FOR THE SOLUTION OF [X] USING INFORMATION OF C, UM,
C DELTA, UINF AND H FROM THE PREVIOUS STEP
C
  SUBROUTINE COEFF(XDIST,C,UM,DELTA,UINF,H,A,
+      CI1,CJ1,CI2,CJ2,CI3,CJ3,CI4,CJ4)
C
  DOUBLE PRECISION XDIST,C,UM,DELTA,UINF,H,A(4,5),
+      UT,TO,USTAR,DSQRC,US,HMD,DENC,DENP25,
+      CI1,CJ1,CI2,CJ2,CI3,CJ3,CI4,CJ4
C

```

Figure D1 Continued

```

UT=UINF+UM
T0=.0424D+3/2.*UM*UM/(UM*DELTA/1.D-6)**.25
USTAR=-UINF+UT*DEXP(-.125)
DSQRC=DSQRT(C)
DENC=DEXP(-C)
US=-UINF+UT*DENC
HMD=H-DELTA
DENP25=DEXP(-.25)
C
C THE FOLLOWING COEFFICIENTS DETERMINED FROM INTEGRATING THE
C CONTINUITY EQUATION
C
A(1,1)=US+2.*CJ2*UT/DSQRC
A(1,2)=-UM/B.+UT*(1.-DENC-2.*CJ2/DSQRC)
A(1,3)=HMD*(CI2/DSQRC-1.)
A(1,4)=7./B.*DELTA+CI2*HMD/DSQRC
A(1,5)=0.
C
C THE FOLLOWING COEFFICIENTS DETERMINED FROM INTEGRATING THE
C MOMENTUM EQUATION FOR 0<=Y<=DELTA
C
A(2,1)=9.807*DELTA
A(2,2)=-7./72.*UM*UM
A(2,3)=0.
A(2,4)=49./72.*DELTA*UM
A(2,5)=-T0/1000.
C
C THE FOLLOWING COEFFICIENTS DETERMINED FROM INTEGRATING THE
C MOMENTUM EQUATION FOR DELTA<=Y<=YSTAR
C
A(3,1)=9.807*HMD/DSQRT(B.*C)-2.*CJ1*USTAR*UT/DSQRC
+      -4.*CJ1*UINF*UT/DSQRC+DSQRT(2./C)*CJ3*UT*UT
A(3,2)=(4.*CJ1/DSQRC-2.*(1.-DEXP(-.125)))*UINF*UT
+      +UT*UT*(1.-DENP25-DSQRT(2./C)*CJ3)
+      +UT*USTAR*(2*CJ1/DSQRC-1.+DEXP(-.125))
+      +UM/B.*(USTAR-UM)
A(3,3)=HMD/DSQRC*(2.*UINF*(1./DSQRT(B.)-CI1)
+      +UT*(DSQRT(2.)*CI3-2.*CI1)
+      +USTAR*(1./DSQRT(B.)-CI1))
A(3,4)=7./B.*DELTA*(UM-USTAR)+HMD/DSQRC*(-CI1*USTAR
+      +DSQRT(2.)*CI3*UT-2.*CI1*UINF)
A(3,5)=-(.019*XDIST)**2*C/2.*(UT/HMD)**2*DENP25
C
C THE FOLLOWING COEFFICIENTS DETERMINED FROM INTEGRATING THE
C MOMENTUM EQUATION FOR DELTA<=Y<=H
C
A(4,1)=9.807*HMD+US*US+DSQRT(2./C)*CJ4*UT*UT
+      -4.*CJ2/DSQRC*UINF*UT
A(4,2)=-UM*UM/B.+UT*UT*(1.-DEXP(-2.*C)-DSQRT(2./C)*CJ4)

```

Figure D1 Continued

```

+      +UINF*UT*(4.*CJ2/DSQRC-2.*(1.-DENC))
A(4,3)=HMD*UT/DSQRC*(DSQRT(2.)*CI4-2.*CI2)
+      +2.*UINF*HMD*(1.-CI2/DSQRC)
A(4,4)=7./8.*DELTA*UM+HMD/DSQRC*(DSQRT(2.)*CI4*UT-2.*CI2*UINF)
A(4,5)=0.
C
  RETURN
  END
C
C THIS SUBROUTINE SOLVES A SET OF LINEAR EQUATIONS USING
C GAUSSIAN ELIMINATION PROCEDURE
C
  SUBROUTINE SOLVE(A,X)
  DOUBLE PRECISION A(4,5),X(4)
  DOUBLE PRECISION BIGGST,ABSLTE,TEMPRY,Y,PIVOT,C
C
C START OVERALL LOOP FOR PIVOTS AND PIVOTAL REDUCTION
C
  M=4
  N=5
  DO 10 I=1,M-1
    BIGGST=0.
    DO 20 K=I,M
      ABSLTE=DABS(A(K,I))
      IF ((ABSLTE-BIGGST).GT.0.) THEN
        BIGGST=ABSLTE
        L=K
      ENDIF
20    CONTINUE
    IF (BIGGST.LE.0.) THEN
      WRITE(6,100)
100   FORMAT('ZERO PIVOT WAS ENCOUNTERED. NO SOLUTION')
      RETURN
    ENDIF
    IF((I-L).NE.0)THEN
      DO 30 J=1,N
        TEMPRY=A(I,J)
        A(I,J)=A(L,J)
        A(L,J)=TEMPRY
30    CONTINUE
      ENDIF
      PIVOT=A(I,I)
      NEXTRW=I+1
      DO 40 J=NEXTRW,M
        C=A(J,I)/PIVOT
        DO 40 K=1,N
          A(J,K)=A(J,K)-C*A(I,K)
40    CONTINUE
10   CONTINUE

```

Figure D1 Continued

```
C
C PERFORM BACK SUBSTITUTION AND COMPUTE X(I)
C
  DO 50 I=1,M
    IRZV=M+1-I
    Y=A(IRZV,N)
    IF((IRZV-M).NE.0)THEN
      DO 60 J=2,I
        K=N+1-J
        Y=Y-A(IRZV,K)*X(K)
60      CONTINUE
      ENDIF
      X(IRZV)=Y/A(IRZV,IRZV)
50    CONTINUE
C
  RETURN
  END
```